Exchange-, Non-Covalent- and Second-Sphere Interactions in Lanthanide Coordination Compounds: A Computational and Synthetic Approach

Zur Erlangung des akademischen Grades eines

Doktors der Naturwissenschaften

(Dr. rer. nat.)
von der KIT-Fakultät für Chemie und Biowissenschaften des
Karlsruher Instituts für Technologie (KIT)

genehmigte

Dissertation

von

Christian Franz Pachl

1. Referentin: Prof. Dr. Karin Fink
1. Referentin: Prof. Dr. Annie K. Powell
Tag der mündlichen Prüfung: 02.02.2026

Für meine Oma Ilse.

Abstract

This thesis provides new insights into three kinds of interactions applicable to lanthanide chemistry. These are exchange interactions, non-covalent bonding and second-sphere effects. Such effects were elucidated by theoretical and synthetic studies designed to highlight the respective interaction both individually and in combination. In the context of their relevance for lanthanide coordination compounds best practices to model these interactions computationally were established.

Firstly, exchange coupled 3d-4f and 4f-4f systems are investigated. In particular, it was shown how the electronic properties of single spin centers can be used to construct the magnetic properties in a series of exchange coupled dinuclear testbed complexes. Furthermore, the exchange coupling in dinuclear Gd(III)-compounds was investigated using Density Functional Theory (DFT) leading to proposing best practice workflows and the investigation of structure property relations.

Secondly, non-covalent halogen bonding interactions, which are largely unexplored in lanthanide chemistry, were investigated. Here computational model structures were investigated highlighting the influence of the metal center on the stability of the halogen interactions.

For the first time it was possible to show how cooperative effects between halogen bonds can stabilize a highly symmetric crystal structure for an inorganic coordination compound.
Finally, the importance of the second coordination sphere around the lanthanide ions was investigated. It was shown that the inclusion of these ions and molecules in the calculations can significantly alter the electronic structure through their electrostatic field and ligand polarization. Through a series of computational and synthetic studies it was established when such effects are important. The inclusion of such second sphere effects have indeed proven to improve the reproduction and simulation of experimental magnetic observables.

Zusammenfassung

Diese Arbeit liefert neue Einblicke zu drei Arten von Wechselwirkungen die für Lanthanidchemie relevant sein können: Die Austauschwechselwirkung, nicht-kovalente Bindungen und Einflüsse der zweiten Koordiantionssphäre. Diese Effekte wurden durch theoretische und synthetische Studien untersucht, die die verschiedenen Effekte und deren Wechselwirkungen beleuchten sollen. Im Hinblick auf die Relevanz für Lanthanidkomplexverbindungen wurden Rechenabläufe etabliert, um die drei Effekte bestmöglich zu modellieren.

Zuerst wurden austauschgekoppelte 3d-4f und 4f-4f Systeme untersucht. Es konnte gezeigt werden, dass die elektronischen Eigenschaften isolierter Spinzentren genutzt werden können, um die magnetischen Eigenschaften einer Reihe zweikerniger Komplexverbindungen zu modellieren. Außerdem wurde die Austauschkopplung in zweikernigen Gd(III)-Komplexen mit Dichtefunktionaltheorie (DFT) untersucht, so dass optimierte Rechenabläufe zur Simulation dieser etabliert und Struktureigenschaftsbeziehungen untersucht werden konnten.

Danach wurden nicht-kovalente Halogenbindungen untersucht, da sie im Bezug auf Lanthanidchemie weitgehend unerforscht sind. Hier wurden verschiedene computergestützte Modellstrukturen vorgeschlagen, die den Einfluss des Metallzentrums auf die Stablität der Bindung verdeutlichten.

Es konnte erstmals gezeigt werden, dass Kooperativität zwischen Halogenbindungen zu einer hochsymmetrischen Kristallstruktur einer Koordinationsverbindung führt.
Schließlich wurde die Bedeutung der zweiten Koordinationssphäre um das Lanthanidion auf dessen elektronische Eigenschaften untersucht. Hier konnte gezeigt werden, dass das Einbeziehen solcher Ionen und Moleküle durch eine direkte elektrostatische Wechselwirkung und Polarisation der Liganden einen signifikanten Einfluss auf die elektronische Struktur haben kann. Durch eine Reihe theoretischer und synthetischer Studien konnte gezeigt werden, wann dieser Effekt relevant wird. Es wurde etabliert, dass das Einbeziehen von Molekülen in der zweiten Koordinationssphäre zu einer Verbesserung der Simulation von experimentellen magnetischen Observablen führte.

Eidesstattliche Erklärung

Bei der eingereichten Dissertation zu dem Thema
Exchange-, Non-Covalent- and Second-Sphere Interactions in Lanthanide Coordination Compounds: A Computational and Synthetic Approach
handelt es sich um eine eigenständig erbrachte Leistung.

Ich habe nur die angegebenen Quellen und Hilfsmittel benutzt und mich keiner unzulässigen Hilfe Dritter bedient. Insbesondere habe ich wörtlich oder sinngemäßäus anderen Werken übernommene Inhalte als solche kenntlich gemacht.

Die Arbeit oder Teile davon habe ich bislang nicht an einer Hochschule des In- oder Auslands als Bestandteil einer Prüfungs- oder Qualifikationsleistung vorgelegt.

Die Richtigkeit der vorstehenden Erklärungen bestätige ich.

Die Bedeutung der eidesstattlichen Versicherung und die strafrechtlichen Folgen einer unrichtigen oder unvollständigen eidesstattlichen Versicherung sind mir bekannt.

Ich versichere an Eides statt, dass ich nach bestem Wissen die reine Wahrheit erklärt und nichts verschwiegen habe.

Karlsruhe, 17.12.2025 Christian Pachl

Abbreviations and Color Codes

AC	Alternating Current
ATR-IR	Attenuated Total Reflection Infrared
BCP	Bond Critical Point
BS	Broken-Symmetry
BSSE	Basis-Set Superposition Error
CAS	Complete Active Space
CASOCI	Complete Active Space Spin Orbit Configuration Interaction
CASPT2	Complete Active Space second order Perturbation Theory
CASSCF	Complete Active Space Self Consistent Field
CI	Configuration Interaction
CSM	Continuous Shape Measure
CSO	Corresponding Spin Orbital
DC	Direct Current
DKH2	Second Order Douglass-Kroll-Hess
DKH4	Fourth Order Douglass-Kroll-Hess

DFT Density Functional Theory

ECP Effective Core Potential

EDA Energy Decomposition Analysis

ELF Electron Localization Function

EPR Electron Paramagnetic Resonance

ESOs Extended Stevens Operators

GGA Generalized Gradient Approximation

HDvV Heisenberg-Dirac-van Vleck

HF Hartree-Fock

HS High-Spin

IUPAC International Union of Pure and Applied Chemistry

J Magnetic Coupling Constant

J Total Angular Momentum

KD Kramers' Doublet

LDA Local Density Approximation

LS Low-Spin

MAE Mean Absolute Error

MaxAD Maximum Absolute Deviation

MD Mean Deviation

MEP Molecular Electrostatic Potential

mGGA meta-Generalized Gradient Approximation

MMCT Metal-Metal Charge Transfer

NMR Nuclear Magnetic Resonance Spectroscopy

NPA Natural Population Analysis

PXRD Powder X-ray Diffraction

QTAIM Quantum Theory of Atoms in Molecules

QTM Quantum Tunneling of Magnetization

RMSD Root Mean Squared Error/Deviation

ROHF Restricted Open-Shell Hartree Fock

SCF Self-Consistent Field

SC-XRD Single Crystal X-ray Diffraction

SD Slater Determinant

SIM Single-Ion Magnet

SMM Single Molecule Magnet

SMT Single Molecule Toroic

SOC Spin-Orbit Coupling

SOMF Spin-Orbit Mean Field

SQUID Superconducting Quantum Interference Device

SR Symbolic Regression

UKS Unrestricted Kohn Sham

X2C Exact Two-Component Theory

XB Halogen Bond

XB_A Halogen Bond Acceptor

XB_D Halogen Bond Donor

XRD X-ray Diffraction

ZFS Zero Field Splitting

Molecular structures will consistently use the following color codes:

Table 1.: Atoms used in pictures in this thesis and their corresponding colors in the pictures.

Element	Color
Br	orange
C	gray
Cl	bright green
Co	light orange
Cu	cyan
Dy	lilac
Er	pink
F	gold
Gd, Ce, I	violet
H	white
K	tan
Mn	rose
N	dark blue
Na	turquoise
O	dark red
P	pink
S	yellow

All lanthanide ions investigated are in the oxidation state +III, all transition metal ions are, unless explicitly mentioned otherwise, in the oxidation state +II.

Contents

1. Introduction

The magnetic and optical properties of lanthanides have been the subject of many decades of research since Stevens proposed parameters quantifying the crystal field of lanthanides which is key to their electronic properties.[1] Over the past 70 years, increasingly convoluted methods were established in order to elucidate the lanthanide's electronic structure, bonding and properties.[2] This research benefited from the emergence of many powerful and useful computational techniques such as DFT,[3,4] Multireference Calculations[5–7] and Spin Hamiltonians.[8,9] These were used to gain deep insight into the origin of static and dynamic magnetic properties,[10] luminescence[11,12] and bonding of lanthanides.[13] Alongside this deeper understanding of the electronic structure, many outstanding properties and applications were found for example in laser-[14] and quantum technologies,[15] thermometry,[16] magnetic cooling[17] and high temperature single molecule magnets.[18]

The development of these technologies highlights how significant improvements in theoretical approaches support advances in applications and improvement in properties.[19,20] At the cutting edge of the second quantum revolution,[21] along with the emergence of more data driven analysis,[22] precise and fast computational methods modeling the properties of new materials are required.

Therefore, it is necessary to understand the strengths and limitations of current computational setups such as the recently proposed Complete Active Space Spin Orbit Configuration Interaction (CASOCI) program.
Three topics are investigated in greater detail:
1. The computational modeling of dinuclear lanthanide complexes has been standard practice for many years.[10] To date, workflows utilizing the substitution of paramagnetic ions with diamagnetic ions in multinuclear coordination compounds are often employed to probe the properties of isolated centers. This substitution is done purely computationally, but yields excellent results to interpret a wide range of experiments. Here, the same approach is tested on a set of 3d-4f-complexes which can be synthesized in order to validate the theoretical substitution.
Furthermore, Broken-Symmetry (BS)-DFT has become an invaluable tool to quantify the magnetic interaction between various spin centers. Here, Gd(III)-ions serve as important model structures for other lanthanides since they have an isotropic electron density distribution. In this thesis, the applicability of BS-DFT for Gd(III)-ions will be reevaluated, best practices suggested and structure property relationships, which have remained vague, elucidated.
2. Spin-Phonon relaxation dynamics are a bottleneck for high performance Single Molecule Magnets (SMMs) giving rise to the need to engineer the crystal packing of lanthanide coordination compounds.[23] Here, non-covalent interactions are an important tool in the crystal engineering toolbox. However, these influences have been hardly explored in their application to lanthanides beyond a geometrical analyses. Thus, the importance of halogen bonding for the crystal structure and magnetic properties is investigated here. This is done both computationally (*in-silico*) and experimentally (*in-vitro*) by including halogens in previously established ligand systems to form lanthanide SMMs.

3. In most quantum chemical calculations, only the first coordination sphere around the lanthanide ions is considered. Here, it will be shown when and how the second coordination sphere may influence the electronic structure of magnetic ions. Furthermore, a number of examples will be provided where the inclusion of larger crystal spaces beyond the first coordination sphere has significant influence on the results of calculations and furthers the understanding of the magnetic properties. This is done through the synthesis of new compounds and the investigation of compounds synthesized by collaborators.

These studies allow for a refinement of the computational workflow for magnetic lanthanide coordination compounds.

2. General Theoretical Background

In this chapter, a general, brief theoretical framework is provided for the following scientific work. This is divided in three sections. This thesis revolves around the magnetic properties of lanthanide containing compounds. In section 2.1 a short introduction into the current state of the art is given and pertinent research questions discussed in later chapters are outlined. In the second section, quantum chemical methods needed to address these questions are described. The last section introduces halogen bonding interactions between molecules in the crystal lattice. This supramolecular approach aims to address central challenges involving phonons in single molecule magnetism.

2.1. Single Molecule Magnetism in Lanthanides

The fact that magnetic hysteresis can be of molecular origin was first discovered for the famous Mn_{12}-molecule.[24–26] It was the first of many molecules found exhibiting this kind of behavior.[27–30]

Ten years later, Ishikawa and coworkers characterized the first lanthanide containing molecule showing such hysteresis, $TbPc_2$.[31]

Around this time, the phrase SMM was coined for molecules showing slow relaxation of their magnetic moment at low temperatures.[33] Two central goals were set for this field of research:

1. Understand and suppress magnetic relaxation processes, mainly quantum tunneling of magnetization.[33]

2. Find and implement possible applications in quantum information processing.[34,35]

Today, the origin of SMM-behavior of lanthanide containing complexes is largely understood based on their inherent electronic structure. The predominant effect splitting the energy-levels is the electron-electron repulsion. This gives rise to so called Russell-Saunders terms collecting the resulting configuration. Next, the obtained terms are subdivided by Spin-Orbit Coupling (SOC) with the ground-state being determined by Hund's rules. Each J-state is 2J+1-fold degenerate. This degeneracy can be lifted by an external electrostatic field, such as the crystal field.[32,36] If J is odd, the m_J-sublevels will be two-fold degenerate according to Kramers' theorem. Such two-fold degenerate states are called Kramers' Doublets (KDs).

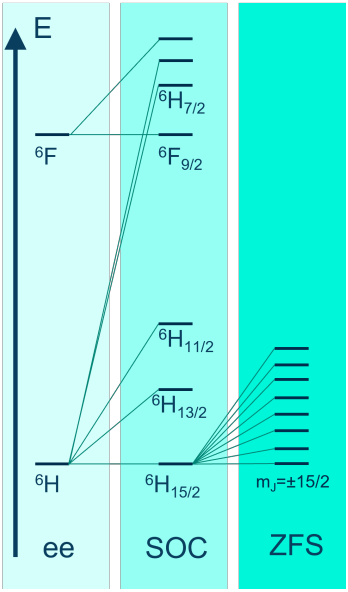

Figure 2.1.: Qualitative Scheme of the Level splitting in a Dy(III)-ion. Electron-electron Repulsion is the largest effect, after which Spin-Orbit-Coupling and Zero Field Splitting have to be considered. Adapted from Ref. [32].

These are the states relevant for magnetic bistability which can be lifted by an external magnetic field.[32] For most lanthanide ions, the lowest J-multiplet is well separated from excited multiplets and the states split by Zero Field Splitting (ZFS) are the only ones thermally accessible.[36–38] Due to the unpredictable coordination environment of lanthanides, modeling the ZFS requires crystal field parameters based on higher order spherical harmonics called Extended Stevens Operators (ESOs).[1] These are a generalization of the simple axial and rhombic crystal field operators D and E.[39] These integrate the anisotropy and splitting of the lowest J-manifold.[32]

Relaxation of the magnetic moment can occur through two kinds of processes dictating different design principles for high-performance SMMs. Firstly, direct tunneling between degenerate states is forbidden by time-reversal symmetry. However, a slight lifting of the doublet's degeneracy can lead to Quantum Tunneling of Magnetization (QTM).[40–42] Hyperfine interaction[43–45] and long-range dipolar coupling can cause such lifting of the degeneracy.[46] These effects are amplified by large transverse components of the KDs g-tensor. Consequently, the design principles to suppress the respective processes are to minimize transversal components by imposing a strictly anisotropic and/or symmetric crystal field,[19,47–49] removing nuclear spins,[44,45,47,50] and spatially separating the spin centers.[44,45,47,51]

The second class of relaxation processes is mediated through lattice phonons and/or molecular vibrations.[42,52,53] These can involve either one (direct) or two (Raman, Orbach) phonons.[54,55] In short, spin-phonon coupling facilitates magnetic relaxation by coupling the crystal-field Hamiltonian to the normal modes of lattice vibrations.[55–58]

For example, it has been suggested that a major relaxation pathway in high performing dysprosocenium Single-Ion Magnets (SIMs) is through the coupling to the molecule bound H-atom vibrations.[18] The underlying design principle therefore appears straightforward but is difficult to achieve synthetically. In addition to the design principles already discussed to suppress QTM, one needs to stiffen the environment around the magnetic center in order to shift phonon frequencies as high as possible, while ensuring that the local crystal field is not affected by the remaining lower frequency vibrations.[52,55,58] Furthermore, there are indications that the hyperfine interaction enhances magnetic relaxation through coupling to phonons.[59,60]

All the previously discussed methods to influence the magnetic behavior can be realized in single ion magnets. Alternative approaches do not take the intrinsic electronic structure of lanthanide ions for granted. Instead, the ground state is modulated through the coupling of several spin centers. This can be done in many ways. The spins of 4f-ions can be coupled to 3d-ions,[61–63] other 4f ions[64–66] or radical spins on the ligand.[67–69] The coupling can also be mediated between two metals through radical bridges,[70–73] directly between ions through mixed valence compounds[74] or arguably by coupling with itself in unusual oxidation states.[75]

With respect to quantum applications of SMMs, significant advances have been made in the past 20 years. The tunable characteristics of SMMs, such as $TbPc_2$, made them potential candidates for a large number of possible applications.[15,76–78] So far, molecular magnets have been used in terms of single molecule transistors[79–81] and applications in quantum sensing.[82–84] Furthermore, it was possible to implement a number of quantum gates and algorithms.[85–89] However, the great majority of the vast chemical space accessible for such applications has not yet been fully explored.[15]

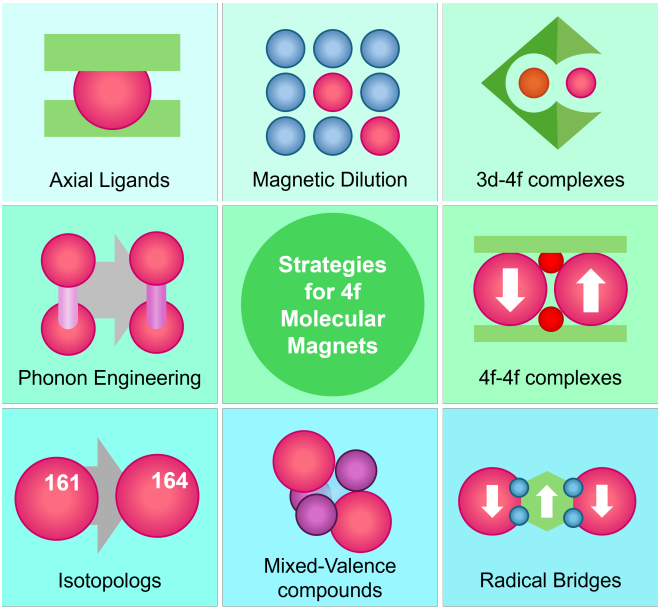

Figure 2.2.: Different strategies to influence the magnetic properties of 4f-SMMs: 1. The use of axial ligands (e.g. Cp) 2. Magnetic dilution in an Y-matrix 3. Coupling 3d with 4f-ions (e.g. with compartmental ligands) 4. Engineering phonon energies (e.g. through intermolecular interactions) 5. Coupling of 4f-ions in one molecule 6. Isotopolog-enrichment 7. Metal-Metal bonding in mixed valence compounds 8. Using bridges carrying organic radicals.

2.2. Quantum Chemical Description

The extensive research in the field of SMMs gave rise to a large number of theoretical models to explain the experimentally observed phenomena. In the following, an overview of some essential concepts and methods used in this thesis will be discussed.

2.2.1. Complete Active Space Spin Orbit Configuration Interaction (CASOCI)

A key requirement for electronic structure theory methods used in this research is that they need to be able to reproduce the energy spectrum shown above in Figure 2.1. For example, due to the near-degeneracy of 4f-orbital energies, this requirement generally cannot be fulfilled by single-determinant methods.[32] The electronic wavefunction needs to be constructed by considering different orbital occupation configurations simultaneously.[32] In general, this can be achieved by using a linear combination of excited orbital occupation configurations (Slater Determinants (SDs)) which refers to Configuration Interaction (CI) methods.

$$\Psi = a_0\phi_{HF} + \sum_S a_S\phi_S + \sum_D a_D\phi_D + ... \tag{2.1}$$

Ψ is a CI wavefunction constructed from excited Slater Determinants ϕ weighted by CI-coefficients a. By defining an orbital set in which all possible configurations are considered, one arrives at Complete Active Space (CAS) methods.[90] configuration.[90] The abbreviation CAS therefore refers to a restriction of the excitations to a selected orbital space. The method Complete Active Space Self Consistent Field (CASSCF) optimizes both the CI-coefficients and MO-coefficients iteratively.[90]

To treat the electronic structure of lanthanides, SOC needs to be considered explicitly.[32] This can be done fully variationally by optimizing both CI and MO coefficients.[91,92] However, the effect on the CI-coefficients is significantly stronger than that on the molecular orbital (MO)-coefficients in the SDs ϕ.[91] Thus, SOC is mostly included in a CI-calculation on top of a CASSCF calculation.[93,94]

A Breit-Pauli Operator can be introduced to describe SOC. It can be separated into one- and two-electron contributions.[95,96] In order to avoid the computationally costly two-electron part, it is commonly approximated as an effective one-electron operator in which an electron only experiences an average (mean) field of the other electrons. This is called the Spin-Orbit Mean Field (SOMF) approach.[95,96]

The method used predominantly in this thesis is called Complete Active Space Spin Orbit Configuration Interaction (CASOCI). Here, a CAS-space is set up using the magnetic orbitals.[7] The Configuration Interaction matrix considering all determinants possible in this space and including SOC is diagonalized in a one-step Block-Davidson diagonalization.[97] This is done using a Hamiltonian of the form:

$$\hat{H} = \hat{H}_{sc} + \hat{H}_{SOC} + \hat{H}_{Ze} + \hat{H}_{MCASCI}. \tag{2.2}$$

$\hat{H}_{sc}$ denotes the scalar relativistic Hamiltonian in the Born-Oppenheimer approximation and $\hat{H}_{Ze}$ the Zeeman-Hamiltonian. $\hat{H}_{MCASCI}$ is a modified CAS-CI Hamiltonian related to energy corrections of charge-transfer states, which is not relevant to this thesis.[98]

A benefit of the method is that the Block-Davidson diagonalization yields the wavefunctions in the form of CI-vectors for each eigenvector (state) of the CI matrix. This means that the properties of each state can be investigated individually in a second step using a pseudospin formalism. This is essentially a dimensionality reduction. A pseudospin $\tilde{S}$ is used to describe a $2\tilde{S}$+1-manifold of wavefunctions. For example, a pseudospin $\tilde{S}$ = 1/2 can be used to describe an isolated Kramers' Doublet with a plus and minus component. Using this formalism, different properties such as g- and D-Tensors,[99,100] the susceptibility, magnetization and transition dipole moments can be calculated.[7,101]

At this point, it makes sense to clearly differentiate the benefits and drawbacks of the CASOCI program with respect to other methods as implemented for example in the program MOLCAS.[6,102,103]

- In CASOCI, a single CI calculation is performed without relaxation of the MO-coefficients. This makes the method more dependent on the starting MOs. This feature will be further examined in this work.
- No dynamic correlation is considered in CASOCI other than that captured within the active space. Excitations outside the active space, such as in Complete Active Space second order Perturbation Theory (CASPT2) as implemented in MOLCAS are not considered.[6] This is linked to the next point.
- Since both the CI and SOC are done in a single step, the CASOCI-calculation on a small active space is generally performed in a few seconds at most. In comparison, CASPT2 calculations can become computationally very costly.[98,104]
- In most methods, one needs to define a number of states that should be coupled within the SOC-scheme, all of which have to be calculated and stored. This can become very costly when many excited states are included. In CASOCI, all configurations are included which means that the CI-space is significantly enlarged. Fortunately only a small number of spectroscopically relevant states need to be saved.[7]

Despite the differences, these methods yield very similar results and for most applications the choice is a matter of preference rather than necessity.

2.2.2. Broken-Symmetry Density Functional Theory

The energy splitting caused by the interaction between two magnetic ions can be described by an effective Spin Hamiltonian, the Heisenberg-Dirac-van Vleck (HDvV)-operator acting on the two spins of the magnetic centers.[36]

$$\hat{H}_{ex} = -2J_{12}\hat{S}_1\hat{S}_2 \tag{2.3}$$

It should be noted, that the pre-factor 2 (or the sign) is sometimes omitted in this equation,[105] but will be used consistently in this thesis. Equation 2.3 can be rewritten to only use $\hat{S}^2$-expectation values.[105]

$$S_t = |S_1 + S_2|, |S_1 + S_2 - 1|, ..., |S_1 - S_2| \tag{2.4}$$

$$E(S) = -J_{12}\left[S_t(S_t + 1) - S_1(S_1 + 1) - S_2(S_2 + 1)\right] \tag{2.5}$$

Two coupled spins S_1 and S_2 give rise to a spin-ladder, dependent on the coupling constant *J*. As is clear from this equation, the highest spin state will be the ground state in the case of a positive coupling constant (ferromagnetic) while the lowest spin state will be the ground state in the case of a negative coupling constant (antiferromagnetic).

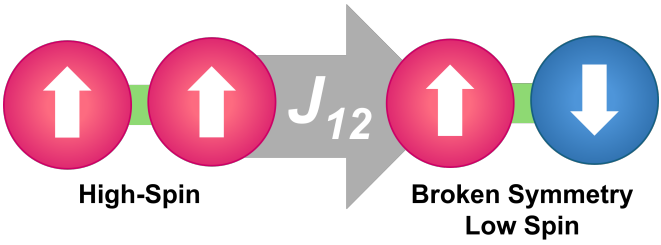

Figure 2.3.: Schematic representation of the Broken-Symmetry approach: First, a high spin ground state is constructed, for which the spins are localized and flipped at one center. The energy-difference is then related to the coupling constant *J*.

The energy difference between these states can be approximated with Noodleman's Broken-Symmetry (BS) approach using DFT.[106] Here, the magnetic orbitals of a High-Spin (HS)-calculation are localized to the magnetic centers and the spins located at one are flipped from α to β. Using this approach, Yamaguchi proposed a formula to obtain the coupling constant.[107]

$$J = \frac{E_{HS} - E_{LS}}{\langle S^2_{LS} \rangle - \langle S^2_{HS} \rangle} \tag{2.6}$$

In comparison to other approaches,[106,108,109] this formula intrinsically corrects for non-physical spin contamination of the density.[107,110] For this reason, this approach will be used for calculations on compounds containing 4f-ions described in later chapters.
Importantly, the coupling constants discussed later are very small. However, one needs to remember that the absolute energy difference calculated was divided by the difference in S^2, which meant that the absolute energy difference is often much larger, especially for high spin multiplicities.

2.3. Halogen Bonding

The influence of non-covalent intermolecular interactions on crystal structures of lanthanide containing molecules will be discussed in this thesis. That being said, the term "non-covalent intermolecular interactions" is fairly broad and covers a number of weak bonding interactions. The most common are hydrogen bonds between a positively polarized hydrogen atom and a negatively polarized Lewis base.[111,112] Further common interactions are π-interactions involving at least one π-system,[113–118] van der Waals interactions,[119–122] and metallophilic interactions.[123–126]

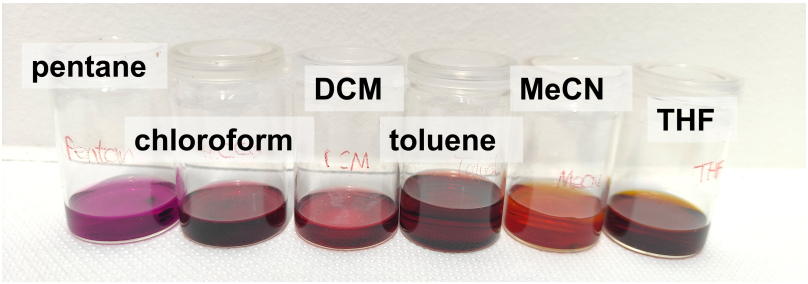

Figure 2.4.: Elemental iodine dissolved in different organic solvents. From left to right: pentane, chloroform, dichloromethane, toluene, acetonitrile, tetrahydrofuran.

Another important group involves σ-hole interactions,[127] which can be realized through halogen-,[128–130] pnictogen-,[131,132] chalcogen-,[133–136] and tetrel-bonding.[137–139] The σ-hole concept can be expanded to a number of other unusual interactions.[140–143] Many of the aforementioned bonding types can be found in lanthanide containing complexes.[144] However, this thesis will focus mainly on halogen bonding interactions.

Halogen Bonding describes a set of anisotropic, weak bonding interactions between two halogen atoms or a halogen atom and an electron density donor.

The origin of such interactions has been the subject of intense research since their discovery in the 19th century.[145,146] At the time, the formation of a metallic liquid from iodine and ammonia as well as differently colored solutions of iodine (see Figure 2.3) sparked the interest of a number of scientists.[128,145,146] In the mid-20th-century, halogen bonded pairs were modeled as charge transfer complexes. The rationale was simple: a bonding σ-orbital will be polarized towards its bond. Consequently, the corresponding anti-bonding σ^*-orbital is localized away from that bond, in fact exactly opposite to it.

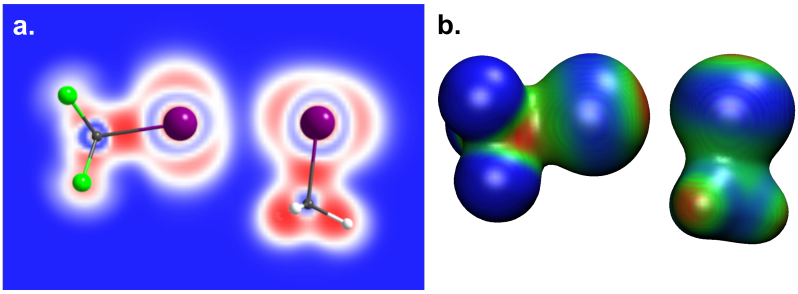

Figure 2.5.: Representations of the interaction between a CF_3I and a CH_3I molecule. a. Electron localization function and molecular structure (C: gray, F: green, H: white, I: purple) b. Molecular electrostatic potential at ρ = 0.02, V_{pot} = 0.05 (blue) - 0.18 (red). Calculation carried out on a m06-d4/rij/def2-TZVP(I),def2-SVP(C,F,H), grid = 7 level of theory.

This unoccupied, de-shielded orbital can now be involved in a charge-transfer interaction with electron density donors.[147–150]
This concept was later overhauled when Politzer and Murray suggested that these interactions are predominantly electrostatic in nature. In this model, electron density is withdrawn from the halogen atom along the R-X bond-axis since the orthogonal halogen-p-orbitals do not contribute to the covalent bond. This leaves an anisotropic electron density around the halogen resulting in a partially positively charged area opposite to the σ-bond, named the σ-hole.[151–153] It can be visualized through the Molecular Electrostatic Potential (MEP) V_{pot} or the Electron Localization Function (ELF).[90,154,155] Figure 2.5 shows the interaction between CF_3I and CH_3I using ELF and MEP plots. The p-orbital belt around the iodine can be seen as red bulges in the ELF and a blue belt in the MEP. The σ-hole equates to an area of low localization in the ELF and to the most positive area at the iodine atoms in MEP.

This picture captures how the p-orbitals of CH_3I are oriented towards the σ-hole of CF_3I, a key feature of σ-hole interactions.
Nowadays, it is widely recognized that orbital-, electrostatic- and dispersion-contributions act simultaneously to stabilize halogen bonding.[156–159]
Regarding terminology, the Halogen Bond Donor (XB_D) is the R-X molecule which is the electron density acceptor in the charge transfer picture. The Halogen Bond Acceptor (XB_A) is the electron density donor, here called Y in Figure 2.6. Y can be another halogen, an atom with a lone pair, or a π-system. This nomenclature can be confusing. In Figure 2.5 the CF_3I molecule is the XB_D whereas CH_3I acts as the XB_A.
In 2013, the International Union of Pure and Applied Chemistry (IUPAC) defined ten features characterizing a halogen bond:[160]

- The bond distance is shorter than the sum of the van der Waals (v.d.W.) radii.
- The R-X bonds are elongated compared to the free molecule.
- The R-X$\cdots$Y angle is close to 180°.
- The more electron-withdrawing the residue R, the more stable is the halogen bond.
- The halogen bond is largely, but not exclusively, stabilized by electrostatics.
- There is a saddle point (BCP) of the electron density along the bond path.
- The halogen bond influences the vibrational spectra of the molecule.
- The halogen bond donor experiences a hypsochromic shift in its UV-Vis absorption spectra.

- Nuclear magnetic resonance chemical shifts of both interacting molecules are influenced.
- X-ray photoemission binding energy peaks shift to lower energy compared to the free R-X.

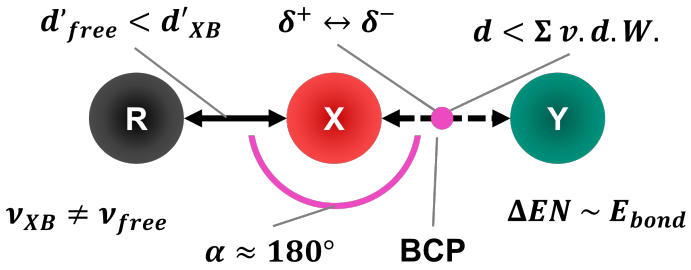

Figure 2.6.: Graphical representation of the seven features of halogen bonding which will be relevant to this thesis. Top from left to right: The bond distance of R-X increases compared to the free molecule, the interaction is largely electrostatic and the XB-distance is smaller than the sum of v.d.W-radii. Bottom from left to right: the molecular vibrations are influenced, the bond angle is close to 180°, there is a bond critical point (BCP) and the bond energy is influenced by electronegativity.

It should be noted that not all of these features need to be satisfied to characterize a halogen bond.[160] The seven characteristics which will be investigated in this thesis are represented in Figure 2.6.
XBs have long established themselves as an important tool in the crystal engineering toolbox for a wide range of applications.[161–163] This also becomes important in the context of SMMs. There are several indications that magnetic coupling can be mediated *via* halogen bonds in metal complexes and organic radicals.[164–167] For lanthanide complexes, compounds were published featuring halogen bonding, but no influence on the magnetic properties has been reported so far.[168–173]

Considering that magnetic superexchange interactions play a minor role in lanthanide compounds, it is not to be expected that halogen interactions will effect them significantly. However, a precise control of phonons is required in order to suppress spin-phonon-relaxation. Given all of the above, halogen bonding interactions could make the crystal lattice more rigid and therefore enhance magnetic properties.

3. Exchange Coupled Lanthanide Systems

3.1. Introduction

The theoretical framework of Spin Hamiltonians for magnetic exchange was first proposed by Heisenberg and expanded by van Vleck and Dirac.[8,174,175]

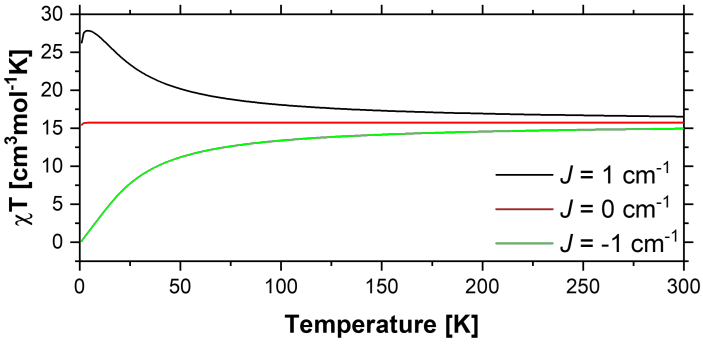

Figure 3.1.: χT-plot of two S = 7/2 spins interacting via a coupling constant J = -1 cm^{-1}, 0 cm^{-1} and 1 cm^{-1}.

In 1951, Guha measured the magnetic susceptibility of various transition metal salts.[176] One year later, Bleaney and Bowers published a landmark paper explaining the anomalous behavior of copper acetate monohydrate $Cu_2(OAc)_4(H_2O)_2$. They suggested that antiferromagnetic exchange coupling between two Cu-ions is responsible for a drop of the susceptibility at low temperatures.[177] Therefore, they derived a formula to model this behavior.[177] This was corroborated by a few similar studies modeling the magnetic interaction between ions anisotropically and including spin-dipolar interactions.[178–180]

Figure 3.1 shows the χT-plot of two S = 7/2 spins for different coupling strengths. This data can be obtained experimentally from Direct Current (DC)-Superconducting Quantum Interference Device (SQUID) measurements from which the magnetic coupling constant can be extracted in a few different ways:

1. Expanding the free energy of a magnetic system as a power series dependent on the magnetic field H and calculating the second derivative, van Vleck obtained an analytic formula for the molar magnetic susceptibility.[175]

$$E_n = E_n^{(0)} + E_n^{(1)}H + E_n^{(2)}H^2 + ... \tag{3.1}$$

$$\chi T = N_A\mu_0 \cdot \frac{\sum_n \left[\left(\frac{{E_n^{(1)}}^2}{kT} - 2E_n^{(2)}\right) \cdot exp\left(-\frac{E_n^{(0)}}{kT}\right)\right]}{\sum_n exp\left(-\frac{E_n^{(0)}}{kT}\right)} \tag{3.2}$$

In this equation, N_A is Avogadro's constant, k Boltzmann's constant and T the temperature. $E_n^{(0,1,2)}$ are the energy contributions depending on their exponent of the magnetic field.

Using this van Vleck equation for the susceptibility, Bleaney and Bowers derived their formula for the coupling of two spin systems by introducing a HDvV-operator ($\hat{H} = -2J\hat{S}_1\hat{S}_2$) to describe the coupled spins. This energy contribution is included in $E^{(0)}$ since it does not contain the magnetic field. Thus a Spin Hamiltonian containing a coupling and Zeeman term is used:

$$\hat{H} = -2J\hat{S}_1\hat{S}_2 + \sum_{i=1,2} \mu_B g \hat{S}_i B.$$

This equation is also dependent on the Landé-factor g, Bohr's magneton μ_B and the coupling constant *J*. The resulting equation for two coupled S = 7/2 spins can be directly fitted to the experimental data with only two free variables g and *J*.[177,181]

$$\chi_m T = \frac{2N_A\mu_B^2 g^2}{k} \cdot \frac{e^{2J/kT} + 5e^{6J/kT} + 14e^{12J/kT} + 30e^{20J/kT} + 55e^{30J/kT} + 91e^{42J/kT} + 140e^{56J/kT}}{1 + 3e^{2J/kT} + 5e^{6J/kT} + 7e^{12J/kT} + 9e^{20J/kT} + 11e^{30J/kT} + 13e^{42J/kT} + 15e^{56J/kT}} \tag{3.3}$$

The exponents are the energies of the different coupled spin states, while the pre-factors in the denominator are their degeneracy.

2. It possible to fit the susceptibility using the Lines model as implemented for example in the program PHI.[182] In its original form, the Lines model was used to compute the susceptibility of orbitally degenerate Co(II) ions.[9] Here, the isotropic coupling between two ground states multiplet is calculated exactly as two pseudospins 1/2. However, thermally excited KDs are treated through temperature dependent effective g-values and spin expectation values.[9] In effect, this model aims to reduce the computational demand by treating the interaction between the ground state KDs exactly, while treating the coupling in excited states of the HDvV-operator through an effective field.[183]

This is done in the basis of $|L_i, m_{L_i}, S_i, m_{S_i}\rangle$ wavefunctions through a Clebsch-Gordon decomposition.[182,183]

3. The original lines model was then generalized through the inclusion of excited states arising from ZFS.[182,183] This can be done for example through Extended Stevens Operators (ESOs) which are more general crystal field operators than D and E.[1,184] All ZFS-operators can be calculated, for example, using the CASOCI-program. Furthermore the Lines model as implemented in PHI was generalize to also act on the $|J_i, m_{J_i}\rangle$ basis and include anisotropic exchange coupling.[182]

The magnetic coupling constant can also be obtained from EPR,[185] μ-SQUID[66,186,187] and Inelastic Neutron Scattering measurements.[188–190] This is important since these interactions are in part responsible for a number of magnetic properties such as SMM-behavior,[65,185,191,192] magnetocaloric effects[17,193–197] and exotic spin states such as Single Molecule Toroics (SMTs).[10,198,199]

Quantum chemical calculations can be invaluable to interpret experimental observations. To date, a number of computational methods is established to calculate exchange couplings. While there are several CAS-based methods,[200,201] the most commonly used method is BS-DFT, as discussed in Section 2.2.2. The central drawback to this method is that it is highly dependent on the often arbitrary choice of functional.

With respect to transition metals, Cu(II)-dimer structures have been the subject of intense research with BS-DFT. One of the main findings is that the accuracy of the calculations is strongly dependent on the amount of Hartree-Fock (HF)-exchange.[202–206] Further studies suggest that range-separated functionals perform somewhat better than hybrid functionals.[207]

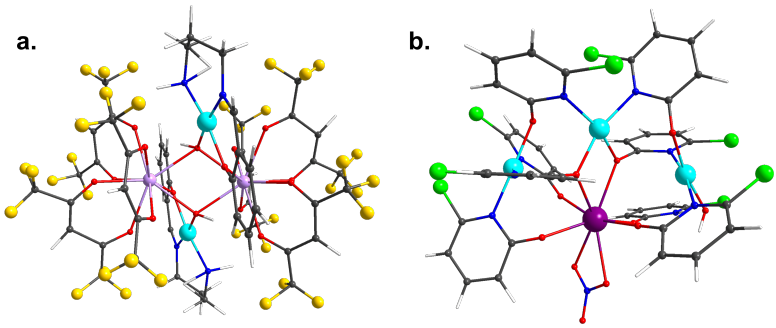

Figure 3.2.: Two important complexes in the study of 3d-4f interactions: a. The first complex for which the importance of charge transfer to the ferromagnetic coupling between Cu and Gd (the Dy-analogue is shown here) was hypothesized.[212] b. The crucial compound in the first study emphasizing the importance of the Gd-Cu distance on *J*.[211]

The combination of Cu(II) and Gd(III) is perhaps the most studied 3d-4f combination.[208–212] It is suggested that spin polarization is a central pathway to stabilize the ground state. Further studies showed that an explicit treatment of relativistic effects is needed whereas the basis set influence is minor.[213,214] It generally suffices to treat only scalar relativistic effects whereas SOC can be neglected for Gd(III).[213,215,216]

A number of studies by the Rajaraman group revolves around other 3d-4f combinations[213,217–220] as well as interactions between organic radicals and 4f-ions.[221] There are several key findings: **1.** The overlap between non-orthogonal magnetic orbitals is an important pathway for antiferromagnetic coupling. **2.** The inclusion of scalar relativistic effects is mandatory, with relativistic Effective Core Potentials (ECPs) being sufficient. **3.** A dependency of J on the amount of HF-exchange was reported. **4.** A key structure property relationship is found between the Gd-bridge-metal angle and J.

While BS-DFT calculations on Gd_2-structures have been standard practice for over 20 years, no conclusive and broad benchmarks have been reported.[222] One of the few perspectives on this topic was published in 2013 by Rajaraman *et al.*[216] They concluded that both pure DFT functionals and hybrid functionals give comparable results in the case of two carboxylate bridged dimers.

In light of these studies it is worth reiterating what facilitates magnetic exchange interactions. This is relevant because the underlying mechanisms dictate the requirements for different computational models. In principle, there are three different exchange mechanisms:[200]

1. Direct exchange occurs when the orbitals of magnetic centers overlap. It can be separated into ferromagnetic potential exchange and antiferromagnetic kinetic exchange. It is worth noting that especially the antiferromagnetic contribution is dependent on the direct mixing of the two sites' orbitals.

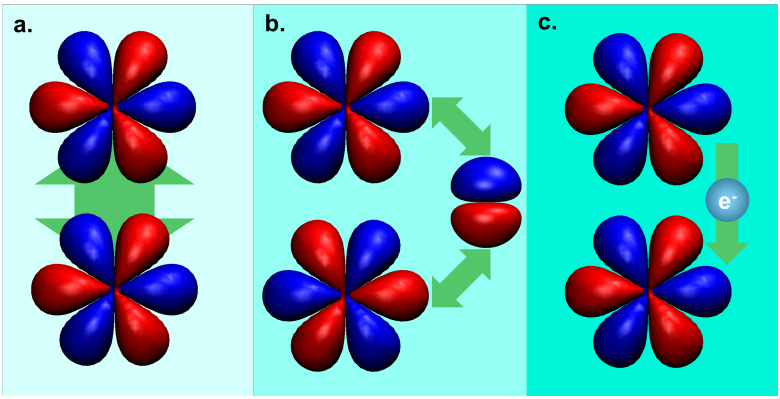

Figure 3.3.: Overview over the three different types of exchange mechanisms. a. Direct exchange between two orbitals. b. Superexchange via a ligand orbital with the correct symmetry. c. Double exchange via the transfer of one electron from one center to the other.

The largest energy contribution here is the kinetic energy operator through the delocalization of electrons.[223]

2. Superexchange occurs when the two interacting atoms are further apart and the exchange is mediated through a doubly occupied ligand orbital.[200] This type of coupling is dependent on the degree of covalency between the spin center and bridge.[224] Consequently, there is a strong dependence on the bridging angle and symmetry.[225,226]

3. The last pathway is double exchange and is related to Metal-Metal Charge Transfer (MMCT) as originally introduced by Zener.[200,227] The original model implied an electron resonating between the two sites.[227,228] Because of Hund's rules, this interaction will lead to both sites aligning their spin and therefore a ferromagnetic interaction.[200] A double-exchange type of pathway is established to be the major route for ferromagnetically coupled 3d-4f pairs. In this case, an electron is excited from a 3d-orbital to a 5d-orbital of the lanthanide.[211–213] Importantly, a correct treatment of this pathway would require a CAS-based method including the MMCT-states in a very large active space.

The following chapter will focus on the calculation of magnetic exchange coupling constants using BS-DFT. It is separated into two parts: In Section 3.2, the coupling and SMM properties of 3d-4f isostructural compounds will be investigated. In Section 3.3 the application of BS-DFT on gadolinium dimer structures is reevaluated in a benchmark study with a view to disentangling structure property relationships.

3.2. 3d-4f Heterobimetallic Compounds

In the following, a series of compounds synthesized by Daniel Seufert, Dr. Ghulam Abbas as well as Peer Räke are described and evaluated. These utilize the bipocket btmp (2-(2-benzothiazolyl)-6-methoxyphenolat$^-$) ligand to incorporate a divalent transition metal ion and a trivalent lanthanide ion (see Figure 2.2).
In the following section, this system is first analyzed to quantify the similarities in a set of isostructural coordination compounds with M = Co(II), Zn(II) and Ln = Y(III), Gd(III), and Dy(III). Afterwards, a small study is conducted to find a suitable method for calculating the exchange coupling constant. This was conducted as part of Franziska Gebhard's Vertiefer-thesis supervised in the context of this dissertation project.
Next, single ion properties were computed and coupled with each other to simulate experimental susceptibilities and magnetization. It will be shown that the theoretical approach when calculating the properties of 3d-4f-heterobinuclear complexes can be recreated 1:1 using synthetic efforts. Finally, this approach will be extended by evaluating the properties of the Tb, Ho and Er isostructural complexes. Here, it will be proposed that it is not necessary to obtain the crystallographic data of each lanthanide analogue.

3.2.1. Introducing the Ideal Testbed Structures

The six isostructural compounds [M(II)(μ-btmp)$_2$(μ-piv)Ln(III)(piv)$_2$] with M = Co, Zn and Ln = Y, Gd and Dy form the "ideal testbed". The structure of the complexes is depicted in Figure 3.4.

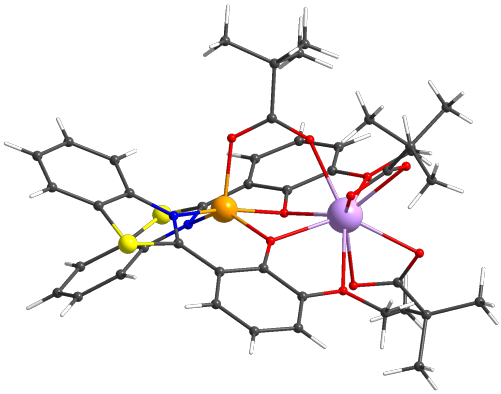

Figure 3.4.: Molecular structure of the ideal testbed as represented by the **(CoDy)** complex.

The magnetic characterization was performed by Dr. Sören Schlittenhardt and Dr. Barbora Brachňaková from the Ruben group at KIT and analyzed by Daniel Seufert. The topological analysis, quantum chemical calculations and fitting of the DC magnetic data are part of this thesis. All compounds within this series will be referred to **(MLn)** (e.g. **(CoDy)**).

In this ideal testbed, the transition metal (M) and lanthanide (Ln) are bridged via two btmp$^-$ ligands and a pivalate ion. Furthermore, two additional pivalate ions complete the coordination sphere of the lanthanide. Consequently, the transition metal is five-fold coordinated, whereas the coordination number for the lanthanide is nine. The metal-metal distance is 3.40 Å for **(CoDy)**.

In the following, the structural similarities between the compounds **(ZnDy)**, **(CoDy)** and **(CoY)** will be discussed. This is important in order to establish that the equivalency in the ions' electronic structure is rooted in the geometric similarity (Tables A.1–A.4).

All structures crystallize in the space group $P2_1/c$. The lattice parameters a, b and c are between 19.15-19.21 Å, 12.15-12.17 Å and 19.51-19.55 Å respectively. The angle β lies between 107.15° and 107.33°, making the unit cells extremely similar.

The coordination polyhedra of Co and Dy in **(CoDy)** are displayed in Figure 3.5. The equivalency of the coordination environment of the lanthanide and transition metal in the different compounds can be evaluated in two ways. The SHAPE analysis[229,230] will give information about the coordination symmetry while a Root Mean Squared Error/Deviation (RMSD) gives information about the deviation between the polyhedra. The polyhedron with the lowest continuous shape measures (CSM) around the transition metal is calculated to be a trigonal bipyramid between 2.273 **(CoDy)** and 2.315 **(CoY)**. The next best fits are square based pyramids or a vacant octahedron, the CSM-values are marginally less in agreement for **(CoDy)** and **(CoY)**. The full information can be found in the appendix. The CSMs for Dy (Y) reveal a capped square antiprism (CSM between 1.720 and 1.788) or a muffin type (CSM between 1.806 and 1.892) shape. The relevance of these values is not the type of polyhedron itself, but rather a low deviation in CSM between the different structures. Importantly, by comparing different polyhedra as calculated by SHAPE, one can get a sense of the similarity in angels between the structures.

Finally, the first sphere coordination polyhedra are compared in terms of their RMSD values. The a RMSD-value is dependent on a correct ordering of the atoms which is not necessarily the same in the different cif files. Furthermore, the structures to be compared might be inverted. Consequently, each permutation-inversion combination was tested. A Kabsch-algorithm is employed to ensure that the two structures compared are oriented optimally in space.[233] Finally, the RMSD value is calculated by averaging the absolute distances between corresponding vertices and

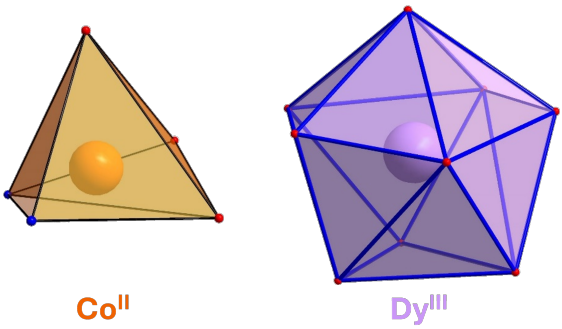

Figure 3.5.: The coordination environment of the Co(II) (left) and Dy(III) (right) in compound **(CoDy)**. This figure was supplied by Daniel Seufert.

taking the square root. Through this procedure, the minimal RMSD between the two compared structures was computed.

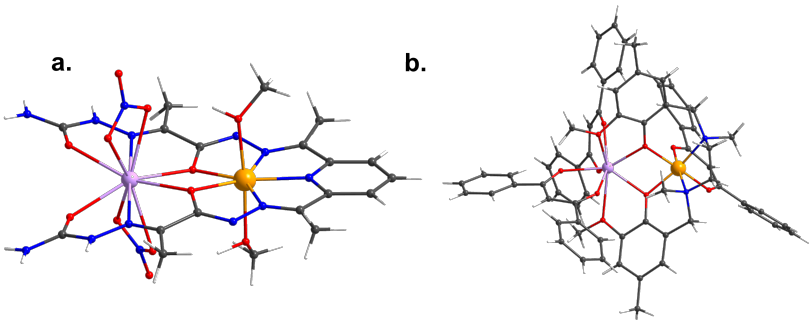

Figure 3.6.: Molecular structures of the two other isostructural Co/Zn-Dy/Y compounds as published by Shen (a.) and Xie (b.).[234,235]

This will result in a number quantifying how closely related two structures are. This analysis was performed for each combination amongst the three compounds. The RMSD value for the Dy (or Y) coordination polyhedra is 0.061 between **(CoDy)** and **(ZnDy)**. Comparatively, the deviation between **(ZnDy)** and **(CoY)** is 2.150 while it is 2.605 between **(CoDy)** and **(CoY)**. Without context, these values seem rather arbitrary. To the best of our knowledge, there are only two more isostructural sets of CoY, CoDy and ZnDy in literature (Figure 3.6). These were published by Shen *et al.*[234] and Xie *et al.*[235] The same geometric features are calculated for these two sets of compounds and summarized in the appendix. Comparing the structures published by Shen *et al.*, it is worth noting that the CoY-complex crystallizes in the space group $C2/c$, while the other two complexes crystallize in $P2_1/c$. Furthermore, while all compounds published by Xie *et al.* crystallize in $P\bar{1}$, the CoDy version crystallizes with 3.5 units of acetonitrile slightly distorting the structure. This highlights the difficulties in obtaining a set of perfectly isostructural compounds.

In summary, there is a number of reasons why this is an ideal testbed to probe 3d-4f interactions:

- The compounds are dinuclear. Therefore there is only one magnetic interaction to be investigated.
- Each paramagnetic ion can be substituted with a diamagnetic ion without structural distortion. This means all compounds are perfectly isostructural as discussed before.
- The compounds are crystalline, stable in air and water while not containing lattice solvent. This facilitates the evaluation of the SQUID results.

These features are especially intriguing considering the computational workflow investigating exchange-coupled multinuclear molecules. Usually, it is assumed that the single-ion properties of all paramagnetic ions couple perturbatively to the properties of the cluster.

In the computational workflow, one first substitutes all but one ion with diamagnetic alternatives and calculates the properties of the remaining center. This is done for all centers. In a second step, the single ion properties are connected by the coupling parameter *J*. The ideal testbed allows to follow this workflow by experimentally confirming each intermediate step (see Section 3.2.3).

3.2.2. Evaluating Gd-Mn Exchange Coupling Constants

The results of the following section are part of a Vertiefer thesis by Franziska Gebhard.[236] The aim was to find a suitable computational workflow to compute 3d-4f exchange coupling constants using BS-DFT. This was done by investigating a similar complex published by Oyarzabal *et al.* (Figure 3.7)[237] and testing the influence of various DFT-parameters. These results were then transferred to the ideal testbed as described in the next section. Here the compound published by Oyarzabal is referred to as **(MnGd)**.

This molecule was chosen because it is structurally similar to **(CoDy)** and magnetically characterized. Considering the electronic structure, the Mn(II)-ion is in a HS-$3d^5$ state and the Gd(III) ion is in a $4f^7$ state. Therefore the HS-state of this molecule has a single reference character with 12 unpaired electrons.

The compound **(MnGd)** is using a bipocket ligand containing a Mn(II) and Gd(III) ion bridged via a μ-phenoxy-group. Additionally, it is bridged via a 1κO; 2κO' acetate. This κ-notation indicates oxygen O coordinates to metal 1 and oxygen O' coordinates to metal 2. This notation will be used throughout this thesis for carboxylate ligands.[238,239]

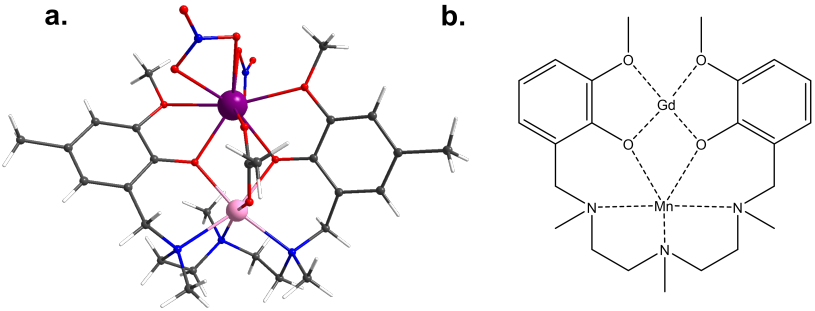

Figure 3.7.: a. Molecular structure of the model compound **(MnGd)** published by Oyarzabal *et al.*[237] b. Simplified scheme highlighting the bipocket ligand while excluding the bridging acetate ion and terminal nitrate ions.

There are two additional terminal nitrate ions coordinated to Gd. Oyarzabal *et al.* reported a coupling constant of J = -0.08 cm^{-1} for **(MnGd)**. In addition, BS-DFT calculations were performed using the pbe-functional, a triple-ζ basis and relativistic ECPs to treat scalar relativistic effects. This resulted in a calculated coupling constant of J = -0.61 cm^{-1}. Clearly, this level of theory is insufficient (see Figure 3.8).

Consequently, a number of tests with different treatments of scalar relativistic effects and different functionals have been carried out. The results indicate that an explicit treatment of scalar relativistic effects is mandatory.[236] Here, such influences are described in more detail in Section 3.3.2. As a starting point, the all electron triple-ζ basis x2c-TZVPPall and one-component X2C are used for the calculations. The coupling constant is calculated using Yamaguchi's formula (Equation 2.6). This section concentrates on the influence of the functional. 15 density functionals are used in this study with increasing levels of sophistication:

- LDA: s-vwn[240,241]
- GGA: b-p,[241–243] b-lyp,[242,244] pbe[245,246]
- mGGA: tpss,[245,247,248] r2scan[249]
- hybrids: tpssh,[242,245,247,248] b3-lyp,[242,244,250,251] hse06,[252,253] pbe0,[245,246,254,255] m06,[205] bh-lyp[242,244,250] m06-2x[205]
- range-separated hybrids: ωb97-x,[256,257] cam-b3lyp[258]

J obtained from each functional is plotted in Figure 3.8 against the reference value of -0.08 cm^{-1}. The numbers are also shown in the appendix, Table A.5. Clearly, Local Density Approximation (LDA) and Generalized Gradient Approximation (GGA) functionals are insufficient.

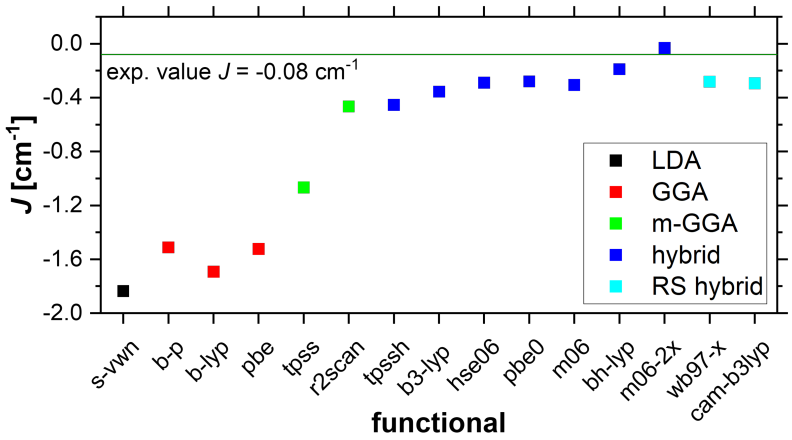

Figure 3.8.: Overview of the coupling constant calculated for compound **(MnGd)** using different functionals, a x2c-TZVPPall basis set and one-component X2C.

Whilst the meta-Generalized Gradient Approximation (mGGA)-functional tpss performs slightly better, r2scan is on par with the worst performing hybrid functionals. Going from low (tpssh, 10 % HF) to high (m06-2x, 54 % HF) contributions of exact exchange (HF), a decrease of the coupling constant can be observed. The functionals bh-lyp and m06-2x are the closest to the experimental value, although the agreement is not very good. Whereas bh-lyp predicts a coupling of -0.19 cm^{-1}, m06-2x underestimates the coupling with -0.03 cm^{-1}.

In this study, both functionals, m06-2x and bh-lyp give the best results, although outperforming all other functionals tested here, the margin of error is still significant. The bh-lyp functional was chosen in order to study the ideal testbed with the justification for this choice explained in Section 3.3.2.

3.2.3. Coupling Single Ion Properties Step by Step

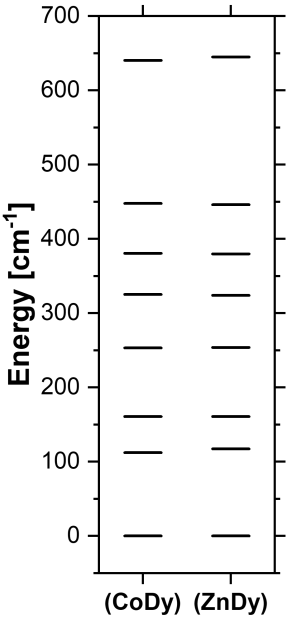

Figure 3.9.: Energy splitting of the $^6H_{15/2}$ ground state of Dy(III) in compounds **(CoDy)** and **(ZnDy)**.

With all preparative stages completed, the electronic properties of **(CoDy)** can be investigated by following the general procedure outlined in Section 7.2. Therefore, the molecular structures of **(CoDy)**, **(CoY)**, **(ZnDy)**, and **(CoGd)** were extracted from the cif-files and the positions of H-atoms optimized. Then CASOCI-calculations were carried out on each paramagnetic ion of the four compounds. First, the single-ion properties of Dy in **(CoDy)** and **(ZnDy)** were compared. Tables summarizing the single ion parameters (splitting, g-tensors and ESOs) can be found in the appendix, Tables B.2, B.4, B.10, B.11, B.20, B.21, B.25, B.26, B.29, B.30, B.34 and B.35. The obtained energy splitting of the $^6H_{15/2}$ ground state is depicted in Figure 3.9. Clearly, the splitting between the two compounds is very similar. The energy of the first excited KD with respect to the ground state is 112.2 cm^{-1} for compound **(CoDy)** and 117.3 cm^{-1} for compound **(ZnDy)**. Comparing the energies of the excited KDs of **(CoDy)** and **(ZnDy)**, this is already the largest deviation. The ground state is predominantly comprised of the m_J = 15/2 wavefunction at circa 93 %. Consequently, it is very anisotropic with g_z = 19.3.

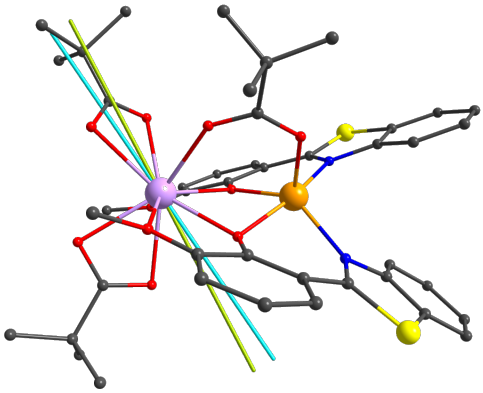

Figure 3.10.: Molecular structure of **(CoDy)** and the magnetic main axis calculated from CASOCI (green) and MAGELLAN (cyan).

The direction of the magnetic main axis can be extracted using the program MAGELLAN based on a pure electrostatic model.[259] The orientation of the main axis calculated with CASOCI and MAGELLAN is compared in Figure 3.10. The two models result in almost colinear axes indicating that the electrostatic approximation is appropriate and the m_J = 15/2-state is truly the ground state.

Similar conclusions can be drawn for the Co(II) ion in **(CoDy)** and **(CoY)**. Both calculations result in a splitting of the lowest quartet state (S = 3/2) in two KDs with an energy difference of 56 cm^{-1}. Consequently it was shown that the single ion properties of Dy(III) in **(CoDy)** and **(ZnDy)** are almost identical, as are the Co(II) single ion properties in **(CoDy)** and **(CoY)**.

Subsequently, a BS-DFT-calculation was performed on **(CoDy)** and **(CoGd)** where Dy(III) was replaced by Gd(III). Consequently, the high spin states contained ten unpaired electrons.

These calculations were performed with the functional bh-lyp and scalar relativistic effects treated with X2C. Locally dense basis sets are basis sets where many functions are employed at positions where a precise calculation of the density is necessary and few functions where this is not the case.[260] Here, such locally dense basis sets were employed where the metal ions were described with a x2c-QZVPall basis, H-atoms with def2-SVP and all other atoms with def2-TZVP.

The obtained coupling constants are 0.253 cm^{-1} for CoGd in the structure of **(CoDy)** and 0.241 cm^{-1} for **(CoGd)**, respectively. However, it is important to realize that these coupling constants are for a Hamiltonian $\hat{H} = -2J\hat{S}_{Co}\hat{S}_{Gd}$ where S_{Co} = 3/2 and S_{Gd} = 7/2. In order to translate these to a Dy(III)-pseudospin $\tilde{S}$ = 15/2, it is necessary to multiply these values with 7/15. Consequently, the BS-DFT coupling constants for CoDy calculated with the molecular structures of **(CoDy)** and **(CoGd)** are almost identical and ferromagnetic (0.118 cm^{-1} and 0.113 cm^{-1}respectively).

Having calculated the crystal field parameters, the magnetic coupling constants can also be fitted for **(CoDy)** and **(CoGd)** using the Lines model as implemented in the program PHI.[182] This has to be done by fitting the coupling constant *J* and an isotropic g-factor only for Dy (Gd). The g-factor essentially acts as a scaling factor to fit the high-temperature values as it would in a perfect Curie-Weiss behavior. The obtained coupling and g-factor for **(CoDy)** are *J* = 0.107 $\pm$ 0.010 cm^{-1} and g = 1.283 $\pm$ 0.001. The theoretical value for g = 4/3. This is a remarkable fit with the calculated coupling constant from BS-DFT. Doing the same for **(CoGd)**, *J* = 0.270 $\pm$ 0.003 cm^{-1} and g = 1.967 $\pm$ 0.001 are obtained, again in agreement with DFT.

This shows that the magnetic properties of both compounds can be simulated based on their geometric structure. However, this was not the central question here.

In the calculations so far, the total properties were described as a sum of single ion properties and a cooperativity *J*. This means that it should be possible to reconstruct the DC-properties of **(CoDy)** by using the crystal field parameters from **(CoY)** and **(ZnDy)** as well as the coupling constant calculated and rescaled from **(CoGd)**.
A fitted g-factor was necessary to reproduce the experimental high-temperature values which does not deviate significantly from the theoretical value in all cases.

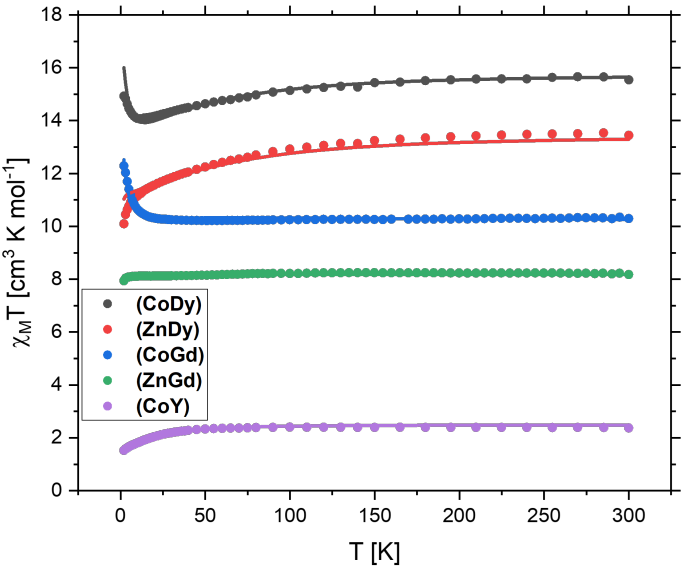

Figure 3.11.: $\chi_M T$ vs T plots of **(CoDy)**, **(CoY)**, **(ZnDy)**, **(CoGd)** and **(ZnGd)**. Dots show the experimental data, lines the data simulated in PHI. All data contains a fitted g-constant close to the theoretical value. For **(CoY)**, **(CoGd)** and **(ZnDy)**, the ESOs from the respective calculations were used. **(ZnGd)** did not use any extra parameters. The data for **(CoDy)** is reconstructed using the ESOs from **(ZnDy)** and **(CoY)** and the BS-DFT coupling constant rescaled from **(CoGd)**.

Furthermore, the reference measurement for **(ZnGd)** is plotted without any additional parameters as it behaves like a simple S = 7/2 system. The corresponding magnetization curves (M vs. B) are shown in the appendix, Figure A.1. These could not be fitted using the same g-factors since the measurements were performed on different machines and the measurements are very sensitive to small deviations in sample mass, calibration, diamagnetic correction etc. The excellent agreement of the reconstructed and fitted susceptibility is depicted in Figure 3.11.
In summary, this section has shown for the first time that there is some physical merit to the quantum chemical workflow used to simulate multinuclear coordination compounds. By investigating an isostructural diamagnetically substituted testbed of molecules it has been shown that the crystal field parameters can be transferred from single center calculations/experiments to the coupled system.

3.2.4. Variation of 4f Ions

Up to now the lanthanide ions in the testbed investigated are Gd, Dy and Y in their +3 oxidation state. These can be expanded to Tb, Ho and Er. The only combination with M = Co, Zn not considered is the ZnY version. Furthermore, no Single Crystal X-ray Diffraction (SC-XRD) structure is available for **(ZnEr)**. The following section will investigate two research questions using this large testbed of molecules as a basis. Firstly, it is possible to reconstruct and thus reproduce the magnetic properties as was done for **(CoDy)** for other lanthanide variations? Secondly, is it feasible to optimize the geometries for different lanthanide variations to gain access to the electronic structure without having to measure the crystal structure for each lanthanide?

To do this, the experimental fits using ESOs from the single ions have to be performed first. CASOCI calculations were carried out for each paramagnetic ion analogously to what was described in Section 3.2.3. The obtained ZFS, m_J-projections and ESOs are summarized in the appendix, Tables B.1–B.44 Furthermore, the ESOs were used to fit the magnetic susceptibility data and isothermal magnetization.
For the additional compounds investigated here it was possible to fit a g-factor to $\chi_M T$ and magnetization simultaneously. The obtained fits and corresponding g-values are summarized in the appendix, Figures A.2–A.4. The coupling constants for the analyzed compounds **(CoLn)** are summarized in Table 3.1. It was not possible to fit **(CoTb)** because of poor data quality as shown in Figure A.5.

Table 3.1.: Coupling constants fitted and calculated with BS-DFT for five compounds of the ideal testbed in cm^{-1}.

	(CoGd)	**(CoDy)**	**(CoHo)**	**(CoEr)**
J_{fit}	0.270	0.107	-0.010	0.018
J_{BS}	0.241	0.118	0.111	0.128

It is not possible to compare these values directly, as they act on different pseudospins (S_{Gd} = 7/2, $\tilde{S}_{Dy}$ = 15/2, $\tilde{S}_{Ho}$ = 8, $\tilde{S}_{Er}$ = 15/2). However, even when converted to the same pseudospin system, it becomes apparent that the coupling constant decreases moving to the heavier ions with **(CoHo)** showing antiferromagnetic coupling. Such an effect is described in the literature and rationalized through a weaker 3d-5d overlap due to a changing bridging angle caused by the lanthanide contraction.[261–263]

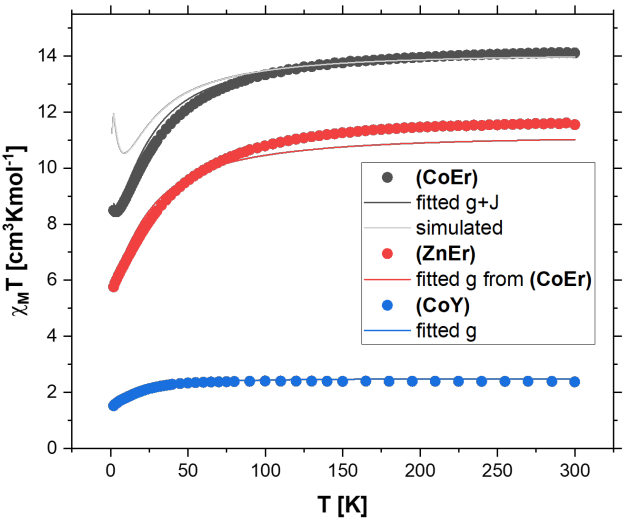

Figure 3.12.: Molar susceptibility for **(CoEr)**, **(ZnEr)** and **(CoY)**. With respect to **(CoEr)**, the pale lines are simulated using the BS-DFT *J* value and no fit of g, while the colorful lines are fitted with g = 1.205 $\pm$ 0.001 and *J* = 0.018 $\pm$ 0.001. The susceptibility for **(ZnEr)** is fitted with g = 1.182 $\pm$ 0.001.

Whereas the real coupling changes significantly along the series, this is not the case for the calculated BS-DFT coupling constants which remain similar to that calculated from the **(CoGd)** structure between 0.253 $cm^{-1}$and 0.275 cm^{-1}. This discrepancy is illustrated in Figure 3.12 using **(CoEr)** as an example. The ferromagnetic coupling simulated using the BS-DFT coupling constant is significantly overestimated as shown by the poor agreement of the pale gray line with the experimental data (gray). Consequently, it appears that DFT is unable to capture this trend and whilst the Gd(III) substitution approach works well for Dy(III) it does not for other lanthanides.

Subsequently, the influence of geometry optimization on the ZFS was probed by performing two additional CASOCI calculations for each lanthanide. In addition to the structure in which the H-positions were optimized (opt) the unoptimized structure taken directly from the cif was also calculated (unopt). Finally, the full geometries are optimized using a relativistic large-core ECP (LC-ECP) in which the f-electrons are described by a pseudopotential. The choice of method is based on a publication by Lukanowski and Weigend.[264] In the current study, the structures were optimized on a pbe-D4/rij level of theory using a def2-TZVP basis for all atoms but the lanthanide and a relativistic large-core ECP without any valence electrons for Ln.[265,266] When Co(II) is in the structure, an unrestricted Kohn-Sham calculation was performed on the quartet state.
At this point it should be noted that the experimentally refined structures are generally more trustworthy than DFT-optimizations. However, the goal of this study is to find out if the structure can be transferred and then relaxed to accommodate other lanthanides. This way, it may not be necessary to measure the structures of all lanthanides, but could give access to reasonable chemical models for the entire series starting from just one experimentally refined model.
The results of these ZFS splittings are summarized in Figure 3.13. For all complexes investigated, the H-positions did not influence the splitting significantly. Consequently, optimizing H-positions will give a more physically accurate model, even if it does not necessarily change the obtained ZFS. Contrarily, it was not possible to retain the same ZFS when optimizing the full structure with pbe. This can be exemplified by calculating the Mean Absolute Errors (MAEs) (Tables A.6–A.7) of the excited states with respect to the ground state. While the MAE of the lowest multiplets energies is less than 3 cm^{-1}, it is between 9 cm^{-1} and 24 cm^{-1} when the structure was optimized with pbe.

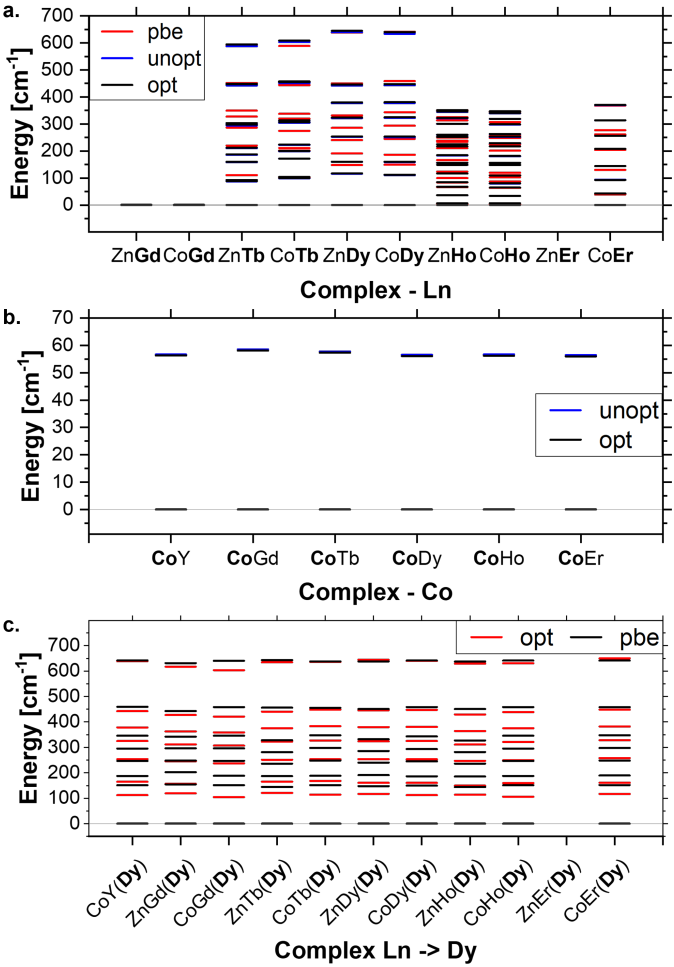

Figure 3.13.: a. Level splitting of all lanthanide ions in the ideal testbed. b. ZFS of the Co(II) quartet state in the Co-compounds in the ideal testbed system. c. ZFS of Dy(III) when the original lanthanide is replaced by Dy(III). "unopt" refers to calculations where the structure was taken directly from the cif. "opt" refers to structures where the H-positions were reoptimized. "pbe" refers to calculations where the full geometry was optimized by using the functional pbe. Here, LC-ECPs were employed. pbe-Dy(III) structures were optimized using the Dy-LC-ECP.

It should be noted that this changes is accompanied by a small rotation of the underlying m_J-contributions. A full list of MAEs can be found in the appendix, Table A.6.

Furthermore, the optimization of hydrogen atoms did not influence the splitting of the quartet state in Co(II) as shown in Figure 3.13b.

Another possible approach is to replace the lanthanide in the structure without further optimization. In this case the coordination symmetry stays intact, while the Ln-bond distances will be overestimated (or underestimated). This is shown as an example for Dy(III) in Figure 3.13 c. Here, calculations where the lanthanide in the opt model was replaced by Dy(III) are compared with calculations where the opt structure was taken as a starting guess and reoptimized with a Dy LC-ECP. The resulting models are depicted schematically in Figure 3.14.

Clearly, all calculations using the opt model give qualitatively similar results. This is illustrated by two features: Firstly, the energy gap between the ground state and first excited KD ranges between 104 cm^{-1} (for **(CoGd)**) and 119 cm^{-1} (for **(ZnGd)**) where the reference values are 112 cm^{-1} and 117 cm^{-1} for **(CoDy)** and **(ZnDy)** respectively. Secondly, the calculated contribution of the m_J = 15/2 state to the ground state ranges from 91.6 % using the **(CoHo)** structure to 94.2 % using the **(ZnTb)** structure. For reference, the contributions are 92.8 % in **(CoDy)** and 93.2 % in **(ZnDy)**.

This is also true for the structures optimized with the pbe functional. A very similar structure (and therefore very similar electronic properties) is obtained when the lanthanide of any testbed molecule is replaced by Dy(III) and subsequently optimized. However, the MAE-values with respect to the Dy(opt) calculation are much higher, between 20 cm^{-1} and 25 cm^{-1}(see Table A.7). Therefore, it can be concluded that the obtained Dy-structure is not the experimentally determined one.

Figure 3.14.: Substitution scheme to approximate Dy(III) structures from other lanthanides. Either the lanthanide is substituted and the full structure relaxed (left) or the lanthanide is exchanged without other structural changes (right).

This is still an encouraging result because if a suitable method for geometry optimization can be found, it should be possible to use the SC-XRD measurement of one compound in order to calculate the electronic properties of the entire series.

In summary, a suitable method was found to accurately calculate the exchange coupling constant for heterobinuclear Co(II)-Ln(III) compounds. This was employed to reconstruct the the magnetic properties of **(CoDy)** using the ESOs from **(CoY)** and **(ZnDy)** in conjunction with the coupling constant calculated for **(CoGd)**. It was shown that the same coupling constant cannot be used to fit other lanthanides but nevertheless one can get access to the single ion properties of the different lanthanides by directly replacing the ions computationally without further optimizing the structure.

3.3. Gadolinium Dimer Exchange Couplings

In the following sections, a number of studies is conducted to investigate the application of BS-DFT to calculate the exchange coupling constant *J* for binuclear Gd(III) structures. To do so, first, a benchmark testbed needs to be assembled as presented in Section 3.3.1. In Section 3.3.2 the influence of various DFT options on the coupling constant is evaluated establishing a best-practice workflow. In Section 3.3.3 the testbed is analyzed for structure property relations before applying the thus established best-practice on a set of Gd_4-clusters in Section 3.3.4. Subsequently, it was attempted to disentangle the structure property relationship in a more systematic way by investigating a series of Gd_2X_6 ($X = F^-$, Cl^-, Br^-, I^-) compounds. Then the electronic properties of the bridge are compared with those of the terminal ligands with respect to the influence on *J*. The chapter is concluded by revisiting a four halide bridged Gd-dimers in light of these results. Overall, this chapter provides an optimal BS-DFT workflow for gadolinium compounds which are an important model system for other exchange coupled lanthanide compounds.

3.3.1. Preparation of a Benchmark Database

No benchmark study has been conducted in the literature on a diverse set of Gd-compounds. To fill this gap the molecules chosen for this study have to fulfill a number of criteria:

- The bridging motifs cover a wide range of the chemical space to investigate possible structure property relations. This includes the bridging atoms, angles and coordination motifs.

- The molecules need to be well characterized by SC-XRD and the cif files must be available. The crystal structure should contain only one crystallographically distinct molecule as the asymmetric unit.
- The molecules should contain two Gd(III) paramagnetic ions.
- The molecules need to be characterized using DC-SQUID measurements from which the coupling constants can be extracted. Ferro- and antiferromagnetic couplings should be included.

In this thesis, the benchmark molecules are labeled with a **b**. Table 3.2 summarizes the 27 compounds chosen for this study, all of which fulfill the above mentioned criteria. Bridging angles, Gd-Gd distances and the bridging atoms are given.
The testbed contains molecules bridged via carbon, sulfur, chloride, nitrogen and oxygen. Since most compounds in the literature are bridged via oxygen, the testbed reflects this structural trend. The O-bridged molecules include a number of different bridging modes such as single oxygen bridges via hydroxides and alcoholates. Multidentate ligands are included as carboxylates, carbonates, nitrates and phosphonates. Furthermore, compounds with additional diamagnetic transition metals are included in four compounds. Most compounds in this testbed are antiferromagnetically coupled although four are ferromagnetically coupled.
The compounds are depicted in the appendix, Figures A.6–A.8.

Table 3.2.: Summary of the molecules **(b1)**-**(b27)** which were tested in the benchmark study including Gd-Gd distance and Gd-L-Gd bridging angle. FM denotes ferromagnetic coupling while AF denotes antiferromagnetic coupling. *: a. hydroxide bridge, b. alcoholate bridge, c. carboxylate bridge, d. carbonate bridge, e. nitrate bridge, f. phosphonate bridge, g. additional diamagnetic transition metals, h. original data available.

Nr.	Formula	Bridge	Gd-Gd dist (Å)	Gd-L-Gd angles (°)	Coupling	*
(b1)	[(pdl')(pdl'$^{-1H}$)(pdl'$^{-2H}$) $Gd_2(THF)_2$][267]	C	3.246	81.0-82.3	FM	h
(b2)	[$KGd_2(C_7H_7)$ $(N(SiMe_3)_2)_4$][268]	C	4.087	102.9-103.5	AF	
(b3)	[(Cp'$_2$Gd(μ-$SSiPh_3$))$_2$][269]	S	4.316	101.5	AF	
(b4)	[Gd_2(3-PAA)$_2$(μ-Cl)$_2$ $(phen)_4](ClO_4)_2$[270]	Cl,O	3.906	89.7	AF	c
(b5)	[$Gd_2(\mu-Cl)_2Cl_4Li_2(L)_2$ $(THF)_6$][271]	Cl	4.379	102.6	AF	
(b6)	[$Gd(Cy_2N)_2(\mu$-Cl) $(THF)]_2$[272]	Cl	4.303	102.6	AF	h
(b7)	[$((THF)_2Li(NtBu)_2$ $S(tBuN)_2GdCl_2)_2$ $\cdot ClLi(THF)_2$][273]	Cl	3.835	86.0/89.4	AF	
(b8)	[Cp_2Gd(2-NH$-$4,6-$Me_2pm)]_2$[274]	N	3.811	98.3/100.2	AF	
(b9)	[$Gd_2(L3)_2(L')_2$ $(MeOH)_2$][275]	O	3.859	110.8	AF	b

Continued on next page

Nr.	Formula	Bridge	Gd-Gd dist (Å)	Gd-L-Gd angles (°)	Coupling	*
(b10)	$[Zn_2Gd_2(\mu_3-CO_3)_2(L^b)_2(NO_3)_2]\cdot 2MeOH$[276]	O	4.070	116.8	FM	dg
(b11)	$[NHEt_3]_3[Gd_2(\mu\text{-}NO_3)_2(NO_3)_2(HL)_2]$[277]	O	3.761	107.9	AF	beh
(b12)	$[Gd_2(HL)_2(NO_3)_4]\cdot 2MeCN$[278]	O	3.855	108.4	AF	b
(b13)	$[Gd_2(F_2HCCOO)_6(hypy)_2]$[279]	O	3.880	106.8	AF	bc
(b14)	$[Gd_2(ClF_2CCOO)_6(hypy)_2]$[279]	O	3.866	106.5	AF	bc
(b15)	$[Gd_2(Cl_2HCCOO)_6(H_2O)_2(hypy)_2]$[279]	O	4.051	107.6	AF	bc
(b16)	$[Zn_2Gd_2L_2Cl_2(OAc)_4(MeOH)_2]$[280]	O	4.081	112.0	FM	bcg
(b17)	$[Gd_2(3m\text{-}L4)_2(L2)_2(DMF)_2]$[281]	O	3.815	106.3	AF	b
(b18)	$[Gd_2(iba)_6(bipy)_2]$[282]	O	3.984	106.4	AF	c
(b19)	$[Gd_2L_2(OAc)_4(MeOH)_2]\cdot 2MeOH$[283]	O	4.099	112.0	AF	c
(b20)	$[Zn_2Gd_2(\mu\text{-}OH)_2(L)_2(OAc)_5(EtOH)(H_2O)]\cdot 2EtOH\cdot 1.5H2O$[284]	O	3.791	105.6/104.5	AF	acg
(b21)	$[Gd_2(dbm)_2L_2(MeOH)_2]\cdot nMeOH$[285]	O	3.987	113.0	AF	bc
(b22)	$[Gd_2(NO_3)_4(teaH_2)_2]$[286]	O	3.719	109.3	AF	b

Continued on next page

Nr.	Formula	Bridge	Gd-Gd dist (Å)	Gd-L-Gd angles (°)	Coupling	*
(b23)	$[Gd(C_9N_3H_{20}(PO_3H)_2(PO_3))(NO_3)(H_2O)]_2 \cdot 8H_2O$[287]	O	4.028	110.1	AF	f
(b24)	$[(\mu_4\text{-}CO_3)_2(ZnL^1Gd(NO_3))_2]\cdot$acetone $\cdot 2H_2O$[288]	O	4.045	116.5	FM	dg
(b25)	$[Gd(\mu\text{-}OH)(DBP)_2(THF)_2]_2$[289]	O	3.748	110.5	AF	a
(b26)	$(HNEt_3)[Gd_2(HL)(L)]$[290]	O	3.896	107.9	AF	b
(b27)	$[Gd_2(Hhmb)_3(NCS)_3]\cdot 2MeOH\cdot py$[291]	O	3.599	101.1/95.7/100.8	AF	b

In order to prepare structures for the following quantum chemical calculations, the molecular structures were extracted from the cif files. Counter ions and lattice solvent not directly bound to the molecule were omitted. If disorder is present, only the major contribution was considered. Then the magnetic ions were replaced with diamagnetic Y(III) and the hydrogen positions optimized on a b3-lyp-D4/def2-TZVP/ri level of theory using Turbomole 7.8. Finally, CASOCI-calculations were performed on all Gd(III)-centers using the general workflow described in the Section 7.2 in order to obtain the ESOs. Obtained splittings and ESOs are shown in the appendix, Tables B.45–B.59.

Exchange coupling constants were reported alongside the magnetic data for most of the molecules given in Table 3.2. However, a number of different Spin Hamiltonians and extraction methods were used to fit these. Thus, in order to properly compare the results the magnetic data were digitized[292] and refitted for all compounds using the three different schemes described in Section 3.1: The Bleaney-Bowers equation, the Lines model and the Lines model including ESOs.

Table 3.3.: Reference values fitted with the Lines model including ESOs for compounds **(b1)**-**(b27)**.

nr.	**(b1)**	**(b2)**	**(b3)**	**(b4)**	**(b5)**
***J* [cm^{-1}]**	0.302(6)	-0.096(1)	-0.098(1)	-0.020(1)	-0.075(2)
	(b6)	**(b7)**	**(b8)**	**(b9)**	**(b10)**
	-0.033(1)	-0.036(1)	-0.069(1)	-0.036(1)	0.024(0)
	(b11)	**(b12)**	**(b13)**	**(b14)**	**(b15)**
	-0.097(1)	-0.058(0)	-0.062(1)	-0.022(1)	-0.014(0)
	(b16)	**(b17)**	**(b18)**	**(b19)**	**(b20)**
	0.020(0)	-0.072(1)	-0.021(1)	-0.006(0)	-0.029(0)
	(b21)	**(b22)**	**(b23)**	**(b24)**	**(b25)**
	-0.032(0)	-0.143(1)	0.011(0)	0.039(0)	-0.115(0)
	(b26)	**(b27)**			
	-0.066(0)	-0.022(0)			

The original data for compounds **(b1)**, **(b6)** and **(b11)** were provided by the authors which allowed for a direct comparison with the refitting procedure. The results of all fits as well as the literature values are summarized in the appendix, Tables B.60–B.62. All methods give comparable and compatible results. The good agreement with the original data suggests that no noteworthy errors are introduced in the digitization procedure. This highlights the validity of all approaches in the literature. For the following discussion, those values fitted with the Lines model and ESOs from CASOCI will be used. These are summarized in Table 3.3.

3.3.2. Influence of DFT Options on Calculated Exchange Couplings

Since the molecular structures and reference values are defined, the influence of different options in DFT on the calculated coupling constants are evaluated. This is achieved by testing the influence of the basis set, scalar relativistic effects, the DFT-grid, diffuse functions and finally the functional. In principle, this can be achieved by optimizing one factor at a time or alternatively to do a simultaneous/global parameter search.[293] Considering that all options apart from the functional used in this study can be systematically improved, these influences are checked first. As a starting functional, bh-lyp will be used as it was shown to perform well in Section 3.2. Scalar relativistic effects are treated with X2C.
To find an optimal basis set, each molecule is divided into three parts: The magnetically active Gd(III)-sites, all hydrogen atoms and the remaining atom types. The latter will be referred to as "ligand atoms", bearing in mind that H is excluded. The basis set for each of these parts is varied independently in order to compare their influence on the results.

The partitioning is visualized in Figure 3.15. This way, it is possible to use large basis sets only for those atoms where a precise description of the density is needed.

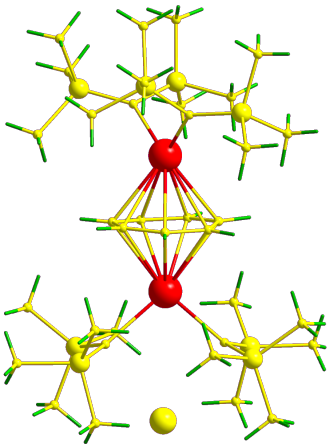

Figure 3.15.: Compound **(b4)** colored to represent the different areas treated with each basis set. The Gd(III)-ions are colored red, hydrogens green and all other atoms yellow.

The basis sets tested for Gd(III) were x2c-SVPall, x2c-TZVPall, x2c-TZVPPall, x2c-QZVPall and x2c-QZVPPall.[294,295] The basis sets x2c-SVPall, x2c-TZVPall and x2c-TZVPPall were tested for the ligand atoms. For the outermost group, the hydrogen atoms, the x2c-SV(P)all, x2c-SVPall and x2c-TZVPall basis sets were explored. In total, this required 45 calculations to be performed on each molecule. For conciseness, the "x2c"-prefix is omitted in the following discussion. The names for the basis set combinations are abbreviated from the three individual names. For example, using a QZVP basis for Gd(III), a TZVP basis for the ligands and an SVP basis for hydrogen would be called QZVP-TZVP-SVP. The largest basis set combination in the testbed (QZVPP-TZVPP-TZVP) will be used as a reference for the other calculations.

The calculated coupling constants for all calculations are shown in the appendix, Tables B.63–B.69. The MAEs for all 27 molecules are calculated and plotted in Figure 3.16. Here, each line is a combination of two fixed basis sets while the third basis set is varied independently. The most pronounced effect can be observed for the metal centers.

Here, the error can be significantly reduced by going from a split-valence to a triple-zeta basis independent of the bases used for the other atoms. The inclusion of additional polarization functions e.g. going from TZVP to TZVPP can be neglected. Going from a triple-zeta to a quadruple-zeta basis the error can be further reduced although the effect is less significant. For the ligand basis, the only noteworthy change is observed going from a SVP-basis to a TZVP basis. The basis used for hydrogen atoms does not seem to have any influence on the calculated coupling constant.

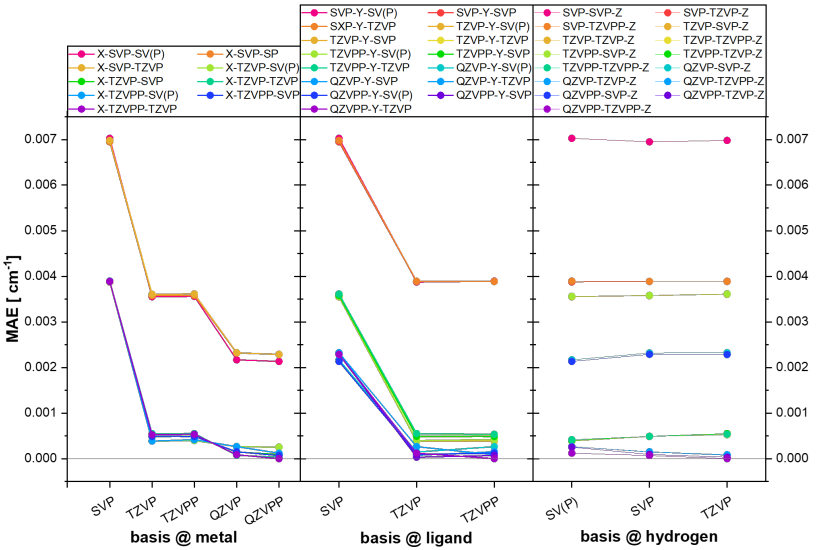

Figure 3.16.: Average error of *J* with respect to the largest basis by varying only the metal basis (X) while keeping the other two basis sets fixed. (left) The basis for the ligand (Y) is varied and the other two basis sets are fixed. (middle) The basis for the hydrogen basis (Z) is varied and the two other basis sets are fixed. (right)

Importantly, the error introduced by using the smallest tested basis with respect to the largest tested basis is only 0.007 cm^{-1}. This is already close to the error margin of the fitting procedures. Consequently, using a TZVP basis for metal and ligand, while using a SV(P) basis for the hydrogen atoms is more than sufficient and a good cost-accuracy balance. This basis set will be used for the remainder of this study.

Next, the influence of scalar relativistic effects is explored. To do so, five calculations are performed on the testbed: **1.** Not considering relativistic effects. **2.** Using relativistic ECPs as included in the def2-basis sets. **3.** Turning on Second Order Douglass-Kroll-Hess (DKH2). **4.** Using Fourth Order Douglass-Kroll-Hess (DKH4) **5.** X2C-is used as a reference value for the other methods.

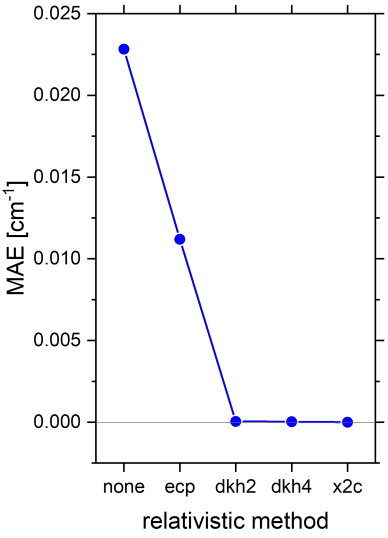

Figure 3.17.: The MAE for all 27 molecules using the different treatments of relativistic effects with respect to X2C.

The results of all calculations can be found in the appendix, Table B.70. Figure 3.17 summarizes the MAE of all methods with respect to X2C. Most noteworthy is that neglecting relativistic effects will lead to a significant error larger than the experimental accuracy. Using ECPs is better, but still 0.01 cm^{-1} away from X2C. This might by a reasonable method, but DKH2 is already essentially converged to X2C.

Therefore, any explicit treatment of relativistic effects will give accurate results and thus DKH2 suffices for the following computations.
It is worth noting that another popular method, the Zeroth Order Regular Approximation (ZORA) could not be tested as it is not implemented in Turbomole. However, it is expected to perform similarly to DKH2.[216,296]
The different Turbomole grids (3, 4, 5 an 6) are tested for their influence on the coupling constant. The MAE of the coarsest grid tested with respect to the finest is smaller than 10^{-4} cm^{-1} and therefore negligible. However, it is possible that other functionals than bh-lyp are more dependent on the grid.[297] Therefore, a grid size 5 will be used throughout all studies. All calculated coupling constants can be found in the appendix, Table B.71.
Finally, it was tested if additional diffuse functions have a noteworthy influence. Since the x2c-basis sets do not include diffuse functions, the functions of the def2-TZVPDD basis set for Gd were added manually to the x2c-TZVPall basis. Consequently, the rij-approximation could not be employed as it relies on an auxiliary basis which is not optimized for this custom set. However, the MAE of this change is $3{\cdot}10^{-4}$ $cm^{-1}$and therefore also negligible.
So far, this means that the x2c-TZVPall basis should be used for Gd(III) and the ligand, while an x2c-SV(P)all basis is sufficient for hydrogen. Relativistic effects should be included at a DKH2 level of theory, grids better than grid 3 suffice and additional diffuse functions are not relevant.
Using these options, the influence of the DFT-functionals can now be investigated. In total, 25 DFT functionals were tested for their application on this testbed. These include LDA, GGA, mGGA and hybrid functionals. Furthermore, range-separated hybrid, local hybrid and range-separated local hybrid functionals are included. This list is designed to contain many different steps of the Jacobs ladder which is a concept to classify functionals based on their sophistication.[90]

It also allows to compare the effect of the exchange and correlation part of selected functionals independently. Finally, hybrid functionals with different amounts of HF-exchange are considered.

- **LDA:** s-vwn,[240,241] pwlda[245]
- **GGA:** b-lyp,[242,244] b-vwn,[241,242] b-p,[241–243] pbe[245,246]
- **mGGA:** tpss,[245,247,248] rev-m06-l,[298] scan[299]
- **hybrid:** b97,[256] b3-lyp,[242,244,250,251] bh-lyp,[242,244,250] bhandhlyp,[242,244,250] pbe0,[245,246,254,255] m06,[205] m06-2x,[205] tpss0,[247,248,300] tpssh[242,245,247,248]
- **range-separated hybrid:** cam-b3lyp,[258] ωb97,[256,257] ωb97-2x[256,257]
- **local hybrid:** lh07tsvwn,[241,301] tmhf,[302] chyf[303]
- **range-separated local hybrid:** ωlh23tde[304]

In short, LDA-functionals use a homogeneous electron gas as a reference to calculate the exchange-correlation contribution. GGA-functionals also take the gradient of the density into account, followed by mGGA-functionals which take higher order derivatives of the density as a parameter. Concerning hybrid functionals, a certain amount of HF/exact exchange is combined with a pure DFT-functional. When the amount of HF-exchange varies between short- and long-range one arrives at range-separated hybrid functionals. Local hybrids assign different amounts of exact exchange at different points in space and range-separated local hybrids combine the last two approaches.[90]

The results of all calculations are summarized in the appendix, Tables B.72 –B.78. *J*-values of compounds **(b1)** and **(b2)** will be excluded from the following discussion, since their errors are much higher than for all other compounds. This would render other errors as insignificant. The results concerning **(b1)** and **(b2)** are discussed later on in more detail. Furthermore the value of **(b8)** calculated with the m06-functional has an error of 1.8 cm^{-1} significantly deviating from the trend observed in all other molecules. Therefore, this calculation was excluded as well.
Figure 3.18 depict MAE, MD, and MaxAD-values for the remaining data set. As discussed before, the Mean Deviation (MD) is the average error with respect to the experimental reference data and can therefore be either positive or negative.

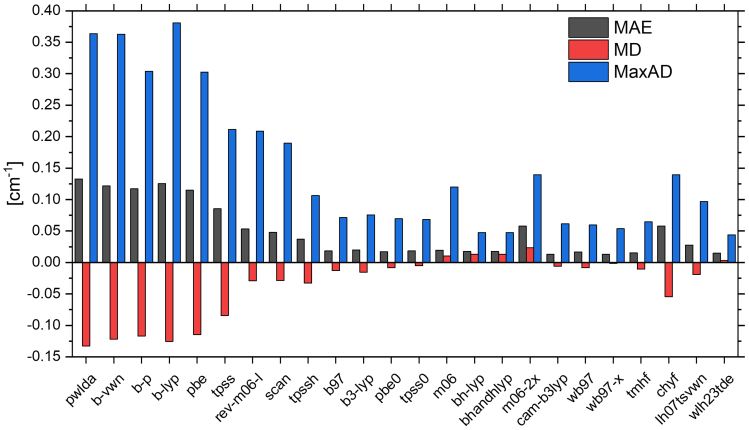

Figure 3.18.: Overview of the different functionals tested in this study and error-measures associated with them: MAE, MD, and MaxAD. All values are given in cm^{-1}.

The MAE calculates the average of the absolute errors and is therefore always positive. The Maximum Absolute Deviation (MaxAD) is the maximum absolute error across all molecules.
The results clearly suggest that LDA- and GGA-functionals perform significantly worse than the higher functionals with MAE-values larger than 0.1 cm^{-1}, which is larger than most coupling constants in the data set. A small improvement can be gained by using mGGA-functionals which have MAE-values close to 0.05 cm^{-1}. However, a number of hybrid and post-hybrid functionals performed exceptionally well: the MAE of pbe0, bh-lyp and bhandhlyp is 0.017 cm^{-1}, followed by b97 and tpss0 with 0.018 cm^{-1}. The commonly used functional b3-lyp has a MAE of 0.020 cm^{-1}. The range-separated functionals cam-b3lyp (MAE = 0.013 cm^{-1}) and ωb97-x (MAE = 0.017 cm^{-1}) performed exceptionally well with cam-b3lyp narrowly having the smallest MAE-value. The best local hybrid was tmhf with a MAE value of 0.015 cm^{-1}. Due to the intense computational demand of the range-separated local hybrid ωlh23tde, many calculation did not converge on six CPUs in 30 days. The remaining values average to a MAE of 0.014 cm^{-1}. Nevertheless, as a results of the investigated molecules' size this functional is unsuitable for such calculations.
It is worth mentioning that the largest errors across all functionals are only distributed over five compounds. These outliers are **(b3)** (once), **(b4)** (4 times), **(b8)** (8 times), **(b14)** (9 times) and **(b22)** (3 times). These MaxADs are in the range of the coupling constants themselves. However, as indicated in Figure 3.19 for the well-performing bh-lyp functional, there is a strong correlation of calculated and fitted coupling constants. Similar agreement can be reported for other functionals (Figure A.9).
One goal of this benchmark was to compare the influence of different correlation functionals on *J*.

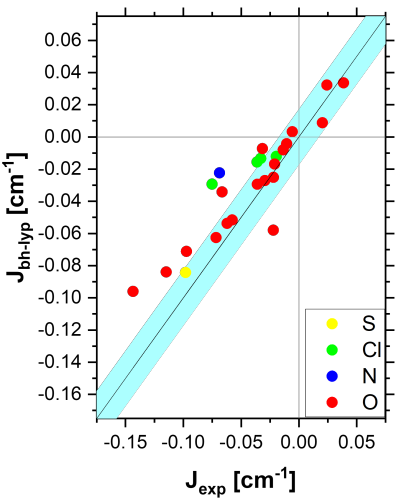

Figure 3.19.: Calculated coupling constants *J* using the bh-lyp functional against the fitted values. The light blue area is the MAE.

For example, the functionals s-vwn and pwlda both calculate exchange as Slater-exchange but use the correlation as suggested by either Vosko, Wilk and Nuisair (vwn) or Perdew and Wang. The MAE of these is very similar suggesting only a minor influence of the correlation term. A similar conclusion can be drawn from the comparison of the GGAs b-lyp, b-vwn and b-p, all of which share the exchange term suggested by Becke in 1988.[242] Here, the change in MAE is less than 0.01 cm^{-1}. A possible reason for this is given in Section 3.3.5.

The testbed also includes a number of functional families from which a direct comparison of GGA or mGGA to hybrid- and range-separated hybrid functionals can be drawn: For example, the pbe0 functional (20 % HF) performs significantly better than the GGA pbe. Accordingly, the tpss mGGA-functional performs worse than the tpssh hybrid (10 % HF) which in turn is slightly worse than the tpss0 functional (25 % HF).

In an even larger comparison, the GGA b-lyp performs worse than its hybrid counterpart b3-lyp (20 % HF). Going towards more exact exchange, the half and half functionals bh-lyp and bhandhlyp are among the best performing hybrid functionals. However, the range-separated version cam-b3lyp is slightly better. In a similar comparison, both range-separated ωb97 and ωb97-x perform better than the hybrid b97.

The only exception to this trend is the m06-family. In this case, the hybrid with less exact exchange m06 (27 % HF) is better than the hybrid with more exact exchange m06-2x (54 % HF) and the mGGA rev-m06-l.
These results clearly indicate the importance of the amount of exact exchange in the functionals. To probe this further, the well known b3-lyp functional was chosen as a basis:

$$E_{xc} = A \cdot E_x^{HF} + (1-A) \cdot E_x^{Slater} + B \cdot E_X^{B88} + C \cdot E_{corr}^{VWN(V)} + (1-C) \cdot E_{corr}^{LYP} \tag{3.4}$$

In this equation, the different exchange contributions are HF-exchange (E_x^{HF}), Slater-exchange and B88-exchange. The correlation part is a mixture of the functionals by Vosko, Wilk and Nuisair as well as that by Lee, Yang and Parr. The standard values for A, B and C are 0.2, 0.72 and 0.19 respectively. In the following, the value A will be scaled from 0 to 1 with a step size of 0.05.
The results of these calculations are summarized in the appendix (Tables B.79–B.84), the absolute errors with respect to the experimental values are depicted in Figure 3.20. The green lines depict the spread of errors in this study, while the blue line is the average error. Again, molecules **(b1)** and **(b2)** are excluded from this discussion.
Most noteworthy is that not all calculations converged for all molecules. For many molecules there was an upper limit of HF-exchange which could be taken into account before the calculations became unstable. The unconverged results indicate that the α- and β-electron density in a former doubly occupied ligand orbital spatially split. The lowest percentile of this occurring can be reported for compounds **(b12)** and **(b21)**, where the calculations did not converge above 65 % exact exchange. It is also important to mention that the coupling constants generally decrease with an increasing amount of exact exchange.

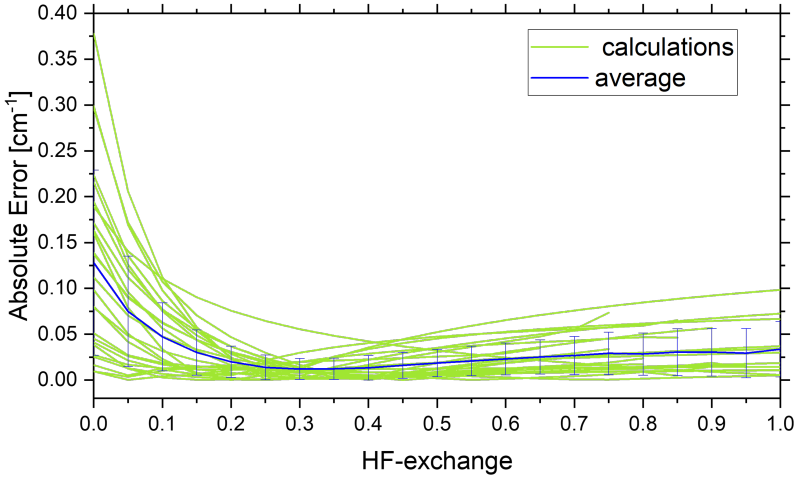

Figure 3.20.: The absolute error for all molecules (green lines) and their average (MAE, blue line) with respect to the amount of exact exchange in the b3-lyp functional. Error bars for each step are the standard deviations for each error.

This means that the experimental value is crossed at a given amount of exact exchange, individually for each molecule. On average, a value of A = 0.35 gives the best result with a MAE value of only 0.012 cm^{-1}. A similar value was found by Moreira investigating the coupling in NiO in 2002.[305] The curve of the average around this value is rather flat and between 20 % and 50 % the MAE is below 0.02 cm^{-1}. This is in line with the previous results where all well performing hybrid functionals contain HF-admixtures in this range.

Considering the results of the functional tests, it is suggested to use four functionals in parallel to find reasonable exchange couplings.

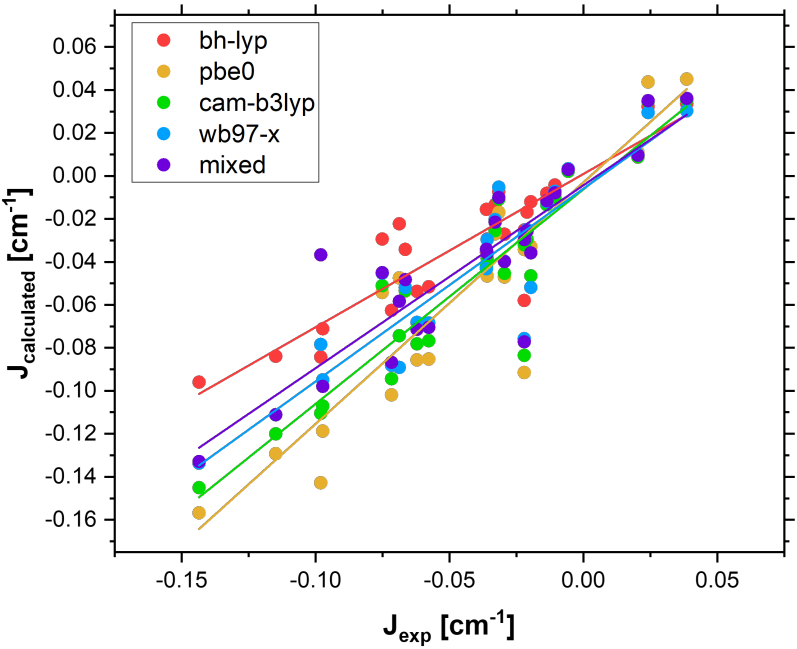

Figure 3.21.: Linear correlation for the four suggested functionals and their average (mixed) with respect to the fitted (experimental) coupling constant.

The hybrid functionals pbe0 and bh-lyp are likely to slightly over- and underestimate the calculated coupling respectively as their HF-admixtures are 25 % and 50 %. Furthermore, the range-separated hybrid functionals cam-b3lyp and ωb97-x performed exceptionally well and add further sophistication to the calculation. The four numbers obtained should be reported side by side to give an idea of the DFT-accuracy.
Figure 3.21 shows the linear correlation fits of these four functionals as well as their average with respect to the fitted reference values.

Whilst bh-lyp and ωb97-x slightly underestimate the coupling constants with slopes of 0.71 $\pm$ 0.07 cm^{-1} and 0.85 $\pm$ 0.09 cm^{-1}, the slope of cam-b3lyp is 1.00 $\pm$ 0.08. pbe0 slightly overestimates coupling constants with a slope of 1.12 $\pm$ 0.10 cm^{-1}.
The choice of these functionals completes the establishment of best practices for the calculations of Gd-dimer exchange couplings using BS-DFT. As discussed earlier the use of a triple-zeta all electron basis for Gd(III) and the ligand is mandatory, while a split-valence basis suffices for hydrogen. Relativistic effects should be included at least on a DKH2-level of theory.

3.3.3. Structure Property Relationships in the Experimental Database

Considering the large number of molecules in the testbed, it was attempted to derive some phenomenological structure property correlations. Three observations will be discussed: First, the shortcoming of BS-DFT in this benchmark with respect to compounds **(b1)** and **(b2)** was investigated. Secondly, a statistical analysis between structural parameters and the calculated coupling constants was performed. Finally, the knowledge gained was applied to rationalize the results for the structurally similar complexes **(b13)**, **(b14)** and **(b15)**.
Compounds **(b1)** and **(b2)** (Figure 3.22) are the only carbon bridged molecules in the testbed. Interestingly, the otherwise best performing functionals failed to reproduce the experimental results. Here, coupling constants between 0.698 cm^{-1} and 0.790 cm^{-1} were calculated for **(b1)**, whereas the fitted value is closer to 0.302 cm^{-1}. Similarly, ferromagnetic values between 0.086 cm^{-1} and 0.366 cm^{-1} were calculated for **(b2)** using the four functionals.

In reality, the value should have a negative sign closer to -0.096 cm^{-1}.
In the literature, Gd(III)-compounds bridged via carbanions can exhibit significantly stronger coupling constants than all other bridges. Strongly antiferromagnetic couplings could be realized through bridges utilizing tetraanionic benzene,[306] or dianionic cyclooctatetraene.[307] Record couplings were reported for tetraanionic biphenyl bridges[308] ($\approx$ -0.65 cm^{-1}) and a different tetraanionic benzene bridge ($\approx$ -2.9 cm^{-1}).[309,310]
Quantum chemical DFT-calculations have been published rationalizing all of these results. The most common explanation for the coupling is a spin polarization mechanism of the ligands. Here, charge transfer takes place from the ligands into the 5d-orbitals of the metal center. The authors derive an interaction with covalent bond character between the metal center and the ligands. This might be expected given the significant negative charge of the ligands, since strongly negatively charged carbanions will have electron density in spatially large antibonding orbitals. It was also recently shown that BS-DFT performs more poorly for covalent systems.[110]
It is accepted that DFT over-delocalizes the spin-density, leading to a

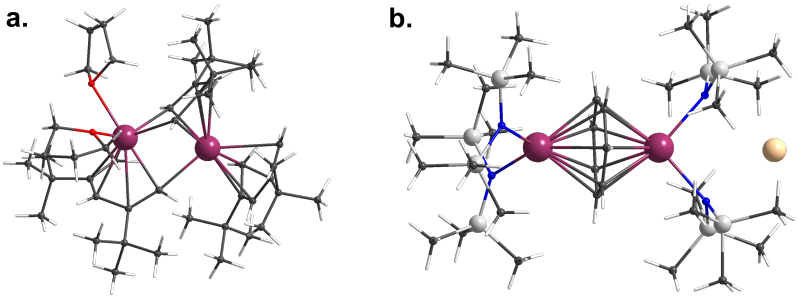

Figure 3.22.: a. Molecular structure of **(b1)**, b. Molecular structure of **(b2)**.

stronger interaction between the metal centers. Therefore, this interaction strength will be more dependent on the amount of exact exchange, which is supported by calculations performed for **(b1)** and **(b2)** described in Section 3.3.2.

A common descriptor used in the literature to argue for certain types of exchange mechanisms are Natural Population Analysis (NPA)-charges[311] and the resulting populations of the 6s and 5d orbitals on the Gd(III)-centers.[216,218] The NPA charges and orbital occupancies for the high spin state are summarized in the appendix, Table A.8. These values are essentially meaningless. For example, compound **(b1)** exhibits the most ferromagnetic coupling constant in the testbed and $\approx$ 0.85 electrons in the 5d orbitals of each Gd(III). In comparison compound **(b8)** is clearly antiferromagnetically coupled, yet according to the calculation it has $\approx$ 1.1 electrons in the 5d orbitals. In summary, there is no direct correlation between the coupling constant and NPA properties, neither to the charge, nor the 5d-population.

Here, the spin density is a more informative observable. Figure 3.23 shows the calculated spin densities for compounds **(b1)** and **(b4)** using the bh-lyp functional. **(b1)** clearly shows a larger separation of α and β spins as indicated by the larger visible area of β spin density. Especially in comparison with **(b4)**, which is well behaved, this separation could be a reason for the larger errors calculated for **(b1)**. An unnecessary separation of α and β spin densities could also be the cause for the incorrect value calculated for compound **(b8)** using the m06 functional as shown in the appendix. The reason why such spin polarization is indicative of strong exchange will be explained in Section 3.3.5.

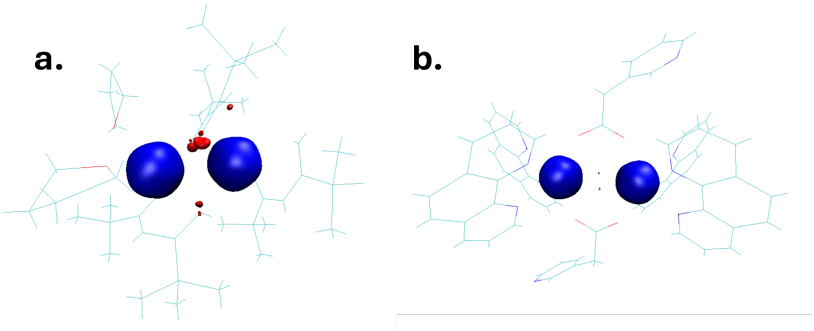

Figure 3.23.: a. Spin density of compound **(b1)**. b. Spin density of compound **(b4)**. Both calculations are performed with the bh-lyp functional. The isodensity is 0.05, blue areas denote α spin, red is β spin density.

The relation between the coupling constant and two geometric features was investigated for the testbed. More precisely, the Gd-Gd distance and the Gd-L-Gd angle are related to the coupling constants. Figure 3.24 summarizes the correlations for the bh-lyp functional. The qualitatively similar figures for the other suggested functionals as well as experimental fits can be found in the appendix, Figures A.11–A.12.

Between 3.7 Å and 4.1 Å, a correlation between the coupling constant and intermetallic distance can be observed, whereas there was no clear correlation observed for the angles. The only information from the angle plot is perhaps that oxygen bridged Gd(III)-binuclear structures tend to have more obtuse angles than other bridges, which however does not seem to affect the coupling constant. This is at odds with previous studies, which however investigated a single structure.[216]

The fact that such a correlation cannot be found in this data set can be accentuated by calculating two different correlation coefficients.

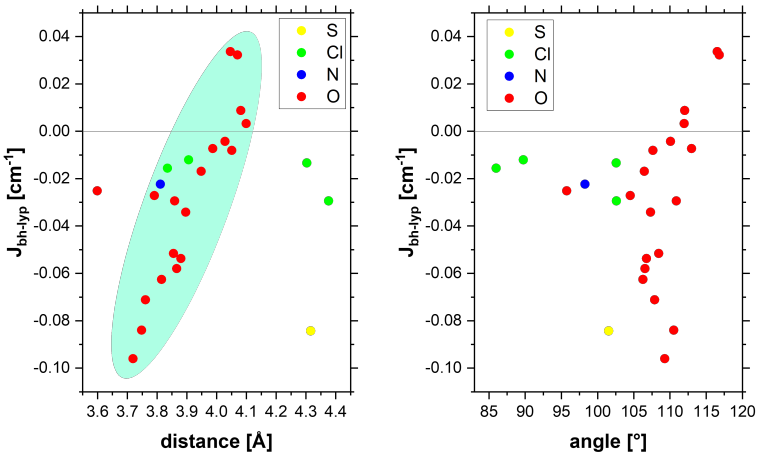

Figure 3.24.: The coupling constant *J* calculated with bh-lyp against the Gd(III)-Gd(III) distance (left) and the Gd(III)-L-Gd(III) angle (right). The green area marks an area of possible correlation.

The strength of a correlation lies between 0 and 1. In Pearson's method, a linear relationship between an observable and parameter is assumed.[312] In contrast, Spearman's correlation coefficient is purely rank based. Values above 0.8 can be considered as a significant correlation.[313]

The correlation coefficients between angles and *J* are clearly insignificant (r_S = 0.31, r_P = 0.15). If only the subset of oxygen bridged compounds are considered, the correlation is still irrelevant (r_S = 0.44, r_P = 0.24). Considering all molecules, the correlation between the Gd-Gd-distance and *J* is also insignificant (r_S = 0.53, r_P = 0.34). Only when considering the subset of oxygen bridged compounds, a noteworthy correlation can be reported with respect to the Gd-Gd distance.

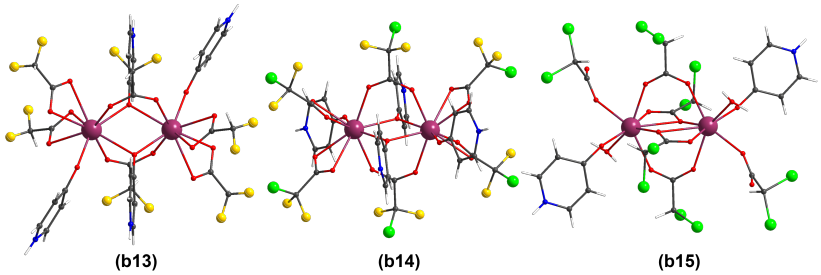

Figure 3.25.: Molecular structures of **(b13)**-**(b15)**

Pearson's correlation coefficient is r_P = 0.77 and Spearman's r_S = 0.82. This is indicative of a weak correlation.

Finally, complexes **(b13)**, **(b14)** and **(b15)** were analyzed in more detail. These compounds are very similar given that the coordinating ligands are deprotonated 4-hydroxypyridine and differently substituted carboxylic acids.[279] Despite their structural similarities, the coupling varies between -0.014 cm^{-1} for **(b15)** and -0.062 cm^{-1} for **(b13)**. The fitted *J* for **(b14)** is -0.022 cm^{-1}. The four suggested functionals calculate *J* lying between -0.054 cm^{-1} and -0.086 cm^{-1} for compound **(b13)** which is close to the experimental value. Additionally, the range calculated for **(b15)** is between -0.008 cm^{-1} and -0.013 cm^{-1} again in perfect agreement with the experiment. However, values between -0.058 cm^{-1} and -0.092 cm^{-1} are calculated for compound **(b14)**, significantly deviating from the experimental value. As discussed before, compound **(b14)** was the compound with the most MaxADs across all functionals. Because compounds **(b13)** and **(b14)** are structurally almost identical, it is curious that their experimental coupling is so different. Their Gd-Gd distance differs only by in 0.1 Å and their bridging angle by 0.1°. This might indicate a problem with the experimental data.

Moreover, a study by Roy *et al.* found that the residue on a carboxylate does not significantly influence the coupling constant.[222] The effect of terminal ligands on the coupling will be investigated in a more general manner in Section 3.3.6.

3.3.4. Application to Gd_4-Clusters

The reliability of the best practices found in Section 3.3.2 is now tested for more complex spin systems: BS-DFT calculations were carried out for two Gd_4-clusters with different symmetries. Compound **(b28)** is a C_2-symmetric, carbamate bridged cluster with two different kinds of bridges. The first type of bridge consists of four carbamate ions coordinating in a 1:2κ^2O; 3κO'-motif between Gd1 and Gd2 (Gd3 and Gd4). The second oxygen connects these pairs by coordinating to Gd3 or Gd4 (Gd1 or Gd2). The second bridge consists of two *syn,syn* 1κO; 2κO'-coordinating carbamate ions connecting Gd1 and Gd3 (Gd2 and Gd4). Because of the cluster's symmetry, there are only three distinct Gd(III)-Gd(III)-distances: 3.882 Å between Gd1 and Gd2 (Gd3 and Gd4), 4.650 Å between Gd1 and Gd3 (Gd2 and Gd4) and 5.033 Å between Gd1 and Gd4 (Gd2 and Gd3).[314] Compound **(b29)** can be best described as an asymmetrical trigonal pyramid bridged via a hydroxide, four phosphate ions and two carboxylates. The triangular base of the cluster is connected via a hydroxide in a μ_3-fashion. Each ion in the base is bridged via a phosphate in 1:2κ^2O; 1κO'-motif. A third oxygen of these ions connects the apical Gd with the base. Furthermore, two edges of the base are additionally bridged via a 1κO; 2κO' carboxylate while the last edge is reinforced with a 1κO; 2κO'-phosphonate bridge.

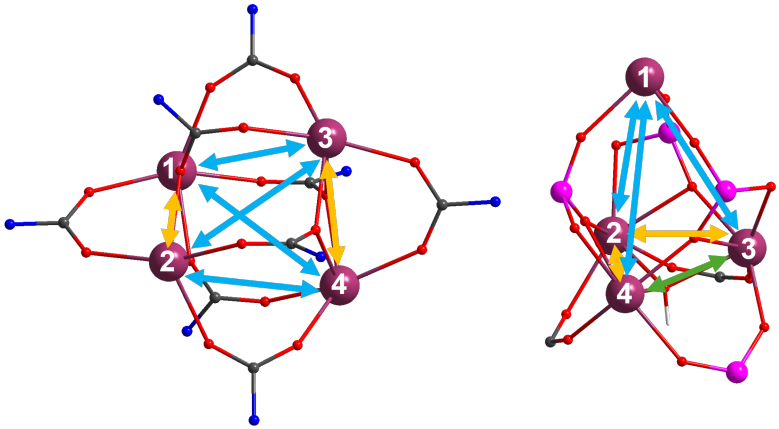

Figure 3.26.: Core structures of compounds **(b28)** (left) and **(b29)** (right). Similar couplings are indicated with same colored arrows. The colors for the atoms are violet, purple, red, blue and gray for Gd, P, O, N and C respectively.

Because of the asymmetric bridging motif, the Gd-Gd distances connecting the apical Gd and the base are between 5.544 Å and 5.604 Å (blue arrows in Figure 3.26, (right)). In the base, the Gd-Gd-distances range between 3.809 Å and 3.863 Å.[315] The models used in the calculation are depicted in Figure 3.27.

By replacing two Gd(III) ions with Y(III), the exchange coupling for each pair interaction was calculated. These are summarized in Table A.9. Regarding compound **(b28)**, the coupling for Gd1-Gd2 and Gd3-Gd4 is identical as expected as a result of the symmetry. The calculated values range from -0.035 cm^{-1} with bh-lyp to -0.055 cm^{-1} with pbe0. All other coupling constants are less than ± 0.003 cm^{-1} and therefore negligibly small (blue arrows in Figure 3.26, left).

Consequently, these calculations suggest that the magnetic behavior of compound **(b28)** stems from two essentially uncoupled Gd(III)-dimers which is at odds with the originally proposed model where the magnetic data was fitted with two coupling constants with J_1 between Gd1-Gd2 and Gd3-Gd4 as well as J_2 between Gd1-Gd3 and Gd2-Gd4.[314]

Using these new sets of coupling constants, the molar susceptibility and magnetization were simulated using the program PHI. Here, the experimental values were scaled to fit with the theoretical high temperature values which is analogous to fitting an anomalous g-factor close to 2. This is a minor change as the experimental high temperature/high field values are 31.2 $cm^3mol^{-1}K$ and 27.0 μ_B instead of the theoretical 31.5 $cm^3mol^{-1}K$ and 28.0 μ_B. Thus, the final simulations did not include any free variables. Figure 3.27 shows the excellent agreement with the experimental values.

The coupling constants calculated for compound **(b29)** reveal that the coupling of the apical position with the base can be neglected, since all constants are below ± 0.002 cm^{-1}. With respect to the coupling in the triangular base, the couplings between Gd2-Gd3 and Gd2-Gd4 (yellow arrows in Figure 3.26, (left)) are similar in magnitude and stronger than the coupling between Gd3-Gd4 (green arrow). Again, the weakest coupling was calculated with the bh-lyp functional (-0.042 cm^{-1} for Gd2-Gd3, -0.040 cm^{-1} for Gd2-Gd4) and the strongest coupling was calculated using pbe0 (-0.072 cm^{-1} for Gd2-Gd3 and -0.067 cm^{-1} for Gd2-Gd4). The range for the coupling between Gd3-Gd4 was -0.021 cm^{-1}– -0.037 cm^{-1}.

This is in line with the results of chapter 3.3.2 where it was found that pbe0 will slightly overestimate the coupling whereas bh-lyp slight underestimates the experimental values.

However, in the case of compound **(b29)** the agreement with the experiment is less satisfactory.

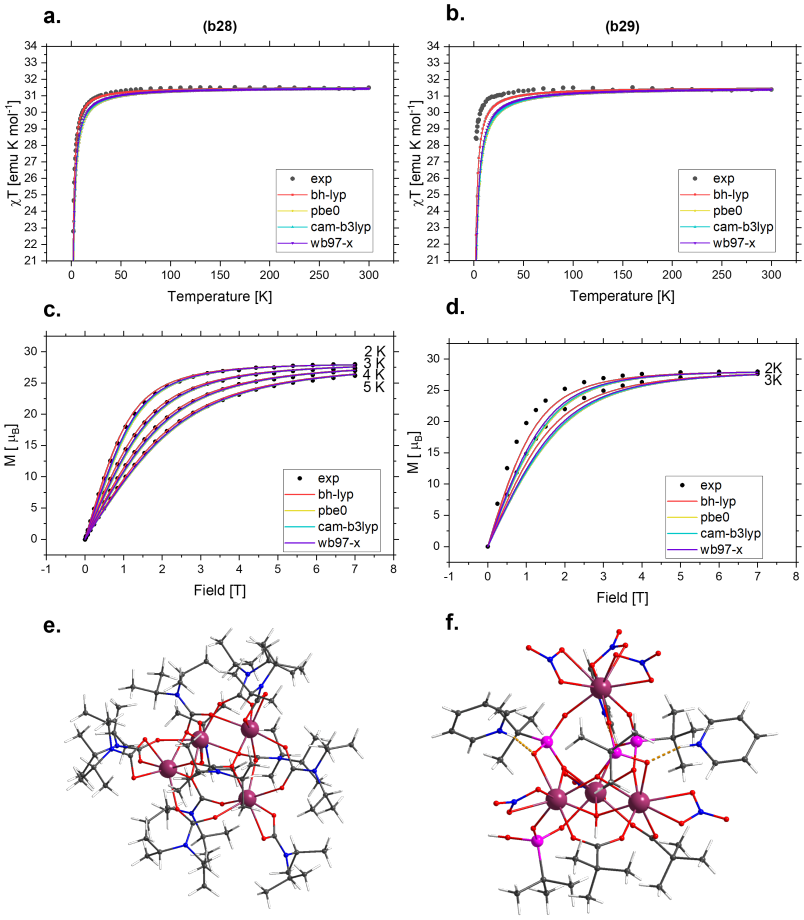

Figure 3.27.: Molar susceptibility (top) and magnetization (middle) for compounds **(b28)** (left) and **(b29)** (right). Experimental data is indicated with dots, data simulated using the coupling constants from BS-DFT are colored lines. The bottom row shows the full computational model.

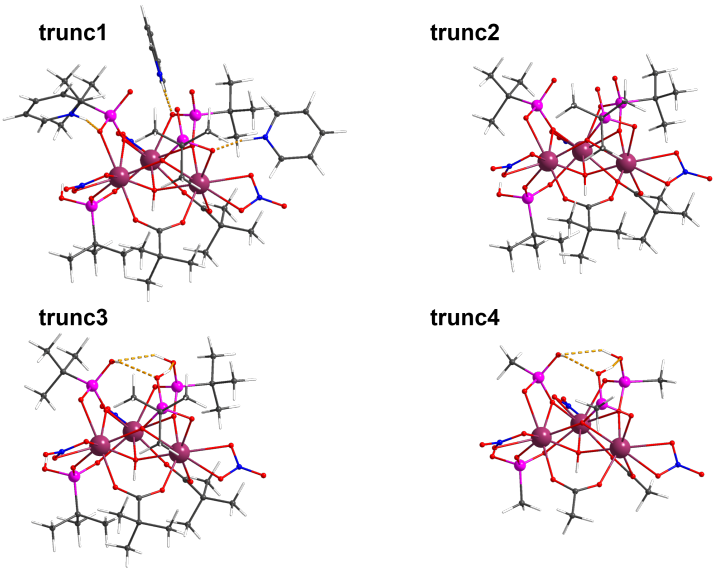

Figure 3.28.: The four truncated chemical models for compound **(b29)**. First, the apical $Gd(NO_3)_3$-moiety is removed. Secondly, the pyridinium-ions H-bonded to the cluster are neglected. Thirdly, three H-atoms are added to saturate the dangling coordination sites. Finally, distant isobutyl-groups are replaced with methyl groups.

Figure 3.27b shows that the coupling is overestimated by all functionals, although these lie within the errors of the preliminary benchmark.
The original fit assuming three equivalent interactions in the triangular base suggested a coupling of -0.01 cm^{-1}.[315] Because of the unsatisfactory agreement with the experiment, it is worth investigating the influence of the model structure on the calculated coupling constants. To do this, four additional chemical models were constructed and calculated. Firstly, since the apical Gd1 does not couple with the base, the $Gd(NO_3)_3$-moiety was removed.

Next, the three pyridinium-ions, which are hydrogen bonded to the central cluster, are removed thus changing the charge of the model cluster from -1 to -4. In the third step, H-atoms were added to the dangling coordination sites where the apical Gd once was. These were reoptimized on a b3-lyp-D4/ri level of theory. In a last step, the isobutyl-residues of all ligands were replaced with methyl groups, the hydrogen atoms of which were optimized on the same level of theory.

As apparent from Figure 3.29, the different models have an influence on *J*. While slightly stronger couplings with respect to the original model are calculated using models 1 and 2, a jump towards a more ferromagnetic interaction is predicted with model 3. This is to be expected since the protonation of coordinating ligands will change the density around the coordinating sites. This explains why the change of isobutyl-groups to methyl groups does not have a large influence on the results while simplifying the calculation considerably.

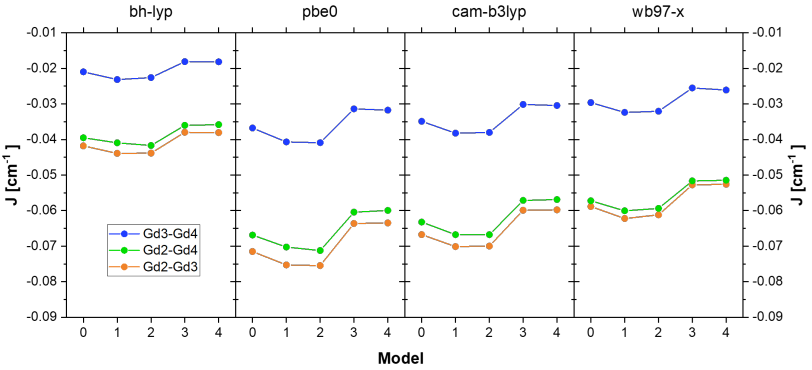

Figure 3.29.: Overview of the exchange coupling constants calculated with the 4 different functionals for all 5 chemical models of compound **(b29)**.

The order of *J* for the three coupling constants does not change in all three models: Gd3-Gd4 always exhibits the weakest coupling, whereas Gd2-Gd4 is slightly weaker than that for Gd2-Gd3. These are are both approximately twice as strong as Gd3-Gd4.
There are two key takeaway messages from this study. **1.** Coupling constants obtained with BS-DFT are sufficient to model the spin structure of larger Gd-clusters. BS-DFT can be used to assist the fitting of magnetic data for structurally similar compounds. **2.** The chemical model employed can be simplified by truncating large aliphatic residues on carboxylates and phosphonates since these do not influence the electronic structure around the lanthanide directly. It should be noted that packing effects in the crystal structure may well play a role.

3.3.5. Structure Property Relationships in Halide-bridged Dimers

In Sections 3.3.1 to 3.3.4 it was shown that BS-DFT is a suitable method to calculate coupling constants of dinuclear Gd-compounds. Furthermore, best practices were established to compute these. However, from this database, it was not possible to find rigorous structure-property relationships. This problem will be addressed in the next sections:
First, a set of model structures was optimized and distorted to calculate the coupling constants. Afterwards, Symbolic Regression (SR) was used to find an explicit formula connecting different features with the observable, *J*. The relevance of the discussed features is then interpreted in the context of established exchange mechanisms. Finally, the influence of exact exchange is revisited and a comparison is drawn to a CASSCF-calculation to put the absolute values into context.

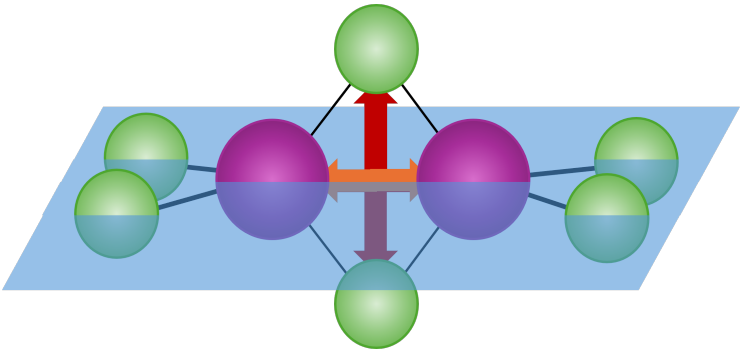

Figure 3.30.: Schematic of the $Gd_2X_2Y_4$ model proposed to investigate structure property relationships. While X and Y are always the same atom, X refers to the bridging, Y to the terminal ligands. Either the Gd-Gd distance including the Y-atoms in the plane can be changed (orange arrow), or the bridging X-X distance outside the plane (red arrow). Violet sphere represent Gd-atoms, green spheres chloride atoms.

It is evident that a simple chemical model is needed to identify unambiguous structure-property relationships. Therefore the $Gd_2X_2Y_4$-molecule (X,Y = F, Cl, Br, I) is proposed as a model structure (see Figure 3.30). This has a number of benefits. Firstly, it contains four relevant structural descriptors: the Gd-Gd-distance, the Gd-X-Gd angle, the Gd-X distance and the X-X distance. Based on its D_{2h}-symmetry, the model can be split into four parts. By moving the two terminal GdY_2-moieties in the plane, the Gd-Gd distance can be modified. By moving the two bridging halide atoms away from the Gd-Gd connection, the X-X distance is changed. Both distortions result in a change in the Gd-X-Gd bridging angle as well as the Gd-X distance. Notably, there is only one other theoretical study investigating Ln_2X_6-dimers published by Kovacs in 2000.[316] The bonding and molecular vibrations in these dimers were investigated.

Furthermore, halide bridged Dy-SMMs and Gd-dimers have gained recent attention based on their ability to promote exchange interactions.[317,318]
In a first step, the molecular structure of Gd_2Cl_6 was optimized with bh-lyp. Exchange coupling constants are calculated on a dft/rij/x2c-TZVPall level of theory with the DFT-functionals bh-lpy, pbe0, cam-b3lyp and ωb97-x with scalar relativistic effects treated on a dkh2 level of theory. The resulting structure has a Gd-Gd distance of 404.9 pm. The Gd-Cl distances are 247.4 pm and 269.8 pm to the terminal and bridging chlorides respectively. For comparison, the distance to the bridging chloride is close to the shortest experimental value in the $GdCl_3$-crystal structure (282 pm).[319,320]
Subsequently, the structure was distorted along the red and orange arrows shown in Figure 3.30. This was done through an elongation and compression of the distances in 7 steps of 5.29 pm (0.1 a_0). The result was a 15x15 grid of distorted structures. In all of these structures, the terminal ligands are fixed with respect to the Gd-atoms they are coordinated to. Therefore, only the bridging geometry changes. At each of these positions, a BS-DFT calculation was carried out using the four suggested functionals (Section 3.3.2). Subsequently, using the same grid, Cl was replaced with F, Br and I and the coupling constants were computed.
Figure 3.31 shows a heat map of the resulting coupling constants for Gd_2Cl_6 calculated with bh-lyp. In addition to the independent parameters (Gd-Gd distance, bridging Cl-Cl distance) two dependent features are shown for reference. The Gd-Cl distance is indicated by dotted lines and the Gd-Cl-Gd angles as dashed lines. For the rest of this section, Gd-Cl distance refers to the distance to the bridging Cl-ion unless explicitly stated otherwise. Two distinct features can be observed: At short Gd-Gd distances and short Cl-Cl distances the coupling constant becomes strongly negative. Contrarily, at short Gd-Gd distances but long X-X distances, the coupling constant becomes strongly ferromagnetic.

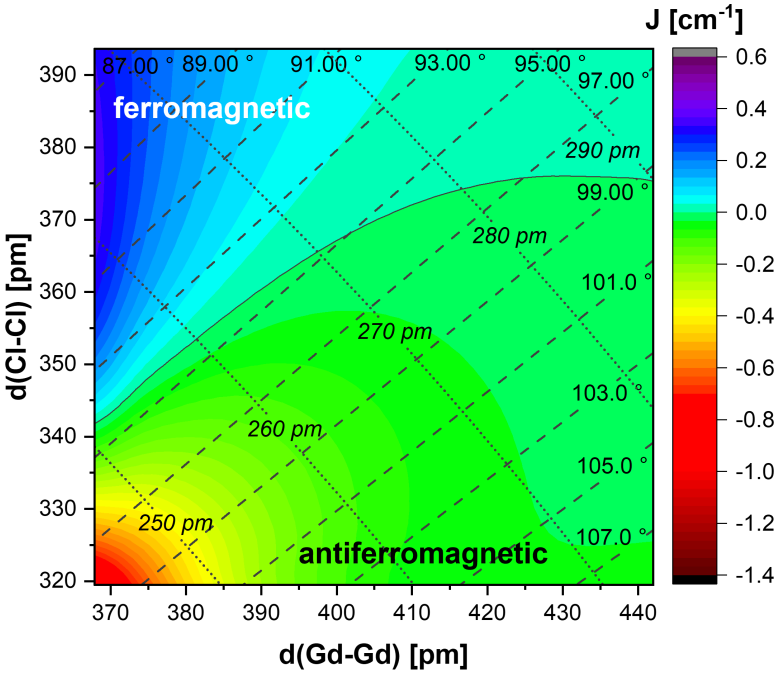

Figure 3.31.: A heat map of the calculated coupling constants on the 15x15 grid for Gd_2Cl_6 using the bh-lyp functional. In addition to the Gd-Gd distance (x-axis) and bridging Cl-Cl distances (y-axis) two dependent parameters are shown: The Gd-Cl distance is shown as dotted lines, the Gd-Cl-Gd angle is shown as dashed lines.

The J = 0 cm^{-1} line first follows an angle of around 94° before curving at medium Gd-Gd distances. At high Gd-Gd distances and high Cl-Cl distances the coupling approaches 0 cm^{-1}.

Interestingly, a similar experiment has been performed previously by Fink *et al.* on a Ni-S-Ni bridge which however yielded two changes of the sign along a given angle.[321]

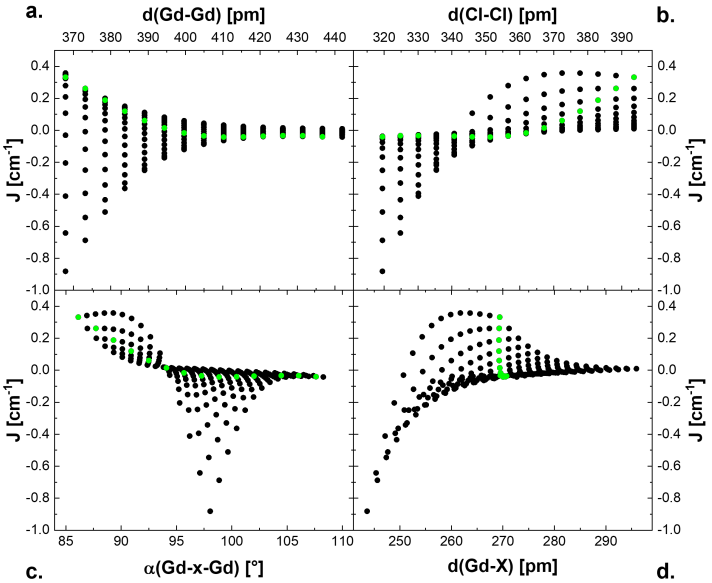

Figure 3.32.: Correlation of the four structural parameters with the coupling constant J in cm^{-1}. a. Gd-Gd distance, b. Cl-Cl distance, d. Gd-Cl-Gd angles, d. Gd-Cl distance. Structures with a Gd-X distance close to the equilibrium Gd-X = 270 pm are marked in green.

A comparison of the structures where X,Y = F, Cl, Br and I reveals that they share the same underlying structure differing only in magnitude. This is to be expected since the reference structure is that of optimized Gd_2Cl_6, the Gd-X and Gd-Gd distances are too long for equilibrated Gd_2F_6 and too short for Gd_2Br_6 and Gd_2I_6. These data are illustrated in Figures A.13-A.17. The relationship between J and the structural parameters is summarized in Figure 3.32. a. J can be either positive or negative at short Gd-Gd-distances, whereas it is always close to 0 cm^{-1} at long Gd-Gd distances. Clearly, the further apart the Gd-centers are, the less active is going to be any exchange pathway.

b. The trend of *J* with respect to the Cl-Cl distance changes sign from negative to positive around 340 pm. c. Furthermore, the relation with the Gd-X-Gd angle appears to have a node at 94°. However, as already established, this is only true for short Gd-Gd distances. The negative sign at more obtuse angles correlates with the negative sign at short X-X distances. d. Finally, the relation with the Gd-X distance seems to be more complex. Clearly, no single structural parameter is responsible for the resulting coupling constant.

The structures with an equilibrium Gd-X distance of 269.8 pm are highlighted in green for a simple comparison along this line.

To find possible structure-property relationships in this dataset, a machine learning model called Symbolic Regression (SR) is employed. Through a genetic algorithm, this model finds human-interpretable equations that reconstruct an observable from a set of features (i.e. input variables). Each equation has a given complexity. The complexity is the number of variables (either free or a feature) plus the number of arithmetic operations. In this thesis, the PySR package is used which suggests a "best" equation for a number automatically selected complexities in a given range.[322] The general workflow and parameters used are summarized in Section 7.2.

In a first step, only the geometric parameters are investigated. The obtained equations are summarized in the appendix, Table A.11 and Figure A.18. One key observation is that for most given complexities and systems, the best equations contain an inverse exponential dependency on either the Gd-Gd distance and/or the Gd-X distance. Whilst the exponential dependence on the Gd-Gd distance appears much more frequently than that on the Gd-X distance for Gd_2F_6, the opposite is the case for Gd_2I_6.

Figure 3.33 demonstrates this dependence. Using a simple exponential function with three free parameters, the calculated coupling constant of Gd_2Cl_6 can be fitted with an exponential decay dependency on the Gd-Gd distance. This equation has a complexity of eight.

$$J = J_0 + A \cdot exp(B \cdot r_{Gd-Gd})$$

This is in line with previous findings where a linear Cr-O-Cr chain was investigated for the coupling constant on the Cr-O distance. Here, Wang *et al.* also reported this exponential dependence.[323] Subsequently, why the Gd-Gd and Gd-X distances are relevant for the different model complexes will be discussed. Furthermore, these results support a finding in Section 3.3.3, suggesting that there is no simple relationship between geometric factors and the coupling constant.

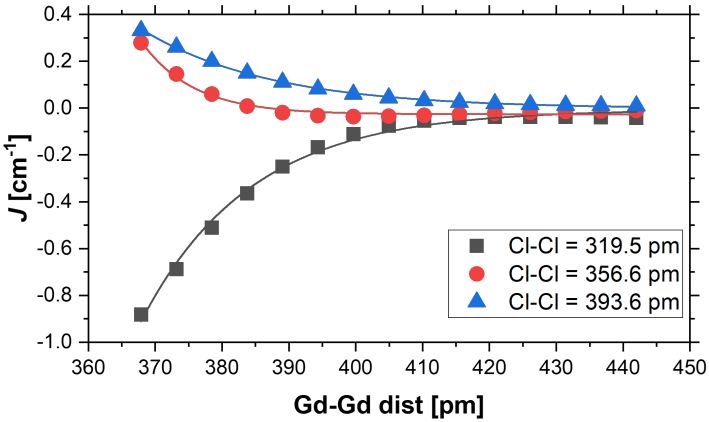

Figure 3.33.: The calculated coupling constant (dots) along three lines keeping the X-X distance fixed and changing the Gd-Gd distance, can be fitted with a simple exponential decay function (lines).

The next step was to find good DFT-descriptors to interpret the observed coupling constants. However, because the grid was constructed with two independent variables (the Gd-Gd distance and the X-X distance) all other features are derived variables. Consequently, the feature space cannot be larger than two without introducing redundancy, as can be shown with Principle Component Analysis (PCA). Also, because of the low dimensionality of the given problem, it will be possible to find an expression dependent on any two features with low correlation. Further discussion will therefore focus on a balance of interpretability of the features and simplicity of the obtained expressions.

Two features will be discussed in the following: "cso-trace" refers to the trace of the spatial overlap matrix between the seven α and β corresponding spin orbitals (CSOs). CSOs are a set of orbitals obtained by rotating the spatial parts of α and β-spin orbitals maximizing their overlap. This is done because the spatial parts of different parity spins may differ significantly in an Unrestricted Kohn Sham (UKS) calculation. Because the overlap between α and β orbitals is calculated here, this analysis has to be performed on the broken symmetry state. Whereas the diagonal elements between Corresponding Spin Orbital (CSO) overlap matrix elements can be calculated with Turbomole, the off-diagonal elements were calculated using a program provided by Dominik Steinmetz. The second feature is the difference in spin-contamination of HS and BS-states. The $\langle \hat{S}^2 \rangle$-expectation value for a UKS-SD can be written as:[324]

$$\langle \hat{S}^2 \rangle = \left(\frac{N^\alpha - N^\beta}{2} \right) \left(\frac{N^\alpha - N^\beta}{2} + 1 \right) + N^\beta - \sum_i^N \sum_j^N |S_{ij}^{\alpha\beta}|^2. \quad (3.5)$$

Whilst the first term in this expression is the exact expectation value of $\hat{S}^2$, the sum of the last two terms becomes non-zero in the case of spatially differing α and β-spin orbitals.

It can be easily extracted from the DFT-calculation by subtracting the ideal $\langle \hat{S}^2 \rangle$-value from the calculated. The descriptor used here is the difference of the HS- and BS-spin polarization (DS2).
Using these two descriptors, SR-was performed as outlined in Section 7.2. It should be noted that the resulting expressions are highly dependent on the starting parameters used. The results for the four model complexes are summarized in the appendix, Table A.12.

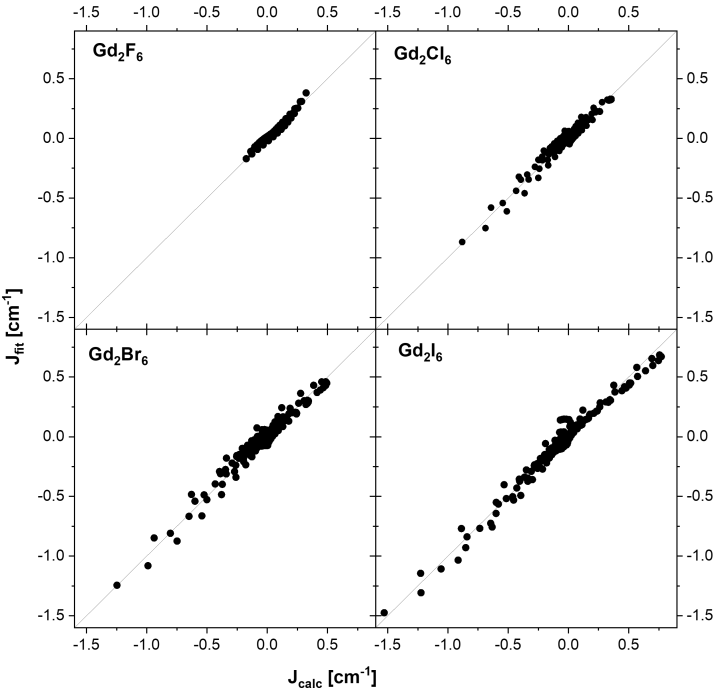

Figure 3.34.: Correlation between *J* fitted with Equation 3.6 and the calculated values using BS-DFT and the bh-lyp functional for the four model compounds.

It becomes apparent from this table that second order polynomials give a good agreement between the calculation and simulation. Using this information, the data for the four model clusters was fitted with a uniform equation:

$$J = ax^2 - axy + by + c. \tag{3.6}$$

Here x is the cso-trace, and y refers to DS2. The results of this fit are shown in Figure 3.34, the fit parameters and goodness of fits are summarized in the appendix, Tables A.13–A.14. Importantly, normalized features are used for this fit. The agreement between simulation and calculation is sufficient. It can be noted that parameter b becomes larger going from Gd_2F_6 to Gd_2I_6. This suggests that spin polarization becomes a more important parameter going to heavier homologs in this series. However, considering the uncertainty of the underlying expression, it is best not to overinterpret this model. The main implication of this study is that if a reasonable connection between these features and the coupling constant can be established, the magnetic overlap and spin polarization change are good descriptors for *J*. This is done in the following.

A direct exchange interaction mechanism as established in Section 3.1 can be modeled within the single determinant ansatz in DFT. The orbital mixing between the different sites is directly modeled by investigating the sum of orbital overlap between the magnetic centers as done in the cso-trace. Unsurprisingly, this overlap has been reported in the literature repeatedly to rationalize antiferromagnetic exchange.[216,325]

The cso-trace is at its maximum at short Gd-Gd distances and short Cl-Cl distances (Figure A.19). Such large values are interesting considering that there should not be any noteworthy overlap between the 4f-orbitals because the inter-lanthanide distance is always significantly larger than the sum of the ionic radii for Gd(III).[326]

To explain this overlap, it is convenient to switch from CSOs to natural orbitals, i.e. orbitals that are generated by diagonalizing the one-particle density matrix. The BS-state results in 14 natural orbitals with eigenvalues (occupation numbers) equal to one. However, if these orbitals are able to mix, the occupation numbers deviate slightly from the ideal value. This is shown in Figure 3.35.

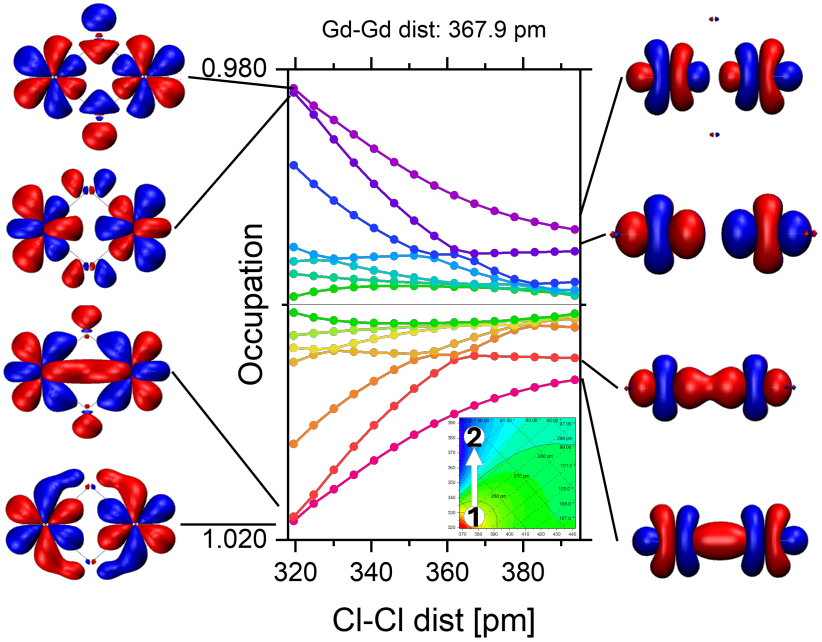

Figure 3.35.: Occupation numbers of the 14 singly occupied natural orbitals in the BS-state with a fixed Gd-Gd distance and various Cl-Cl distances. It is demonstrated that some naturals overlap more via the ligands at small distances which increases the overlap integral and the occupation number. Calculated with the bh-lyp functional and plotted with a isodensity of 0.01.

Importantly, there is a 1:1 correspondence between total overlap calculated for the CSOs (cso-trace) and the total, absolute deviation of the natural orbitals occupation number from one.
When metal orbitals weakly mix with ligand orbitals, this leads to "bonding" and "anti-bonding" combinations with occupation numbers slightly deviating from one. This increases the orbital overlap significantly. Similar observations have been reported using multireference calculations.[105,200]
In the present case, an energy decomposition was performed based on the different contributions to the Hamiltonian to gain further insight into the change of energy contributions between HS- and BS-states. This approach partitions the energy difference between the two states in one-electron, Coulomb, exchange and correlation contributions. This is not an Energy Decomposition Analysis (EDA) as implemented for example in Turbomole,[327] considering that no division in subsystems was performed. The result is summarized in dependence on the Cl-Cl distance in Figure 3.36.
In essence, this shows that the energy difference is almost completely governed by the negative one-electron (i.e. kinetic energy) and positive electron-electron Coulomb repulsion contributions, which are up to two orders of magnitude larger than the other contributions. The sum of these two contributions already summarizes the qualitative trend in *J*. Since both of these parameters are dependent on the localization of electrons, this is in line with the direct exchange interaction model. However, as previously discussed, this cannot be explained solely with the overlap of the magnetic orbitals.
The exchange contribution to the Hamiltonian will stabilize the energy if many electrons with the same spin localize at a given center. In a HS-system this can be achieved when ligands donate α-spin density to the magnetic centers leaving the ligand β-spin polarized.

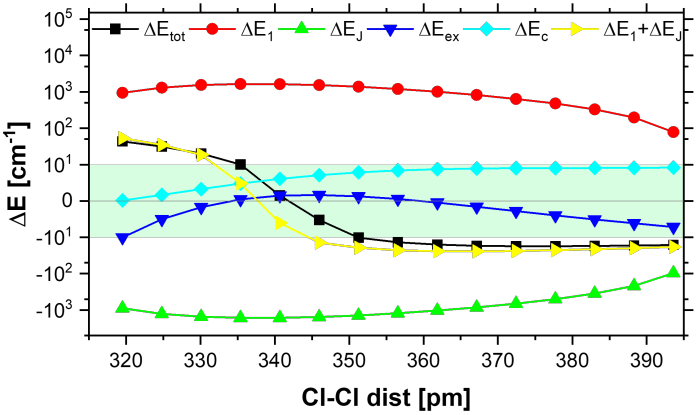

Figure 3.36.: Different energy contributions to the HS-LS gap. The area highlighted green scales linearly, whereas the remaining graph scales logarithmic. The values are depicted for the shortest Gd-Gd distance using the Gd_2Cl_6 molecule and the bh-lyp functional. The terms investigated are the differences in total energy (E_{tot}), one-electron contributions (E_1), Coulomb repulsion (E_J), exchange (E_{ex}) and correlation (E_c).

Here, the 5d-orbitals are the lowest available orbitals at the Gd(III) which can accept this additional density.

Spin polarization in the BS-state is not as straightforward: Whilst there are 14 orbitals interacting through exchange in the HS case (196 non-zero exchange integrals) there are only two 7x7 exchange-matrices in the BS-state (98 non-zero exchange integrals). Consequently, it is not expected that further spin polarization will stabilize the BS-state as much as the HS-state. It should be noted here, that a BS-state is inherently spin polarized. This is illustrated in Figure 3.37. Therefore, the difference of spin polarization of the ligands in the HS and BS-state contains information on how much the different states are stabilized and consequently about the magnetic coupling constant *J*.

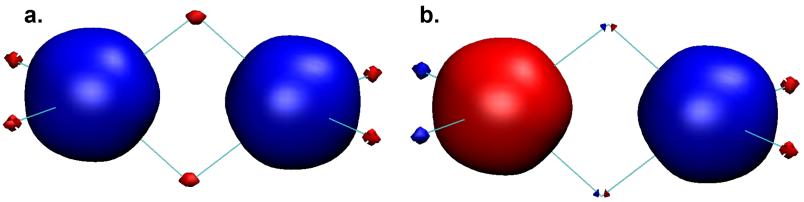

Figure 3.37.: Comparison of (a.) HS- and (b.) BS-spin densities at Gd_2Cl_6 with the shortest Gd-Gd and Cl-Cl distances calculated with bh-lyp. The isodensity depicted is 0.005. It can be seen that there is more spin polarization of the bridge in the high spin case whereas the spin polarization of the bridge vanishes in the BS-case.

The heat maps for spin polarization in the HS and BS-state as well as their difference are shown in the appendix (Figures A.20 and A.21).
Whereas it was shown that various charge transfer states are important to describe the magnetic ground state,[105,200] there is no experimental indication of spin polarization accompanied by an at least partial reduction of the Gd(III)-center. However, as shown here and previously by Noodleman and Davidson, it has a significant influence on the coupling constant.[328] This is intuitive because a spin polarization mechanism is also related to the (de-) localization of electrons. Consequently, it will also contribute to kinetic and Coulomb energy contributions of the interaction. However, it is found here that, if there is significant ligand spin polarization in the BS-DFT-calculation it is most likely that it will give a result based on a principle not observable in experiment.
Earlier in this chapter, it was shown that this polarization mechanism becomes more prevalent for the models with non-physical Gd-X distances (Br, I) similar to the strongly coupled Gd-dimers in Section 3.3.3. This explains why BS-DFT is so unreliable in these specific cases.

The NPA occupation[311] of the 5d-orbitals is given as a reason for charge transfer states being important for magnetic coupling, especially in 3d-4f-complexes.[217,218] DFT can indeed mimic the contributions of charge transfer states through an orbital rotation. However, the observed occupations in the 5d-orbitals are more likely a result of ligand spin polarization and not metal-metal charge transfer. The current analysis shows that the 5d-occupation is indeed strongly and non-linearly correlated with magnetic orbital overlap (Figure A.22) and could therefore act as an alternative descriptor to *J*. Future studies could help to understand the meaning of this observation.

The current section established a strong dependency of *J* on the spin-localization which is indicative of an influence of the amount of HF-exchange in the functional employed. Therefore, a similar study as described in Section 3.3.2 was performed: For two fixed Gd-Gd distances, the amount of exact exchange in the b3-lyp functional is scaled from 0 to 1 using a step size of 0.05. The results are shown in Figure 3.38 for the Gd_2Cl_6 molecule. At low amounts of exchange exchange, the coupling is calculated to be significantly more antiferromagnetic compared to higher amounts of exact exchange. The coupling constant becomes more ferromagnetic quickly, before approaching almost linear behavior at around 40 % exact exchange. Because of this monotonic behavior, the sign of the coupling constant changes for many geometries, similar to the observations presented in Section 3.3.2.

Finally, it should be noted that the coupling constants calculated on the 15x15 grid are often significantly higher than the experimentally observed couplings. In order to put the extreme values into context, a CASSCF calculation was performed on the Gd_2Cl_6 model which has the shortest Gd-Gd combined with the shortest and longest Cl-Cl distances. This is done by using a modified CAS-CI approach.[98]

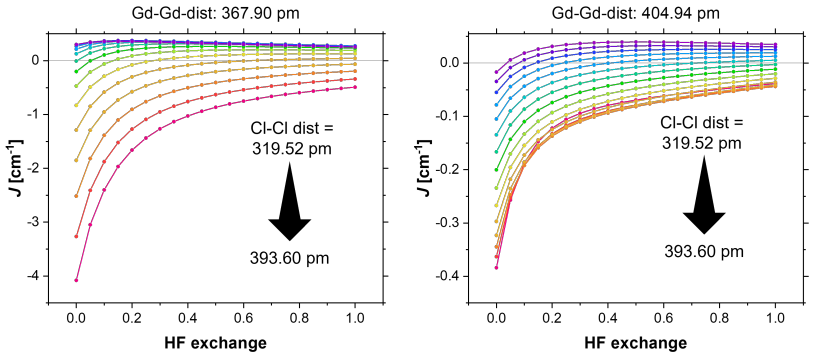

Figure 3.38.: Dependence of *J* on the amount of HF-exchange using a variation of the b3-lyp functional. This is shown for two Gd-Gd distances and the respective 15 Cl-Cl distances.

Using this approach, the inter-Gd charge transfer states' energy is corrected and more precise coupling constants can be obtained. The workflow for this approach is summarized in Section 7.2.

Thus, the coupling constants -0.469 cm^{-1} and 0.105 cm^{-1} are obtained for the shortest and longest Cl-Cl distance respectively. This shows that DFT significantly overestimates the coupling, nevertheless giving the correct sign.

Summarizing this section, a group of $Gd_2X_2Y_4$ molecules with X,Y = F, Cl, Br and I was investigated for structure property relationships with respect to the exchange coupling constant *J*. It was shown that there is no single structural parameter responsible for the coupling. However, the Gd-Gd and Gd-X distances are related exponentially to the coupling. Furthermore, two features of DFT calculations are discussed in terms of their influence on the magnetic coupling:

The trace of the spatial overlap matrix between corresponding spin orbitals and the difference in spin polarization between HS- and BS-states. It is rationalized why these are good descriptors for the observable (J) and how these are related to common shortcomings of BS-DFT.

3.3.6. Influence of the Bridge vs. Terminal Ligands

In the previous section, the effect of structural parameters on the coupling constant was investigated by changing the molecular geometry while keeping the same composition. In the following section, the electronic parameters of the ligands will be discussed and the effect of terminal and bridging atoms distinguished. To do so, different ligands are used for the bridging and terminal ions.

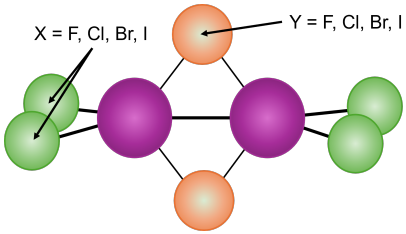

Figure 3.39.: Schematic of the $Gd_2X_4Y_2$ model proposed to investigate structure property relationships. Either the terminal ligands (green) or bridging ligands (orange) can be exchanged while maintaining D_{2h}-symmetry.

A first testbed is provided by the $Gd_2X_4Y_2$ molecules where the halide is changed independently for the two positions as shown in Figure 3.39. Comparisons are done with the Gd_2Cl_6 molecule as the reference.

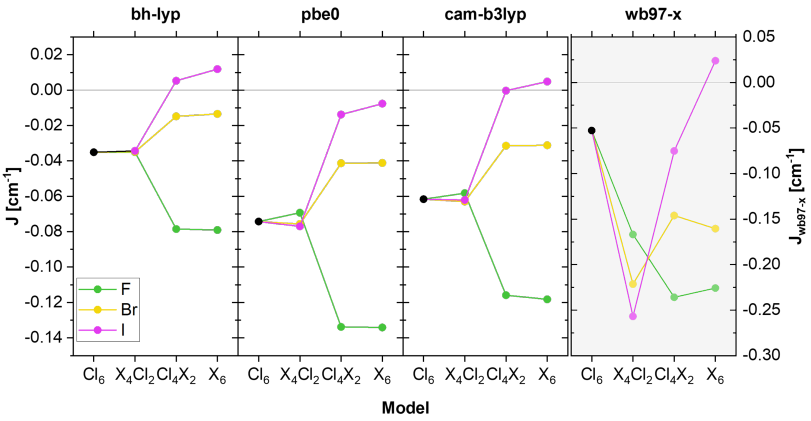

Figure 3.40.: Plot of the influence of terminal versus bridging ligands in the $Gd_2X_4Y_2$ model for four different functionals. X and Y are the same atom as indicated in the figure. All molecules are optimized using the same level of theory as is used to compute the coupling constant.

Starting from this molecule, the bridge and terminal ions are independently replaced by F, Br, and I. A geometry optimization is performed for each molecule using the same functional as used for the calculation of *J*. The results are summarized in Figure 3.40.

Notably, the coupling constants with altered terminal ligands calculated with bh-lyp are essentially the same irrespective of the terminal ion. This plot clearly shows that a change of the terminal ligand only has a marginal impact on the coupling. However, changing the bridge while keeping the terminal ligands fixed significantly changes the couplings. *J* becomes more ferromagnetic with Br and I, whereas it becomes more antiferromagnetic for F. Changing the terminal ligands additionally has an almost negligible influence.

Because the functional ωb97-x gives qualitatively different and physically unreasonable results, the following discussion is limited to the functionals bh-lyp, pbe0 and cam-b3lyp.

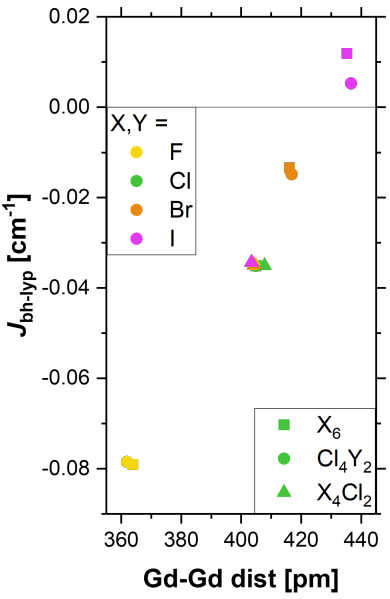

Figure 3.41.: A correlation using the different models Gd_2X_6, $Gd_2Cl_4X_2$ and $Gd_2X_4Cl_2$ between the coupling constant and the Gd-Gd distance. Shapes indicate the models, wheres the color indicates the atoms X and Y of the respective models.

The change in the coupling strength can be clearly correlated with the Gd-Gd distance as shown in Figure 3.41. The shorter the distance (F-bridges), the stronger the antiferromagnetic coupling. Again, changing the terminal ligands only changes the distance and consequently also the coupling marginally.

In Section 3.3.3, it was discussed that it is very difficult to compare structure-property relationships when the bridging atoms differ. Whilst the relationship seems more clear using the current simple model complex, it was decided to keep the same bridging atom in a series, but alter its electronic properties.

This aims to mimic a change in the electronic structure of Gd-dimers bridged via alcoholate ligands. Hypohalite ligands (OX^-, X = H, F, Cl, Br, I) are suggested as a model system for this study.

The widely ranging electronegativity and overall charge of -1 make this ligand ideal for the testing purposes. Furthermore, the simple linear arrangement preserves the D_{2h}-symmetry. It is worth noting that there are no accounts on $Gd(OX)_n$ compounds reported in the literature.

Figure 3.42 shows the coupling constant J dependency on the bridging ligands. In this case, the full molecular geometry was relaxed and vibrational frequency calculations performed to ensure a minimum is reached. Noteworthy is that the OBr^--bridge calculated with ωb97-x differs from the trend observed for all other calculations. The frequency calculation with the module NumForce did not converge for this geometry. Aside of this outlier, a clear trend can be observed going from F to I. This trend could be explained in terms of the Gd-Gd distance, ranging from 393.66 pm for OF^- to 364.45 pm for OI^-. OH^- (361.57 pm) is a clear outlier with a Gd-Gd distance shorter than that of OI^- but a coupling constant between that of OCl^- and OBr^- bridges. An equivalent trend in bond distances can be observed for the Gd-O distance.

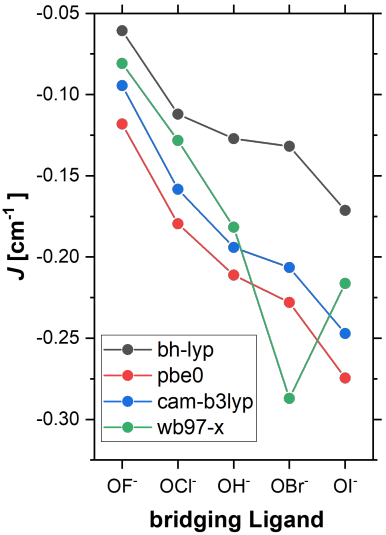

Figure 3.42.: The coupling constant dependent on the bridging ligand and functional used to compute geometry and J.

To eliminate the influence of the bridges' geometric relaxation, their coordinates were fixed in the third experiment of this section.

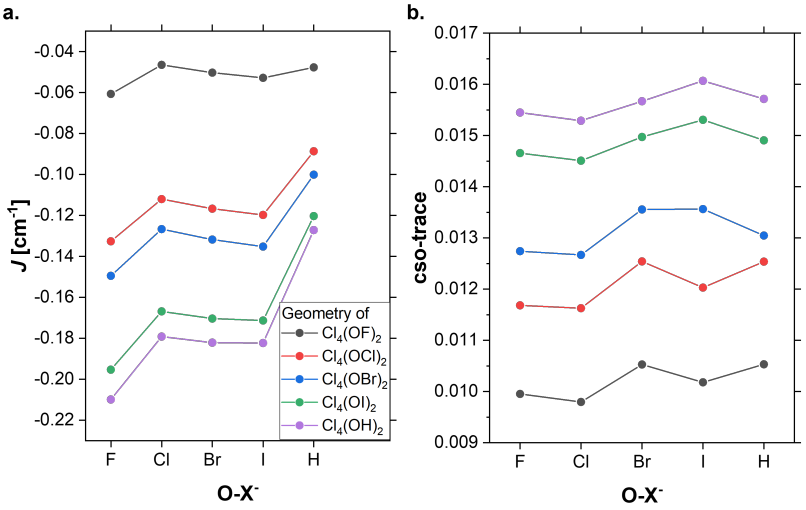

Figure 3.43.: Using the basic models optimized for the different hypohalite ions (lines), the halogen atom is varied (x-axis). The calculated coupling (a.) and trace of the spatial overlap matrix of CSOs in the BS-state are shown (b.).

Now, using the geometries of the five bridges, the halide atom at the bridge was replaced and only the O-X distance optimized on the respective levels of theory in order to obtain reasonable models. The idea is to use the oxygen atom as a fixed probe and to only change its partial charge and electron density via the adjacent halide atoms. The obtained coupling constants of the 25 generated structures as well as the trace of the magnetic orbital spatial overlap matrix are shown in Figure 3.43 and in the appendix in Figure A.23.

In line with earlier results reported in this thesis, a larger CSO-overlap corresponds to a stronger antiferromagnetic coupling.

This explains the large differences between the different base geometries shown in different colors. The change in *J* upon varying the halide follows the same rationale for the $Gd_2Cl_4(OI)_2$ and $Gd_2Cl_4(OBr)_2$ base structures. However, the remaining examples follow a different trend. In comparison to earlier sections, other exchange mechanisms such as spin polarization must be active here.

The key result here is that a change in the electronic structure of the bridge through an organic backbone is related to a change in the coupling constant. However, changing the geometry of the bridge has a much larger effect on *J*. This is especially important considering that the electronic changes at the bridging O-atom are significant when going from F to H as its substituent. The effect caused by different organic residues is therefore likely to be somewhat smaller. A similar conclusion on carboxylates was previously drawn by Roy *et al*.[222]

3.3.7. Applications to Halide Bridged Gd-Dimers

The previous two sections focused on the calculations of Gd-exchange coupling constants based on simple, idealized model structures. It is important to consider how these geometric principles can be applied to understand the coupling in actual molecules. A number of molecules utilizing halide bridges in lanthanide coordination compounds has been reported in the literature.

Dinuclear Gd(III)-compounds bridged linearly via a single halide could only be obtained with fluoride.[329,330] Bridging modes via two halides have been crystallographically investigated for fluorides[331–333], bromides[334,335] and iodides.[74] Chloride bridged molecules crystallize both with[270,336] and without[271,272,337] additional bridging ligands. Bridges via three halides are also only known for chloride.[273] Larger clusters such as tri-[338] and tetranuclear[339,340] compounds via bridges of different configurations are reported in the literature. For example, Buschmann *et al.* synthesized a set of square Gd(III)-tetrameters where the lanthanides are bridged via Cl, Br, or I.[340] A selection of the bridging motifs are summarized in Figure 3.44.

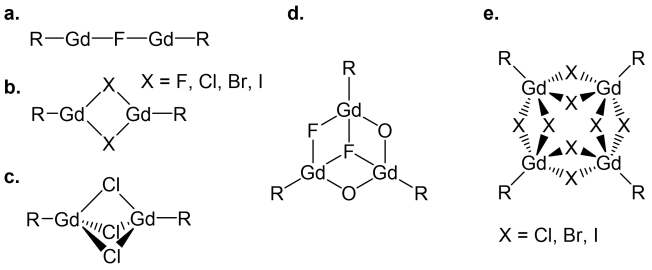

Figure 3.44.: Different bridging motifs with halides for Gd(III) ions. Dimers can be bridged via (a.) one, (b.) two or (c.) three halides. There are also larger clusters such as (d.) triangles and (e.) tetramers.

Table 3.4.: Geometric factors for the for halide bridged dimers, as well as calculated and experimental coupling constants. For reference the calculated value from the Gd_2X_6-2D maps is shown as well.

	(b5)	**(b6)**	**(b30)**	**(b31)**
Gd-Gd dist [pm]	4.376	4.303	4.302	4.513
angle [°]	102.6	102.6	104.5/103.3	99.5/100.8
Gd-X [pm]	268.1/292.3	274.3/277.1	272.8-274.8	286.3-304.9
J_{exp}	-0.09	-0.037	-0.035	-0.015
$J_{bh\text{-}ly}$	-0.029	-0.013	-0.025	-0.020
J_{pbe0}	-0.054	-0.027	-0.050	-0.043
$J_{cam\text{-}b3lyp}$	-0.051	-0.025	-0.044	-0.041
$J_{\omega b97\text{-}x}$	-0.045	-0.020	-0.035	-0.036
$J_{bh\text{-}lyp,ref}$	-0.022	-0.022	-0.026	-0.015
$J_{pbe0,ref}$	-0.041	-0.041	-0.044	-0.034
$J_{cam\text{-}b3lyp,ref}$	-0.028	-0.028	-0.030	-0.022
$J_{\omega b97\text{-}x,ref}$	-0.006	-0.006	-0.004	-0.003

However, most of these structures are not magnetically characterized. In order to compare the GdX_6 models with experimental observations, the individual centers should be bridged via two halides and magnetically characterized. Only four complexes fit the desired criteria. Compounds **(b5)** and **(b6)** have already been investigated in Sections 3.3.1-3.3.3. Furthermore, compound **(b30)** is also bridged via two chloride ligands,[337] wheres compound **(b31)** is an asymmetrical bromide bridged dinuclear complex.[335] Relevant structural parameters as well as reported and calculated coupling constants are summarized Table 3.4.

As can bee seen from the table, the agreement between measured and calculated *J* is around the determined accuracy as discussed in Section 3.3.2 for **(b5)**, **(b30)** and **(b31)**.

The calculations underestimate the coupling in **(b5)** and **(b6)**. However, it should be noted that the refitting in Section 3.3.1 resulted in a slightly lower coupling constant of 0.076 cm^{-1} for **(b5)**, closer to the simulated values. Interestingly, the BS-DFT-values scatter around and are close to the experimental value for **(b30)**. Finally, the coupling is slightly overestimated for the Br-bridged **(b31)**.

These values are then compared to the values approximated from the distorted Gd_2X_6-geometries. Surprisingly, the agreement with experiment is slightly better than the values calculated with the experimental structures for **(b6)**, **(b30)** and **(b31)** when using the functionals bh-lyp, pbe0 and cam-b3lyp. The functional ωb97-x is again an outlier as it was in the previous sections.

Compound **(b5)** represents an outlier in this series. Here, the calculated values deviate less from the experimental value than those approximated from the 2D-plots. This could be rationalized in terms of the different bridging geometry. While in all other cases, the bridge itself is close to an equilateral rhombus, this is distorted for **(b5)**. Here the Gd-Cl distances differ by around 40 pm, which is much more than for the other molecules. Considering that it was previously discussed that not only the Gd-Gd distance is relevant but also the Gd-X distance, this explains why the coupling is so different to for example **(b6)** which features the same bridging angle as **(b5)**.

These results align nicely with the previous results: When terminal ligand effects are negligible, a coupling constant could be approximated with a small model system. Importantly, the bridging geometry and rough charge distribution around the Gd-ion still need to be correct. At this point, it would be interesting to extend this model to alcoholate or carboxylate bridged dimers given there are significantly more experimental reference data.

4. Relevance of Halogen Bonding

This chapter will discuss non-covalent bonding facilitated through halogen bonding as a tool to influence the crystallization of lanthanide coordination compounds. This will be done in three sections: In Section 4.1 different computational analysis methods of Halogen Bonds (XBs) will be introduced before they are applied in the following sections. Secondly in Section 4.2, the influence of XBs on the crystal packing of lanthanide coordination compounds synthesized by Dr. Jonas Braun is examined from two perspectives. The symmetrical arrangement of halogen bonding is shown to be the result of the crystal packing in Section 4.2.1 whereas it is shown to result in a symmetrical crystal packing in Section 4.2.2. Finally, the influence of such intermolecular bonding on magnetic properties is exemplified in a set of isostructural compounds in Section 4.3. In this case, the structures were synthesized and characterized as a part of this project.

4.1. Introduction

In this section, the key computational metrics to investigate halogen bonding will be introduced in more detail. These will then be applied to investigate a range of halogen bonds in lanthanide coordination compounds in the following sections. Notably, halogen bonds were previously introduced in Section 2.3. Three computational and topological metrics were employed to characterize XBs:

The Molecular Electrostatic Potential (MEP) was already introduced in Section 2.3 and is defined as the force perceived by a positive test charge at a given position r due to the repulsion of the nuclei and attraction of the electrons.[90]

$$V(r) = \sum_A \frac{Z_A}{|R_A - r|} - \int \frac{\rho(r')}{|r' - r|} dr' \tag{4.1}$$

Here, Z_A and R_A are the nuclear charge and position of an atom A. The second term is the Coulomb attraction between the electron density and the test charge. Consequently this metric is positive in areas where the nuclear repulsion is stronger than the electron attraction. The MEP is generally plotted on a surface which is an isodensity which has to be defined for reference.

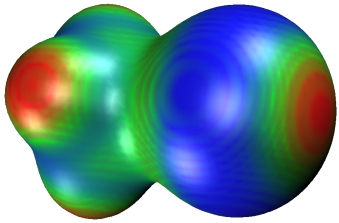

Figure 4.1.: Molecular Electrostatic Potential (MEP) plotted for the CH_3I molecule, ρ = 0.02, V_{pot} = 0.05 (blue) to 0.14 (red). The hydrogen positions and the σ-hole are indicated by the more positive areas (red). Calculation performed on a b-p-D4/rij/def2-TZVP level of theory.

The Electron Localization Function (ELF) was introduced by Becke in 1990 as a metric that is able to reproduce the shell structure of atoms since it is usually not obvious from the density itself.[155]

A conditional same spin pair density is constructed which can be described as the probability to find an electron in close proximity to a reference electron with the same spin. To obtain the ELF, this metric is expanded in a Taylor series, cut after the linear term and then renormalized between 0 and 1. A value of 0 means complete delocalization, a value of 0.5 is the delocalization of electrons in the free electron gas with the same density and a value of 1 means complete localization.

The benefit of this metric is that it is much more susceptible to changes than the electron density, since it contains the kinetic energy density for example.[155] Consequently, the σ-hole appears as an area of low localization in comparison to lone pairs and bonds which appear as areas of high localization.[154] A comparison of ELF and ρ for the Xe-atom is shown in Figure 4.2. The ELF is usually plotted on planes through the molecule which have to contain the bond axis to allow for a meaningful interpretation of the halogen bond.

Bader's theory of Atoms in Molecules (AIM), also called the Quantum Theory of Atoms in Molecules (QTAIM), is an approach to use the three-dimensional topology of the electron density to define atoms, partial charges and bonds.[341] In this theory, bond paths of maximum electron density connect neighboring atoms in a molecule or in an intermolecular interaction. Importantly, this does not necessitate a covalent bond between the interacting atoms.[342] An essential characteristic along these bond paths is the Bond Critical Point (BCP) which is a saddle point in the electron density.[343] At this BCP, the second derivative of the electron density called the Laplacian $\nabla^2\rho$ contains information about the nature of the bond. If it is negative, a bond with covalent character is present, whilst a positive Laplacian indicates a bond between closed shell molecules or ions.[343] This is also the case for halogen bonding.

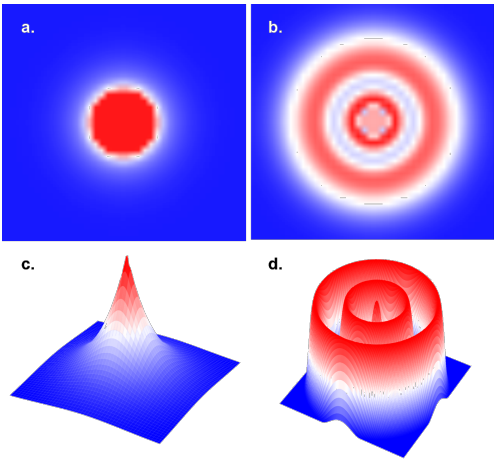

Figure 4.2.: a. Density and b. ELF of a Xe-atom calculated with on a HF/rij/X2C/x2c-QZVPall level of theory. The density appears as a circle, since it steeply increases towards the nucleus. This cannot be captured with a linear heat map. In comparison, the ELF clearly shows the desired shell structure. Both plots are displayed from 0 (blue) to 1 (red). c. and d. visualize how such heat maps would look in a 3D-space. These are not calculated values for a Xe-atom, but are an abstract representation.

Importantly, there have been several studies indicating that the strength of a bond is directly correlated with the electron density ρ at the BCP.[344,345] However, with respect to halogen bonding this comparison only works for very similar reference systems where e.g. the same two halogen atoms are interacting as described by Kuznetsov.[346] Furthermore, it is important not to generally equate the presence of a bond critical point with the presence of a chemical bond. Rather, BCPs indicate an interaction between two atoms, which could be either bonding or antibonding.[347,348]
The former methods help to visualize and quantify the electron density topology of a halogen bond interaction. However, the central feature of interest is the energy gain of the system through an interaction.

Notable, the dissociation energy -D_E between two subsystems can be separated in two contributions:[349]

$$-D_E = \Delta E_{prep} + \Delta E_{int}. \tag{4.2}$$

The preparation energy ΔE_{prep} is related to the geometric distortion of the unbound subsystems to the form in which they are bound. The interaction energy ΔE_{int} is the energy difference between the deformed subsystems and the combined supermolecule.[349] In the following, only the interaction energy between molecular structures as they occur in the crystal will be investigated. Furthermore, E_{int} will be referred to as E_{tot} when it is emphasized that there are different energy contributions to an interaction. This was described on a DFT-level of theory and contrary to the Gd-exchange coupling constants in Section 3.3.2 a number of comparative studies have been performed and described in the literature. Studies by Kozuch and Martin[350] as well as Anderson *et al.*[159] indicate the necessity for hybrid functionals and the treatment of dispersion effects. Notably, dispersion effects are not included in DFT by default. Furthermore, Siiskonen and Priimagi tested smaller basis sets with various DFT-functionals.[351] Based on these three studies, the m06-2x, pbe0 and cam-b3lyp functionals were selected for the following experiments. pbe0 and m06-2x are hybrid functionals with a smaller (35 %) and larger (54 %) amount of exact exchange whereas cam-b3lyp is a range separated hybrid functional. Importantly, to obtain accurate interaction energies, two effects need to be considered:

1. The Basis-Set Superposition Error (BSSE) is an error that occurs due to the finite basis used in quantum chemical calculations. The energy of a bonding partner will be artificially lowered by interacting with small amounts of the other molecules basis set. This error can be corrected by using a counterpoise correction.[352]

Here, the energy of the bonded complex E_{AB} is corrected by the relaxation of the monomers due to the other monomers basis set.

$$E_{AB}^{CP} = E_{AB} - (E_{A(B)} - E_A) - (E_{B(A)} - E_B) \tag{4.3}$$

In this equation, the energy of monomer A is lowered when the basis set of molecule B is included in the calculation ($E_{A(B)}$). Here, neither the nuclei nor the electrons of B are considered, only the basis set. It should be mentioned that there has been some criticism about this approach.[353] Furthermore, the incompleteness of basis sets in general might lead to another, yet smaller error in ΔE_{int}.[354]

2. The determination of the bond energy is straightforward if the two fragments only interact through this bond. However, in this thesis extended systems are investigated and the interaction between two molecules may also include significant π-bonding and dispersion. In order to disentangle these contributions, a simple, spatial energy decomposition of the total interaction energy is proposed between two molecules R_1-X and R_2-Y:

$$\Delta E_{tot} = \Delta E_{XY} + \Delta E_{XR_2} + \Delta E_{YR_1} + \Delta E_{R_1R_2}. \tag{4.4}$$

The interaction energy is decomposed into four contributions between the halogens (ΔE_{XY}), the halogens and the opposite residues (ΔE_{XR}) and the residues ($\Delta E_{R_1R_2}$). By replacing the halogens with hydrogen, reoptimizing this position and recalculating the interaction energy, the halogen bond can be effectively "turned off". Therefore the remaining interaction energy will be $\Delta E_{R_1R_2}$. Subtracting this contribution from the total energy will give a corrected interaction attributable only to the halogen atoms.

There is a number of established decomposition schemes based only on the total interaction energy between the fragments. These give valuable insights into which the effects which stabilize different interactions.

These are often based on the comparison of the wavefunctions for the monomer units with that of the resulting supermolecular system. Early models for such energy decomposition schemes have been proposed by Ziegler and Rauk[355,356] as well as Kitaura and Morokuma.[357] Based on these studies, the fragments' orbitals are orthogonalized to construct the supermolecular orbitals. This can be achieved, for example, using canonical molecular orbitals as implemented by Su and Li.[327] An alternative approach utilizes natural orbitals as suggested by Reed *et al*.[358] The latter are chemically more intuitive. A conceptually different approach is Symmetry Adapted Second-Order Perturbation Theory (SAPT) where the interaction between the monomers is treated as a perturbation to the isolated molecules.[359] Furthermore, orbital free methods based on real space decomposition have been suggested.[360] Here it is important to emphasize that none of these approaches to energy decomposition gives a clear cut solution.[361]

The method chosen in this thesis is the first method presented here, called Energy Decomposition Analysis (EDA) in the form suggested by Su and Li and implemented in Turbomole. It decomposes the interaction energy into electrostatic, exchange repulsion, orbital relaxation, correlation and dispersion contributions.[327]

$$\Delta E_{tot} = \Delta E_{el} + \Delta E_{exrep} + \Delta E_{orb} + \Delta E_{corr} + \Delta E_{disp} \tag{4.5}$$

Similar methods have been shown to be practical in their application characterizing halogen bonds.[362]

In the following sections, two current topics of research revolving around halogen bonding will be investigated and applied to lanthanide coordination compounds.

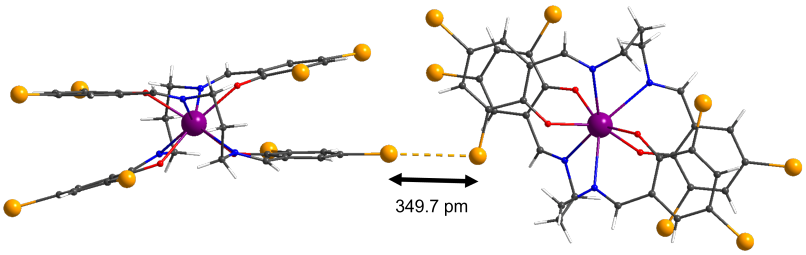

Figure 4.3.: Ce compound synthesized by Wu *et al.* showing clear halogen bonding between molecules in the crystal lattice.[169] Calculations of a the MEP indicated the presence of σ-holes.

1. What is the influence of the metal center on the halogen bond? A number of studies have been reported of metal atoms being either directly or indirectly involved in halogen bonding leading to special properties. For example, Wolf *et al.* demonstrated how halogen bonding can activate metal-halogen bonds for catalysis.[363] Other authors reported an influence on Pt(II) optical properties[364] or on the magnetic exchange between Cu(II)[164–166] and Cr(III) centers.[167] Only a few computational studies have been performed quantifying the bonding properties of such complexes.[365,366] However, while halogen bonding has been reported for lanthanide containing compounds[144,169–173] no computational studies have been performed to quantify the bonding in such complexes. Furthermore, no analysis of such supermolecular interactions influencing the magnetic and optical properties of lanthanide complexes has been performed. In the present work, the influence of halogen bonding on the packing and magnetic properties of lanthanide containing compounds will be discussed in the following sections.

2. How can cooperative effects stabilize or destabilize halogen bonded supermolecular systems? Given that in water clusters cooperative effects between the hydrogen bonds lead to an increased stability of the cluster this indicates that the total interaction energy cannot be explained using pair-interactions alone.[367,368] Such effects have been predicted to yield significant stabilization for halogen bonded triangles,[369,370] squares,[371] larger clusters[372–374] and infinite chains.[375,376] Furthermore, there are indications of negative cooperativity where the addition of another halogen bond destabilizes the first.[377] The majority of studies investigating this use theoretical model structures rather than experimental crystal structures. One rare such example characterized the interaction between N-halo-guanine quartets.[378] In Section 4.2.2 this concept was applied for the first time to a synthesized structure containing metals rather than being exclusively organic.

4.2. Crystal Engineering with Lanthanide Coordination Compounds

Halogen bonding has long been established as an important tool in crystal engineering but is hardly explored in lanthanide based coordination compounds. Firstly, Section 4.2.1 will discuss an example where an arrangement of halogen bonds obeys a given crystal symmetry. A converse example is shown where the halogen bonds cause a high crystal symmetry which will be discussed in Section 4.2.2. Here, synergistic effects between halogen bonds are highlighted for the first time between halogenated coordination compounds.

4.2.1. Solvent Disorder in Symmetric Crystal Cavities

Compound **(X1)** (Figure 4.4) is a C_i-symmetric dinuclear Dy(III)-complex bridged by two Br-opch$^-$ ligands which is the depronated (5-bromo-2-hydroxy-3-methoxy benzyliden)pyrazin-2-carbohydrazide (Br-H_2opch). Furthermore, there are two terminal Cl^--ligands coordinated to each Dy-center and one CCl_4-molecule lattice solvent per molecule. This compound was synthesized and characterized by Dr. Jonas Braun.[379] Calculations of the magnetic properties were conducted in the maser thesis of the author.[101] Up to now, only a superficial analysis of the supermolecular network was conducted.[379] In the following section, a complete topological analysis of this compound will be described and the presence of halogen bonding investigated using quantum chemical methods.

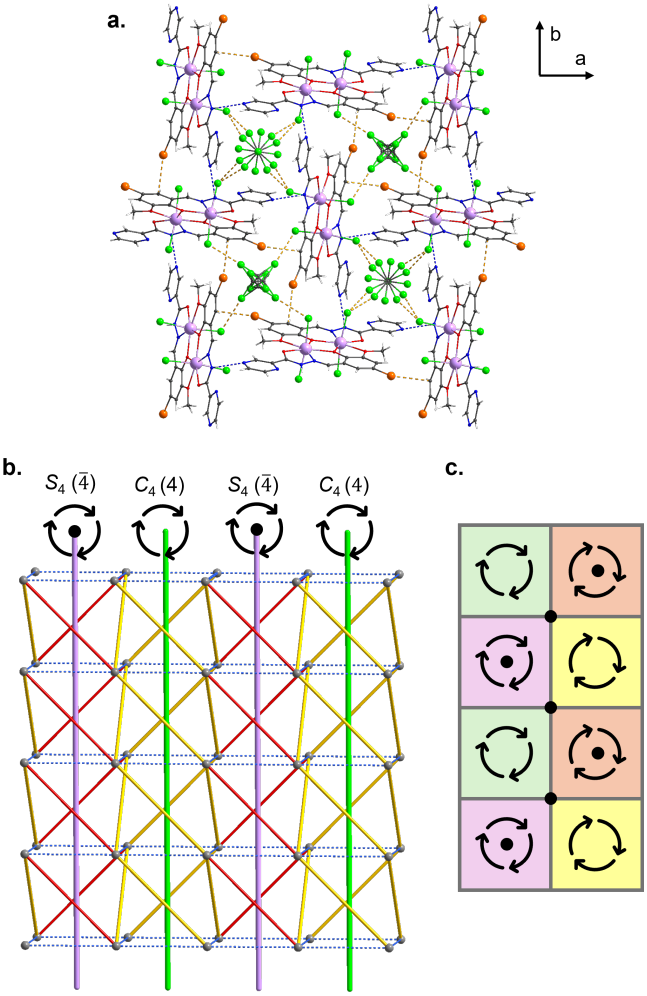

Figure 4.4.: a. Packing of compound **(X1)** viewed along the crystallographic c-axis showing the disorder of the CCl_4 molecules. Intermolecular H-bonds are marked as dashed blue lines, intermolecular XBs are given as brown lines. b. Simplified intermolecular connectivity diagram only considering H-bonds and Br-π-bonding. H-bonds are marked as blue dashed lines, XBs are separated into yellow and red lines. The XB_D is above the XB_A for the yellow lines and *vice versa* for red lines. c. Central symmetry elements along the c-axis. Green and yellow areas are (inverted) 4-axes, whereas red and violet areas are (inverted) $\bar{4}$-axes.

The Schönflies notation will be used for symmetry elements related to closed units, whereas the Hermann-Mauguin notation was used for symmetries within the crystal lattice.
Compound **(X1)** crystallizes in the space group *P*4/*n*. Two types of intermolecular contacts form a three-dimensional network. Hydrogen bonds between N2-H2 and N4 of the molecule at {-y+1/2, x, z} form a network of two-dimensional sheets, which are then connected through halogen bonds between Br as XB_D and the C5 atom in *o*-position to the Br atoms of the neighboring molecule at {x+1/2, 1-y, -z}. This symmetry is shown in Figure 4.4. The two 4-axes in the crystal act as screw axes where the XB_A and XB_D form helices either up or down the c-axis. The cavities created by this consequently show C_4-symmetry. Between the 4-axes, $\bar{4}$-axes are present. Cavities on the inversion points of the roto-inversion axes have S_4-symmetry. These are depicted in the appendix in Figure A.24.

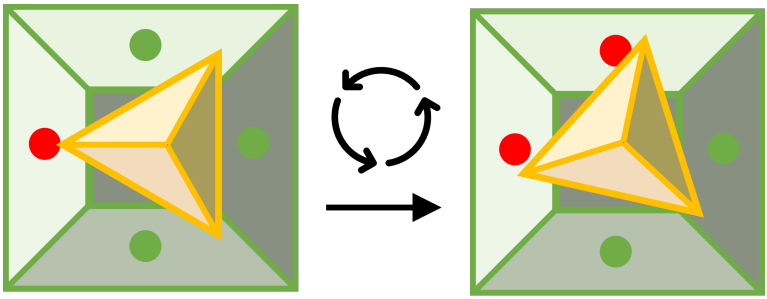

Figure 4.5.: Scheme of the symmetry problem of fitting a CCl_4-tetrahedron (yellow tetrahedron) in a cavity with C_4-symmetry (green walls). By slight rotation and distortion, two out of the four Cl-atoms in the base can interact with the cavity walls. Green and red dots indicate (non-) interacting Cl^--ions in the cavity walls.

However, the supermolecular framework was not the subject of this research but rather the intriguing symmetries formed by the solvent disorder, which results from the incompatibility of the CCl_4 T_d molecular symmetry and the crystallographic site symmetry. The two distinct disorders are at Wyckoff-positions 2b ($\bar{4}$) and 2c (4). The basic geometric problem is visualized in Figure 4.5. The CCl_4-molecule is a tetrahedron which can only fit in the C_4-symmetric cavity by aligning one Cl-with the crystal axis. This leaves a C_3-axis in an environment with fourfold symmetry. Consequently, there are four equivalent rotations. Furthermore, by slight distortion of the base triangle, two XBs can be formed.

The disorder in the bisphenoidal S_4-cavity can be explained similarly. Here, carbon atom C22 is slightly off the $\bar{4}$ inversion center and consequently disordered over four closely spaced sites. In this case, S_4 (the symmetry of the cavity) is a sub-group of T_d (the molecular symmetry of the CCl_4), but the cavity is too wide to stabilize two halogen bonds to chloride ligands on opposite sites of the $\bar{4}$-axis. Consequently, halogen bonds to any two non-opposite terminal chloride ligands can be formed leaving the other two Cl-atoms of CCl_4 dangling.

In total, this leaves four distinct Cl-Cl XBs across the two sites which are shown in Figure 4.6. The deviation of the C-Cl-Cl angle from the ideal 180° can be explained by the fact that the distortion was necessary to optimize the energy of two contacts rather than just one (Figure 4.5). The Dy-Cl-Cl angles, which should consequently be close to 90°, are omitted since the terminal Cl-ion is expected to essentially isotropic and therefore not exert any directionality on the bond.

To compare these four bonds beyond structural parameters, a series of DFT-calculations has been carried out.

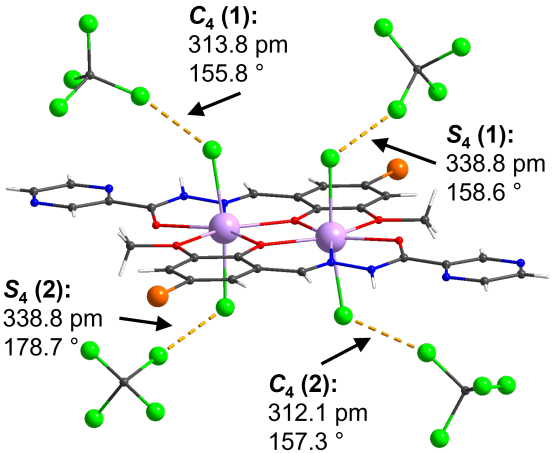

Figure 4.6.: Distances and angle for the four different halogen bonds with the solvent molecules in compound **(X1)**. The top left and bottom right are in a C_4-cavity, whilst the other two are in an S_4 cavity. The sum of the van der Waals (v.d.W.) radii for two Cl-atoms is 350 pm.

Here, Dy(III) was replaced with Y(III), and the basis employed was def2-QZVP for the two interacting atoms, def2-TZVP for the residual CCl_4 molecule and the Y(III)-ion. A def2-SVP basis was employed for the rest of the molecule. Thus, larger basis sets were used for atoms closer to the interaction. Furthermore, D4-dispersion correction was considered and the rij-approximation employed. The density functionals employed were m06-2x, pbe0 and cam-b3lyp. The obtained energies using a counterpoise-correction are between -23.6 kJ/mol and -30.0 kJ/mol across the different interactions and functionals. A full list of the obtained energies can be found in the appendix, Table B.85. For all three density functionals, interaction S_4(1) was the most negative (the strongest interaction) by approximately 4 kJ/mol.

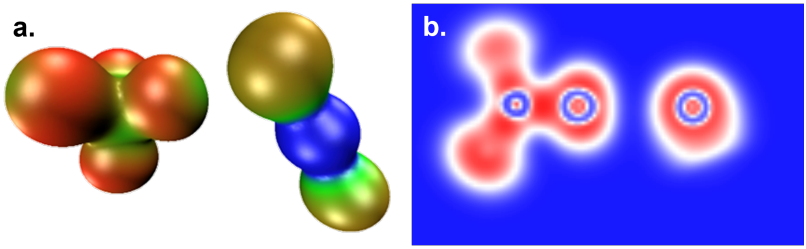

Figure 4.7.: a. MEP for the geometry of S_4(1). For simplicity, the Dy-complex was replaced with a $[YCl_2]^+$-moiety. The MEP is plotted on an isodensity of 0.02 from 0.09 (red) to 0.50 (blue). b. ELF of the same interaction, plotted from 0 (blue) to 1 (red) The σ-hole can be clearly observed in both pictures. The density was optimized on a m06-2x-D4/rij/def2-QZVP level of theory.

Therefore, it can be concluded that all four interactions are similar in strength.

The presence of a σ-hole was confirmed by calculating the MEP and ELF for a simple model complex and is displayed in Figure 4.7 as well as in the appendix. The σ-hole can be clearly seen in the CCl_4-molecule but not for the Cl^--ion coordinating to the Y(III). A very similar density (ρ) between 0.008 and 0.015 is obtained across the four interactions at the BCPs. The Laplacian is small and positive as expected for the interaction between two closed shell molecules. It is worth noting that no correlation between ρ and ΔE can be reported.

By replacing the interacting Cl-atom at the CCl_4 molecule with hydrogen, the contribution of the Cl-atom can be approximated. It is worth noting that this correction will consequently underestimate the coupling.

This is because the remaining electrostatic and dispersion interactions with the hydrogen atom will affect the result. The obtained energies are significantly smaller and between -3.9 kJ/mol (C_4(2)) and -11.2 kJ/mol (S_4(1)).

An EDA is carried out using the pbe0-functional and D4-dispersion correction on the full interaction energy and that attributed to the halogen atom. While the latter is shown in Figure 4.8, the full analysis is shown in the appendix, Table B.86. Both pictures show a large positive exchange-repulsion which is overcompensated by negative contributions from electrostatics, orbital relaxation, correlation and dispersion simultaneously. There is no qualitative difference between the four interactions.

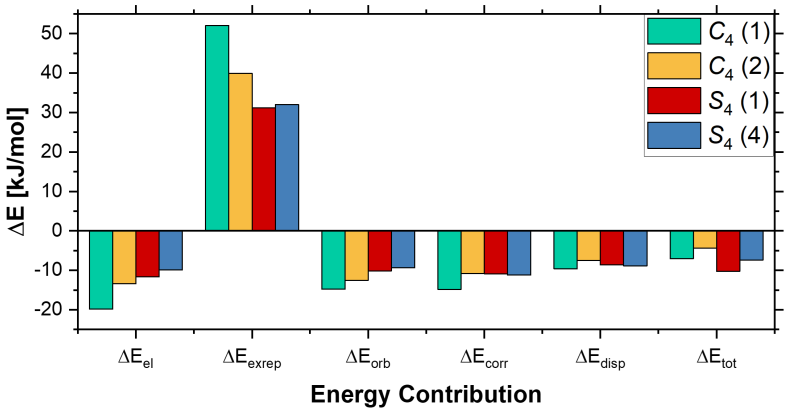

Figure 4.8.: Energy decomposition analysis for the contribution of the Cl-atom to the full interaction energy as calculated with Equation 4.4. The calculation is performed on a pbe0-D4 level of theory.

In conclusion, it is proposed that a combination of hydrogen bonding and halogen bonding is responsible for the highly symmetric crystal packing of compound **(X1)**. This leads to the formation of symmetric crystal cavities which can accommodate one solvent molecule. Due to the mismatch of the cavities' and solvent's symmetry, a fourfold disorder results. By optimal orientation in the cavities, each solvent forms two halogen bonds to terminal chloride ligand atoms. These are energetically very similar despite their differing bond-angles and distances.

4.2.2. Cooperativity in Halogen Bonding

The results of this section were previously published in Crystal Growth & Design 2025, 25, 65936603. All figures are adapted from this reference.[380] The synthesis was carried out by Dr. Jonas Braun and the crystal structure measured and solved by Dr. Olaf Fuhr and Dr. Christopher Anson. The topological analysis and quantum chemical characterization of the halogen bonds were performed within this work.

Compound **(X2)** is a hexanuclear, trigonal prismatic Er(III)-cluster bridged via two (μ_3, η^3-CO_3)$^{(2-)}$ ions and six Br-opch ligands. In this structure, each Br-atom is involved in halogen bonding. Pictures of these motifs are shown in Figure 4.9. The five crystallographically distinct contacts are given in Table 4.1.

Compound **(X2)** crystallizes in the high symmetry tetragonal space group $P\bar{4}2_1c$. All of the halogen bonds connect Er_6-clusters to symmetry equivalent molecules. Whereas the Br3-Br5-interaction results in chains through the lattice, pairs of Er_6-clusters are linked via two Br2-Br6 contacts across a two fold rotation axis (2) in the crystal. Furthermore, each Br1 is involved in four intermolecular interactions: two Br1-Br1 contacts, one longer Br1-Br1' contact and a Br1-Br4 contact.

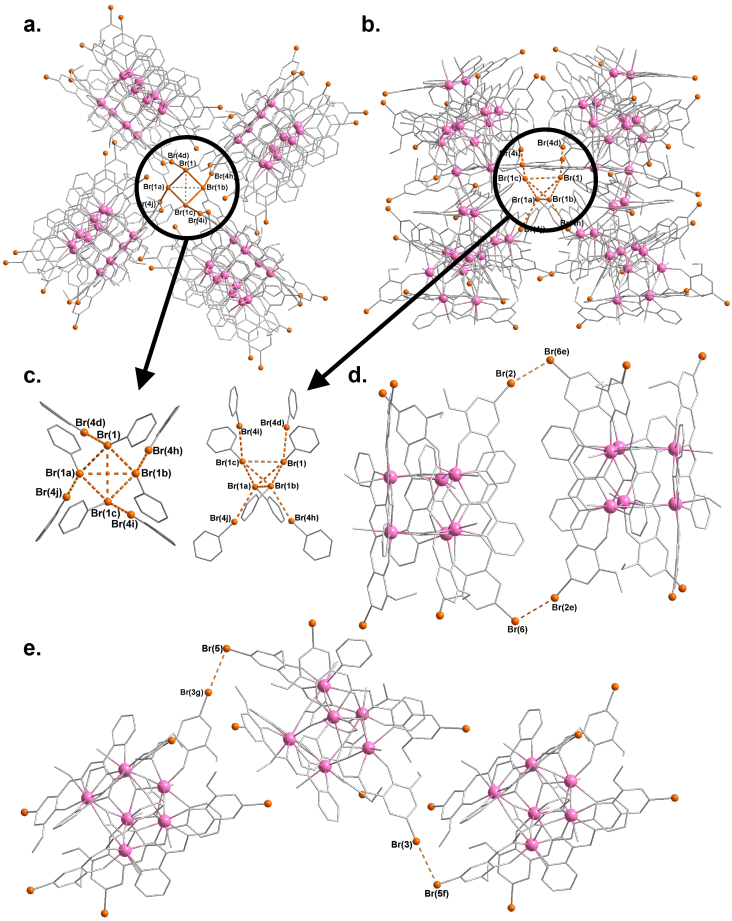

Figure 4.9.: Highlighted Br-Br interactions in compound **(X1)**. a. Central motif viewed along the c-axis. b. The same motif but viewed along the a-axis. c. A simplified version of the two perspectives. d. The Br2-Br6 halogen bond linking two Er_6-clusters via two bonds. e. Chains of Br3-Br5 Halogen bonds. Adapted with permission from Ref. [380].

Table 4.1.: List of the five crystallographically distinct Br-Br contacts in compound **(X2)**.

Interaction	Br-Br dist (pm)	wide C-Br-Br angle (°)	acute Br-Br-C angle (°)	symmetry code
Br1-Br1	357.3(2)	162.9(4)	98.5(3)	x, -y, 1-z
Br1-Br1'	393.9(3)	108.5(5)	108.5(5)	-x, -y, z
Br1-Br4	364.3(2)	163.5(6)	74.5(4)	1/2-x, y-1/2, 1/2-z
Br2-Br6	358.0(2)	162.0(4)	108.2(3)	-x, 1-y, z
Br3-Br5	368.0(2)	175.6(4)	92.5(3)	x-1/2, 1/2-y, 1/2-z

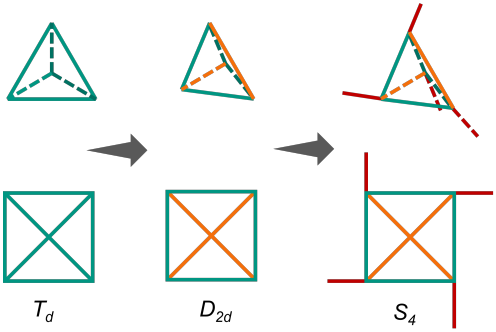

Figure 4.10.: Scheme to explain the central XB-motif in **(X2)**. Each vertex represents a Br-atom, while each line represents a bond. Equivalent bonds are shown in the same color. Adapted with permission from Ref. [380].

This leads to a cluster of eight XBs across the $\bar{4}$-axis. This central motif is investigated in more detail.

Figure 4.10 visualizes the symmetry of the central motif. Starting from an ideal tetrahedron, two opposite edges are compressed to obtain a tetragonal, bisphenoidal shape with D_{2d}-symmetry. Now, each of the edges can be elongated to a point outwards yielding a final S_4-symmetry. Each vertex in this model represents one Br-atom.

This leaves three distinct connections in the arrangement: The diagonal edges (orange) of the former tetrahedron are the Br1-Br1' contact whereas the short edges (green) are the Br1-Br1 contact. Thirdly, the connection to the outer points (red) represents the Br1-Br4 interactions.
As a result of the Er_6-clusters being too large to perform a series of hybrid functional DFT-calculations on them, a simple model structure was proposed to compare the five interactions. The protonated 5-bromo-*o*-vanillin is used as a reference structure. To obtain the starting structures, the respective interaction was extracted from the crystal structure and the Dy(III)-ions replaced with hydrogen. Furthermore, the imine-nitrogen was replaced by oxygen. Afterwards, all H-positions and the added oxygen in the aldehyde group were optimized using the respective functional, D4-dispersion correction, the rij approximation and a def2-QZVP basis for Br-atoms. A def2-TZVP basis was employed for all other atoms. If the interaction was across a symmetry element, this symmetry was was taken into consideration in the calculations. Furthermore, the H-correction (Equation 4.4) was employed for all data discussed in the following.

Table 4.2.: Calculated interaction energies of the five crystallographically distinct Br-Br contacts in compound **(X2)**. The density ρ and Laplacian $\nabla^2\rho$ are calculated with the m06-2x functional.

Interaction	m06-2x in kJ/mol	pbe0 in kJ/mol	cam-b3lyp in kJ/mol	ρ	$\nabla^2\rho$
Br1-Br1	-4.0	-6.1	-5.6	0.0092	0.0274
Br1-Br1'	-2.5	-4.6	-4.2	0.0054	0.0176
Br1-Br4	-5.8	-7.2	-7.0	0.0080	0.0246
Br2-Br6	-4.4	-6.0	-5.6	0.0081	0.0246
Br3-Br5	-5.8	-7.8	-7.6	0.0066	0.0203

The obtained interaction energies and densities at the BCP are summarized in Table 4.2 and the appendix, Tables B.87–B.88.
Firstly, it should be noted that all interactions are of the same order of magnitude. Secondly, it is apparent that the Br1-Br1' interaction is lower in energy than the other interactions. This is not surprising considering that the Br-Br distance for this contact is above the sum of van der Waals radii for two Br-atoms (370 pm). The same trend can be seen for the properties of the BCPs where a small positive Laplacian indicates an interaction between closed shell molecules. The small density at the BCP for the Br1-Br1' interaction is a result of the long bond distance and less than ideal angles. However, it is still expected that this interaction contributes to the stabilization of the cluster.
An EDA complements this picture and is shown in Figure 4.11 and in the appendix, Table B.89. A few noteworthy points result from the comparison of the five interactions:

- The longer Br-Br distance for interaction Br1-Br1' is mirrored in the smallest exchange repulsion, electrostatic and orbital relaxation contributions.
- Using the pbe0 functional, interaction Br3-Br5 is the most stable. This can be explained with the C-Br-Br angle approaching 180°. This leads to the minimization of exchange repulsion, the only destabilizing contribution.[381]

A more detailed analysis of the bonding motifs' topologies was conducted by plotting the ELF and MEP as shown in Figure 4.12 and in the appendix, Figures A.29–A.31. Two volume slices are cut through the central motif highlighting the donor-acceptor relations in this arrangement.

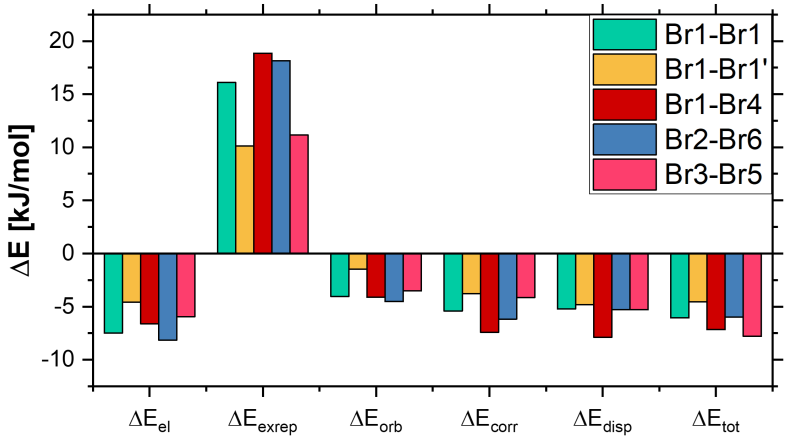

Figure 4.11.: Energy Decomposition Analysis (EDA) for the different pair interactions in compound **(X2)** as calculated with Equation 4.4. Adapted with permission from Ref. [380].

This reveals that each Br1 acts as a XB_D for another Br1 while it acts as the XB_A for a third Br1 and a Br4 respectively. The lone pairs point towards each other in the Br1-Br1' interaction. A similar conclusion can be drawn from the MEP, but due to the dense, three-dimensional packing this is more difficult to identify. Furthermore, it becomes apparent that Br2 is the XB_A for Br6 while Br3 acts as the XB_D for Br5.

This concludes the analysis of the pair-interactions in compound **(X2)**. However, in the central motif, which includes the three interactions between Br1 and Br4-atoms as listed in Table 4.1, it is important to realize that these interactions are not isolated but the Br1-atoms are involved in four simultaneous (concerted) contacts. Consequently, it is worth investigating whether additional stabilization energy can be gained through such concerted bonding resulting in a stabilization of this high symmetry.

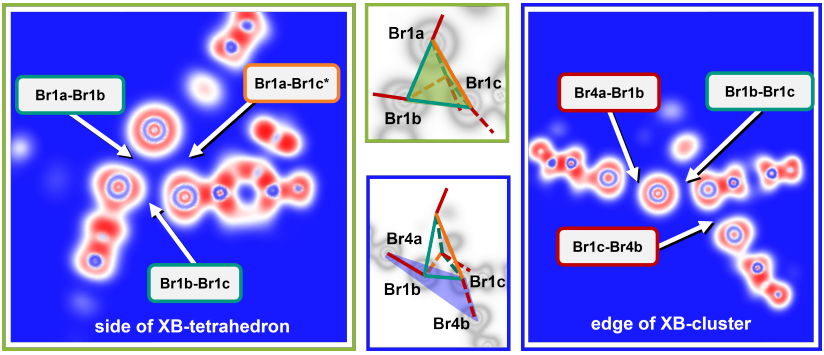

Figure 4.12.: ELF of the central motif plotted on two volume slices as indicated by the green or blue frames. It can be seen that Br1 acts as the XB_D for another Br1, whereas it acts as the XB_A for a different Br1 and Br4. Finally, no σ-hole interaction can be deduced for interaction Br1-Br1'. Adapted with permission from Ref. [380].

To test this hypothesis, a full cluster including eight interacting molecules was constructed by starting from a pair interaction and then adding one molecule at a time. In each of the following seven steps, the resulting interaction energy between the additional molecule and the previously calculated cluster is computed. This workflow avoids double counting of interactions. The total cooperative effect can be calculated as follows:

$$E_{coop} = \sum_{i=2}^{8} E_{M_i} - (4 \cdot E_{Br1-Br1} + 4 \cdot E_{Br1-Br4} + 2 \cdot E_{Br1-Br1'}). \quad (4.6)$$

In this equation, E_{M_i} are the interaction energies obtained for each step. The second term is the sum of pair interaction energies obtained for the central cluster. A scheme of this workflow is visualized in Figure 4.13.
A summary of the obtained interaction energies for each step can be found in the appendix, Table B.90.

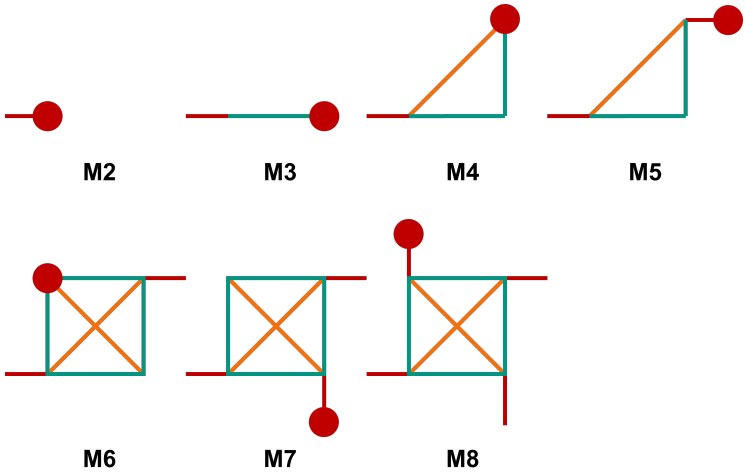

Figure 4.13.: The seven interactions investigated to calculate the total interaction energy. Each vertex represents a Br-atom, each line the halogen bonds included in the calculation. The interaction between the molecule indicated with the red dot and the remaining framework is calculated in each step. Adapted with permission from Ref. [380].

All functionals give qualitatively the same results, thus an average total interaction energy of -90.3 kJ/mol is calculated to stabilize the cluster. Using Equation 4.6, -26.4 kJ/mol of this energy can be attributed to cooperative effects, which is 29.5 %. Interestingly, the same percentile can be obtained when using the H-correction as described earlier. Cooperativity contributions for each functional are given in Table A.15.

Whilst attributing one third of the total interaction to cooperative effects may seem like a lot at first glance, this result is comparable to bromoamine- and *N*-bromo-guanine-quartets where cooperative effects were calculated to contribute between 18.7 % and 30.3 % to the total stabilization.[371,378]

Such significant cooperative contributions suggest that the halogen bonding plays a crucial role in the formation of this highly symmetric crystal structure. This analysis is supported by the fact that the ligand without a Br-atom also forms discrete hexanuclear trigonal prisms of Er(III), but crystallizing in the space group $P\bar{1}$, similar to a previously reported complex.[380,382] Importantly, this is the first time that cooperative effects between halogen bonds have been proposed to influence the crystal structure of a lanthanide coordination compound.

4.3. Halogen Bonding and Single Molecule Magnets

The previous section has established that halogen bonding can play a crucial role in the crystallization of lanthanide coordination compounds. Building upon this foundation, the importance of the metal center on the intermolecular bonding is discussed here. Furthermore, to investigate the potential influence of halogen bonding on the SMM-properties of lanthanide coordination compounds, a test system of isomorphic compounds needs to be established in which the packings are identical apart from the halogen involved in halogen bonding. In the following sections, the synthesis, characterization and quantum chemical analysis of a set of complexes utilizing a chemically modified 2-methoxy-6-(pyridine-2-ylhydrazonomethyl)phenol ligand (Hmph) (Figure 4.14) is presented.

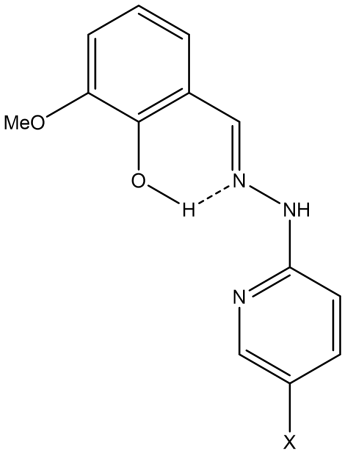

Figure 4.14.: Structure of the modified Hmph proligand, with X = H, Cl, Br.

The unsubstituted ligand has been used on a number of studies in main group,[383] transition metal,[383–387] 3d-4f[284,388] and pure lanthanide chemistry.[389–391] Given the versatile coordination geometries found for this complex, it was attempted to introduce halogens on the ligand backbone to trigger intermolecular halogen bonding. Such ligands were obtained pure by reacting 5-halo-2-hydrazinyl-pyridine with *o*-vanillin in acetonitrile.

The 5-chloro and 5-bromo derivatives were used in this study.
All complexes were characterized with SC-XRD, Powder X-ray Diffraction (PXRD) and Attenuated Total Reflection Infrared (ATR-IR) spectroscopy. The SC-XRD measurements were conducted by Dr. Olaf Fuhr and Dr. Christopher Anson (KIT). Magnetic measurements were performed by Prof. Yan Peng (Ganzhou).

4.3.1. Intermolecular Interactions in Hmph-Dinuclear Complexes

By reacting the Cl-hmph and Br-hmph ligands with $Dy(NO_3)_3$ in a mixture of MeOH/MeCN, yellow crystals suitable for SC-XRD were obtained after one day. $[Dy_2(Cl-mph)_2(NO_3)_4] \cdot 2MeCN$ **(C1)** and $[Dy_2(Br-mph)_2(NO_3)_4] \cdot 2MeCN$ **(C2)** are isostructural Dy-dimers that crystallize in the space group $P\bar{1}$ (Figure 4.15). Here, an inversion center at the center of the molecule makes it centrosymmetric. The two magnetic centers are bridged via the two phenoxo oxygens with Dy(III)-Dy(III) distances of 373.01(5) pm and 371.96(5) pm, respectively. Through their coordination via the two N-donor sites, bridging phenoxo oxygens and methoxy oxygens, the two ligands form an approximate equatorial plane. Above and below this plane, two terminal nitrate ions coordinate to each Dy(III)-center in a bidentate, chelating fashion. Two MeCN lattice solvent molecules act as hydrogen bond acceptors to the hydrazone N-H groups. Consequently, the Dy(III)-ions exhibit a N_2O_7 coordination environment. The molecular structures and packing diagrams are presented in Figure 4.15.
The local coordination environments around the Dy-centers were evaluated with the SHAPE software to gain Continuous Shape Measures (CSMs) of their similarities to a given polyhedron.[230]

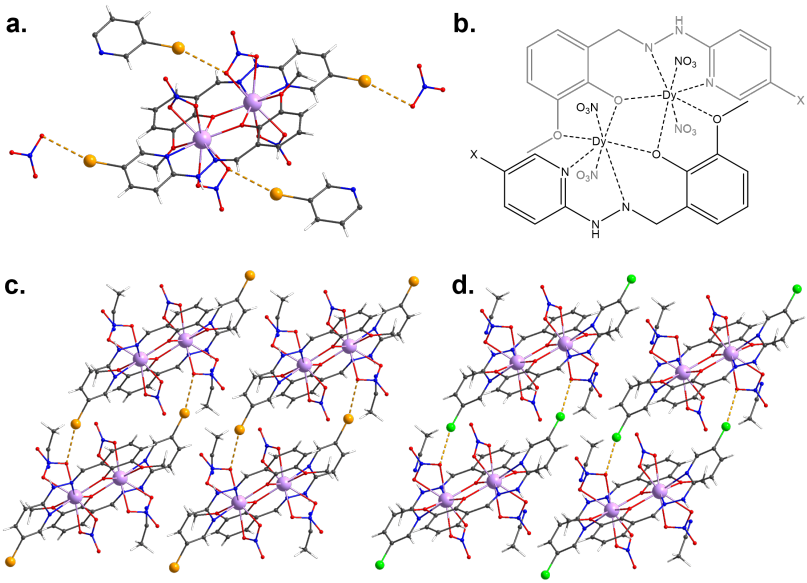

Figure 4.15.: a. Molecular structure and intermolecular halogen bonding of **(C1)**. Compound **(C2)** is isostructural. b. Scheme of the molecular structure of **(C1)** and **(C2)**. c. and d. Crystal packing of **(C1)** and **(C2)** viewed along the crystallographic a-axis.

The environments can be described as intermediates between muffin type (CSM = 1.81, 1.91) and capped square antiprism (CSM = 1.93, 2.02) geometries.[229]

The most interesting feature of the two structures is the intermolecular halogen bonding. Each halogen atom is involved in a short contact with a coordinating nitrate oxygen O8 of the neighboring molecule with a symmetry code of {x, 1+y, z}. The respective X-O distances and C-X-O angles are 318.5(2) pm and 158.44(11)° for compound **(C1)** and 325.1(3) pm as well as 157.62(13)° for **(C2)**.

The respective sums of van der Waals radii are 330 pm for Cl-O and 340 pm for Br-O.[392] Consequently, both contacts are approximately 10 pm shorter than the sum of the corresponding van der Waals radii. Each molecule is involved in four identical bonds, two where it acts as the XB_D with the halogen atom at the ligand and two where it acts as the XB_A through the nitrate ligands.

In the previous sections, only a single model system extracted from the crystallographic data was investigated. In the following discussion, different structures will be investigated that are designed to gauge how much of the molecules have to be included in the model system to obtain a reasonable interaction energy. Here, three model structures were proposed as presented in Figure 4.16: the halogenated pyridine, now referred to as "py", the aminohalopyridine "apy" and the hydrazinylhalopyridine "hypy". Furthermore, the Dy(III)-ion is replaced by Na(I) considering their similar ionic radii.

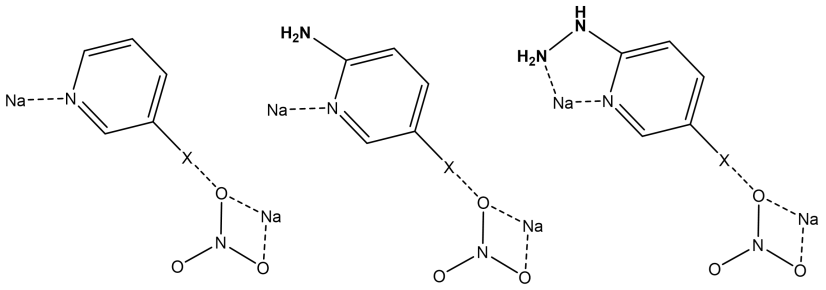

Figure 4.16.: The three different model interactions investigated for **(C1)** and **(C2)**. The interaction of 2-halopyridine and nitrate referred to as py (left), 2-amino-5-halopyridine and nitrate as apy (center), 2-hydraziyl-5-halopyridine and nitrate as hypy (right).

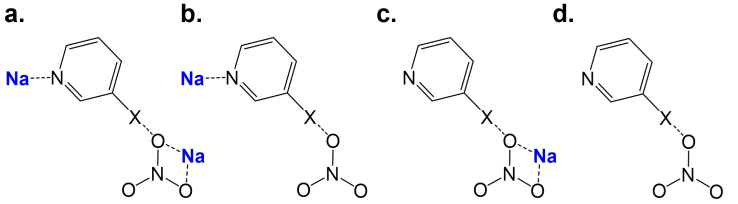

Figure 4.17.: Four investigated model structures for the halopyridine (py) interaction. a. na-na, b. na-no, c. no-na, d. no-no.

This is done because the other countercharges around the metal ion are missing in these simplified model structures and a Dy(III)-ion in these positions would polarize the system too much.
However, the influence of the sodium atoms at either position is tested by constructing four model structures. The two Na-ions are either included or omitted at either position in the model structures. The structures "na-na", "na-no", "no-na" and "no-no" indicate whether a Na-atom is (not) included at the halopyridine and nitrate moiety, respectively (see Figure 4.17). Therefore, 12 model interactions were investigated for **(C4)** and **(C5)**. The respective models are prepared by extracting the coordinates from the cif files and optimizing the hydrogen positions on a b3-lyp-D4/rij/def2-TZVP level of theory. Subsequently, the interaction energies are calculated using the same three functionals as before, m06-2x, pbe0 and cam-b3lyp.
The results are visualized in Figure 4.18 for the m06-2x functional and in the appendix, Tables B.91–B.92. These clearly indicate a strong dependency on the model structures. The most important observation is that the interaction energies calculated with the counterpoise correction obtained for the same models in compounds **(C1)** and **(C2)** are very similar. Considering the different models, whilst the interaction energy for na-na, no-na and no-no is below -30 kJ/mol, it is over -160 kJ/mol for the na-no model.

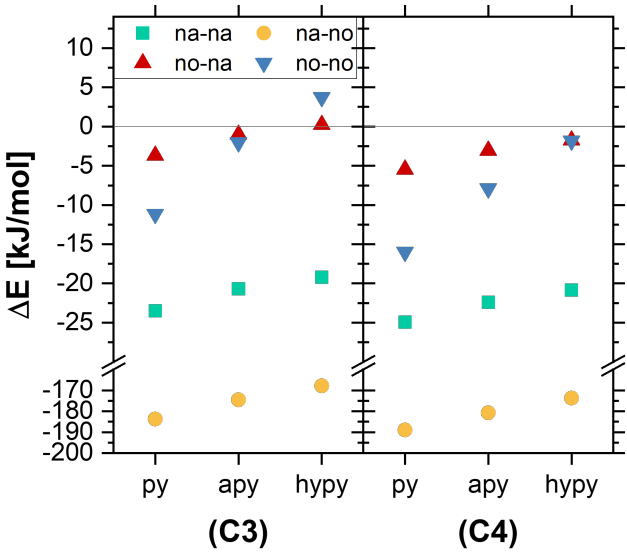

Figure 4.18.: Interaction energy in kJ/mol for compounds **(C1)** and **(C2)** for the three models py, apy and hypy including or excluding the Na-atoms at either fragment. All energies calculated with the m06-2x functional.

This can be immediately visualized considering the charges of the four model structures. Halopyridine fragments including the sodium atom are positively charged whereas the [$NaNO_3$] fragment is neutral. Thus, the model na-no is the only anion-cation interaction which might be the cause for the increased interaction energy as discussed later. The trend in the other interactions can be at least partially rationalized considering if the groups at the pyridine ring are electron withdrawing or donating. Here, a positive polarization of the pyridine ring (through e.g. the Na-ion) may lead to an increased σ-hole and therefore an increased interaction energy.

When comparing the different models for the ligands, it needs to be noted that the interaction energy decreases going from py to hypy by 5-15 kJ/mol. In conjunction with the observations comparing the different models including the cations, this highlights that a sufficient description of the charge density at the interacting fragments is of importance.
Similar conclusions have been reported by Lu *et al.* for the interaction of bromobenzene with various electron donors highlighting that the interaction strength with anions is significantly increased.[156] Furthermore, Riley *et al.* found that the interaction energy of bromobenzenes and bromopyrimidines could be significantly increased through the substitution of ring positions with electron withdrawing groups.[157] The results of this study therefore indicate that the metals play an indirect, but crucial role in stabilizing the intermolecular halogen bond network.
For a deeper understanding of the differences between the four models including or excluding the metal ions an Energy Decomposition Analysis (EDA) is performed using the pbe0 functional and summarized in the appendix, Tables B.93–B.94. Figure 4.19 shows the results for the models involving the hydrazinylpyridine molecule whereas the results for the other models are summarized in the appendix. The most apparent feature of this figure is the strongest electrostatic contribution to the stabilization of the na-no model. Unsurprisingly, this cation-anion interaction is governed by electrostatics. Moreover, electrostatics play a further crucial role in stabilizing the different model interactions. The electrostatic contribution in the na-na model is approxiamtly -15 kJ/mol, but it vanishes for the no-na model and becomes positive for the no-no model. This supports the aforementioned arguments where the Na-atom increases the σ-hole and therefore the interaction energy through electrostatics. Exchange-repulsion and dispersion terms stay almost constant throughout the four models.

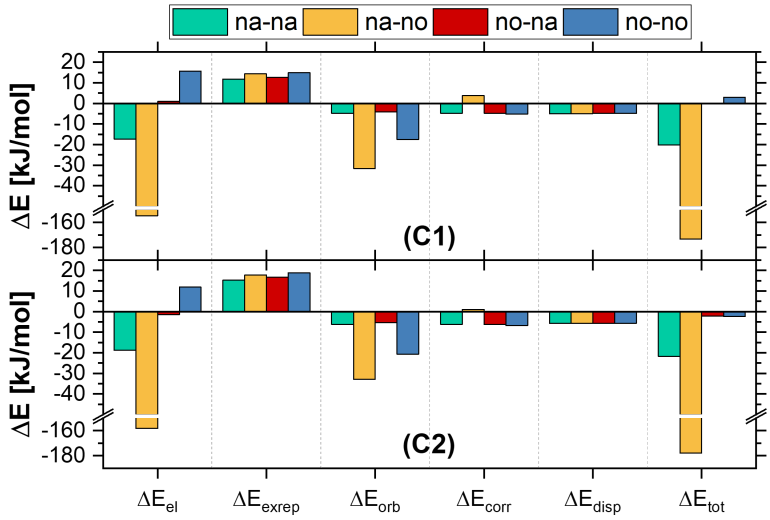

Figure 4.19.: Energy Decomposition Analysis (EDA) for **(C1)** and **(C2)** for the different models of the hypy interactions calculated with the pbe0 functional.

Another intriguing feature is the fact that orbital relaxation increases significantly for models where the nitrate fragment is anionic. This can explained by the fact that the negative charge of the nitrate in [$NaNO_3$] is polarized towards the sodium atom whereas more density is able to interact with the XB_D when it is anionic.

At this point, the σ-hole of the halogen was used in the rationalization of the calculations, yet no proof has been provided that it exists in the model systems. This is shown in Figure 4.20 for the na-na interaction in the hypy model of compound **(C2)** with the m06-2x functional.

Finally, one might ask oneself which of the many discussed models is the most reasonable.

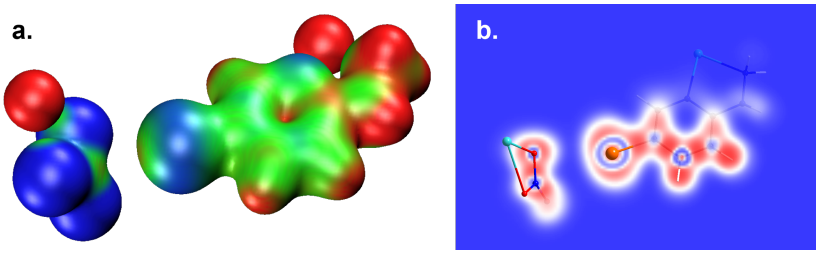

Figure 4.20.: a. Molecular Electrostatic Potential (MEP) of the interaction in structure na-na in the hypy model of **(C2)** plotted on an isodensity of 0.02 where V*pot* ranges from 0.08 (blue) to 0.25 (red). These colors are scaled to highlight the σ-hole, the MEP at the nitrate oxygen and sodium atoms are outside the window. b. Electron Localization Function (ELF) for the same interaction overlayed with the molecular structure. Both pictures show the results calculated with the functional m06-2x.

To answer this question, the interaction between the full molecules was computed. A second calculation was performed by replacing the halogen with hydrogen, reoptimizing this position and recalculating the interaction energy. Considering the fact that two molecules always interact via two halogen bonds, the obtained interaction energies were divided by two. These results are shown in the appendix, Tables B.95–B.96. Whilst the three functionals calculate interaction energies between -47 kJ/mol and -52 kJ/mol for each interaction, the H-correction resulted in values between -6 kJ/mol and -8 kJ/mol for **(C2)** wheres the corrected energy is between -2 kJ/mol and -4 kJ/mol for **(C1)**. Considering the fact, that this correction underestimates the interaction energy and the calculation between the full fragments cannot be solely attributed to the XB, the true bond energy is likely somewhere in between. Interestingly, this is only the case for the na-na model in the present study.

Summarizing this section, the synthesis of two isostructural compounds has been reported which feature XBs where the halogen can be replaced from Cl to Br. These were subsequently investigated highlighting the similarity in interaction energy between them. Furthermore, a series of model structures was calculated probing the influence of chemical substitution on the pyridine ring and the inclusion of the metal ions. This highlighted the importance of the lanthanides' coordination to stabilize the halogen bonds.

4.3.2. CASOCI Calculations and Magnetic Properties

Having set up halogen bonding in close proximity to Dy(III)-centers, it was of interest to investigate if this has any influence on the magnetic properties. Therefore, a series of CASOCI calculations and magnetic measurements were performed. The resulting splitting, ESOs and m_J-compositions are collected in the appendix. Here, two model structures were computed for each complex, either with (opt) or without (unopt) a preliminary optimization of hydrogen positions. The two acetonitrile molecules hydrogen bonded to the hydraozone N-H groups were included in the calculations. ZFS, diagonal elements of the g-tensor, ESOs and m_J-composition are provided in the appendix, Tables B.97–B.102.

Figure 4.21 shows the magnetic main axes for **(C1)** and **(C2)** calculated with a purely electrostatic model as implemented in MAGELLAN (blue) and the g_z-axis of the ground state KD as calculated with CASOCI. Notably, the hydrogen optimization did not influence the direction of the main axis for either compound.

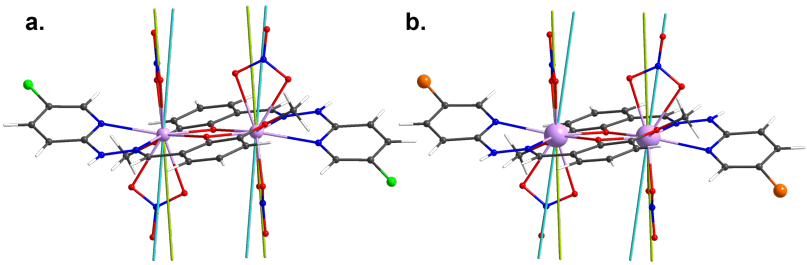

Figure 4.21.: Ground state magnetic main axis calculated with CASOCI (green) and MAGELLAN (blue) for a. **(C1)**, b. **(C2)**.

Furthermore, the main axis is oriented along the vector between the Dy(III) and one of the nitrate nitrogen atoms (terminal ligands). Interestingly, the two calculations seem to prefer different nitrate ions for the main axis. However, the difference between the simulations is minor which suggests that the anisotropy is dominated by electrostatics.
Furthermore, the perpendicular orientation of the axes to the Dy-Dy vector indicates antiferromagnetic dipolar coupling.
The good agreement between CASOCI and MAGELLAN immediately indicates that the ground state for both compounds is predominantly the m_J = 15/2 state. This is confirmed when calculating the m_J-composition revealing a contribution between 80 % and 90 % of m_J = 15/2 to the ground state state KD. However, while the ground state is indeed largely anisotropic, there are significant transverse components to the ground state g-tensor indicating a very active QTM-channel.
An investigation of the total ZFS of the $^6H_{15/2}$ ground multiplet as plotted in Figure 4.22 shows that **(C1)** and **(C2)** behave qualitatively similarly. However, the energy of the first excited KD is decreased by approximately 20 cm^{-1} from **(C1)** to **(C2)**. Furthermore, the optimization of hydrogens does have a small influence on the splitting through increasing the barrier by circa 10 cm^{-1} compared to the unoptimized structure.
To further probe the intramolecular coupling, the Dy(III)-centers in the opt models were replaced by Gd(III) and BS-DFT calculations were performed to compute the exchange coupling constants. Here, the methodology derived in Section 3.3.2 was employed and four calculations using the functionals pbe0, bh-lyp, cam-b3lyp and ωb97-x were performed (Table A.18). This revealed antiferromagnetic coupling constants between -0.098 cm^{-1} and -0.164 cm^{-1} for **(C1)** and between -0.102 cm^{-1} and -0.169 cm^{-1} for **(C2)**.

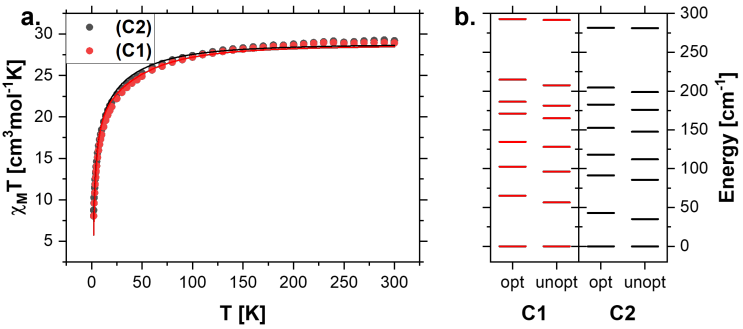

Figure 4.22.: a. Measured and fitted DC-susceptibility for **(C1)** and **(C2)**. b. Energy splitting for **(C1)** and **(C2)** with (opt) and without (unopt) preliminary hydrogen optimization.

As expected from the results of Section 3.3.2, bh-lyp yielded the lowest coupling constants whereas pbe0 yielded the largest. Note that these values refer to a (pseudo)spin $\tilde{S}$ = 7/2. Furthermore, the dipolar coupling between the Dy(III)-centers can be calculated from the interaction energy of two classical magnetic dipoles. Here, a pseudospin of $\tilde{S}$ = 1/2 is assumed yielding J_{dip} = -1.483 cm^{-1} and -1.421 cm^{-1} for **(C1)** and **(C2)** respectively. These values suggest that the couplings in **(C1)** and **(C2)** are indeed very similar as would be expected for two isostructural compounds.

Variable temperature DC susceptibility measurements and isothermal magnetization measurements have been performed to investigate the static magnetic properties of both complexes. The χ_MT versus T plots are shown in Figure 4.22a, whereas the M versus B figures are shown in the appendix, Figure A.34. As expected for two antiferromagnetically coupled Dy_2-complexes, χ_MT stays at around 29.9 $cm_3mol^{-1}K$ at higher temperatures before dropping sharply below approximately 50 K. The high temperature values are close to the expected 28.34 $cm_3mol^{-1}K$ for two free, spin-orbit coupled ions with S = 5/2 and L = 5.

The obtained data was simulated using the ESOs up to k = 6 computed with CASOCI for the optimized model and fitting a coupling constant *J* and an anomalous g-factor to the experimental data. This gave coupling constants J_{fit} = -0.0125 cm^{-1} for **(C1)** and -0.0137 cm^{-1} for **(C2)**. Note that a pseudospin $\tilde{S}$ = 15/2 was assumed in this fit. Because three different pseudospins were assumed for the three coupling constants (dipolar, BS, fit) obtained for this system, Table 4.3 summarizes them scaled to a pseudospin $\tilde{S}$ = 1/2.

Table 4.3.: Summary of obtained coupling constants for **(C1)** and **(C2)** using a pseudospin $\tilde{S}$ = 1/2 in cm^{-1}.

	J_{fit}	J_{dip}	$J_{BS,min}$	$J_{BS,max}$
(C1)	-2.815	-1.483	-5.005	-8.297
(C2)	-3.085	-1.421	-4.823	-8.025

Clearly, whilst BS-DFT significantly overestimates the antiferromagnetic coupling, the dipolar contribution alone is not sufficient to explain the observed downturn of the χ_MT curve.

It is worth pointing out that the observed antiferromagnetic coupling can also be shown by a Curie-Weiss fit with gives a negative Weiss-Temperature and also by a maximum in the derivative of the isothermal magnetization at 1.8 K. These are shown in the appendix, Figures A.34-A.35. Therefore, no effect on the static magnetic properties was observed.

Finally, a series of Alternating Current (AC) susceptibility measurements at 2 K with applied fields between 0 T and 0.3 T were performed probing the SMM behavior of these compounds.

Unfortunately, no out-of-phase signal was observed in any of the measurements as shown in the appendix, Figures A.36-A.37. Thus, the influence of the halogen bonds on the relaxation dynamics could not be investigated.

4.3.3. Intramolecular Coupling in $Gd_2(mph)_4(NO_3)](NO_3)$

Using the same reaction conditions as for **(C2)**, and reacting $Gd(NO_3)_3$ with Br-Hmph in a mixture of MeOH and MeCN, complex $[Gd_2(Br-mph)_4(NO3)](NO3)\cdot 5MeOH$ **(C3)** forms as large diamond shaped crystals after one week. Subsequently, SC-XRD, PXRD and IR measurements were performed to analyze the composition. In contrast to compound **(C2)**, an asymmetric dinuclear complex with four Br-mph ligands and two nitrates is formed. The molecular structure is shown in Figure 4.23.
Compound **(C3)** crystallizes in the triclinic space group $P\bar{1}$ with Z = 2. Three Br-mph$^-$ ligands bridge the two centers via their deprotonated phenoxo group.

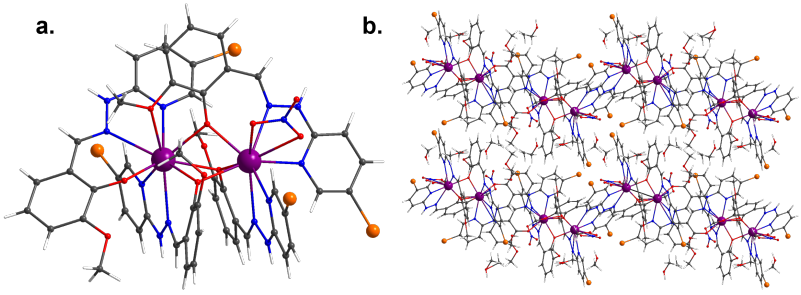

Figure 4.23.: a. Molecular structure of **(C3)**, counterion and lattice solvent omitted for clarity. b. Packing of **(C3)** viewed along the crystallographic a-axis.

Each Gd(III)-center is coordinated to two Br-mph ligands via two N-donor sites and the phenoxo group. Consequently, one Br-mph ligand is coordinated in a non-bridging fashion to Gd2. The resulting empty coordination sites at Gd1 are satisfied with a bidentate nitrate ion. All four hydrazone hydrogens are involved in hydrogen bonding to either methanol lattice solvent or the remaining nitrate counterion.

Both Gd(III) centers feature a N_4O_5 coordination environment and can be best described as a spherical capped square antiprisms (CSAPR) with CSMs of 1.625 and 1.398 for Gd1 and Gd2 obtained from a SHAPE analysis. The next best polyhedron is the closely related muffin type geometry with CSMs of 2.073 and 1.764 for the two centers. The Gd-Gd distance is 360.85(3) pm and the bridging Gd-O-Gd angles are 93.68(8)°, 98.77(9)° and 100.55(9)°.

To probe the intramolecular coupling between the two Gd-ions, DC-SQUID measurements were preformed in collaboration with Prof. Yan Peng. These are shown in the appendix, Figure A.38. The high temperature/high field behavior deviates significantly from what might be expected, for which there is no current explanation.

Finally, BS-DFT calculations have been performed using the functionals bh-lyp, pbe0, cam-b3lyp and ωb97-x revealing antiferromagnetic coupling constants of -0.054 cm^{-1}, -0.090 cm^{-1}, -0.082 cm^{-1} and -0.072 cm^{-1}. However, to validate these results the magnetic measurements will have to be repeated.

5. Second-Sphere Effects on the Magnetic Anisotropy

The influence of ions and molecules in the second coordination sphere around paramagnetic lanthanide ions on that ions magnetic properties was explored in a series of projects.

In Section 2.1, general theories relevant for SMMs have been introduced before. It was established that the different splitting of the lowest J-multiplet by the ligand field is an important feature of lanthanide based magnetic systems. This Zero Field Splitting (ZFS) can be modeled with so called Extended Stevens Operators (ESOs). In this last chapter, a detailed investigation into the ZFS and especially into the chemical model used to compute it will be presented. In Section 5.1 a number of key metrics such as the magnetic anisotropy, and the characterization of the ZFS will be introduced. Section 5.2 illustrates when second-sphere effects might be relevant. This is exemplified by a number of structures synthesized and characterized within this project. In Section 5.3 the proposed effects are tested on a mononuclear Er(III) compound. Then, the effect of halogen bonding in conjunction with second-sphere effects on the magnetic properties of mononuclear Dy(III)-SIMs is explored in Section 5.4.

Finally, in the last Section 5.5 of this chapter, second-sphere effects, halogen bonding and intramolecular coupling will be investigated simultaneously for a set of three Dy_3-triangles. In particular, the influence on toroidal magnetic moments and their analysis are discussed.

5.1. Introduction

A key feature of SMMs is the anisotropy of the magnetic ground state. This means that the magnetic response of the system has to be described with a 3x3 g-tensor, rather a scalar g-factor. The eigenvalues of this g-tensor are referred to as $g_{x,y,z}$ with the respective eigenvectors describing the magnetic main axes frame. Notably, all g-tensors mentioned in the following are for an isolated KD described by a pseudospin $\tilde{S}$ = 1/2 whereas ESOs are calculated for a pseudospin of the ground J-multiplet.
To achieve slow relaxation, the magnetic ground state needs to be as anisotropic as possible where $g_{x,y}$ = 0 and g_z is large. As a matter of fact, the magnitude of the transversal components of the g-tensor ($g_{x,y}$) is directly related to fast QTM. Furthermore, the anisotropy of the m_J-states with the largest value can be directly determined with Hund's rules.

Figure 5.1.: Ground state quadrupole moments of (from left to right) Tb(III), Dy(III), Ho(III), Er(III), Tm(III), Yb(III) and Lu(III) highlighting three oblate, three oblate, three prolate anisotropies and an isotropic ion. Reprinted with permission from Ref. [19].

This was realized by Rinehard and Long in 2011 who consequently defined the most important design principle for SMMs: To achieve the best possible SMM-properties, the ligand field needs to be designed to reinforce the intrinsic ground state anisotropy of the incorporated lanthanide.[19] This means that an axial ligand field should be employed to stabilize oblate Ln(III)-ions such as Dy(III) and an equatorial field to stabilize the ground state of a prolate ion such as Er(III).

After this realization, many new ligand systems were proposed to design ligand fields as axial as possible. A central focus was on cyclopentadienyle complexes[20,74,75,393,394] and more recently N-based donors.[394–399] Furthermore it has to be considered that the symmetry of the ground state has to obey the (local) symmetry of the coordination environment. This explains the success of D_{5h}-symmetric complexes, where the magnetic main axis has to align with the C_5-axis.[49,400]

If the magnetic ground state is well isolated, a simple electrostatic model can be employed to search for the direction of the anisotropy. This is can be calculated e.g. for the $m_J = \pm 15/2$ state of the $^6H_{15/2}$ ground multiplet using the program MAGELLAN.[259] This program will rotate a $m_J = \pm 15/2$ wavefunction in an electrostatic point charge field to determine the lowest energy based on an azimuth and polar angle. This is shown in Figure 5.2a for a purely axial point charge field. Importantly, the energy barrier between them is not the energy barrier that has to be overcome to reverse the magnetization, the system would tunnel through the barrier.

Figure 5.2b shows this potential when significant charges are introduced at the equatorial positions. Local minima occur on the x- and y-axis only slightly higher in energy than the ground state. Now the electronic situation becomes much more complex.

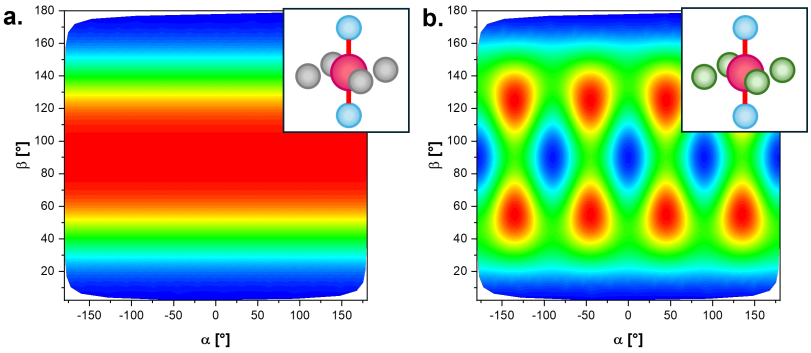

Figure 5.2.: Visualization of the crystal field calculated with MAGELLAN. The energy of the $m_J = \pm 15/2$ state of a $^6H_{15/2}$ Dy(III) ground state when it is rotated in an axial (a.) or almost octahedral (b.) crystal field. Blue indicates stable orientations, red disfavorable. α is the angle to the x-axis, β is the angle to the z-axis. Clearly, multiple local minima at the x- and y- axis can be observed in the field shown in b.

It is not hard to imagine that in such a case of low axial symmetry, small changes around the system may stabilize one or the other direction making them the global minimum. This can lead to strong changes of the magnetic anisotropy direction, the mixing of m_J-states and therefore of the magnetic properties. This exact effect was recently shown experimentally and computationally by Mattei *et al.*[401]

To give just one example, the dipolar interaction between two magnetic dipoles can be written as

$$E_{dip} = -\frac{\mu_0}{4\pi r^3}(3(\vec{\mu}_1\vec{r})(\vec{\mu}_2\vec{r}) - \vec{\mu}_1\vec{\mu}_2)$$

and is therefore directly related to the angle between the two g_z axes indicating the direction of the magnetic moment of a Dy(III)-ion.

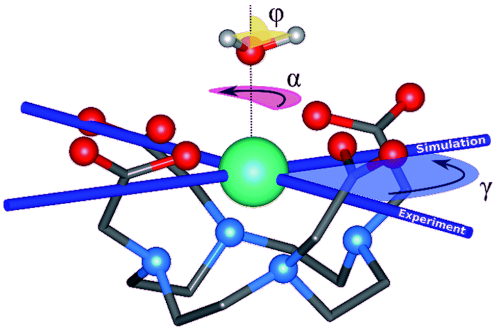

Figure 5.3.: The anisotropy axis follows the direction of the hydrogens on a water ligand in the DyDota complex. Reprinted with permission from Ref. [402].

In experiments, such small effects are hard to decipher. The most complete analysis has been performed on lanthanide DOTA complexes. Here, considering the strong axial ligands, an easy plane anisotropy should be observable for Dy(III) where the main axis is oriented in the DOTA-plane.[402,403] However, an axial anisotropy was observed in magnetic torque measurements. It could be rationalized that the position of the water ligands was directing the main axis, a very small electronic change with significant effects.[402] By chemically removing the water ligands, it was shown that easy plane anisotropy was achieved.[404]

There are a few studies on Dy(III) and Er(III) complexes highlighting that the second coordination sphere can be relevant to describe the electrostatic potential around the magnetic centers.[405,406] Considering that most calculations in the literature are carried out on a single model structure, this makes it important to find structural indicators when this effect might be relevant. Consequently, several model structures are calculated for the compounds discussed in the next sections which include more and more of the crystal space.

These calculations are then, whenever possible, compared to experimental results. This was done for a number of compounds within this dissertation project, some of which were synthesized as a part of this project but also in several collaborations with the research groups Powell, Hanf, Roesky and Ruben. Only some of the most interesting results will be summarized in the following sections.

5.2. Multidentate Carbohydrazide Ligands

A number of complexes based on the 2,6-diacetylpyridyl-bis(pyrazine-2-carbohydrazone) (H_2dappyzh) ligand system synthesized within this dissertation project may serve as an introduction to second-sphere effects. SC-XRD measurements were performed by Dr. Olaf Fuhr and Dr. Christopher Anson, the SQUID characterization was conducted by Prof. Yan Peng.

By reacting pyrazine-2-carboxylic acid with thionyle chloride in methanol, the acid is esterified to methyl pyrazine-2-carboxylate. By reacting this product with hydrazine in ethanol, the pyrazine-2-carbohydrazide was obtained as pale yellow crystals.[379]

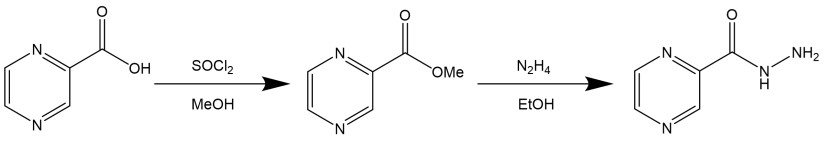

Figure 5.4.: Synthetic route to obtain pyrazine-2-carbohydrazide.

This ligand could then be reacted with 2,6-diacetylpyridine in a Schiff base reaction to obtain the large, multidentate H_2dappyzh ligand in the presence of a metal salt. Three of the coordination complexes based on this ligand system will be discussed in the following. It should be noted that the reaction of this ligand with lanthanide chlorides was reported before by Kumar in 1998.[407]

However, no structural analysis was carried out on the obtained crystals and the assignment of the coordination sphere was purely based on the symmetry of the photoluminescence spectrum of the Nd(III)-complex.[407] Similar structures as to those reported here were obtained by Armenis *et al.* for the ligand where the pyrazine function is replaced by pyridine.[408] Furthermore, a Eu(III)-complex has been reported by Lozovan *et al.* in 2025 where the pyrazine function is replaced by quinoline.[409]

5.2.1. Introducing Second-Sphere Effects in $[Dy(H_2dappyzh)\ (H2O)_3(MeOH)]Cl_3$

By reacting 2,6-diacetylpyridine with two equivalents of the previously prepared pyrazine-2-carbohydrazide in the presence of $DyCl_3 \cdot xH_2O$, compound **(C4)** crystallized within 2 weeks as large yellow crystals suitable for SC-XRD. The obtained structure is ideal to introduce some theoretical concepts about second-sphere effects influencing the electronic structure of Dy(III)-SMMs. Unfortunately, the crystals are not stable when ground outside the solution, which means that they are not suitable for any kind of measurements requiring a powder samples such as SQUID-measurements. Furthermore, the space group including mirror planes makes them unsuitable for single crystal measurements such as μ-SQUID or torque magnetometry.

Compound **(C4)** crystallizes in the monoclinic space group $P2_1/c$ with Z = 4. The first coordination sphere around the Dy(III)-center is made from the pentadentate, neutral H_2dappyzh-ligand. This ligand is slightly distorted to a cone with the Dy(III)-ion at the top. One water ligand is coordinating inside this cone (above the plane) whereas two water ligands and one methanol ligand coordinate below the cone.

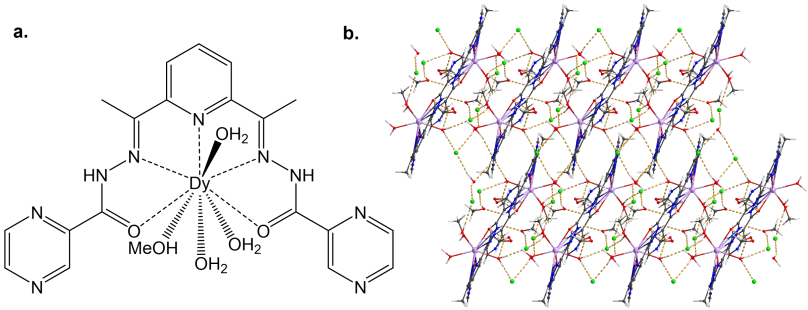

Figure 5.5.: a. Scheme of the structure of **(C4)**. b. Packing of **(C4)** viewed along the crystallographic b-axis. Intermolecular hydrogen bonds are shown as dashed orange lines.

Consequently, the metal features an N_3O_6 coordination geometry with an approximate muffin type geometry (CSM = 2.377). Furthermore, since all ligands are neutral, the bare molecule is charged +3.

This large charge is countered with three chlorides, a water and two methanol molecules in the crystal lattice. Importantly, each hydrogen attached to a coordinating oxygen is involved in hydrogen bonding to either counterions or lattice solvent. As apparent from Figure 5.5b, the molecules pack in sheets separated by the lattice solvent and counterion hydrogen bond network, which explains why the structure is unstable upon being ground. Through the hydrogen bonding network, the smallest Dy(III)-Dy(III) distance is 809.60(3) pm.

This molecule is particularly interesting with respect to its crystal field since the negative charges are non-coordinating but and only located in the second coordination sphere. Moreover, considering that six chloride ions form hydrogen bonds to the water/methanol ligands, each chloride is relevant for the crystal field of multiple Dy(III)-ions.

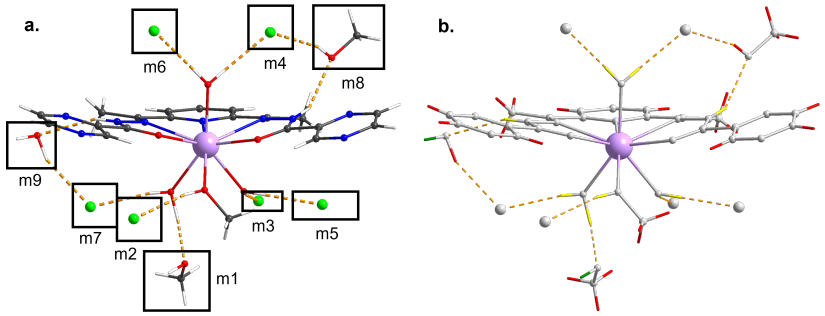

Figure 5.6.: a. Structure of **(C4)** and the order in which the additional counterions/lattice molecules are included in the structure. b. Structure of **(C4)** with highlighted hydrogen atoms in the order in which they are relaxed. unopt (none), opt1 (red), opt2 (yellow), opt3 (green).

The two lattice methanol and water molecules are involved in this bonding network as well. This ponders two questions about the local anisotropy:

- How dependent is the Dy(III) local anisotropy on the position of hydrogens involved in hydrogen bonding?
- How do the additional counterions and lattice solvent molecules influence the crystal field around the Dy(III)-ion?

These two questions were subsequently investigated. A combination of geometry optimizations and CASOCI calculations was performed as shown in Figure 5.6. Four steps of subsequent geometry optimizations were performed on a b3-lyp-D4/def2-TZVP level of theory where the Dy(III)-ion was treated with a large-core ECP. unopt: no hydrogen positions were optimized and CASOCI calculations were performed on structures directly extracted from the cif.

opt1: All C-H bonds as well as hydrogens involved in hydrogen bonding except of those bound to a ligand were optimized (red). opt2: All remaining hydrogens of the ligands were optimized (yellow). opt3: This left two hydrogens in the second coordination sphere for which no H-bonding partner was considered in this model. These are optimized in a last step (green).

Furthermore, the second-sphere ions indicated in Figure 5.6a were incrementally included in the calculation ordered by their distance to the central Dy(III)-ion including all molecules of the previous model. This was done in ten steps starting with the +3 naked molecule (m0) and ending with a -3 charged cluster where all hydrogen bonds of first coordination sphere hydrogens are considered (m9). In total this means that 40 CASOCI calculations were performed on **(C4)**. ESOs, ZFS and diagonal g-tensor elements are provided in the appendix, Tables B.103–B.118.

Figure 5.7 shows the energy splitting of the lowest $^6H_{15/2}$ multiplet for all 40 model structures. This figure contains a considerable amount of information to be discussed in the following. The first important information is that the change from the unopt (black) to the opt1 (red) model is negligible. For most states the energies of these two models overlap. Here, the RMSD between the unopt and opt1 models is less than 3.2 cm^{-1}. This means that the effect of the backbone H-positions has, as expected, no significant effect on the splitting. RMSD-values comparing all models are provided in the appendix, Tables A.21–A.22.

A similar effect can be observed when comparing the models opt2 (green) and opt3 (blue) where only the two remaining dangling H-positions were optimized. Here, the RMSD is lower than 5.7 cm^{-1} and therefore still negligible. However, when the H-positions close to the Dy-center, i.e. those of water ligands are optimized (going from opt1 (red) to opt2 (green)), a much larger deviation can be observed.

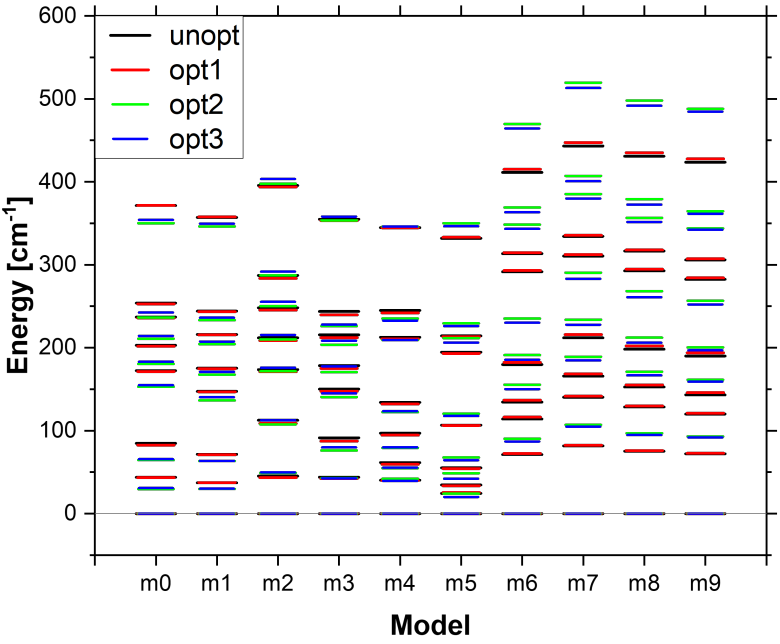

Figure 5.7.: Energy splitting of the lowest $^6H_{15/2}$ multiplet into eight Kramers doublets for the four optimization levels (unopt, opt1, opt2, opt3) and 10 model structures.

Whilst this is apparent from Figure 5.7, the RMSD for this change is between 3.6 cm^{-1} in structure m2 and 63.6 cm^{-1} in structure m7. The latter is a significant difference. Interestingly, the RMSD values between opt1 and opt2 are below 21 cm^{-1} up to model m5 before steeply increasing above 48 cm^{-1} starting at model m6.

These results highlight, that an optimization of H-positions in close proximity to the metal centers should be performed before calculating magnetic properties.

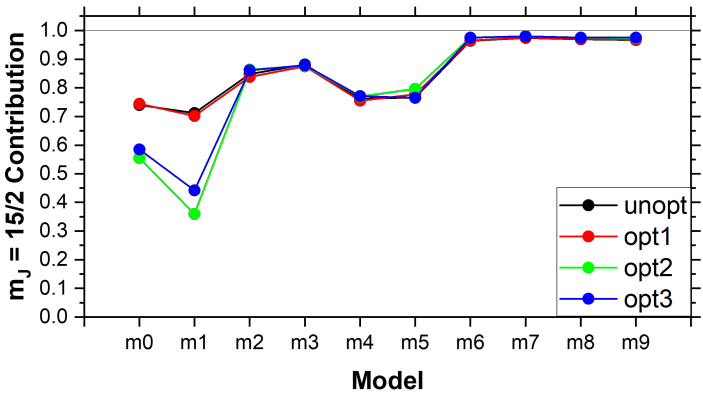

Figure 5.8.: Contribution of the $m_J = \pm 15/2$ state to the ground state across all 40 models.

In fact, this is a general trend as it will reemerge in later sections.
The contribution of the $m_J = \pm 15/2$ wavefunction to the ground state is also dependent on the optimization of the hydrogen positions as shown in Figure 5.8. A full list of all contributions can be found in the appendix, Tables B.119–B.122. For structures m0 and m1, a large deviation between the optimized and unoptimized models can be observed. This vanishes upon the inclusion of larger crystal spaces.
Figure 5.7 also shows the difference between the increasingly larger model structures m0 to m7. At this point, it should be noted that between models m1 and m7, all hydrogen bonds to ligands around the Dy(III)-center are slowly constructed. Furthermore, while the energy of the first excited state does not change notably up to model m4, the m_J-composition and energy of higher excited KDs does. When the second coordination sphere is saturated with counterions in model m7, the energies and m_J-compositions of the excited KDs converge.

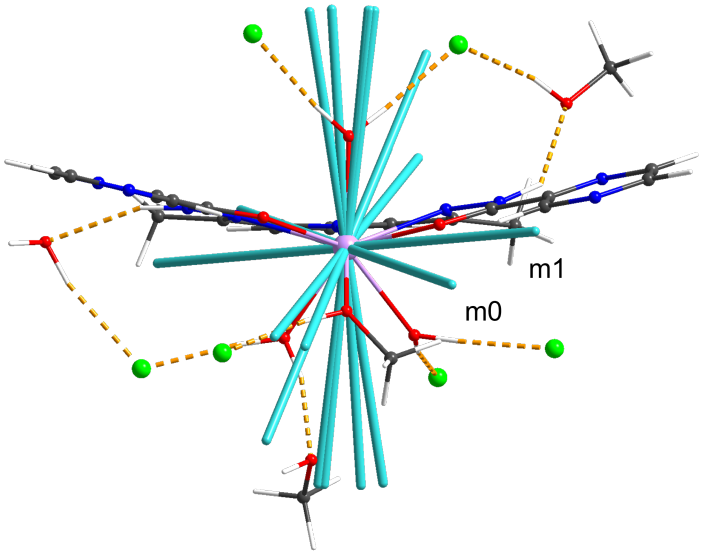

Figure 5.9.: Direction of the ground state magnetic main axis for **(C4)** upon for the ten structures for model opt2 in compound **(C4)**. The directions of models m0 and m1 are in the approximate ligand plane and indicated.

The central conclusion of this study is that in the case of such hydrogen bonding networks, it is compulsory to include the full second coordination sphere in the calculation.

Naturally, it is important to check this influence on the ground state magnetic main axis. This is shown for the structures with model opt2 in Figure 5.9. Here, the main axis flips from an in-plane arrangement to the H_2dappyzh ligand into the axial position along the single water ligand. Clearly, this change is gradual and upon the inclusion of the first few counterions, the axis only rotates in the plane before flipping in the axial position.

This highlights how second-sphere ions can steer the molecular anisotropy.

A possible pathway of this interaction will be discussed in Section 5.5.2. For now, it is concluded that second-sphere effects may become predominant when: **1.** The crystal field in the first coordination is non-axial, i.e. through exclusively charge neutral ligands in a low symmetry crystal field. **2.** When protonated oxygen atoms coordinate to the Dy(III)-center whilst forming hydrogen bridges to second-sphere ions.
At this point, these conclusions are only phenomenological and will be tested for their influence and origin in the next sections.

5.2.2. $[Dy_2Na_2(dappyzh)_2(OAc)_4(H_2O)_2]$

The reaction of the H_2dappyzh precursors with Dy(III)triflate and sodiumacetate in acetonitrile lead to the crystallization of compound **(C5)** after one day. The crystal structure for this compound was collected and solved by Dr. Olaf Fuhr, magnetic measurements were conducted by Prof. Yan Peng and analyzed within the present work. The phase purity was determined with PXRD (Figure A.39).
Compound **(C5)** crystallizes in the monoclinic space group *C*2/*c* with Z = 4 on a twofold rotation axis and with two molecules of MeCN in the crystal lattice. The molecular structure is depicted in Figure 5.11. Each Dy(III)-ion is coordinated by a pentadentate dappyzh^{2-} ligand in an approximate plane and two bidentate acetate groups above and below the ligand plane. These consequently feature a N_3O_6 coordination sphere with a geometry between a spherically tricapped trigonal prism and a spherical capped square antiprism with CSM values of 2.744 and 2.989, respectively. Two such $[Dy(dappyzh)(OAc)_2]^-$-complexes are then connected across the twofold rotation axis via a $Na_2(H_2O)_2$ moiety.

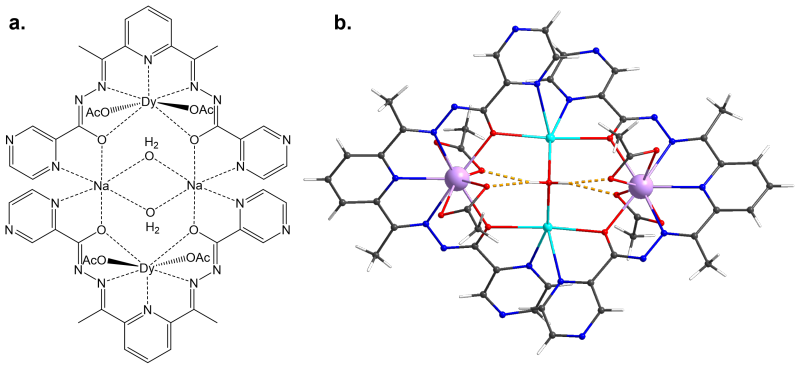

Figure 5.10.: a. Scheme of complex **(C5)**, hydrogen bonds are omitted for clarity. b. Molecular structure of **(C5)** as obtained from the SC-XRD experiment.

These water molecules then form hydrogen bonds to the axial acetate ligands. Thus, the full complex is $[Dy_2(dappyzh)_2(OAc)_4Na_2(H_2O)_2]\cdot 2MeCN$. The Dy(III)-Dy(III) distance between the two centers is 746.49(15) pm, whereas all intermolecular Dy-Dy distances are longer than 866 pm. The packing of **(C5)** is shown in Figure 5.11 along the crystallographic a- and c-axes.

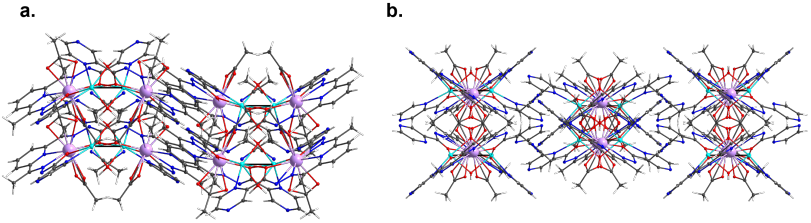

Figure 5.11.: a. Packing of **(C5)** along the crystallographic a-axis. b. Packing of **(C5)** along the crystallographic c-axis.

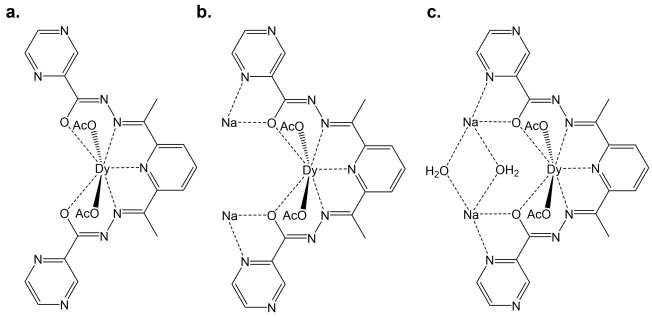

Figure 5.12.: Model structures used to compute the magnetic properties of **(C5)**: a. The "bare" monoanionic molecule, b. "na" including the Na-cations, and c. "half" including the water molecules.

This packing is dominated by the stacking of the distorted dappyzh ligands. Considering the large Dy(III)-Dy(III) distances, it was first assumed that the two centers are magnetically decoupled. However, it was intriguing to investigate if the diamagnetic bridge has any electrostatic influence on the Dy(III)-centers magnetic properties.

Thus, four model structures were investigated with CASOCI calculations as depicted in Figures 5.10 and 5.12. Starting from the "bare" model structure, which only includes one Dy(III)-ion and the first coordination sphere, the model was expanded to the sodium cations "na". Subsequently, the water molecules included in the hydrogen bonding were considered. Finally, single ion properties were calculated for the full molecule by replacing one center with diamagnetic Y(III).

Calculations on these four models were performed with and without a preliminary optimization of the hydrogen positions. This was conducted on a b-p-D4/rij/def2-TZVP level of theory considering the C_2-symmetry of the full molecule and using a large-core ECP for Dy(III).

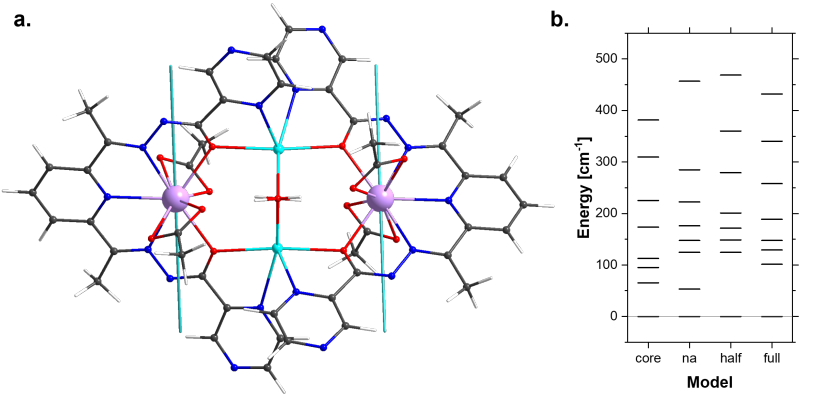

Figure 5.13.: a. The magnetic main axis of **(C5)** lies approximately in the dappyzh^{2-} ligand plane. b. Energy splitting of the $^6H_{15/2}$ multiplet for the four model structures used to investigate **(C5)** with optimized H-positions.

Subsequently, the structure was reduced to the different model structures. However, this optimization revealed no noteworthy influence on the results and thus, only the results for the optimized model will be discussed in the following. Tables containing the energy splitting, diagonal g-tensor elements, ESOs and m_J-compositions for all eight models are shown in the appendix, Tables B.123–B.128.

Figure 5.13b shows the splitting of the lowest $^6H_{15/2}$ multiplet into eight KDs. Upon addition of the Na-ion, the energy of the first excited KD decreased by approximately 13 cm^{-1}, whereas the total ZFS increased by 75 cm^{-1}. Subsequently, upon addition of the water molecules, the energy of the first excited state doubles to 124 cm^{-1} before it is slightly reduced to 101 cm^{-1} for the full model. Furthermore, it can be noted that the ground state magnetic main axis remains at the same orientation as indicated in Figure 5.13a.

It lies in the equatorial ligand plane parallel to the alkoxide donor sites of the dappzyh^{2-} ligand.
Interestingly, the water molecules show the largest influence from the bare molecule to the full structure. This change is not trivial considering that it does not affect the ground state significantly, but rather the first excited state. Across the four models, the ground state is predominantly composed of the $m_J = \pm 15/2$ with contributions between 94.7 % (bare) and 98.1 % (half). Furthermore, it is largely anisotropic with g_z-values between 19.39 (bare) and 19.72 (half).
Within the first excited KD, the differences are much more significant. For example, the g_z-value of KD1 changes from 12.75 in the bare cluster to 18.97 in the model with sodium atoms before decreasing again to a value between 15 and 16 for the last two models. In conjunction with the m_J-composition and $g_{x/y}$ changing significantly, this indicates that the properties of the first excited state are significantly influenced by second-sphere effects.
Based on the sufficiently high energy gap to the first excited KD and the large anisotropy in the ground state, **(C5)** was expected to show SMM behavior. Therefore, magnetic measurements were performed by Prof. Yan Peng and subsequently analyzed within the framework of this thesis. Whilst the obtained high temperature χ_MT value of 26.50 cm^{3}mol^{-1}K is too low compared to the theoretical value of 28.34 cm^{3}mol^{-1}K, the measured value of the magnetization is too high with 12.11 μ_B compared to the theoretical value of 10 μ_B. This discrepancy cannot be fully rationalized with crystal solvent evaporating which would lead to a lower molecular weight of the sample. This would lead to both values being too high. Consequently, for the following discussion, the χ_MT-value was scaled to the simulated high temperature value which is analogous to fitting a g-factor close but not equal to the theoretical 4/3.

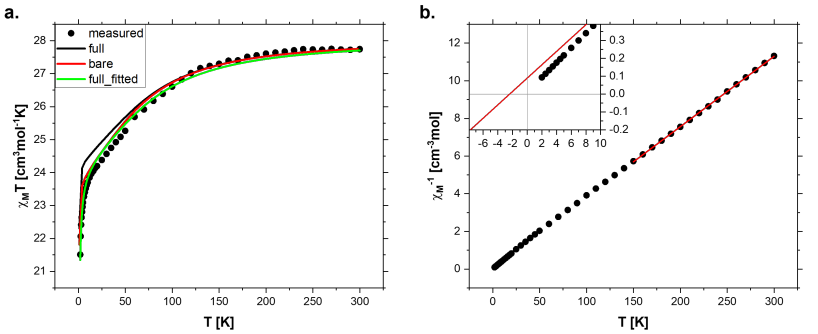

Figure 5.14.: a. χ_MT measured for **(C5)** as well as three model curves: full and bare are twice the calculated susceptibility for the respective single center models. full_fitted refers to the use the ESOs of the full model and the fitting of an exchange coupling constant between the two centers. The experimental data is scaled to fit the simulated high temperature value. b. Inverse susceptibility versus temperature including a linear fit above 150 K. Inset: extrapolation of the linear fit to its intersection with the x-axis.

Figure 5.14 shows the obtained χ_MT versus T and χ^{-1} versus T plots. As expected, the χ_MT graph saturates at high temperatures above approximately 150 K. Subsequently, the susceptibility calculated with CASOCI models bare and full were plotted against the experimental data. Here, no coupling between the centers was assumed which means that the total susceptibility is twice that of the monomers. Whilst the bare model fits exceptionally well, the full model overestimates the χ_MT curve at low temperatures. However, when a coupling constant between the two spin centers is fitted to the full model, the agreement is as good as for the bare model. The isotropic coupling constant is fitted between the two pseudospins $\tilde{S}$ = 15/2 and then rescaled for a pseudospin $\tilde{S}$ = 1/2 for better comparability. Thus, a very small, antiferromagnetic coupling of -0.299 cm^{-1} is results in a good agreement with the experiment.

This clearly ponders the question if such a coupling constant is physically reasonable. Firstly, the Curie-Weiss plot (Figure 5.14b) is fitted with a linear function at high temperatures above 150 K.

$$\chi^{-1} = \frac{T - \theta}{C} \tag{5.1}$$

Where C is the Curie-constant and θ the Weiss-temperature. An extrapolation of this fit to low temperatures shows an intersection with the x-axis at -2 K which is indicative of a weak, antiferromagnetic interaction. Notably, the Weiss-temperature is not the coupling constant. Therefore, it must be assumed that a weak interaction is indeed responsible for the downturn of the χ_MT curve at low temperatures in conjunction with depopulation of the excited KDs.

Calculating the dipolar coupling between the lowest KDs at either center yields an antiferromagnetic coupling of -0.17 cm^{-1}. This is, as expected, very weak but with the correct sign and magnitude of the observed coupling. Thus, a simulation using ESOs and J_{dip} from the CASOCI calculation only fitting an effective g-tensor is shown in the appendix, Figure A.41. It should be noted that the coupling constants order of magnitude is in the range where also intermolecular dipolar coupling may play a role considering that the next Dy(III)-ion is only circa 120 pm further away. As discussed in earlier chapters, exchange coupling generally decreases exponentially and therefore cannot contribute here.

To probe the dynamic properties of **(C5)**, a series of AC-SQUID measurements was conducted. Firstly, the in-phase and out-of-phase susceptibility was recorded at 2 K at different fields ranging from 0 Oe to 3000 Oe. This is shown in Figure A.42 in the appendix. At zero field, the edge of a band can be observed at high frequencies around 1000 Hz. Upon applying a magnetic field, this maximum shifts towards lower fields until it is below 1 Hz at 3000 Oe.

Thus, a variable temperature measurement was performed at this applied field. The results of this measurement are shown in Figure 5.15. The collected in-phase and out-of-phase susceptibilities from 1.8 K to 9 K were fitted with a generalized Debye model for one relaxation process.[36]

$$\chi'_M(\omega) = \chi_S + (\chi_T - \chi_S)\,\frac{1 + (\omega\tau)^{1-\alpha}\sin\left(\frac{\pi\alpha}{2}\right)}{1 + 2(\omega\tau)^{1-\alpha}\sin\left(\frac{\pi\alpha}{2}\right) + (\omega\tau)^{2-2\alpha}} \tag{5.2}$$

$$\chi''_M(\omega) = (\chi_T - \chi_S)\,\frac{1 + (\omega\tau)^{1-\alpha}\cos\left(\frac{\pi\alpha}{2}\right)}{1 + 2(\omega\tau)^{1-\alpha}\sin\left(\frac{\pi\alpha}{2}\right) + (\omega\tau)^{2-2\alpha}} \tag{5.3}$$

In this equation, $\chi_{S,T}$ are the isothermal and adiabatic susceptibility and τ is the thermal equilibrium time. α describes how broad the observable peak is, where large α values may indicate that several relaxation processes with similar relaxation times act simultaneously.
Here, χ'_M and χ''_M were fitted simultaneously to use as much data as possible for the fit. The extracted relaxation times were then fitted in an Arrhenius plot with the following equation:

$$ln(\tau) = -\ln\left(\tau_0^{-1}\exp\left(\frac{-U_{eff}}{k_B T}\right) + V_b\frac{\exp(\frac{w_b}{k_B T})}{(\exp(\frac{w_b}{k_B T}) - 1)^2}\right). \tag{5.4}$$

In this equation, τ_0 is the rate of an Orbach process with an effective barrier U_{eff}. V_b is the rate of a Raman process with a vibrational frequency of w_b. Notably, the two lowest and three highest temperature curves were excluded from this fit, considering the fact that the maxima are outside the measurement window and the obtained relaxation times therefore less reliable.
The obtained parameters for the Orbach process are τ_0 = 1.1717·10^{-7} $\pm$ 3.070·10^{-8} and U_{eff} = 38.02 $\pm$ 0.88 cm^{-1}. In comparison with the energy spectrum calculated with CASOCI, this clearly indicates that the first excited KD is not involved in the relaxation process.

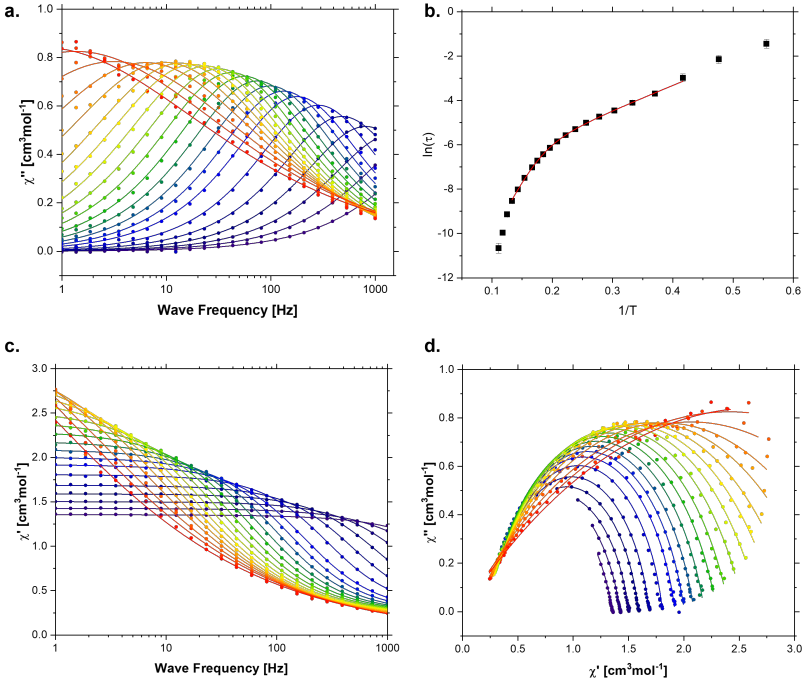

Figure 5.15.: Plots of the AC-SQUID-measurement of **(C5)**. a. Out-of-phase susceptibility, b. Arrhenius plot, c. in-phase susceptibility, d. Cole-Cole plot.

This is because all model structures result in energy gaps significantly larger. Furthermore, the obtained parameters for the Raman process are V_b = 2218.34 $\pm$ 268.03 and w_b = 7.66 $\pm$ 0.27 cm^{-1}. Thus, this low frequency Raman process is very active and responsible for severely limiting the relaxation times.

Summarizing this section, a dinuclear Dy(III)-complex was synthesized and characterized. In this case, the diamagnetic bridge was shown to not influence the ground state significantly, considering the prominent uniaxial anisotropy of the crystal field. However, the bridge influences the energy and composition of the first excited state considerably, highlighting how second-sphere effects may not only influence the ground state.

5.2.3. $[Dy_4(dappyzh)_2(OH)_2(OAc)_6]$

In the following, a structurally similar complex to complex **(C5)** with the same ligand, but a different bridge will be investigated. Reacting $Dy(OAc)_3 \cdot xH_2O$ in a mixture of MeCN and MeOH in the presence of the H_2dappyzh precursors, $[Dy_4(dappyzh)_2(OH)_2(OAc)_6] \cdot 2\,MeOH$ **(C6)** forms as yellow crystals suitable for SC-XRD. The PXRD and packing are shown in the appendix, Figures A.39–A.44. The space group is $P2_1/c$. Considering that the molecule is on the inversion center two molecules can be found in the unit cell.

Compound **(C6)** is centrosymmetric and features two pairs of equivalent Dy(III)-ions in a slightly distorted rhombus. Here, Dy1 sits at the top positions whereas Dy2 is in the bridge. The respective Dy(III)-Dy(III) distances are 395.10(3) pm and 380.07(3) pm between Dy1 and Dy2, where it is 336.877(5) pm between the two Dy2 sites. The distance between the two Dy1 centers is 681.99(4) pm. Thus, this compound is slightly more compact than **(C5)**. The two dappyzh^{2-} ligands in **(C6)** lie above and below the Dy_4 plane. In the two triangles made of two Dy2 and one Dy1, a μ_3-OH^- bridges the three centers respectively. Furthermore, four acetate molecules bridge Dy1 and Dy2 in a $1\kappa O; 2\kappa O'$ motif.

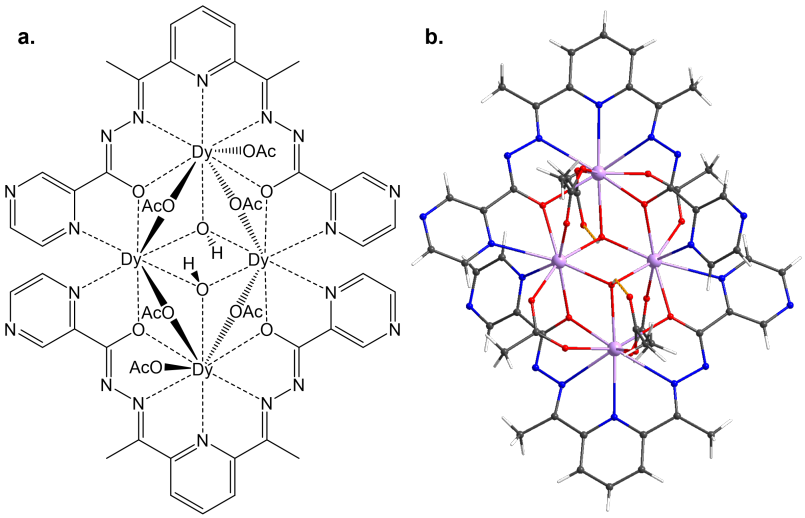

Figure 5.16.: a. Scheme of the central molecule in **(C6)**, hydrogen bridges are omitted for clarity. b. Molecular structure of **(C6)** as determined by SC-XRD. Lattice solvent molecules are omitted for clarity.

The two remaining acetate ions coordinate monodentate to a Dy1 site and form a hydrogen bridge to the central hydroxide ions and a methanol lattice solvent with the second oxygen.

Dy1 features a N_3O_6 coordination which is very asymmetric. The lowest CSM value is obtained for a muffin type coordination as 3.483. In comparison, Dy2 features a N_2O_6 coordination with a symmetry between a biaugmented trigonal prism and triangular dodecahedron with CSM values of 2.399 and 2.480. Considering the similarity with **(C5)**, a series of quantum chemical calculations were carried out investigating compound **(C6.)**

Single center calculations have been performed by replacing all but one Dy(III)-ion to diamagnetic Y(III) and performing a CASOCI calculation.

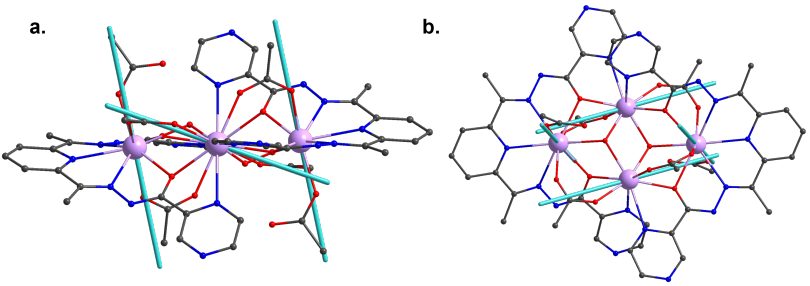

Figure 5.17.: Ground state main axes computed for **(C6)** using CASOCI. a. side view, b. top view.

An optimization of hydrogen positions on a b-p-D4/rij/def2-TZVP level of theory considering the C_i-symmetry and treating the Dy(III)-ions with large-core ECPs did not influence the results and is thus not discussed in the following. The splittings of the lowest $^6H_{15/2}$ state, diagonal g-tensor elements, m_J-composition and ESOs are shown in the appendix, Tables B.129–B.131.

The two Dy(III)-centers behave distinctly, where the energy of the first excited KD is 45.0 cm^{-1} for Dy1 and 101.0 cm^{-1} for Dy2. Interestingly, despite featuring a significantly larger energy gap, the transversal components of Dy2 are larger by one order of magnitude. Considering $g_{x,y}$ values of 0.29 and 0.75 for Dy2, no SMM behavior is expected for **(C6)**.

Figure 5.17 shows the magnetic main axes of the Dy(III)-centers in **(C6)**. Notably, only one calculation was performed on each crystallographically unique Dy(III)-center and the centrosymmetry used to construct the symmetry equivalent ion. Whilst the main axes of Dy1 follow the axial acetate ligands, those of Dy2 are in the Dy_4 plane in between the alkoxide and hydroxide ligands.

This has important implications for the coupling between the centers.

Before comparing the dipolar coupling between the two different centers, BS-DFT calculations were performed using the established four functionals. A summary of all obtained coupling constants scaled to a pseudospin $\tilde{S}$ = 1/2 is provided in Table 5.1. A scheme for the four coupling constants is provided in Figure 5.18. Comparing the four functionals, bh-lyp results in the most ferromagnetic coupling in comparison to the other functionals. Clearly, the interaction between the two Dy2-ions is strongly antiferromagnetic, both in terms of dipolar and exchange coupling. Furthermore, the interaction between the two Dy1-ions can be neglected. Assuming an Ising type interaction also for the exchange, a Spin Hamiltonian of the form $\hat{H} = -2J_{12}S_{z1}S_{z2}cos(\theta)$ has to be employed. It must be considered that the angle θ between the main axes of Dy1 and Dy2 is 59.6°.

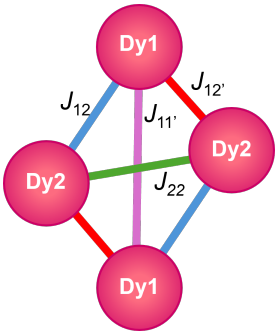

Figure 5.18.: Coupling scheme in **(C6)**.

Table 5.1.: Distances and coupling constants *J* for the four distinct interactions in **(C6)** scaled to a pseudospin $\tilde{S}$ = 1/2. BS-DFT are calculated from the Gd(III)-Gd(III) pairs.

	Dy-Dy dist	J_{dip}	$J_{bh\text{-}lyp}$	J_{pbe0}	$J_{cam\text{-}b3lyp}$	$J_{\omega b97\text{-}x}$
	pm	cm^{-1}	cm^{-1}	cm^{-1}	cm^{-1}	cm^{-1}
$J_{11'}$	682	0.318	0.013	-0.004	-0.004	-0.005
J_{12}	395	-0.034	-0.270	-0.712	-0.604	-0.483
$J_{12'}$	380	-0.369	-0.621	-1.112	-1.178	-1.250
$J_{22'}$	369	-1.193	-4.322	-6.907	-6.606	-6.106

This means that the calculated exchange coupling constants between nonequivalent ions need to be multiplied with 0.506. Thus, in first approximation, these couplings are one order of magnitude smaller than $J_{22'}$. Based on this analysis, it is proposed that **(C6)** acts as an antiferromagnetically coupled Dy-dimer with the Dy1 sites effectively decoupled.
Unfortunately, since only a small number of crystals was obtained, no SQUID measurements could be performed.

5.3. Mononuclear Er(III)-Complex

Circumstances under which second-sphere effects may play a substantial role have been identified in the previous sections. In this section, this knowledge was applied to a mononuclear Er(III) complex which was investigated with high field Electron Paramagnetic Resonance (EPR) spectroscopy. The results of this section are published in Inorganic Chemistry[arneth.2026] and are currently under review at Inorganic Chemistry. The synthesis was carried out by Dr. Gerlinde Greif, the spectroscopic characterization was performed by Dr. Jan Arneth. The quantum chemical calculations were conducted within the scope of this thesis. All figures are reprinted with permission from Ref. [**arneth.2026**].

Compound **(G1)** is a mononuclear Er(III) complex coordinated by one water ligand and two chelating, neutral PPTM ligands ((4- (6-(1,10-phenanthrolin-2-yl)pyridin-2-yl)-1H 1,2,3- triazol-1-yl)methyl pivalate). Consequently, the bare cluster is +3 charged. Three triflate ions act as counterions in the lattice.

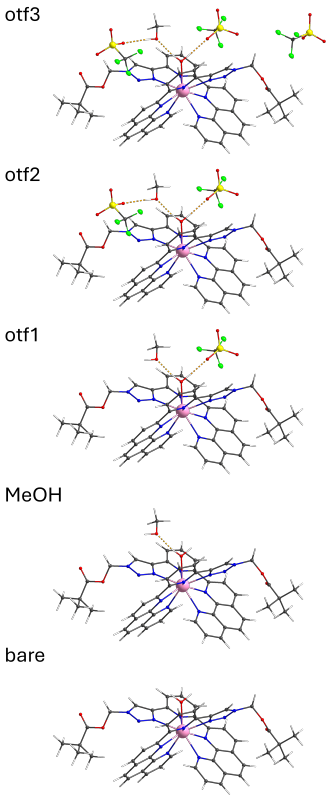

Figure 5.19.: Structure of the five model structures investigated for compound **(G1)**. Reprinted with permission from Ref. [**arneth.2026**].

The full formula of this compound is therefore $[Er(PPTM)_2(H_2O)](OTf)_3 \cdot MeOH$. The complex is almost C_2-symmetric where the Er(III)-O bond acts as pseudo-rotation axis. Because of the low symmetry and the water ligand with respective hydrogen bonds to the counterions, this complex was investigated for second-sphere effects. Furthermore, extensive SQUID and high field EPR studies on this complex give experimental reference values for the splitting and composition of the lowest two KDs.

Five model structures were extracted from the cif starting from the naked cluster by consecutively including the MeOH and three counter ions as shown in Figure 5.19. Afterwards, three types of CASOCI calculations were performed on these structures: **1.** Calculations with the reference structures taken directly from the cif (unopt). **2.** Standard CASOCI calculations as outlined in Section 7.2 are performed with optimized H-positions (opt). **3.** Calculations during which a CASSCF calculation for further optimization of the orbitals was performed between the Restricted Open-Shell Hartree Fock (ROHF)-calculation and the calculation of the integrals (cas). This could not be done for the largest structure due to an intrinsic basis set limit of the program employed called wavels.[411] The obtained ZFS, m_J-compositions and ESOs for the eight KDs of the $^4I_{15/2}$ ground multiplet of the Er(III)-ion are given in Figure 5.20a and in the appendix, Tables B.133–B.144.

Interestingly, the obtained ZFS is very similar across the different model structures and computational methods. The energy of the first excited KD ranges from 21.8 cm^{-1} to 27.5 cm^{-1}. It is slightly lower for the MeOH-model compared to the naked model and increases upon inclusion of additional counterions. The different models were then compared to the experimentally determined χT versus T and M versus B measurements as shown in Figure 5.20b for model opt-otf3 and in the appendix for all other models. The agreement between experiment and calculation is satisfactory.

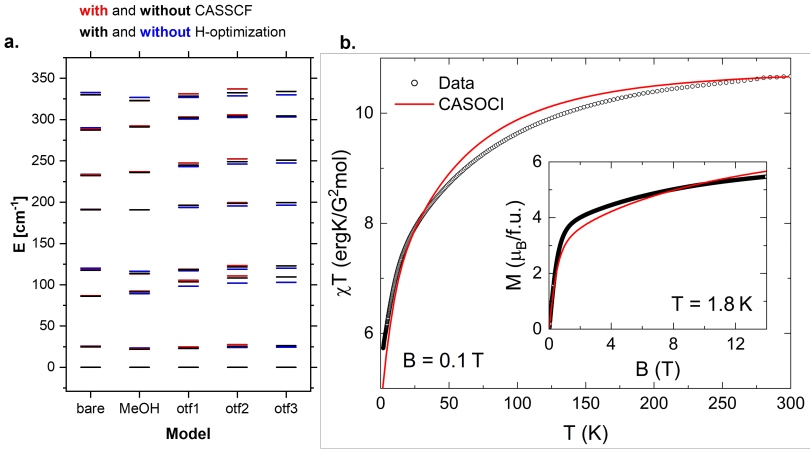

Figure 5.20.: a. Calculated splitting of the $^4I_{15/2}$ ground multiplet of the Er(III)-ion for the different models. b. Calculated versus experimental molar susceptibility and magnetization. Reprinted with permission from Ref. [**arneth.2026**].

Interestingly, there is no qualitative difference between the various models as shown in the appendix, Figure A.45.

Differences are more pronounced for the diagonal elements of the ground state KD g-tensor.This change is small in relative terms for g_z between 11.8 and 12.8. For the transversal components the same absolute difference is a change by one order of magnitude across the different models. g_x ranges between 0.10 and 1.63 and g_y between 0.89 and 2.71. These are shown in Table 5.2.

This is in line with the projection of the obtained wavefunctions onto the pure m_J states of the free ion. The ground state is strongly mixed for all clusters where the main contributions are $m_J = \pm 15/2$ between 24–33 % and $m_J = \pm 9/2$ between 33–52 % for most of the investigated models.

Table 5.2.: Diagonal g-tensor elements of the ground state KD for compound **(G1)** for the different computational models.

unopt	bare	MeOH	otf1	otf2	otf3
g_x	0.99	0.10	1.61	1.34	1.33
g_y	1.51	0.89	1.87	1.74	1.78
g_z	11.86	12.42	12.47	12.59	12.58

opt	bare	MeOH	otf1	otf2	otf3
g_x	0.46	0.74	1.63	1.11	1.10
g_y	1.33	1.55	2.71	1.98	1.95
g_z	12.07	12.48	12.23	12.57	12.62

cas	bare	MeOH	otf1	otf2	otf3
g_x	0.44	0.86	1.49	0.97	-
g_y	1.22	1.53	2.52	1.73	-
g_z	12.15	12.52	12.37	12.73	-

This is not the case for all otf1 models and unopt-otf2 and unopt-otf3 where main contribution is the $m_J = \pm 11/2$ state between 36 % and 45 %. For the other models, this state is not significant for the ground state KD.
This strong mixing correlates with the large transversal components which can be directly attributed to fast relaxation of magnetization through QTM in the ground state without an applied field. To check what relaxation times can be expected for the computed g-tensors, relaxation times τ were calculated using an equation proposed by Yin *et al.*[412–414]

$$\tau_{QTM} = \frac{h}{\mu_B \cdot B} \cdot \frac{\sqrt{g_x^2 + g_y^2 + g_z^2}}{g_x^2 + g_y^2}. \tag{5.5}$$

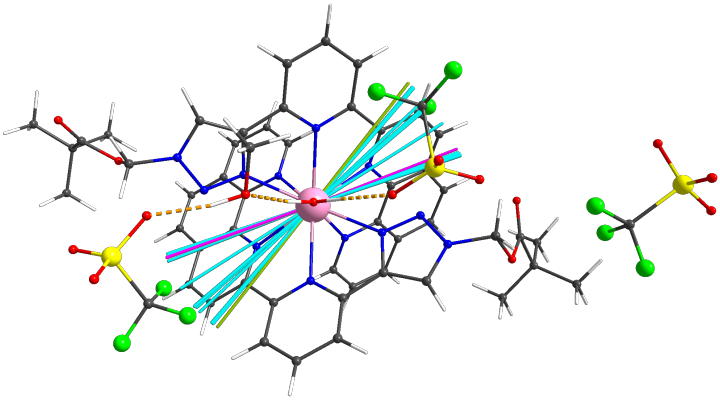

Figure 5.21.: Calculated ground state anisotropy axes using the different models. Highlighted are the models unopt-bare (pink) and opt-otf3 (green). Reprinted with permission from Ref. [**arneth.2026**].

Another approach was published by Prokof'ev and Stamp[415–417]

$$\tau_{QTM} = \frac{h}{\mu_B \cdot B} \cdot \frac{g_z}{2\sqrt{2\pi} \cdot (g_x^2 + g_y^2)}. \tag{5.6}$$

All number are summarized in the appendix, Table A.24. The obtained relaxation times are in the order of 10^{-8} s and therefore significantly below experimental resolution. Furthermore, the transition moments of the magnetic dipole operator were calculated using an implementation by Andreas Bischoff who performed this work in a Vertiefer-thesis supervised within the scope of the thesis.[418] Again, large transition moments indicating fast QTM were computed.

In the next step, the directionality of the ground state anisotropy axis was calculated as depicted in Figure 5.21. The axis for all models are in a plane approximately orthogonal to the Er-O bond with angles between 86° and 90° (Table B.145). Within this plane the angles differ by up to 35°.

This can be easily rationalized given the prolate ground state anisotropy of Er(III).[19] Here, the magnetic main axis will be directed along the minimal crystal field. The C_2-symmetry only allows for orientation of the main axis along or perpendicular to this axis. Given the pronounced oxophilicity of lanthanide ions,[419] the water ligand exerts the strongest crystal field. As discussed in Section 5.1 the main axis for a prolate ion has to be oriented orthogonal to strongest ligand field direction. However, within this plane, the ligand field is not directional leaving small changes of the field as exerted by the H-optimization or counterions to influence the anisotropy significantly.
The majority of this discussion focused on a purely quantum chemical investigation of the electronic structure. However, for this compound it was possible to measure high-field EPR. This technique is particularly powerful in this case, considering the low energy gap to the first excited KD which could be probed in conjunction with the ground state KD. By applying a magnetic field up to 14 T, and measuring with continuous high frequency microwaves, EPR signals could be observed up to approximately 6 T. Four lines correspond to the transitions within the ground state KD and into the first excited state. This allows to fit effective $g_{x,y,z}$ values of 1.4(2), 2.2(4) and 11.8(1), respectively.
In order to compute these spectra, one needs to consider the fact, that this was measured on a loose powder and at low temperatures (1.8 K). Consequently, the ground state magnetic main axis is aligned with the magnetic field whereas the Zeeman interaction within the first excited state needs to be projected onto this axis. The obtained Zeeman diagrams for the opt and unopt models are shown in Figure 5.22 and for the cas models in the appendix (Figure A.46).
Clearly, the general trend is well captured by all models. However, there are differences between various computational models.

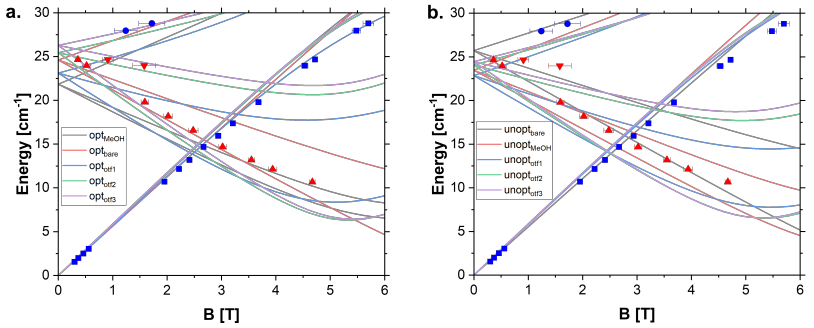

Figure 5.22.: a. Calculated and experimental Zeeman diagram using the opt models. b. Calculated and experimental Zeeman diagram using the unopt models. Reprinted with permission from Ref. [**arneth.2026**].

To quantify these deviations, R^2, MAE and RMSD values were calculated (Table A.23). The best agreement can be reported with the bare models independent of the hydrogen optimization or intermediate CASSCF calculation. Upon inclusion of larger crystal spaces, the agreement becomes worse first, before increasing again. On first glance, this might indicate that the bare model structures are the best.

However, an extrapolation of the linear behavior close to zero field would predict an avoided level crossing of the ground state and first excited state at around 6 T as shown in the appendix, Figure A.47. This leads to a deviation of the linear trend observable starting around 4 T. This characteristic behavior is not captured with the bare models, which show a linear trend across the entire simulated range. Conversely, the model with the largest crystal space and optimized H-positions (opt-otf3) shows such an avoided level crossing between 5 T and 6 T.

This model has a number of benefits:

- It includes reasonable bond distances for hydrogens and the largest crystal space.
- It agrees quantitatively well with the measured Zeeman splitting across the measurement range.
- It predicts the correct avoided level crossing.
- It shows good agreement of the diagonal ground state g-tensor elements and the correct ground state $m_J = 9/2$.

Consequently, it is chosen as the model of choice for the electronic structure of compound **(G1)**.
In conclusion, the in-depth analysis of the electronic structure of **(G1)** reveals two key lessons. Even if the energy difference is very small, second-sphere effects can significantly influence the ground state main axis direction and transversal components of the ground state. Furthermore, high-field EPR is a powerful technique to validate the results of various computational models. This way, the importance of second-sphere effects could be investigated and a model was found with which the numerical results are in exceptional agreement with experiment.

5.4. Two Dy-Complexes with a Chlorinated Pentaaza Ligand

In the following section, two similar complexes coordinated with a pentaaza-ligand "Cl-H2dapp" will be presented. Here, the synthesis, characterization and quantum chemical calculations were performed within the framework of this thesis. The X-ray Diffraction (XRD)-measurements were conducted by Dr. Olaf Fuhr and the magnetic measurements were provided by Dr. Barbora Brachňaková (KIT). The obtained data were analyzed within the scope of this current work. Within this thesis, coordination complexes have been investigated either for halogen interactions or second-sphere effects. A set of compounds with prospective halogen bonding and second-sphere effects was investigated in conjunction with magnetic properties.
The ligand used in this study is the pentadentate 2,6-bis(1-(2-(5-chloropyridin-2-yl)-hydrazineylidene)ethyl)pyridine (Cl-H_2dapp). The unchlorinated ligand has been used in the past for a number of studies with transition metals,[420–422] lanthanides[192,423–427] and actinides.[428,429] Considering its rich coordination chemistry, it was attempted to substitute the ligand with halogens to enable intermolecular halogen bonding. Furthermore, some studies have been reported utilizing the 6-chloro-hydrazinylpyrinine derivative as a ligand for transition metal complexes.[430,431] In the following, two Dy(III) complexes with the Cl-H2dapp ligand are discussed. Their general structure is shown in Figure 5.23.

5.4.1. Crystal Packing and Halogen Bonding

By reacting 5-chloro-2-hydrazinylpyridine with 2,6-diacetylpyridine and $Dy(NO_3)_3$ in acetonitrile, $[Dy(Cl-H_2dapp)(NO_3)_3]$ ·0.5MeCN **(C7)** crystallizes as yellow crystals after one day. By reacting the three components in methanol in the presence of additional sodium chloride, $[Dy(Cl\text{-}H_2dapp)(NO_3)_2(H_2O)]$ $[Dy(Cl\text{-}H_2dapp)(NO_3)_2(H_2O)_{0.5}\ (MeOH)_{0.5}](NO_3)_2$ ·4.5MeOH **(C8)** crystallizes as yellow single crystals after two weeks. The complexes and their packing are shown in Figure 5.24, the powder patterns are supplied in Figures A.48–A.49. Both compounds feature a Dy(III)-center penta-coordinated by the helically distorted pentaaza ligand. Additionally, two NO_3^- ions coordinate in a bidentate, chelating fashion above and below the ligand plane. In contrast to the complex with the unsubstituted ligand,[426] here an additional coordination site at the Dy(III)-center is occupied. This is a monodentate nitrate ion in the case of **(C7)**. Compound **(C8)** crystallizes with two distinct molecules in the unit cell where the additional ligand is either water in one molecule, or a water/methanol disorder in the other. Overall, both compounds feature an N_5O_5 coordination environment.

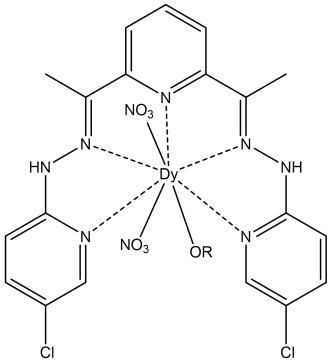

Figure 5.23.: Simplified scheme of the molecular structure of **(C7)** and **(C8)**. Here, OR can be either NO_3 or $MeOH/H_2O$ in **(C7)** and **(C8)** respectively.

More precisely, **(C7)** crystallizes in the monoclinic space group *C*2/*c* with Z = 8.

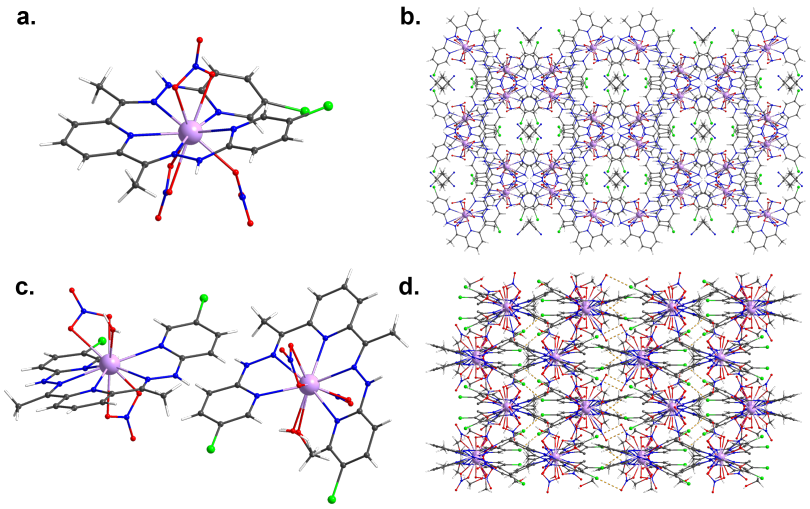

Figure 5.24.: a. Molecular structure of **(C7)**. b. Packing of **(C7)** along the crystallographic c-axis. c. Molecular structure of **(C8)**. d. Packing of **(C8)** along the crystallographic c-axis. Counter ions and lattice solvent are omitted in a. and c.

The molecular packing is dominated by rows of molecules where hydrazone hydrogens form hydrogen bonds to neighboring nitrate ions and *vice versa*. In the crystal cavities, there is one MeCN molecule in the asymmetric unit corresponding to 1/2 MeCN per complex molecule. The coordination symmetry around the Dy(III) is best described as a Sphenocorona (JSPC) from a continuous SHAPE analysis with a CSM of 2.46. Recall that this value is a similarity index with respect to a given polyhedron between 0 and 100 where 0 is a perfect match.

Compound **(C8)** also crystallizes in a monoclinic space group, but in $P2_1/c$ with Z = 8 and thus with two independent molecules in the asymmetric unit.

The first molecule, centered on Dy1, will now be referred to as m1x. Here a water molecule coordinates to the Dy(III) in addition to the two nitrate ions and the Cl-H_2dapp. The second molecule in the asymmetric unit exhibits a disorder of this additional ligand and is a disordered superposition of two molecules (this assists with the quantum chemical interpretation later). *Viz.*: one with a methanol ligand occupying the last coordination site (molecule m2x) and one with a water ligand in that position (molecule m3x). Consequently, mx1 and mx3 have the same ligand arrangement but differ in the precise coordination geometry and surrounding environment.
Throughout the crystal lattice, a hydrogen bonding network connects the molecules. This contains two nitrate counter ions for charge balance, four MeOH lattice solvent molecules and one lattice methanol only present in m3x.

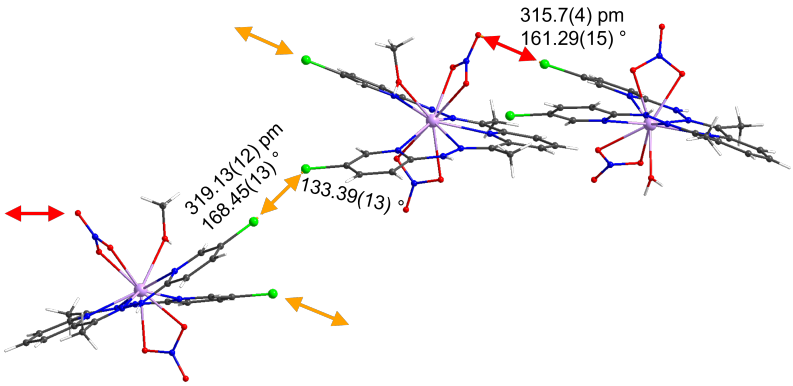

Figure 5.25.: Short intermolecular contacts in **(C8)**. Cl-Cl contacts are marked in orange, Cl-O contacts are marked in red.

Analogously to **(C7)**, the coordination environment can be best described as a Sphenocorona with CSM values of 3.65, 2.14 and 2.30 respectively. This shows that the local environments around the Dy(III)-ions are very similar in the two compounds, whereas the packings differ significantly. The shortest Cl-Cl contact observed in **(C7)** is 350.9 pm and therefore slightly longer than the sum of the van der Waals radii for two Cl atoms (350 pm).[392,432] This interaction is depicted in Figure A.50. Considering the symmetry of this interaction across a two fold rotation axis, the C-Cl-Cl angles are both 116° and consequently cannot feature a distinct σ-hole interaction. This however is not uncommon.[433]
Compound **(C8)** features a chain of XBs as visualized in Figure 5.25. A chain of Cl-Cl contacts between mx3 molecules forms a zigzag structure as indicated by orange arrows. This XB has a Cl-Cl contact significantly shorter than the sum of the van der Waals radii with 319.1 pm and a C-Cl-Cl angle of 168.5° approaching the ideal 180°. A nitrate ion on each molecule in this chain acts as the XB_A for a second halogen bond to a m1x molecule.

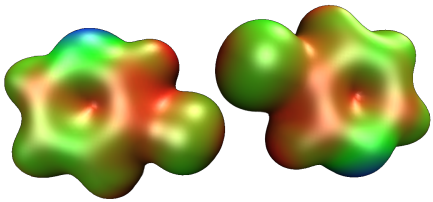

Figure 5.26.: Molecular Electrostatic Potential (MEP) for two chloro-pyridine rings as they are interacting in **(C7)**. The isodensity is 0.01, the MEP ranges from 0.15 (blue) to 0.37 (red). Calculated on a m06-2x-D4/ri/def2-TZVP level of theory.

Here, the Cl-O distance is also shorter than the sum of the van der Waals radii with 315.7 pm compared to 327 pm.[392,432] The C-Cl-O angle is 161.3°. Preliminary calculations of the interaction energy between chlorinated pyridine rings on a m06-2x-D4/def2-TZVP level of theory indicate that the observed Cl-Cl contacts are not a significantly stabilizing contribution within the crystal. For **(C7)**, this can be interpreted in terms of the MEP as shown in Figure 5.26. Here, the interaction of the two chloro-pyridine rings of **(C7)** is plotted. It is clear that, while the two p-orbital belts of the chlorine atoms are oriented towards each other, the positive σ-hole is oriented towards positively charged H-atoms. Consequently, no attractive interaction is expected. Calculation on the halogen interactions of **(C8)** are still to be performed.

5.4.2. Second-Sphere Effects and Magnetic Characterization

Given what has been discovered so far, the next step was to perform CASOCI calculations to investigate the electronic structure of **(C7)** and **(C8)**. The choice of model structure for **(C7)** is straightforward: Considering that the molecule itself is neutral, there are no counterions in the lattice and no H-bonds in close proximity to the magnetic center, only the bare molecule is investigated. This is done with and without optimization of the H-positions.

Given the disordered structure of **(C8)**, it is not immediately clear which model structure should be investigated to predict the magnetic properties. Thus, different possibilities are discussed in the following.

Considering that three distinct molecules are present in the crystal structure, all of these have to be investigated for their individual magnetic properties. Furthermore, each molecule is cationic with a protonated oxygen ligand (water/methanol) involved in hydrogen bonding interactions. As a result the full hydrogen bonding network and counterions in the lattice up to a distance of approximately 6.5 Å are considered in the calculations. In total, up to five lattice counterions are in close proximity to the metal centers resulting in a charge of -4. In a step-by-step procedure, these additional molecules are considered in the calculation, in order of the oxygen atoms proximity to the Dy(III)-center. This was done with and without H-optimization. In total, 48 model structures were investigated. The order of molecules considered in the calculations as well as the ground state magnetic main axes for the calculations with optimized H-positions for **(C8)** are displayed in Figure 5.27. ESOs, m_J compositions and the splittings of the $^6H_{15/2}$ ground multiplet are summarized in the appendix, Tables B.146–B.168.

Notably, the large negative charge leads to some occupied ligand orbitals with positive orbital energies, which is physically counterintuitive. However, the obtained active spaces feature pure f-orbitals with negative orbital energies, so the effect on the CASOCI calculation was deemed negligible.

The calculated magnetic main axes for the optimized model compared to the fully electrostatic model of MAGELLAN can be found in the appendix (Figure A.51). The main axis of **(C7)** calculated using MAGELLAN lies in the plane of the three NO_3^- anions. This was expected given that these are the only positions where negative charges were considered.

The ground state main axes of **(C7)** and m2x and m3x of **(C8)** lie between the axial NO_3^- ligands and the Cl-H_2dapp plane. This orientation does not change notably on the inclusion of larger crystal spaces.

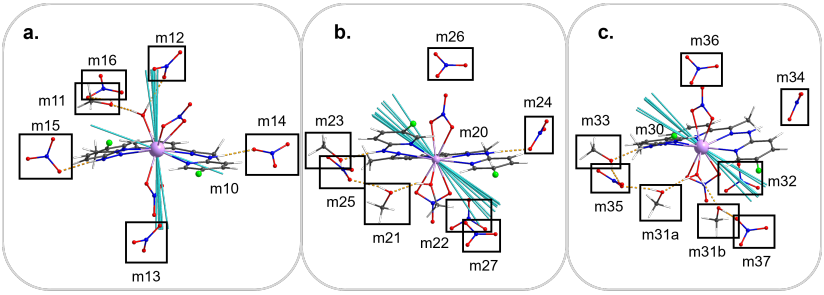

Figure 5.27.: The different models considered in the calculations as well as an overview of the different ground state main axes calculated with CASOCI for the different models. a. m1x; b. m2x; c. m3x.

The main axis calculated with CASOCI for the bare molecule of m1x in **(C8)** similarly lies in between the axial and equatorial ligands. However, it switches into an axial orientation through the water and nitrate ligands upon inclusion of larger crystal spaces. This switch indicates a weak axial crystal field similar to the situation in Figure 5.2.

Figure 5.28 depicts the crystal field splitting of the lowest $^{6}H_{15/2}$ state of Dy(III) for the different models with (black) and without (red) the preliminary optimization of H-positions. Interestingly, the optimization of H-positions lowers the energy of the first excited KD for m3x of **(C8)** by approximately 20 cm^{-1}. Conversely, the optimization has a smaller influence on **(C7)** and m2x of **(C8)** while it slightly increases the gap for models m1x of **(C8)**.

When comparing the different energies between the models, a very strong dependence on the model cluster can be reported for m1x of **(C8)** whereas the influence is more moderate for m2x and m3x.

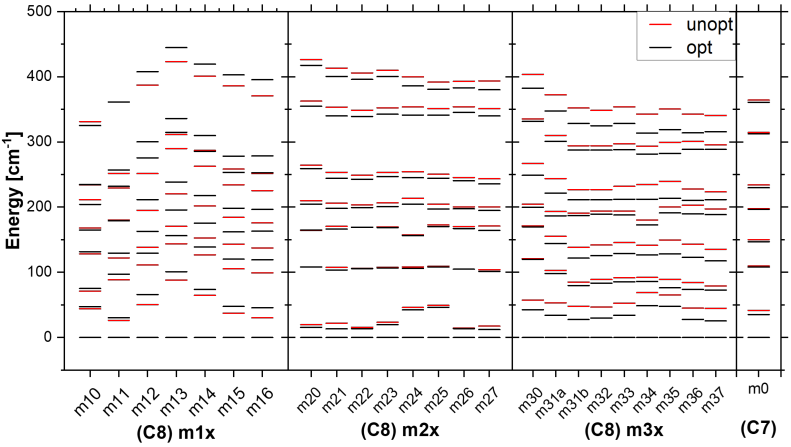

Figure 5.28.: Energy splitting of the lowest $^6H_{15/2}$ state of Dy(III) for the different models calculated for **(C7)** and **(C8)**.

In m1x, the energy of the first excited state increases by a factor of *circa* three from 30 cm^{-1} in model m11 to 100 cm^{-1} in model m13. Alongside this observation, the m_J-composition of the ground state varies significantly. The ground state of model m10 is predominantly $m_J = \pm 13/2$ (59 %) and only 23 % $m_J = \pm$ 15/2. However, upon the inclusion of additional lattice solvent and counter ions, the ground state becomes strongly anisotropic with a ground state composed of 89–96 % $m_J = \pm 15/2$.

Interestingly, the $m_J = \pm 15/2$ state is the majority contribution in all models of m2x and m3x and varies between 55 % and 70 % for m2x and between 45–70 % for m3x. This low contribution of the $m_J = \pm 15/2$ state to the ground state indicates a low anisotropy insufficient to show pronounced SMM behavior. This is in contrast to models m1x which are significantly more anisotropic and are therefore expected to show SMM behavior.

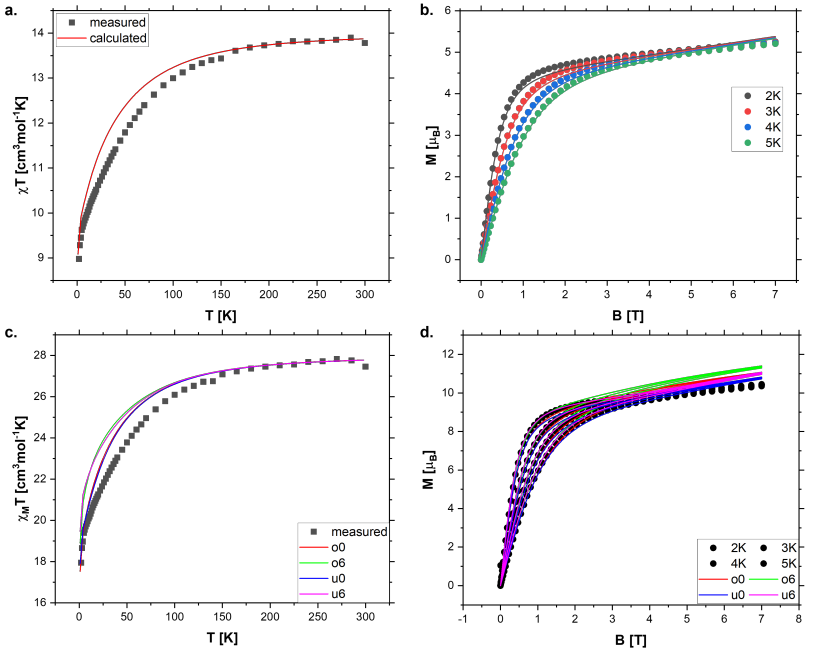

Figure 5.29.: a. χ_MT versus T measurement for **(C7)** compared with the simulated data from CASOCI. b. M versus B measurement of **(C7)** compared with simulated data from CASOCI. c. χ_MT versus T measurement for **(C8)** compared with the simulated data using four different models from CASOCI. b. M versus B measurement of **(C8)** compared with simulated data using four different models from CASOCI.

To experimentally probe the calculated data, AC- and DC-SQUID measurements were carried out on **(C7)** and **(C8)**. Firstly, the DC-results will be discussed. Figure 5.29 summarizes the molar susceptibility and isothermal magnetization curves for **(C7)** and **(C8)**. Both molecules behave very similarly.

The experimental data is slightly scaled to the calculated reference values from CASOCI for easier comparison. This can be motivated through Equation 3.1 in Section 3.1 where the susceptibility is proportional to the square of the magnetic moment and thus g. Therefore, this scaling is equivalent to fitting a g-factor close to the ideal value of 4/3 for a free Dy(III)-ion.

These measurements are then compared to the simulated data from CASOCI which is straightforward in the case of **(C7)**. Whilst the agreement of the curve is very good at high and low temperatures, this is not the case for intermediate temperatures. Interestingly, the agreement between experiment and calculation is much better when plotting the isothermal magnetization curves from 2 K to 5 K.

Modeling the magnetic response of **(C8)** is more complex taking the three different molecules into consideration. Thus a mix of the single center calculations was constructed by adding a calculation of m1x to an average of the calculations for m2x and m3x. This was achieved by matching seven models with the same overall charge for all three systems as shown in Figure 5.30. Consequently, model m10 is mixed with m20 and m30 to simulate the magnetic response of the naked molecules. Model m11 was mixed with m22 and m32, model 12 with m23 and m33 and so on. Furthermore, this was done for the optimized (ox) and unoptimized (ux) structures. The obtained data were then compared to the measured data, with simulations for the other models added in the appendix, Figures A.52 and A.53.

As seen in Figure 5.29, the agreement is remarkably similar to that for **(C7)**. For the isothermal magnetization, the agreement between the full model clusters (o6 and u6) and the experimental data is excellent at low fields. However, the calculations did not saturate at higher fields, as a result of mixing with low lying excited states.

Figure 5.30.: Scheme of which models are combined for **(C8)** to simulate the magnetic data. The prefixes "u" and "o" refer to the unoptimized and optimized structures.

The main result is that the ordered **(C7)** and the disordered **(C8)** behave very similarly. Thus, although the different parts in **(C8)** behave distinctly, the separate contribution average to a collective magnetic response. This is similar to the results in Section 5.3 where the simulation of DC-SQUID data was not very susceptible in changes caused by second-sphere effects. Whereas the simulation of DC-SQUID measurements were not influenced by second-sphere effects, the large changes in the ground state g-tensors components suggested a more pronounced influence on the dynamic properties. Thus, AC-SQUID measurements were performed to investigate this dynamic magnetic behavior. Firstly, a field optimization was conducted at 2 K revealing no out-of-phase (χ") signal for both compounds at zero field. Testing different fields up to 2500 Oe revealed an optimal field of 1000 Oe for **(C7)** with a distinct maximum at approximately 200 Hz. The same test for **(C8)** revealed an optimal field at 1250 Oe with a maximum at approximately 3 Hz. Figures A.54 and A.55 show the respective graphs, including the fit with a generalized Debye model. At these optimal fields, variable temperature AC-susceptibility measurements were performed for both compounds.

To allow for a better comparison, an additional variable temperature AC-susceptibility measurement was performed at 1250 Oe (the optimal field of **(C8)**) for **(C7)**. The data of χ' and χ'' were simultaneously fitted with a generalized Debye model with one relaxation pathway. The resulting in-phase and Cole-Cole plots are shown in the appendix, Figures A.56–A.59. The obtained relaxation times are subsequently fitted using the following equation:

$$ln(\tau) = -ln\left(\frac{A}{T} + \tau_0^{-1} exp\left(\frac{-U_{eff}}{k_B T}\right) + V_b \frac{exp(\frac{w_b}{k_B T})}{(exp(\frac{w_b}{k_B T}) - 1)^2}\right). \quad (5.7)$$

The first term accounts for a direct relaxation process, the second for an Orbach process and the last for a Raman process. The fitted relaxation times of temperatures where the maximum in the out-of-phase susceptibility is not inside the measurement window are omitted. The remaining relaxation times can be fitted with a Raman and an Orbach process. Here, an effective barrier U_{eff} of 14.7 cm^{-1} and a vibrational frequency of 3.5 cm^{-1} for the Raman process can be extracted.

Figure 5.31 shows the out of phase susceptibility and Arrhenius plots for **(C7)** and **(C8)** under 1250 Oe applied field. Clearly, **(C8)** relaxes significantly slower. Again, the relaxation times of **(C7)** can be fitted only using a Raman and Orbach process where U_{eff} = 10.5 cm^{-1} and w_b = 2.6 cm^{-1}. In contrast, a direct process as well as Orbach and Raman processes are necessary to fit the relaxation of **(C8)**. Here, an effective barrier of 35.3 cm^{-1}, w_b = 16.4 cm^{-1} and A = 8.3 can be extracted.

Notably, it is also possible to fit the data with two Raman processes and one Orbach process without a direct process as shown in Figure A.60.

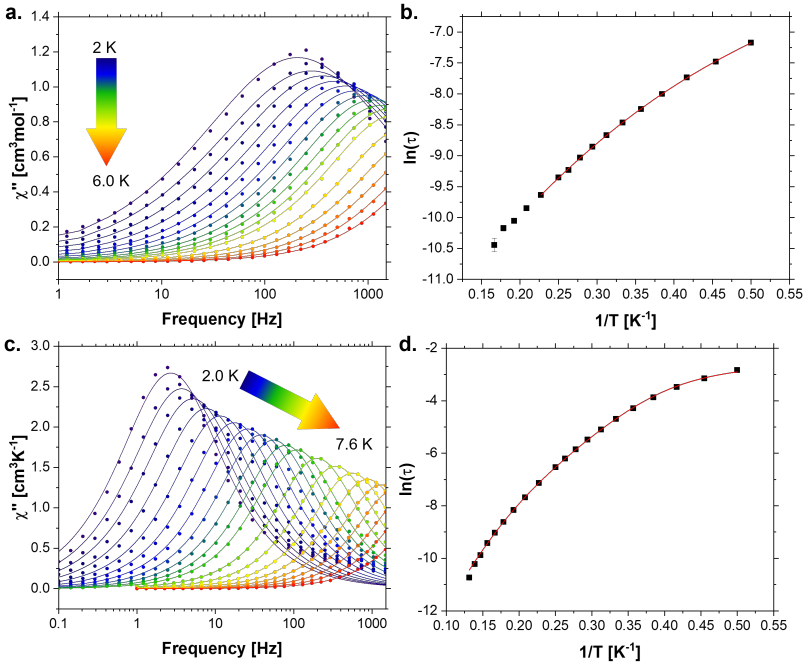

Figure 5.31.: a. Out of phase contribution of the variable temperature susceptibility measurement of **(C7)** at a fixed field of 1250 Oe fitted with a generalize Debye model. b. Arrhenius plot of the obtained relaxation times using Equation 5.7, without a direct process. c. Out of phase contribution of the variable temperature susceptibility measurement of **(C8)** at a fixed field of 1250 Oe fitted with a generalize Debye model. d. Arrhenius plot of the obtained relaxation times using Equation 5.7.

Here, U_{eff} increases to 45.5 cm^{-1}, and the two Raman frequencies are w_b = 4.1 cm^{-1} and w_b = 19.5 cm^{-1}. The latter process is significantly more active than the first Raman process at the lower frequency.

Considering the ambiguity of the obtained fits, it is not clear if one of the Orbach processes fitted can be attributed to a relaxation over the first excited KD. For **(C7)**, it appears that the relaxation is an under barrier process considering that the first excited KD is significantly above U_{eff}.
One possibility is that the cumalative negative charge by taking more anions into account in the calculation for **(C8)** could lead to errors. If one neglects the last two additional anions, the energy of the first excited KD of m2x and m3x fits well with the observed U_{eff}.
If m1x relaxes significantly more slowly than m2x and m3x under the 1250 Oe applied field, this suggests that the resulting dynamics are dominated by m2x and m3x. In case of m2x and m3x dominating the relaxation dynamics, it should be kept in mind that the ground state anisotropy between m2x/m3x and **(C7)** is very similar and consequently should also behave similarly. In this case, it is possible that the slower relaxation of **(C8)** compared to **(C7)** can be attributed to the intermolecular hydrogen and/or halogen bonding.
However, considering the low anisotropy of m2x and m3x, it is possible that these centers relax so fast that the only measurable response is from mx1. In this case the difference between **(C7)** and **(C8)** could be directly attributed to increased anisotropy of center m1x through the different coordination and second-sphere effects.
Overall, it is not possible to determine which molecule(s) are responsible for the slow relaxation of magnetization in compound **(C8)**.

5.5. Influence of Halogen Bonding on Toroidal Magnetic Moments

In the following sections, three halogen substituted Dy_3-triangles were investigated (Figure 5.32). Here, the topics of all three main chapters are relevant. Firstly, the intermolecular halogen bonding was investigated in order to rationalize the crystal packing. Then, second-sphere effects are shown to play a significant role on the direction of the g_z-magnetic axis. Next, the exchange interaction between the Dy(III)-centers was approximated using BS-DFT. Finally, the influence of these second-sphere effects on the toroidal magnetic ground state of the compounds under study was demonstrated.

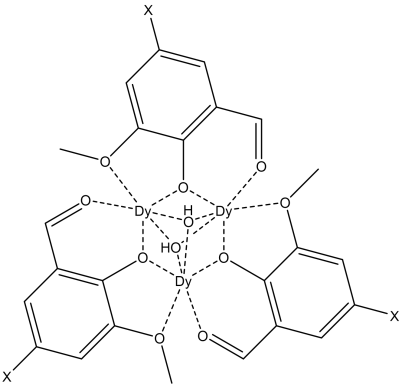

Figure 5.32.: Scheme of the core of compounds **(X3)**, **(X4)** and **(X5)**. In addition, each Dy-ion is coordinated to two terminal ligands which are either MeOH, H_2O or Cl^-, not shown here. X = Cl, Br, I.

The three halogen substituted Dy_3-triangles are bridged via two μ_3-hydroxide ions in the center and three 5-halo-*o*-vanillin ligands. Furthermore, each Dy(III)-center is coordinated by two terminal ligands above and below the plane which are either MeOH, H_2O or Cl^-. The halogen shown as X in Figure 5.32 is Cl for **(X3)**, Br for **(X4)** and I for **(X5)**. These halogen atoms are involved in the halogen bonding.

Terminal ligands in all compounds are disordered and involved in hydrogen bonding which, as established earlier in this chapter, could make second-sphere effects relevant. The compounds were synthesized by Dr. Yannik Schneider.[434] The analysis of the halogen bonds and calculations of the magnetic properties were performed in the context of the present study.

5.5.1. Halogen Bonding and Crystal Packing

Compounds **(X3)**–**(X5)** crystallize in the space groups $P2_1/c$, $R\bar{3}$ and C_c respectively. In the following, a rationalization of these differences will be provided based on an increased stabilization through halogen bonding. Each XB in these networks is between a ligand halogen atom and a terminal chloride ligand at a neighboring molecule. This is visualized in Figure 5.33 for **(X4)** and in Figures A.61–A.62 for **(X3)** and **(X5)**.

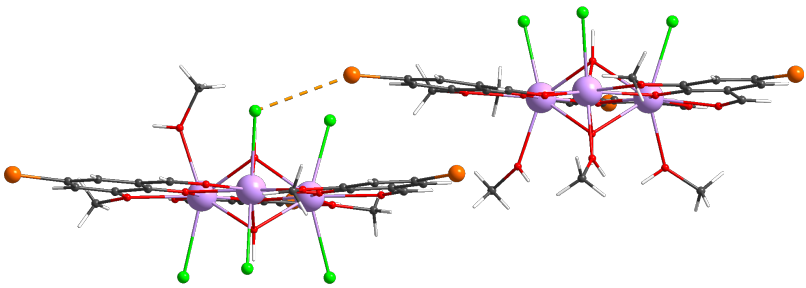

Figure 5.33.: Halogen interaction between adjacent molecules in **(X4)**. The ligand-halogen atom acts as the XB_D for a terminal ligand atom of the neighboring molecule. Notably, the second top chloride on the left molecule is involved in an equivalent interaction omitted for clarity.

Table 5.3.: X-Cl distances and obtuse angles characterizing the XBs in **(X3)**–**(X5)**. Compound **(X4)** features two identical XBs per molecule, while **(X5)** features three distinct XBs (see Figures 5.33, A.61, A.62). The sum of the van der Waals radii (v.d.W.r.) for Cl-Cl, Cl-Br and Cl-I are given for reference.

	(X3)	**(X4)**	**(X5)'**	**(X5)"**	**(X5)"'**
X-Cl dist [pm]	339.1(4)	339.8(6)	337.8(5)	342.4(7)	349.5(4)
C-X-Cl angle [°]	172.7(4)	154.4(3)	165.8(4)	162.8(4)	173.1(5)
v.d.W.r.[432] [pm]	350	358	373	373	373

Considering the geometric properties, halogen-halogen distances and the obtuse angles of the investigated interactions are shown in Table 5.3. All five investigated contacts are shorter than the sum of the van der Waals radii with angles above 150°. This renders them likely candidates for halogen bonds. As discussed in Section 4.2.1, the acute angle in a XB does not need to constitute 90° when it is a chloride coordinated to a metal center and is thus not discussed in the following. Importantly, due to a disorder over the $\bar{3}$ axis, **(X4)** exhibits two identical XBs.

To validate that the observed contacts constitute halogen bonds and extend the discussion of the model structures in Section 4.3.1 a series of DFT calculations was performed. Here, five model structures were prepared for each contact by extracting the respective coordinated from the cif files. The structures are schematically shown in Figure 5.34a. The five combinations investigated are denoted as Y-Z and subsequently called Na-H, Na-Na, ECP-ECP, ECP-H and X-H. ECP refers to the 10-electron ECP for Na published by Fuentealba *et al.*[435] In these calculations, the respective Na(I)-cation is only described with an ECP and no basis set. For all other atoms, the def2-QZVP basis set was employed.

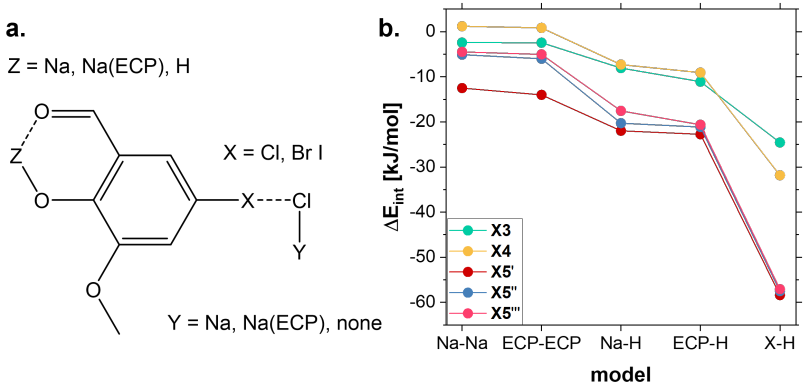

Figure 5.34.: a. Scheme of the model structures calculated to investigate the halogen bonds in **(X3)**–**(X5)**. X is the respective halogen in the compound, Y is replaced to either Na, a Na-ECP or omitted. Z (Dy(III)) is replaced to either Na, a Na-ECP or H. b. The five interaction energies for the five models were calculated using the m06-2x functional.

The in Section 4.1 established DFT-functionals m06-2x, pbe0 and cam-b3lyp were used for the subsequent calculations. The resulting interaction energies are summarized in Figure 5.34b for the m06-2x functional and in the appendix, Table B.169. Across the three functionals, a few key points can be noted:

1. The metal center could be replaced with a simple ECP without a noteworthy change in the interaction energy. This is important for future investigations where lanthanides can be treated as large-core ECPs.

2. The interaction energy increased in absolute terms when a protonated ligand was used instead of the sodium ion. In the case of **(X4)**, the interaction energy calculated with two Na(I)-cations is smaller than 1 kJ/mol which increases to around -10 kJ/mol when the protonated ligand was used as a model.

This effect will be subsequently investigated in more detail using EDA.

3. When a free chloride ion is used as the XB_A, the interaction energy increased significantly more, up to around 60 kJ/mol for interactions in **(X5)**.

4. The interaction energies for the Cl-Cl **(X4)** and Br-Cl **(X5)** bonds are very similar, whereas the interaction energy of the three I-Cl **(X5)** contacts is always greater than for the Cl-Cl and Br-Cl contacts. Comparing **(X3)** and **(X5)**, it becomes apparent that the loss in interaction energy due to the less obtuse angle can be balanced out due to the shorter bond distance with respect to the sum of the van der Waals radii.

These results indicate that indeed a significant interaction energy between the contacts can be reported across the observed contacts. In the following, it was attempted to rationalize the differences in interaction energies across the five contacts. Thus, an EDA of the interaction energy using the pbe0 functional was carried out. Exemplary data is shown in Figure 5.36, a full list is shown in Table B.170. Interestingly, the X-H model differs from all other models considering significantly increased orbital relaxation, electrostatic and exchange-repulsion contributions. This indicates that the metal ion needs to be considered in the model structure as was previously discussed in Section 4.3.1. Apart from X-H, all other models exhibit similar energy contributions for dispersion, correlation, orbital relaxation and exchange-repulsion. The only noteworthy difference can be reported for electrostatic contributions which can be directly correlated with the total interaction energy. This reiterates earlier findings where the interaction energy was extremely sensitive to countercharges on the other side of extended π-systems.

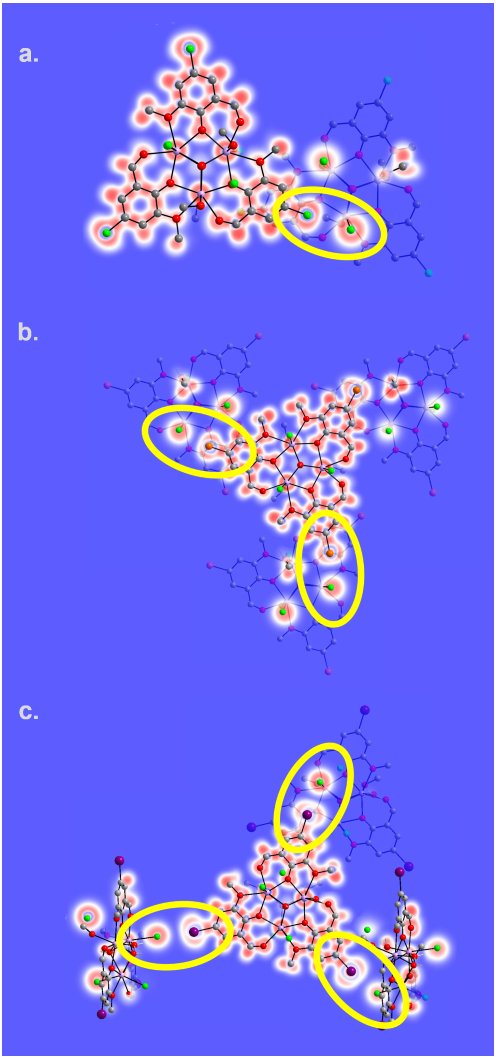

Figure 5.35.: Electron Localization Function (ELF) highlighting the XBs in compounds a. **(X3)**, b. **(X4)**, c. **(X5)**. Yellow circles highlight the respective interacting areas. All pictures were modified for better visualization and should not be interpreted quantitatively. Picture adapted from Ref. [434].

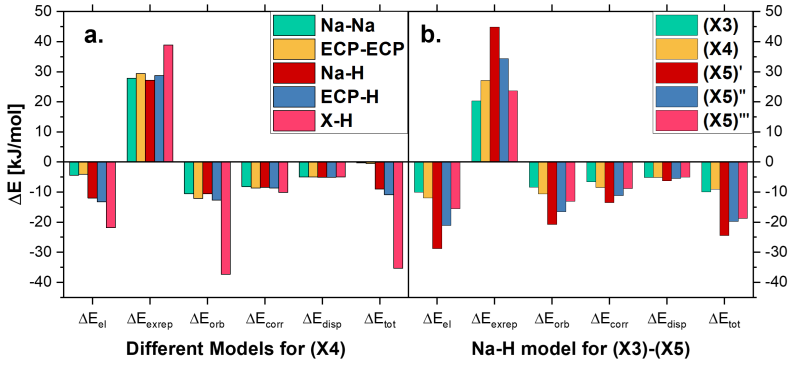

Figure 5.36.: a. Energy Decomposition Analysis (EDA) of the XB in **(X4)** for the five different models. b. EDA of all interactions in **(X3)**-**(X5)** using the Na-H model structure.

The differences between the three I-Cl contacts in **(X5)** can be rationalized by considering that the different energy contributions have a very unique distance dependence.[362] Whilst all energy contributions become smaller in magnitude going from **(X5)**' to **(X5)**''', the relative decrease of the different contributions can then be attributed to the relative change in interaction energy. Dispersion is the most long-ranging energy contribution here which hardly changes between the three bonds.

The ELF plotted in Figure 5.35 for all contacts highlights the presences of pronounced σ-hole interactions for all investigated contacts. Thus, in conjunction with the preceding analysis the contacts can be unambiguously classified as halogen bonds.

Importantly, regardless of the model used, the total interaction energy in the crystal lattice attributed to halogen bonding increases going from Cl to Br to I.

Whilst one Cl-Cl bond is present in **(X3)**, two Br-Cl bonds of similar strength stabilize the lattice in **(X4)**. Three stronger I-Cl bonds are then acting simultaneously in **(X5)**. This is in correlation with the crystallization of the three compounds.

5.5.2. Second-Sphere Effects on the Anisotropy

Based on the insights gained so far within Chapter 5, compounds **(X3)**–**(X5)** were expected to show significant second-sphere effects on the anisotropy: In these complexes, MeOH and water ligands are disordered and coordinated to the metal centers. The implications of second-sphere effects are elucidated in Section 5.5.4.

As shown in previous sections, the influence of precisely calculated hydrogen positions, the disorder and molecules in the second coordination sphere were investigated using a series of model structures. Hydrogen positions were optimized in a step-by-step procedure. First, the unoptimized structure was calculated. Second, the position of hydrogen atoms which are not directly bonded to coordinating atoms were optimized. Third, all H-positions were optimized. The respective structures are given as "unopt", "opt" and "full". Furthermore, the deformed Br-C angles in **(X4)** were optimized (bropt). In the case of **(X5)**, the hydrogen positions at the hydroxide groups were optimized in a separate step (hopt) because they are not involved in hydrogen bonding. Structures with and without the second coordination sphere are labeled as "cl" and "core" respectively.

For **(X3)** and **(X5)**, "part 1" and "part 2" are the respective majority and minority contributions of the disorder.

Compound **(X4)** crystallizes as ion pairs connected via three hydrogen bonds between three MeOH-ligands of the cationic molecule with three Cl^--ligands of the anionic molecule. On the other side of the anionic molecule, two Cl^- and one MeOH ligands are disordered over the three positions. However, since all three possible combinations are symmetry equivalent and therefore ambiguous only one structure is investigated referred to as "part 1".

As apparent from Figure 5.32, the three *o*-vanillin ligands coordinate either clockwise or counterclockwise. These two orientations are disordered in the cationic molecule in **(X4)**, which will be denoted as "part 2" and "part 3". Importantly, these molecules are the only C_3-symmetric and therefore only calculations on a single center had to be performed. Pictures of all structures indicating the different disorders are provided in the appendix, Figures A.63–A.65.

For example, the model "unoptcore part 1" would indicate that for the majority disorder (part 1), the structure was directly extracted from the cif (unopt) and possible second-sphere ions neglected (core). "Part 2 optcl" would indicate that for part 2 (either minority disorder or cationic molecule in **(X4)**) only the ligand backbone hydrogens were optimized while the hydrogens bonded of water/methanol ligands are frozen.[4]

After the optimization, CASOCI calculations were performed according to the procedure in Section 7.2. For the three molecules, 48 model structures were investigated, most of which contain three non-equivalent Dy(III)-centers. Given the number of calculations is far to large to investigate each one individually, those with the most outstanding characteristics were chosen for further investigation. The results for the cationic molecule in **(X4)** (part 2) will be discussed first and the conclusions transferred to other structures.

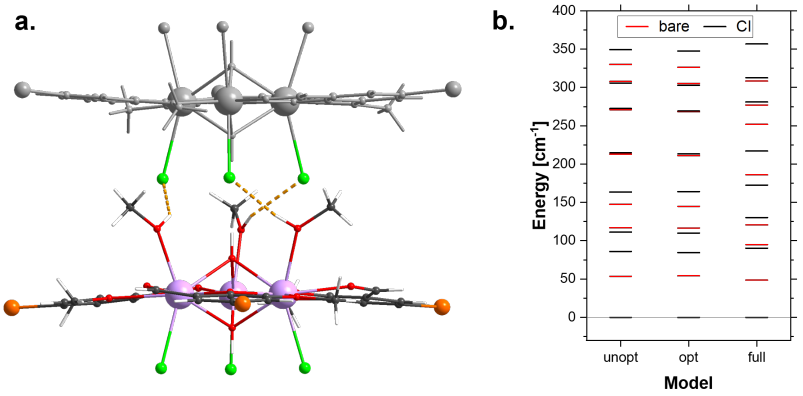

Figure 5.37.: a. Picture of **(X4)** showing the interaction of the cationic molecule with the anionic molecule (the disorder is omitted for clarity). Highlighted is the cationic molecule and the Cl^--ligands of the molecule above. b. Energy splitting for the six model structures investigated. Including (Cl) and excluding (bare) the additional Cl^--ions as well as unoptimized (unopt), distant (opt) and all H-positions optimized (full).

The ZFS, g-tensor, m_J-composition and ESOs of all calculations are provided in the appendix, Tables B.171–B.232.

Figure 5.37 shows the investigated model structure of **(X4)** part 2, as well as the ZFS of the six associated models, which are the three stages of H-optimization (unopt, opt, full) as well as the bare molecule (core) and the model including counterions (cl). It is found that the energy splitting to the first excited KD is higher when the additional Cl^--ions are considered. Furthermore, as expected from earlier sections, an optimization of H-positions not directly bonded to coordinating ions does not have any notable effect on the splitting. The influence of the hydrogen optimization is small in comparison to the second-sphere effects and thus not further discussed.

Most interesting is the change between the models including and excluding the additional counterions. Structurally, one might argue that the effective charge of the additional Cl^--anions should be lowered because these are coordinated to strongly charged Dy(III)-cations. Thus, a possibly reduced effective charge of the Cl^--ions was investigated. In a simple approximation the Cl^--ions are replaced by point charges which are scaled in 0.1 steps from 0 to -1.

At each point, a CASOCI calculation is carried out and the magnetic main axis and m_J-composition are calculated. For a better comparison, the m_J-composition is calculated in the magnetic reference frame of the model where the full Cl^--ions are considered.

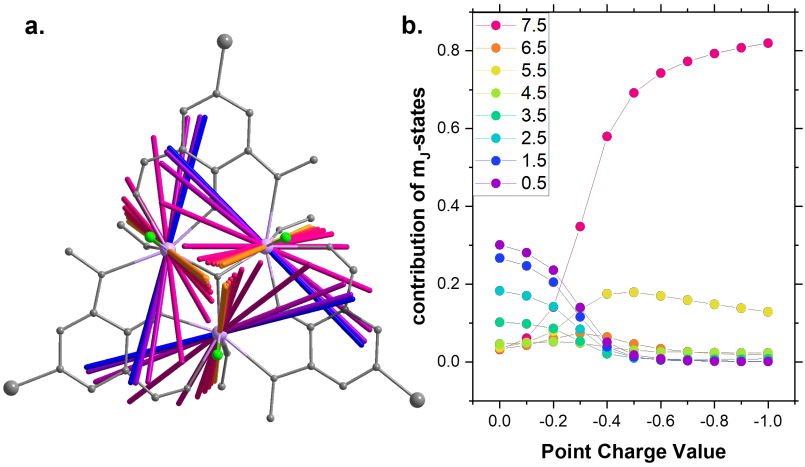

Figure 5.38.: a. Magnetic main axes highlighting the change from no Cl^- ions considered (blue) to full Cl^- ions considered (orange) with intermediate steps calculated in steps of 0.1 as point charges. b. m_J-composition of the calculations slowly including the Cl^- ions in the reference frame calculated for the full ions ground state KD.

The results are shown in Figure 5.38.
When the full Cl^- ions are considered, the ground state main axes point out of the Dy_3-plane (orange). On decreasing the value of the point charges, the main axes first slowly, then rapidly change from this perpendicular position into the Dy_3-plane (blue). Whilst the angle of the main axis to the plane is 70.0° including the full Cl^--ions, it is only 6.6° for the core model. A similar picture is obtained for the m_J-composition. Here, the ground state including the counterions is approximately 80 % $m_J = \pm 15/2$ and 20 % $m_J = \pm 11/2$.
In order to compare these values, the J_z-operator was diagonalized in the magnetic reference frame of the fullcl model for all steps. This revealed that the m_J-contributions of the $\pm 15/2$ state slowly decreases before abruptly approaching zero at point charges between -0.2 and -0.4. At the same time, most other m_J-contributions become more relevant here. Both such observations indicate that the axial crystal field becomes less dominant when the point charges are reduced and the axiality of the ligand field switches at around -0.3 into the Dy_3-plane. Here, one could imagine the m_J-contributions as indicators of the ligand field direction, similar to ESOs. However, the key point is that ground state compositions at either extreme of the crystal field with or without Cl^--ions are mutually exclusive. At the highest field, only $m_J = \pm 15/2$ and $\pm 11/2$ are relevant within this reference frame whereas all other m_J-states contribute to the low field case. Notably, the first excited state in the low field case (core) is predominantly a mixture of $m_J = \pm 15/2$ and $\pm 11/2$ with smaller contributions of the other states.
Figure 5.39 follows this change in the energy domain. Clearly, the relative energy of the first excited KD is at a minimum at around -0.3. However, this energy does not approach 0 cm^{-1}, but minimizes at circa 21 cm^{-1}.

This behavior indicates that this is an avoided level crossing because the lowest two states effectively interchange through mixing strongly in an intermediate regime. Thus, one could conjecture Figure 5.39 as an effective Tanabe-Sugano diagram.[436]

A second avoided level crossing can be suspected at around -0.8 because the energies of the first and second excited states first approach each other before diverging again at higher fields.

It should be mentioned at this point that the switching of the magnetic main axis from in-plane to the perpendicular direction is reproduced when using the simple MAGELLAN electrostatic model[259] and is shown in the appendix in Figure A.66.

The agreement with the MAGELLAN program indicates already that the electrostatic interaction between the Cl^--ions and the Dy(III)-centers is a key in understanding why second-sphere interactions can have such pronounced effects.

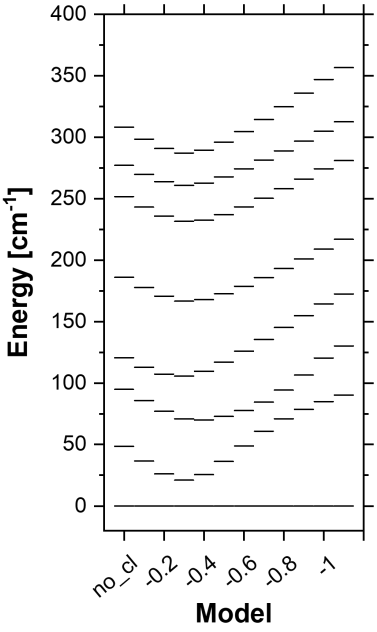

Figure 5.39.: Energy splitting of model **(X4)** part 2, when the addition Cl^- charge is scaled from 0 to -1.

This raises the question if the direct influence of the Cl^--ion can be separated from the indirect influence through ligand polarization.

At this point it is important to recapitulate the workflow to perform a CASOCI calculation as discussed in more detail in Section 7.2. First, the f-orbitals are optimized and localized in a ROHF calculation. Then all integrals needed to perform the CASOCI calculation are written to the hard drive. Finally, the CASOCI calculation is performed. If countercharges are considered in the orbital optimization, these will be polarized by the countercharge. However, it is possible to optimize the orbitals without the countercharge and only add it before calculating the necessary integrals. This way, the electrostatic potential of the point charge is considered in the CASOCI calculation, but the polarization is not.

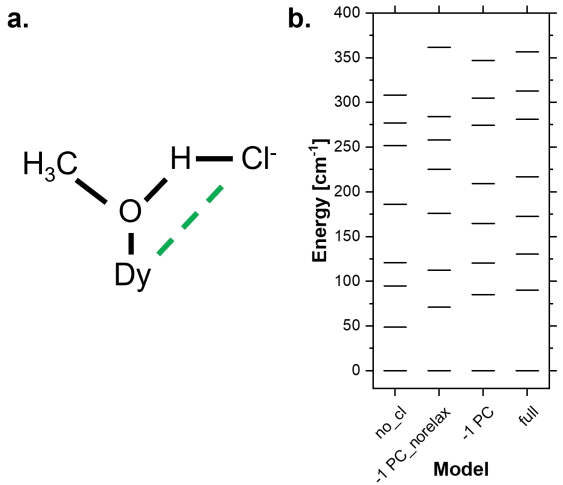

Figure 5.40.: a. Scheme of the bridge between Cl^- and Dy(III). The green line indicates a possible direct, electrostatic interaction between the Cl^- and Dy(III). b. Energy splitting fully including/excluding the Cl^- ions, treating it as a -1 point charge and just adding the point charges potential, but not relaxing the wavefunction.

Through such a workflow, a chloride ion can be included step-by-step in the calculation as shown in Figure 5.40b. Starting at the core model, the point charge potential without orbital relaxation changes the energy splitting significantly. Letting the orbitals relax when including the point charges further increases the energy difference between the ground state and first excited KD. Finally, a small increase of the ZFS can be seen when the full Cl^--anion is considered.

This analysis highlights that electrostatics and polarization act simultaneously to facilitate second-sphere effects which was shown by reconstructing the chloride anion in three simple steps.

This analysis was made straightforward by the fact that there was only one crystallographically distinct Dy(III)-ion in the model structure. Whereas this is also the case for **(X4)** part 3, the Dy(III)-ions within all other models do not share the same coordination environment. However, similar effects in the splitting can be observed from the respective tables in the appendix.

A notable difference between the models including and excluding second-sphere molecules was also found, for example, for **(X3)** part 1. Thus, a similar simulation was performed where the additional chloride ions replaced by point charges are again scaled from 0 to -1 as shown in Figure 5.41. Again, a dependence of the countercharges on the ZFS is observed. Here, no avoided level crossing can be observed. However, the three additional MeOH molecules were not considered in this simulation because the point charges cannot be unambiguously assigned. The fact that the point charge test does not converge to the result of the structure including all second-sphere molecules (green) clearly highlights the importance of neutral lattice solvent involved in hydrogen bonding.

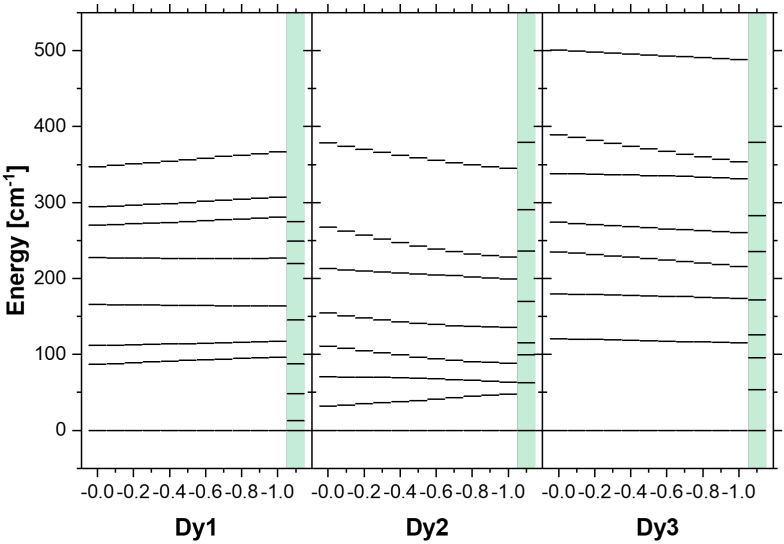

Figure 5.41.: ZFS for **(X3)** part 1 when the bare molecule is considered in the calculation and the additional Cl^- ions are scaled from 0 to -1 as point charges. The green background indicates a calculation including the counter ions and lattice solvent, leading to a significant change from the point charge model.

5.5.3. Broken-Symmetry Calculations

In the next section, the magnetic coupling between the Dy(III)-ions was investigated. Considering that anisotropic, magnetic ions interact via exchange and dipolar interactions, BS-DFT calculations were carried out to obtain coupling constants for the exchange interaction. These calculations were performed using the fully optimized structures and including all counterions. Here, the x2c-QZVPall basis set was used for all metal centers, while the def2-TZVP basis set was used for the ligand atoms. A def2-SVP basis was used for H-atoms and an x2c-TZVPall basis set for iodine. Scalar relativistic effects were considered on an X2C level of theory. The four functionals bh-lyp, pbe0, cam-b3lyp and ωb97-x suggested in Section 3.3.2 and the b3-lyp functional were compared. All obtained coupling constants are summarized in the appendix, Table B.233.

The results of all calculations are summarized in Figure 5.42 and in the appendix. When comparing data points of the same color (same functional, different models), it becomes apparent that the disorder does not influence the coupling between any two centers significantly. However, there are a few exceptions, e.g. the interaction between centers 2 and 3 in **(X3)**. Furthermore, it should be noted that parts 2 and 3 in **(X4)** are C_3-symmetric and the result of one calculation has been duplicated for the other pair interactions.

More important, is the range of values obtained for the same interaction with different models. As expected, functionals with less exact exchange (b3-lyp and pbe0) give the lowest, most antiferromagnetic values. The functional with the most exact exchange (bh-lyp) gives the most positive, yet still antiferromagnetic coupling constants.

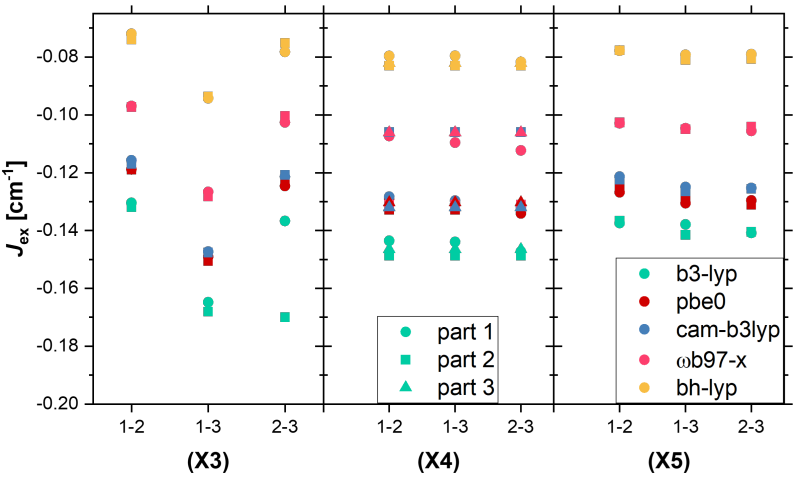

Figure 5.42.: BS-DFT exchange coupling constants J_{ex} calculated for **(X3)**–**(X5)** using the fully optimized model structures and the largest model structure. The legends refer to all structures. Shown are the constants calculated for part 1 (circle), part 2 (square) and part 3 (triangle, only **(X4)**). Five functionals were tested. Values are given for two interacting S = 7/2 spins.

The difference between pbe0 and bh-lyp is between 0.045 cm^{-1} and 0.056 cm^{-1}, and therefore slightly larger as would be expected from the sum of the MAEs computed in Section 3.3.2. Whilst the interaction is always antiferromagnetic, this approximate error is too large for a further analysis.

5.5.4. Dipolar Interaction and Toroidal Magnetic Moments

To understand this next section, a very brief introduction into Single Molecule Toroics (SMTs) needs to be provided. When three antiferromagnetically coupled, isotropic spins 1/2 are placed in a triangular configuration, the ground state will be sixfold degenerate (3 KDs) as shown in Figure 5.43. This is called "spin frustration" and has been reported for example in Fe_3-triangles over the past 30 years.[437–443]

In comparison, when sufficient magnetic anisotropy is present and the magnetic main axes are oriented in the triangle plane, the same coupling leads to a twofold degenerate state where the spins are arranged head to tail in an either clockwise or counterclockwise orientation. The first characterization of a toroidal magnetic moment in a Dy_3-cluster was published in 2006 by the Powell group and characterized by subsequent calculations and measurements.[10,198,444]

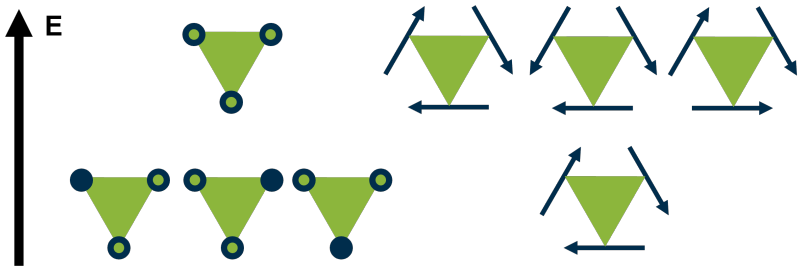

Figure 5.43.: When three, antiferromagnetically coupled Ising type spins are placed in triangle, the ground state will be six fold degenerate (3 KDs) and "spin frustrated". When anisotropic spins are arranged in the plane around a triangle, the ground state will be an isolated KD in a head to tail configuration called toroidal.

Such orientations could be observed for many other compounds such as Dy-clusters of different sizes[445–452] as well as for mixed 3d-4f-clusters.[453–458] The vortex like arrangement of spins in the ground state leads to a toroidal moment defined as[199,459]

$$\vec{T} = \sum_i \vec{r}_i \times \vec{\mu}_i. \tag{5.8}$$

The cross product of all magnetic moments $\vec{\mu}_i$ of spin centers *i* with their position vectors $\vec{r}_i$ give rise to a moment vector perpendicular to the triangle. This explains why the direction of the magnetic moment which is the direction of the magnetic main axis is so important. Thus, as discussed in Section 5.5.2, second-sphere effects become relevant.

Toroidal and spin frustrated systems can be investigated with μ-SQUID measurements as shown in the case of **(X3)**–**(X5)** and presented in Figure 5.44. For a perfectly toroidal moment system, the ground state is non-magnetic and thus a plateau of the magnetization at zero field should be visible. This however is not the case for the compounds discussed here. Several reasons can explain this behavior. When the spins are not perfectly in-plane, a small residual magnetic moment may arise out-of-plane. Considering that these plots show the magnetization of a crystal along a certain direction which cannot be unambiguously assigned as the crystals used for μ-SQUID cannot be indexed. Furthermore, there is more than one orientation of the molecule in the crystal structures of **(X3)** and **(X5)**. Thus, it is possible that the step at zero field is attributed to an almost toroidal moment.

Based on the μ-SQUID data, it is also possible that the ground state is not a vortex like arrangement. The following discussion is aimed to gain an understanding about the low energy electronic structure which could be used to interpret the experimental μ-SQUID data.

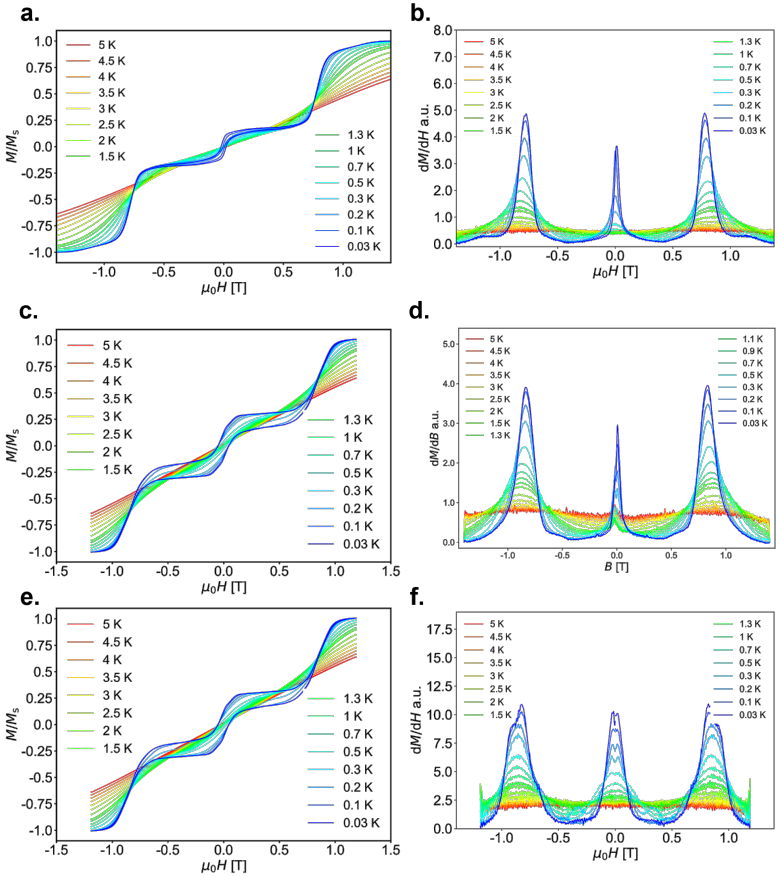

Figure 5.44.: μ-SQUID magnetization measurements at a sweep rate of 8 mT/s for compounds a. **(X3)** c. **(X4)** e. **(X5)** and their derivatives. Courtesy of Dr. Sagar Paul (AG Wernsdorfer) and previously published in Ref. [434].

In the following, the ground state KDs as obtained from the CASOCI calculation performed in Section 5.5.2 are assumed to act as pseudospins $\tilde{S}$ = 1/2. To find the lowest energy state coupled through dipolar coupling for a given triangle, a Spin Hamiltonian is used to calculate the dipolar energy:

$$\hat{H}_{dip} = \sum_{i<j} -\frac{\mu_0|\mu_i||\mu_j|}{4\pi|R_{ij}|^3}(3(\vec{\mu}_i \cdot \vec{R}_{ij})(\vec{\mu}_j \cdot \vec{R}_{ij}) - (\vec{\mu}_i \cdot \vec{\mu}_j)). \tag{5.9}$$

In this equation, the sum goes over all combination of centers i and j, where $\mu_{i/j}$ is the magnetic moment and R_{ij} is the distance between the respective centers. The direction of $\vec{\mu}_i$, and therefore the vector products are highly dependent on the second-sphere effects. All vector quantities are normalized. The dipolar coupling constants for the pair interactions are shown in the appendix, Table B.234.

The wavefunction is assumed as a normal product wavefunction of three $\tilde{S}$= 1/2 spins with quantum numbers $m_S = \pm 1/2$. Consequently, the energies of wavefunctions, where the direction of all spins are reversed, are degenerate.

$$\hat{H}_{dip}\,|1/2, 1/2, 1/2\rangle = \hat{H}_{dip}\,|-1/2, -1/2, -1/2\rangle \tag{5.10}$$

For a toroidal state these refer to clockwise and counterclockwise orientations of the toroidal moment. The resulting relative energies of the lowest four KDs and the toroidal moment of all models are visualized in Figure 5.45 and provided in the appendix, Table B.235. Furthermore, the angle of all ground state anisotropy axes with respect to the Dy_3-plane are given in the appendix, Table B.236. The splitting of the lowest four KDs in all models is less then 4 cm^{-1}. This is significantly lower than the first excited KDs in the different single center calculations. These means that the lowest exchange multiplet is well separated.

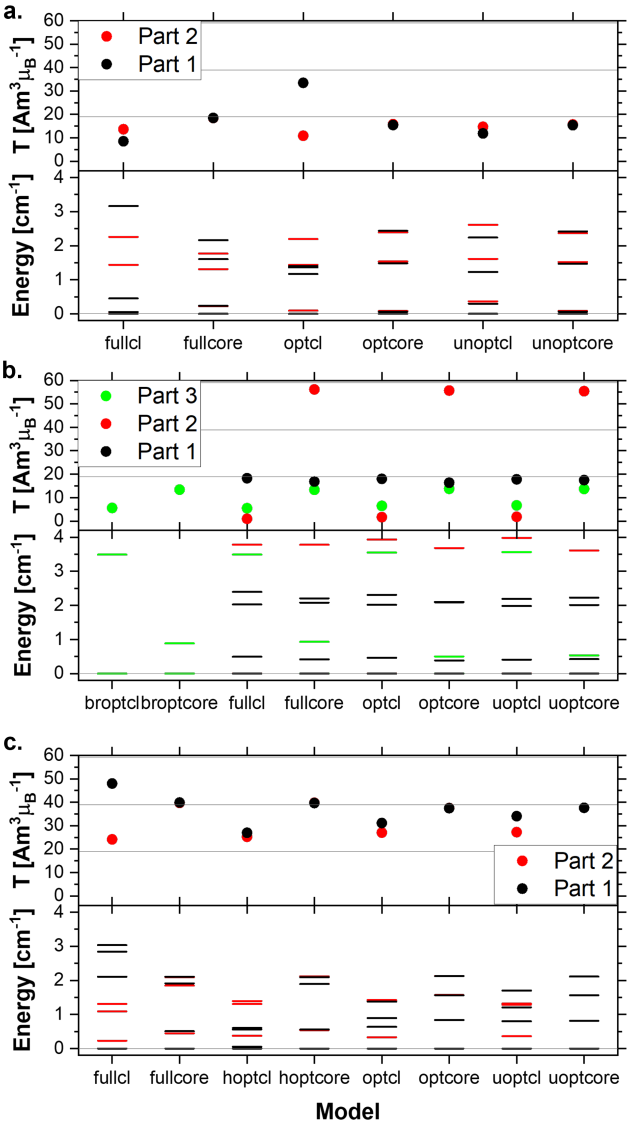

Figure 5.45.: Overview of the splitting of the lowest exchange multiplets as well as the toroidal moment of the lowest KD across the 48 models (x-axis) calculated for compounds a. **(X3)** b. **(X4)** c. **(X5)**.

As apparent from Figure 5.45, there are many qualitatively different splittings observable. In the case of a spin frustrated or toroidal ground state, there are only two distinct energy levels (Figure 5.43). This can be seen e.g. for the model "broptcl" in **(X4)**, which is a model where the additional anions are taken into account and the distorted Br-position was optimized in addition to the hydrogen atoms. Here, the ground state is sixfold degenerate, while the excited state is a single KD with a relative energy of 3.5 cm^{-1}. This is clearly a spin frustrated state as also apparent from the calculated small toroidal moment. In contrast, the previously discussed model "fullcore" in part 2 of **(X4)** has a twofold degenerate ground state and a sixfold degenerate excited state with a splitting of 3.8 cm^{-1} and a significant high toroidal moment.
A third possible spin arrangement can also be envisaged for the calculations presented here. This occurs when two Dy(III)-centers are strongly coupled (ferro- or antiferromagnetically) whereas the third Dy(III)-ion is weakly coupled to the two centers. Here, the four KDs are first split by the large coupling constant before being split by the small.

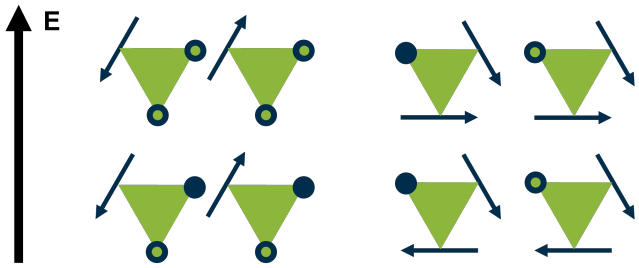

Figure 5.46.: When only two centers are strongly coupled and either in-plane or out-of-plane while the third couples weakly with the latter two, the ground and excited states are two (quasi-) degenerate KDs.

This can be compared to a "doublet of doublets" in Nuclear Magnetic Resonance Spectroscopy (NMR) spectra. Figure 5.46 shows such an arrangement.

An example for this splitting pattern can be reported for example for model "fullcl" in part 1 of **(X4)**. Here, the lowest eight states are split into two quartets which in turn are split into two distinct KDs each.

The key property of interest here was the toroidal magnetic moment, as calculated with Equation 5.8. However, the interpretation of this equation can be problematic: In principle, if any spin is not perfectly orthogonal to the Dy_3-plane the toroidal moment in this direction may become non-zero. This is of relevance if the local site-symmetry at each center is different. A toroidal moment will be calculated for ground states featuring clearly non-vortex like configurations (e.g. Figure 5.46). Therefore, reference lines where one, two or three effective spins lie in the plane were drawn in Figure 5.45. For simplicity, only those spin configurations where all spins are in-plane were considered as truly toroidal states.

Analyzing the toroidal magnetic moments calculated for the lowest energy state of the four KDs, the ideal scenario with all three spins perfectly in plane would result in T = 58.14 $Am^3 \mu_B^{-1}$ (the moment is given in units of μ_B). Such an ideal scenario is only realized in models fullcore, optcore and unoptcore in part 2 in **(X4)**. For most other models in **(X4)** and **(X3)** the spins are either not in-plane or not coupled to stabilize a toroidal ground state. A similar situation can be reported for **(X5)** where the toroidal moments are slightly larger.

Thus, in agreement with experiment, it can be concluded that it is unlikely that a toroidal state is indeed the ground state in **(X3)**–**(X5)**. These results are particularly intriguing considering that toroidal ground states in Dy_3-triangles are well know.

This was found for example by Vignesh and Rajaraman comparing 17 Dy_3-containing compounds in 2021.[460] The present study represents a rare case where the ground state is non-toroidal.[461] Thus the presence of second-sphere effects in low symmetry Dy_3-triangles suppressing a toroidal moment is an important result to assist in tailoring single molecule toroics.

To conclude this section, it was demonstrated that halogen bonding interaction energies are correlated to distinct crystal symmetries in three Dy_3-triangles. The electronic properties of these triangles were calculated resulting in a large number of model structures. It was shown how second-sphere effects can tune the toroidicity by flipping spin orientations from in-plane to out-of-plane leading to avoided level crossings. The intramolecular coupling was investigated to identify possible toroidal moments. Experiment and theory proofed a lack of toroidicity.

6. Conclusion

In this thesis, the influences of exchange-, non-covalent- and second-sphere interactions on the crystallization and magnetic properties of lanthanide based single molecule magnets (SMMs) were thoroughly investigated using a combined theoretical and synthetic approach. These studies enabled the establishment of useful best practices for the computational modeling of these interactions which are supported by high-quality data. The key findings relevant for future investigations are summarized below:

Exchange Coupled Lanthanide Systems The first step in this study was the investigation of a set of isostructural heterodinuclear 3d-4f compounds with either Zn(II) or Co(II) as the 3d-metal ion and the trivalent lanthanide ions Gd(III), Tb(III), Dy(III), Ho(III) and Er(III). These compounds have proven to be an ideal testbed for computational studies. The theoretical treatment of such compounds requires a computationally expensive multireference calculation with large active spaces including the 3d and 4f orbitals. Here the calculations are simplified by first investigating each magnetic center individually before coupling the single-ion properties via a Spin Hamiltonian approach to the magnetic properties of the whole ensemble. Daniel Seufert and Dr. Ghulam Abbas (KIT) synthesized a series of compounds that enabled this workflow to be experimentally substantiated.

It was possible to simulate the magnetic properties of the **(CoDy)** compound using the "classic" approach of first modeling the isolated paramagnetic centers and combining these calculations using a Spin Hamiltonian. This was done through a series of CASOCI and BS-DFT calculations. It was also possible to reproduce the same workflow in a second, alternative approach utilizing the electronic structures of the experimentally isolated model structures and their magnetic properties. More precisely, it was possible to show that the ZFS parameters of **(CoY)** and **(ZnDy)** could be coupled with the exchange interaction calculated for **(CoGd)** to simulate the data of **(CoDy)**. This finding is very important because it validates a simulation practice which was a necessity for many years in the field using real synthetic examples as a benchmark.

Section 3.3 revolved around a second, common practice in the computational investigation of magnetic properties for lanthanide coordination compounds. The magnetic exchange coupling between trivalent lanthanide ions is often approximated using BS-DFT, in particular between Gd(III)-centers which serve as model structures. However, a critical gap here is that the rigorous quantification of the reliability of this approach has not been conducted by a systematic comparison of calculated and experimental data.

This gap was addressed by investigating 27 literature-known dinuclear Gd(III)-complexes. Their magnetic data were digitalized, refitted with three approaches to obtain the experimental coupling constant J in a uniform framework. Then, J was simulated using a series of DFT-calculations in order to quantify errors occurring during the computational modeling. It was found that triple-ζ basis sets are a requirement to treat the paramagnetic centers and surrounding ligands.

Furthermore, scalar relativistic effects need to be treated explicitly using appropriate computational methods (DKH, X2C). Most importantly, it was found that hybrid DFT-functionals with contributions of 20–50 % exact exchange give the best results. A Mean Absolute Error (MAE) below 0.02 cm^{-1} was obtained for the simulation of exchange couplings J when the functionals bh-lyp, pbe0, cam-b3lyp and ωb97-x are used in parallel giving a range of values indicating the errors of DFT. These results were used to simulate the data of larger Gd(III)-clusters. Noting that the experimentally observed coupling constants are generally below 0.1 cm^{-1}, this is a remarkable accuracy. This work established for the first time a best practice workflow to simulate the magnetic coupling in Gd(III)-coordination clusters.

Also, structure property relations between the exchange coupling constant and the geometry of the bridging unit between the two spin centers were explored. A series of D_{2h}-symmetric model structures was proposed. Through Symbolic Regression (SR) studies based on the geometric distortion of the model structures, different features of BS-DFT coupling constants for Gd(III)-complexes could be rationalized.

The influence of terminal ligands on the coupling was found to be rather small. Considering that the bridging geometry is the only important feature, it was indicated that very simple model structure give reliable results for large coordination clusters. Given that the latter study focused predominantly on halide bridged Gd(III)-dimers, it can, as an outlook, be expanded to more common oxygen bridged dimers.

Relevance of Halogen Bonding Intermolecular, non-covalent halogen bonding interactions were investigated in Chapter 4 for lanthanide coordination clusters. Halogen bonding was previously suggested for short interhalogen bond contacts in the crystal structure of lanthanide coordination compounds, however, the energy and bonding properties of these contacts have not been classified. In this work, the aim was to quantify these bonding interactions beyond simple geometric arguments and thus establish the presence of bonds according to IUPAC rules.

In order to achieve this, a series of DFT-calculations has been carried out rationalizing possible halogen bonding interactions in a number of compounds. Here, in-depth topological analysis of the crystal structures, calculation of the interaction energies between the involved molecules, MEP, EDA and QTAIM analyses were used to investigate the bonding.

To establish the influence of halogen bonding on the crystallization of lanthanide coordination compounds, two complexes synthesized by Dr. Jonas Braun were investigated in Section 4.2. In the first example, a highly disordered tetrahedral symmetry of halogen-halogen interactions between CCl_4 and dinuclear Dy(III)-complexes was attributed to the special geometric arrangement. In the second example, the highly symmetric crystal structure ($P\bar{4}2_1/c$) of a trigonal prismatic Er_6-cluster was analyzed. This is the first time that the presence of a complex halogen bonding network has been identified as a stabilizing influence via cooperative effects between the halogen bonds. Notably, these represent two cases where halogen bonds are influenced by and influence a given crystal symmetry.

The complexes featuring halogenated ligands synthesized within this work were discussed in Section 4.3. Computational model interactions of different sizes were tested to gauge their influence on the halogen bonds. It was found that the presence of the metal ion plays a central role in the stabilization of the interactions.

Finally, CASOCI and BS-DFT calculations were employed to quantify the magnetic properties measured. Further studies should enable the rationalization of the influence of different lanthanides on the halogen interactions.

Second-Sphere Effects on the Magnetic Anisotropy Chapter 5 of this thesis considered the influence of ions and molecules in the second coordination sphere around the lanthanide ions. This has been largely neglected in the literature. It was examined when these effects become relevant, rationalized how they act and investigated how they may influence the properties of the investigated compounds. This effect was explored considering three different Dy(III)-complexes based on a large multidentate ligand synthesized and characterized within the present work. A series of CASOCI calculation utilizing different model structures was compared with the magnetic properties.

It can be highlighted that second-sphere effects significantly alter the direction of the ground state magnetic main axis by cumulatively including larger amounts of the active crystal space. An important finding is that the assumption that the crystal field around lanthanides is dominated by the first coordination sphere is insufficient in low symmetry complexes where water and/or methanol ligands are involved in hydrogen bonding.

Two mononuclear Dy(III)-compounds synthesized by the author were investigated, one of which showed a pronounced influence of the second coordination sphere on the ZFS and ground state m_J-composition. These results were correlated with AC-SQUID measurements performed by Dr. Barbora Brachňaková which revealed a significant quenching of the relaxation pathways.

Finally, all of the above lessons were combined in the investigation of a series of halogen bonded Dy_3-triangles. Importantly, the strength in interaction energies through halogen bonding can be correlated with a change in the crystallographic space groups. It was furthermore shown how second-sphere effects significantly affect the magnetic ground state. The reasons for this are are a direct electrostatic interaction between the second-sphere molecules as well as a polarization of the first sphere ligands. These results were shown to affect the (absence of) a toroidal ground state in agreement with μ-SQUID measurements conducted by Dr. Sagar Paul.

These interdisciplinary and comprehensive computational and synthetic studies, lead to important findings regarding the analysis of lanthanide coordination clusters, in particular with respect to best practices for the calculation of exchange coupling constants and the suitability of different model structures for the investigation of halogen bonding and elucidation of magnetic properties.

7. Experimental

7.1. Synthesis

General Procedure

Lanthanide chlorides, nitrates and acetates were prepared using the respective trivalent lanthanide oxides and acids. All other chemicals were obtained from commercial sources and used without further purification. All syntheses were carried out under aerobic conditions.

Instruments

Attenuated Total Reflection Infrared (ATR-IR) spectroscopy was performed on a Bruker Platinum Alpha ATR IR located at the Institute of Inorganic Chemistry at KIT Campus South.
Powder X-ray Diffraction (PXRD) experiments were performed on a STOE STADI-P equipped with a Cu-Kα source and thus with a characteristic wave length of 1.5405 Å at the Institute of Nanotechnology at KIT Campus North.
Single Crystal X-ray Diffraction (SC-XRD) was performed on a STADIVARI by STOE with Ga-Jet X-ray source by Excilium using Ga-Kα radiation with

a wavelength of 1.3143 Å located at the Institute of Nanotechnology at KIT Campus North.
Superconducting Quantum Interference Device (SQUID) measurements were performed on a Quantum Design MPMS XL-1 located at the Institute of Nanotechnology at KIT campus north in collaboration with Dr. Barbora Brachňaková in the group of Prof. Dr. Mario Ruben and on a Quantum Design MPMS3 located at the Jianxi University of Science and Technology in Ganzhou by Prof. Yan Peng.

Experimental procedures

Cl-hmph *o*-vanillin (2.05 g, 13.50 mmol, 1 Eq.) and 5-chloro-2-hydrazinlypyridine (1.94 g, 13.5 mmol, 1 Eq.) were dissolved in 200 mL MeCN and heated for 4 hours. The reaction mixture was thus cooled to -20 °C where a pale yellow precipitate formed. The crude product was filtered and residual solvent removed under vacuum. The product was a pale yellow solid in a yield of 2.44 g (65 %).
^{1}H-NMR (400 MHz, DMSO-d_6), δ (ppm): 11.09 (s, 1H, OH), 9.74 (s, 1H, NH), 8.33 (s, 1H, CH_{Ar}), 8.14 (dd, J = 2.6, 0.8 Hz, 1H CH), 7.72 (dd, J = 8.9, 2.7 Hz, 1H CH_{Ar}), 7.26 (dd, J = 7.9, 1.6 Hz, 1H CH_{Ar}), 7.11 (dd, J = 9.0, 0.5 Hz, 1H CH_{Ar}), 6.95 (dd, J = 8.1, 1.4 Hz, 1H CH_{Ar}), 6.81 (t, J = 8.0 Hz, 1H CH_{Ar}), 3.82 (s, 3H, CH_3), **ATR-IR:** Figure A.33

Br-hmph *o*-vanillin (2.04 g, 13.50 mmol, 1 Eq.) and 5-bromo-2-hydrazinlypyridine (2.54 g, 13.5 mmol, 1 Eq.) were dissolved in 200 mL MeCN and heated for 4 hours. The reaction mixture was thus cooled to -20 °C where a pale yellow precipitate formed. The crude product was filtered and residual

solvent removed under vacuum. The product was a pale brown solid in a yield of 2.86 g (62 %).
^{1}H-NMR (400 MHz, DMSO-d_6), δ (ppm): 11.08 (s, 1H, OH), 9.77 (s, 1H, NH), 8.33 (s, 1H, CH_{Ar}), 8.21 (dd, J = 2.5, 0.7 Hz, 1H CH), 7.81 (dd, J = 9.0, 2.5 Hz, 1H CH_{Ar}), 7.26 (dd, J = 4.0, 1.4 Hz, 1H CH_{Ar}), 7.08 (dd, J = 9.0, 0.6 Hz, 1H CH_{Ar}), 6.95 (dd, J = 8.1, 1.5 Hz, 1H CH_{Ar}), 6.81 (t, J = 7.9 Hz, 1H CH_{Ar}), 3.82 (s, 3H, CH_3), **ATR-IR:** Figure A.33

(C1) [$Dy_2(Cl-mph)_2(NO_3)_4$] Cl-hmph (137.7 mg, 0.5 mmol, 1 Eq.) and $Dy(NO_3)_3 \cdot xH_2O$ (228.2 mg, 0.5 mmol, 1 Eq.) were dissolved in 10 mL of a 1:1 mixture of MeCN and MeOH, Et_3N (70.2 μL, 0.5 mmol, 1 Eq.) added, stirred for 30 min at room temperature yielding a clear, deeply yellow solution. After one day, yellow crystals suitable for SC-XRD were obtained. **PXRD:** Figure A.32, **ATR-IR:** Figure A.33, **SC-XRD:** Table A.16

(C2) [$Dy_2(Br-mph)_2(NO_3)_4$] Br-hmph (160.7 mg, 0.5 mmol, 1 Eq.) and $Dy(NO_3)_3 \cdot xH_2O$ (228.1 mg, 0.5 mmol, 1 Eq.) were dissolved in 10 mL of a 1:1 mixture of MeCN and MeOH, Et_3N (70.2 μL, 0.5 mmol, 1 Eq.) added, stirred for 30 min at room temperature yielding a clear, deeply yellow solution. After one day, yellow crystals suitable for SC-XRD were obtained. **PXRD:** Figure A.32, **ATR-IR:** Figure A.33, **SC-XRD:** Table A.16

(C3) $[Gd_2(Br-mph)_4(NO_3)](NO_3) \cdot 5\,MeOH$ Br-hmph (158.6 mg, 0.5 mmol, 1 Eq.) and $Gd(NO_3)_3 \cdot xH_2O$ (225.7 mg, 0.5 mmol, 1 Eq.) were dissolved in 10 mL of a 1:1 mixture of MeCN and MeOH, Et_3N (70.2 μL, 0.5 mmol, 1 Eq.) added, stirred for 30 min at room temperature yielding a clear, deeply yellow solution. After one week, large, yellow crystals suitable for SC-XRD were obtained.
PXRD: Figure A.32, **ATR-IR:** Figure A.33, **SC-XRD:** Table A.17

Methyl Pyrazine-2-carboxylate Pyrazine-2-carboxylic acid (15 g, 0.12 mol, 1 Eq.) was suspended in 400 mL MeOH and cooled in an ice bath to 0 °C. Under constant stirring $SOCl_2$ (35 mL, 0.48 mol, 4 Eq.) was slowly added over the course of an hour. After the completed addition, the reaction mixture was allowed to warm up to room temperature and excess $SOCl_2$ removed under reduced pressure. The crude product was quenched with 200 mL of saturated Na_2CO_3-solution and extracted three times with 60 mL DCM, dried over $NaSO_4$. The solvent was removed under reduced pressured and the crude product obtained as a colorless solid. The yield was 6.97 g (42 %).
^{1}H-NMR (400 MHz, DMSO-d_6), δ (ppm): 9.22 (d, J = 1.4 Hz, 1H, CH_{Ar}), 8.91 (d, J = 2.5 Hz, CH_{Ar}), 8.83 (dd, J = 2.5, 1.5 Hz, 1H, CH_{Ar}), 3.93 (s, 3H, CH_3)

Pyrazine-2-carbohydrazide Methyl Pyrazine-2-carboxylate (6.97 g, 50.5 mmol, 1 Eq.) was dissolved in 150 mL EtOH and hydrazine hydrate (80%, 40.7 mL, $\approx$0.6 mol, $\approx$12 Eq.) was added dropwise. The suspension was heated to reflux over night yielding a dark yellow solution. The reaction mixture was cooled in an ice bath, the product formed as pale yellow needles. Upon filtration, the crude product was washed twice with Et_2O

and dried in vacuum. The yield was 5.00 g (72 %). **^{1}H-NMR (400 MHz, DMSO-d_6)**, δ (ppm): 10.13 (s, 1H, NH), 9.13 (d, J = 1.5 Hz, 1H, CH_{Ar}), 8.84 (d, J = 2.5 Hz), 8.70 (dd, J = 2.5, 1.6 Hz, 1H, CH_{Ar}), 4.65 (s, 2H, NH_2)

(C4) [Dy(H_2dappyzh)(H_2O)$_3$(MeOH)]Cl_3 $DyCl_3 \cdot 6$ (37.3 mg, 0.1 mmol, 1 Eq.) were dissolved with 2,6-diacetylpyridine (16.1 mg, 0.1 mmol, 1 Eq.) and pyrazine-2-carbohydrazid (27.8 mg, 27.6 mmol, 2 Eq.) in 8 mL MeCN and 2.5 mL MeOH, stirred for 30 min, and filtered. Large pale yellow crystals formed after one day suitable for SC-XRD. **SC-XRD:** Table A.19

(C5) [Dy_2Na_2(dappyzh)$_2$(OAc)$_4$(H_2O)$_2$] $Dy(OTf)_3$ (61.4 mg, 0.1 mmol, 1 Eq.), 2,6-diacetylpyridine (16.3 mg, 0.1 mmol, 1. Eq.), pyrazine-2-carbohydrazid (27.8 mg, 27.6 mmol, 2 Eq.) and $NaOAc \cdot 3\,H_2O$ (30.6 mg, 0.2 mmol, 2 Eq.) were dissolved in 8 mL MeOH. Et_3N (28 μL, 0.2 mmol, 2 Eq.) were added to the solution under stirring. The reaction mixture was stirred for 30 min before it was filtered. After 2 days, yellow crystals formed suitable for SC-XRD formed.
PXRD: Figure A.39, **SC-XRD:** Table A.19

(C6) [Dy_4(dappyzh)$_2$(OH)$_2$(OAc)$_6$] $Dy(OAc)_3$ (34.4 mg, 0.1 mmol, 1 Eq.), 2,6-diacetylpyridine (16.3 mg, 0.1 mmol, 1. Eq.) and pyrazine-2-carbohydrazid (27.3 mg, 27.6 mmol, 2 Eq.) were dissolved in 16 mL of a 1:1 mixture of MeCN and MeOH. The reaction mixture was stirred for 30 min before it was filtered. After 2 months, yellow crystals formed suitable for SC-XRD formed.
PXRD: Figure A.43, **SC-XRD:** Table A.20

(C7) $[Dy(Cl-H_2dapp)(NO_3)_3] \cdot 0.5\,MeCN$ 2,6-diacetylpyridine (33.0 mg, 0.2 mmol, 1. Eq.) and 5-chloro-2-hydrazinylpyridine 56.3 mg, 0.4 mmol, 2. Eq.) were dissolved in 15 mL MeOH. $Dy(NO_3)_3 \cdot xH_2O$ (90.1 mg, 0.2 mmol, 1 Eq.) were dissolved in 5 mL MeOH and slowly added to the ligand solution under vigorous stirring. The reaction was heated to reflux for 15 min, cooled to room temperature and filtered. Yellow crystals suitable for SC-XRD formed in the yellow solution after one day.
PXRD: Figure A.48

(C8) $[Dy(Cl\text{-}H_2dapp)(NO_3)_2(H_2O)]$ $[Dy(Cl\text{-}H_2dapp)(NO_3)_2(H_2O)_{0.5}(MeOH)_{0.5}]$ $(NO_3)_2 \cdot 4.5MeOH$ 2,6-diacetylpyridine (65.5 mg, 0.4 mmol, 1. Eq.) and 5-chloro-2-hydrazinylpyridine 113.6 mg, 0.8 mmol, 2. Eq.) were dissolved in 15 mL MeOH. $Dy(NO_3)_3 \cdot xH_2O$ (183.0 mg, 0.4 mmol, 1 Eq.) and NaCl (24.6 mg, 0.4 mmol, 1 Eq.) were dissolved in 4 mL MeOH and 1 mL H_2O and slowly added to the ligand solution under vigorous stirring. The reaction was stirred for 10 min and filtered. Yellow crystals suitable for SC-XRD formed in the yellow solution after six weeks.
PXRD: Figure A.49

7.2. Calculations

General Workflow for CASOCI Calculations

Unless otherwise mentioned, the following workflow is used to perform CASOCI calculations in this thesis. If the calculation is on a multinuclear compound, all but one centers are replaced with a diamagnetic ion, which is Y(III) for lanthanides and Zn(II) for transition metals.
In a first step the magnetic ion is replaced to Gd(III) (or Mn(II)) to perform preliminary calculations on an f^7 (or d^5) system. An x2c-TZVPall basis is used for all atoms.[294] For some calculations a def2-TZVP basis is used for light atoms.[462] These will be indicated in the text. A UKS calculation is performed on b3-lyp/ri level of theory[242,244,250,251,463,464] treating scalar relativistic effects with one-component X2C.[465] Fermi-smearing is turned on for a clean convergence. All calculations using the "regular" version of Turbomole are performed with either Version 7.7.1 or 7.8.[4]
In a second step, natural orbitals are calculated and it is checked if only the appropriate number of single occupied orbitals was obtained. These will be the 4f (or 3d) orbitas of interest. With these orbitals in the active space, a ROHF calculation is performed using the Roothaan-parameters a = 1 and b = 2 for half filled shells. This is done with a custom version of Turbomole provided by C. v. Wüllen. Because of this version, scalar relativistic effects need to be treated with DKH.[466,467]
Using the obtained orbitals, the central atom is exchanged to the metal of interest and a new basis generated. The new Roothaan Parameters are generated using a script by C. v. Wüllen and summarized in Table 7.2.

Table 7.1.: Overview of the Elements, CAS-spaces and Roothaan.

Element	CAS Space (nelec,norb)	Roothaan Parameters a, b
Gd(III)	(7,7)	1, 2
Tb(III)	(8,7)	63/64, 49/32
Dy(III)	(9,7)	238/243, 308/243
Ho(III)	(10,7)	49/50, 28/25
Er(III)	(11,7)	119/121, 126/121
Tm(III)	(12,7)	427/432, 217/216
Yb(III)	(13,7)	168/169, 168/169
Co(II)	(7,5)	93/98, 45/49

In the last orbital optimization step, DKH4 is turned on and tighter convergence criteria are employed. The energy is converged to $10^{-8} E_h$ and the density to 10^{-7}. Afterwards, the necessary integrals are calculated and the CASOCI calculation preformed to compute the wavefunctions of the lowest 100 states.[7] In a last step the wavefunctions are analyzed with a pseudospin formalism.

Workflow for PySR Symbolic Regression

In this work a number of equations were generated with Symbolic Regression using Python 3.15.5. This was done with the package PySR.[322] To perform these calculations, the initial data was first normalized using the pandas StandardScaler.[468] Afterwards, the PySR Regression was performed using 20 populations, each population size was 40. The maximum complexity was set to 15, and the model was converged with 3000 iterations.

The operators allowed were "+", "-", "*", "/", "exp" and "log".
Simulations to generate equations from the cso-trace and DS2 features are generated with a simpler model only using 10 populations of a size 20, 1500 iterations and only allowing binary operators. It should be noted that the obtained expressions are highly dependent on the exact parameters used.

Workflow to Obtain MCASCI-Exchange Coupling Constants

This section summarizes a workflow previously discussed by Fink *et al.* to obtain accurate exchange coupling constants from a modified CAS-CI approach.[98] It is shown that an overestimation of the energy of charge transfer states is responsible for a wrong contribution of antiferromagnetic exchange. To remedy this, the following workflow is employed:
First, a CASSCF-calculation is performed using a CAS(14,14) space to obtain the energy of the charge transfer states E_{CT} as well as the difference between the HS and LS states (ΔE_{CT}). The second calculation performed is a CASSCF calculation excluding the CT-states. The obtained energy difference between HS and LS is ΔE_{FM}. From this, the coupling constant can be divided in a ferro- and antiferromagnetic contribution:

$$\begin{aligned} J &= -\tfrac{\Delta E}{2S}, \\ J_{AF} &= J_{CT} - J_{FM}. \end{aligned}$$

Next, one center is replaced to diamagnetic Y and the same CASSCF calculation is performed to optimize the Octet ground state in a CAS(7,7). By performing a valence-CI calculation with and without an additional electron and averaging of the 7 obtained sextet states, the energy of the

non-relaxed charge transfer state can be approximated. Next, a CASSCF calculation is performed relaxing both models. E_{CT} is then corrected with this relaxation energy.
Finally, the antiferromagnetic contribution to the coupling is approximately inversely proportional to the charge transfer energy. Consequently, the corrected antiferromagnetic contribution can be corrected as follows:

$$\begin{aligned} J'_{AF} &= J_{AF} \frac{E_{CT}}{E_{CT,corr}}, \\ J_{corr} &= J'_{AF} + J_{FM}. \end{aligned}$$

The starting orbitals were generated with a ROHF calculation, using a DKH2-model Hamiltonian and a x2c-SVPall basis for all atoms. CASSCF calculations are performed with the wavels program.[411]

8. Bibliography

[1] K. W. H. Stevens, *Proc. Phys. Soc. A* **1952**, *65*, 209–215.

[2] *Computational Methods in Lanthanide and Actinide Chemistry*, 1st ed., (Ed.: M. Dolg), Wiley, **2015**.

[3] W. Kohn, L. J. Sham, *Phys. Rev.* **1965**, *140*, A1133–A1138.

[4] S. G. Balasubramani, G. P. Chen, S. Coriani, M. Diedenhofen, M. S. Frank, Y. J. Franzke, F. Furche, R. Grotjahn, M. E. Harding, C. Hättig, A. Hellweg, B. Helmich-Paris, C. Holzer, U. Huniar, M. Kaupp, A. Marefat Khah, S. Karbalaei Khani, T. Müller, F. Mack, B. D. Nguyen, S. M. Parker, E. Perlt, D. Rappoport, K. Reiter, S. Roy, M. Rückert, G. Schmitz, M. Sierka, E. Tapavicza, D. P. Tew, C. van Wüllen, V. K. Voora, F. Weigend, A. Wodynski, J. M. Yu, *J. Chem. Phys.* **2020**, *152*, 184107.

[5] O. Vahtras, H. Ågren, P. Jo/rgensen, H. Jo/rgen Aa. Jensen, T. Helgaker, J. Olsen, *J. Chem. Phys.* **1992**, *96*, 2118–2126.

[6] G. Karlström, R. Lindh, P.-Å. Malmqvist, B. O. Roos, U. Ryde, V. Veryazov, P.-O. Widmark, M. Cossi, B. Schimmelpfennig, P. Neogrady, L. Seijo, *Comput. Mater. Sci.* **2003**, *28*, 222–239.

[7] T. Bodenstein, A. Heimermann, K. Fink, C. van Wüllen, *Chemphyschem* **2022**, *23*, 202100648.

[8] P. A. M. Dirac, *The Principles of Quantum Mechanics*, 3rd ed., Clarendon Press, Oxford, **1947**.

[9] M. E. Lines, *J. Chem. Phys.* **1971**, *55*, 2977–2984.

[10] L. F. Chibotaru, L. Ungur, A. Soncini, *Angew Chem Int Ed* **2008**, *47*, 4126–9.

[11] M. Dahlen, N. Reinfandt, C. Jin, M. T. Gamer, K. Fink, P. W. Roesky, *Chemistry* **2021**, *27*, 15127–15135.

[12] D. Esteban-Gómez, L. A. Büldt, P. Pérez-Lourido, L. Valencia, M. Seitz, C. Platas-Iglesias, *Inorg. Chem.* **2019**, *58*, 3732–3743.

[13] A. Rajabi, R. Grotjahn, D. Rappoport, F. Furche, *Dalton Trans.* **2024**, *53*, 410–417.

[14] J. E. Geusic, H. M. Marcos, L. G. Van Uitert, *Appl. Phys. Lett.* **1964**, *4*, 182–184.

[15] E. Moreno-Pineda, W. Wernsdorfer, *Adv Quantum Tech* **2025**, *8*, 2300367.

[16] C. Brites, A. Millán, L. Carlos in *Handbook on the Physics and Chemistry of Rare Earths*, *Vol. 49*, Elsevier, **2016**, pp. 339–427.

[17] Y.-Z. Zheng, G.-J. Zhou, Z. Zheng, R. E. P. Winpenny, *Chem. Soc. Rev.* **2014**, *43*, 1462–1475.

[18] F.-S. Guo, B. M. Day, Y.-C. Chen, M.-L. Tong, A. Mansikkamäki, R. A. Layfield, *Science* **2018**, *362*, 1400–1403.

[19] J. D. Rinehart, J. R. Long, *Chem. Sci.* **2011**, *2*, 2078.

[20] C. A. P. Goodwin, F. Ortu, D. Reta, N. F. Chilton, D. P. Mills, *Nature* **2017**, *548*, 439–442.

[21] M. Atzori, R. Sessoli, *J. Am. Chem. Soc.* **2019**, *141*, 11339–11352.

[22] L. Frangoulis, Z. Khatibi, L. A. Mariano, A. Lunghi, *JACS Au* **2025**, *5*, 3808–3821.

[23] D. Gatteschi, R. Sessoli, J. Villain, *Molecular Nanomagnets*, Reprinted., Oxford University Press, Oxford, **2008**, 395 pp.

[24] T. Lis, *Acta Crystallogr. B* **1980**, *36*, 2042–2046.

[25] A. Caneschi, D. Gatteschi, R. Sessoli, A. L. Barra, L. C. Brunel, M. Guillot, *J. Am. Chem. Soc.* **1991**, *113*, 5873–5874.

[26] R. Sessoli, D. Gatteschi, A. Caneschi, M. A. Novak, *Nature* **1993**, *365*, 141–143.

[27] S. M. J. Aubin, M. W. Wemple, D. M. Adams, H.-L. Tsai, G. Christou, D. N. Hendrickson, *J. Am. Chem. Soc.* **1996**, *118*, 7746–7754.

[28] S. M. J. Aubin, N. R. Dilley, L. Pardi, J. Krzystek, M. W. Wemple, L.-C. Brunel, M. B. Maple, G. Christou, D. N. Hendrickson, *J. Am. Chem. Soc.* **1998**, *120*, 4991–5004.

[29] S. L. Castro, Z. Sun, C. M. Grant, J. C. Bollinger, D. N. Hendrickson, G. Christou, *J. Am. Chem. Soc.* **1998**, *120*, 2365–2375.

[30] C. Sangregorio, T. Ohm, C. Paulsen, R. Sessoli, D. Gatteschi, *Phys. Rev. Lett.* **1997**, *78*, 4645–4648.

[31] N. Ishikawa, M. Sugita, T. Ishikawa, S.-Y. Koshihara, Y. Kaizu, *J. Am. Chem. Soc.* **2003**, *125*, 8694–5.

[32] R. A. Layfield, M. Murugesu, *Lanthanides and Actinides in Molecular Magnetism*, Wiley-VCH, Weinheim, **2015**, 346 pp.

[33] G. Christou, D. Gatteschi, D. N. Hendrickson, R. Sessoli, *MRS Bull.* **2000**, *25*, 66–71.

[34] A. Ardavan, O. Rival, J. J. L. Morton, S. J. Blundell, A. M. Tyryshkin, G. A. Timco, R. E. P. Winpenny, *Phys. Rev. Lett.* **2007**, *98*, 057201.

[35] L. Bogani, W. Wernsdorfer, *Nature Mater* **2008**, *7*, 179–186.

[36] J. Tang, P. Zhang, *Lanthanide Single Molecule Magnets*, Springer Berlin Heidelberg, Berlin, Heidelberg, **2015**.

[37] F. Hund, *Z. Physik* **1925**, *33*, 855–859.

[38] W. C. Martin, R. Zalubas, L. Hagan, Atomic Energy Levels - the Rare-Earth Elements, National Bureau of Standards, Gaithersburg, MD, **1978**.

[39] L. F. Chibotaru in *Computational Modelling of Molecular Nanomagnets*, *Vol. 34*, (Ed.: G. Rajaraman), Springer International Publishing, Cham, **2023**, pp. 1–62.

[40] D. Gatteschi, R. Sessoli, *Angew Chem Int Ed* **2003**, *42*, 268–297.

[41] L. Ungur, L. F. Chibotaru, *Inorg Chem* **2016**, *55*, 10043–10056.

[42] S. T. Liddle, J. van Slageren, *Chem Soc Rev* **2015**, *44*, 6655–69.

[43] L. Tesi, Z. Salman, I. Cimatti, F. Pointillart, K. Bernot, M. Mannini, R. Sessoli, *Chem. Commun.* **2018**, *54*, 7826–7829.

[44] F. Pointillart, K. Bernot, S. Golhen, B. Le Guennic, T. Guizouarn, L. Ouahab, O. Cador, *Angew Chem Int Ed* **2015**, *127*, 1524–1527.

[45] Y. Kishi, F. Pointillart, B. Lefeuvre, F. Riobé, B. Le Guennic, S. Golhen, O. Cador, O. Maury, H. Fujiwara, L. Ouahab, *Chem. Commun.* **2017**, *53*, 3575–3578.

[46] D. Aravena, *J. Phys. Chem. Lett.* **2018**, *9*, 5327–5333.

[47] A. Swain, T. Sharma, G. Rajaraman, *Chem. Commun.* **2023**, *59*, 3206–3228.

[48] L. Ungur, L. F. Chibotaru, *Phys Chem Chem Phys* **2011**, *13*, 20086–90.

[49] Y.-C. Chen, J.-L. Liu, L. Ungur, J. Liu, Q.-W. Li, L.-F. Wang, Z.-P. Ni, L. F. Chibotaru, X.-M. Chen, M.-L. Tong, *J. Am. Chem. Soc.* **2016**, *138*, 2829–37.

[50] J. Flores González, B. Lefeuvre, B. Degraeve, O. Cador, F. Pointillart, *Dalton Trans.* **2021**, *50*, 11466–11471.

[51] L. Llanos, D. Aravena, *J. Magn. Magn. Mater.* **2019**, *489*, 165456.

[52] M. Briganti, F. Santanni, L. Tesi, F. Totti, R. Sessoli, A. Lunghi, *J. Am. Chem. Soc.* **2021**, *143*, 13633–13645.

[53] D. W. Feldman, J. G. Castle, J. Murphy, *Phys. Rev.* **1965**, *138*, A1208–A1216.

[54] C. E. Jackson, I. P. Moseley, R. Martinez, S. Sung, J. M. Zadrozny, *Chem. Soc. Rev.* **2021**, *50*, 6684–6699.

[55] A. Lunghi, F. Totti, R. Sessoli, S. Sanvito, *Nat Commun* **2017**, *8*, 14620.

[56] A. Lunghi, F. Totti, S. Sanvito, R. Sessoli, *Chem. Sci.* **2017**, *8*, 6051–6059.

[57] L. Escalera-Moreno, N. Suaud, A. Gaita-Ariño, E. Coronado, *J. Phys. Chem. Lett.* **2017**, *8*, 1695–1700.

[58] A. Lunghi, S. Sanvito, *Sci. Adv.* **2019**, *5*, eaax7163.

[59] S. Gómez-Coca, A. Urtizberea, E. Cremades, P. J. Alonso, A. Camón, E. Ruiz, F. Luis, *Nat Commun* **2014**, *5*, 4300.

[60] E. Moreno-Pineda, G. Taran, W. Wernsdorfer, M. Ruben, *Chem. Sci.* **2019**, *10*, 5138–5145.

[61] S. Osa, T. Kido, N. Matsumoto, N. Re, A. Pochaba, J. Mrozinski, *J. Am. Chem. Soc.* **2004**, *126*, 420–421.

[62] J.-W. Yang, Y.-M. Tian, J. Tao, P. Chen, H.-F. Li, Y.-Q. Zhang, P.-F. Yan, W.-B. Sun, *Inorg. Chem.* **2018**, *57*, 8065–8077.

[63] M. Perfetti, J. Rinck, G. Cucinotta, C. E. Anson, X. Gong, L. Ungur, L. Chibotaru, M.-E. Boulon, A. K. Powell, R. Sessoli, *Front. Chem.* **2019**, *7*, 6.

[64] Y.-Z. Zheng, Y. Lan, W. Wernsdorfer, C. E. Anson, A. K. Powell, *Chemistry* **2009**, *15*, 12566–70.

[65] Z. Zhu, S. Paul, C. Zhao, J. Wu, X. Ying, L. Ungur, W. Wernsdorfer, F. Meyer, J. Tang, *J. Am. Chem. Soc.* **2024**, jacs.4c07412.

[66] M. Dolai, E. Moreno-Pineda, W. Wernsdorfer, M. Ali, A. Ghosh, *J Phys Chem A* **2021**, *125*, 8230–8237.

[67] C. Benelli, A. Caneschi, D. Gatteschi, L. Pardi, P. Rey, *Inorg. Chem.* **1989**, *28*, 275–280.

[68] E. M. Fatila, M. Rouzières, M. C. Jennings, A. J. Lough, R. Clérac, K. E. Preuss, *J. Am. Chem. Soc.* **2013**, *135*, 9596–9599.

[69] S. Kumar Kushvaha, P. Ravichandran, C. Dan, L. Ungur, N. Suryadevara, M. Ruben, K. Chandra Mondal, *Eur J Inorg Chem* **2024**, *27*, e202300598.

[70] J. D. Rinehart, M. Fang, W. J. Evans, J. R. Long, *Nature Chem* **2011**, *3*, 538–542.

[71] F. Liu, D. S. Krylov, L. Spree, S. M. Avdoshenko, N. A. Samoylova, M. Rosenkranz, A. Kostanyan, T. Greber, A. U. B. Wolter, B. Büchner, A. A. Popov, *Nat Commun* **2017**, *8*, 16098.

[72] P. Kumar Sahu, S. Konar, *Chemistry A European J* **2024**, *30*, e202402439.

[73] S. De, A. Mondal, J. Pitcairn, L. Clark, J. Tang, A. Mansikkamäki, R. A. Layfield, *Angew Chem Int Ed* **2025**, *64*, e202502455.

[74] C. A. Gould, K. R. McClain, D. Reta, J. G. C. Kragskow, D. A. Marchiori, E. Lachman, E.-S. Choi, J. G. Analytis, R. D. Britt, N. F. Chilton, B. G. Harvey, J. R. Long, *Science* **2022**, *375*, 198–202.

[75] M. Liu, Y.-C. Chen, H. Wang, T. Shang, M.-L. Tong, R. A. Layfield, A. Mansikkamäki, F.-S. Guo, *J. Am. Chem. Soc.* **2025**, *147*, 18307–18316.

[76] Y. Chen, F. Ma, X. Chen, B. Dong, K. Wang, S. Jiang, C. Wang, X. Chen, D. Qi, H. Sun, B. Wang, S. Gao, J. Jiang, *Inorg. Chem.* **2017**, *56*, 13889–13896.

[77] M. Gonidec, I. Krivokapic, J. Vidal-Gancedo, E. S. Davies, J. McMaster, S. M. Gorun, J. Veciana, *Inorg. Chem.* **2013**, *52*, 4464–4471.

[78] M. Mannini, F. Bertani, C. Tudisco, L. Malavolti, L. Poggini, K. Misztal, D. Menozzi, A. Motta, E. Otero, P. Ohresser, P. Sainctavit, G. G. Condorelli, E. Dalcanale, R. Sessoli, *Nat Commun* **2014**, *5*, 4582.

[79] R. Vincent, S. Klyatskaya, M. Ruben, W. Wernsdorfer, F. Balestro, *Nature* **2012**, *488*, 357–360.

[80] S. Thiele, R. Vincent, M. Holzmann, S. Klyatskaya, M. Ruben, F. Balestro, W. Wernsdorfer, *Phys. Rev. Lett.* **2013**, *111*, 037203.

[81] S. Thiele, F. Balestro, R. Ballou, S. Klyatskaya, M. Ruben, W. Wernsdorfer, *Science* **2014**, *344*, 1135–1138.

[82] C. Godfrin, S. Lumetti, H. Biard, E. Bonet, S. Klyatskaya, M. Ruben, A. Candini, M. Affronte, W. Wernsdorfer, F. Balestro, *J. Appl. Phys.* **2019**, *125*, 142801.

[83] F. Troiani, A. Ghirri, M. Paris, C. Bonizzoni, M. Affronte, *J. Magn. Magn. Mater.* **2019**, *491*, 165534.

[84] C. Bonizzoni, A. Ghirri, F. Santanni, M. Affronte, *npj Quantum Inf* **2024**, *10*, 41.

[85] M. D. Jenkins, Y. Duan, B. Diosdado, J. J. García-Ripoll, A. Gaita-Ariño, C. Giménez-Saiz, P. J. Alonso, E. Coronado, F. Luis, *Phys. Rev. B* **2017**, *95*, 064423.

[86] C. Godfrin, A. Ferhat, R. Ballou, S. Klyatskaya, M. Ruben, W. Wernsdorfer, F. Balestro, *Phys. Rev. Lett.* **2017**, *119*, 187702.

[87] C. Godfrin, R. Ballou, E. Bonet, M. Ruben, S. Klyatskaya, W. Wernsdorfer, F. Balestro, *npj Quantum Inf* **2018**, *4*, 53.

[88] F. Luis, P. J. Alonso, O. Roubeau, V. Velasco, D. Zueco, D. Aguilà, J. I. Martínez, L. A. Barrios, G. Aromí, *Commun Chem* **2020**, *3*, 176.

[89] E. Macaluso, M. Rubín, D. Aguilà, A. Chiesa, L. A. Barrios, J. I. Martínez, P. J. Alonso, O. Roubeau, F. Luis, G. Aromí, S. Carretta, *Chem. Sci.* **2020**, *11*, 10337–10343.

[90] F. Jensen, *Introduction to Computational Chemistry*, Third edition, Wiley, Chichester, West Sussex; Hoboken, NJ; Oxford, **2017**, 638 pp.

[91] D. Ganyushin, F. Neese, *J. Chem. Phys.* **2013**, *138*, 104113.

[92] M. Kleinschmidt, J. Tatchen, C. M. Marian, *J. Chem. Phys.* **2006**, *124*, 124101.

[93] P. Å. Malmqvist, B. O. Roos, B. Schimmelpfennig, *Chem. Phys. Lett.* **2002**, *357*, 230–240.

[94] D. Ganyushin, F. Neese, *J. Chem. Phys.* **2006**, *125*, 024103.

[95] B. A. HeSS, C. M. Marian, U. Wahlgren, O. Gropen, *Chem. Phys. Lett.* **1996**, *251*, 365–371.

[96] F. Neese, *J. Chem. Phys.* **2005**, *122*, 34107.

[97] E. R. Davidson, *J. Comput. Phys.* **1975**, *17*, 87–94.

[98] K. Fink, V. Staemmler, *Mol. Phys.* **2013**, *111*, 2594–2605.

[99] L. F. Chibotaru, L. Ungur, *J. Chem. Phys.* **2012**, *137*, 064112.

[100] A. Abragam, B. Bleaney, *Electron Paramagnetic Resonance of Transition Ions*, First published in paperback, Clarendon Press, Oxford, **2012**, 911 pp.

[101] C. Pachl, MA thesis, Karlsruhe Institute of Technology, Karlsruhe, **2022**.

[102] L. F. Chibotaru, L. Ungur, C. Aronica, H. Elmoll, G. Pilet, D. Luneau, *J. Am. Chem. Soc.* **2008**, *130*, 12445–55.

[103] L. Ungur, W. van den Heuvel, L. F. Chibotaru, *New J. Chem.* **2009**, *33*, 1224.

[104] K. Andersson, P.-Å. Malmqvist, B. O. Roos, *J. Chem. Phys.* **1992**, *96*, 1218–1226.

[105] O. Kahn, *Molecular Magnetism*, VCH, Weinheim New York Cambridge, **1993**.

[106] L. Noodleman, *J. Chem. Phys.* **1981**, *74*, 5737–5743.

[107] T. Onishi, D. Yamaki, K. Yamaguchi, Y. Takano, *J. Chem. Phys.* **2003**, *118*, 9747–9761.

[108] E. Ruiz, J. Cano, S. Alvarez, P. Alemany, *J. Comput. Chem.* **1999**, *20*, 1391–1400.

[109] G. Singh, S. Gamboa, M. Orio, D. A. Pantazis, M. Roemelt, *Theor Chem Acc* **2021**, *140*, 139.

[110] N. Iwahara, Z. Huang, A. Mansikkamäki, L. F. Chibotaru, *J. Chem. Phys.* **2025**, *162*, 164701.

[111] L. Pauling, *The Nature of the Chemical Bond and the Structure of Molecules and Crystals: An Introduction to Modern Structural Chemistry*, 3. ed., 17. print, Cornell Univ. Press, Ithaca, NY, **1960**, 644 pp.

[112] G. A. Jeffrey, *An Introduction to Hydrogen Bonding*, Oxford University Press, New York, **1997**, 303 pp.

[113] S. Grimme, *Angew Chem Int Ed* **2008**, *47*, 3430–3434.

[114] C. A. Hunter, K. R. Lawson, J. Perkins, C. J. Urch, *J. Chem. Soc. Perkin Trans. 2* **2001**, 651–669.

[115] C. A. Hunter, J. K. M. Sanders, *J. Am. Chem. Soc.* **1990**, *112*, 5525–5534.

[116] J. C. Ma, D. A. Dougherty, *Chem. Rev.* **1997**, *97*, 1303–1324.

[117] C. R. Martinez, B. L. Iverson, *Chem. Sci.* **2012**, *3*, 2191.

[118] I. A. Rather, S. A. Wagay, R. Ali, *Coord. Chem. Rev.* **2020**, *415*, 213327.

[119] I. Dzyaloshinskii, E. Lifshitz, L. Pitaevskii, M. Priestley in *Perspectives in Theoretical Physics*, Elsevier, **1992**, pp. 443–492.

[120] R. Eisenschitz, F. London, *Z. Physik* **1930**, *60*, 491–527.

[121] J. N. Israelachvili, *Contemporary Physics* **1974**, *15*, 159–178.

[122] R. H. S. Winterton, *Contemporary Physics* **1970**, *11*, 559–574.

[123] L. H. Doerrer, C. Del Rosario, A. Fan in *Comprehensive Inorganic Chemistry III*, Elsevier, **2023**, pp. 665–739.

[124] H. Schmidbaur, A. Schier, *Chem. Soc. Rev.* **2012**, *41*, 370–412.

[125] H. Schmidbaur, A. Schier, *Angew Chem Int Ed* **2015**, *54*, 746–784.

[126] Q. Zheng, S. Borsley, G. S. Nichol, F. Duarte, S. L. Cockroft, *Angewandte Chemie* **2019**, *131*, 12747–12753.

[127] L. Brammer, A. Peuronen, T. M. Roseveare, *Acta Crystallogr C Struct Chem* **2023**, *79*, 204–216.

[128] D. A. Decato, E. A. John, O. B. Berryman in *Halogen Bonding in Solution*, (Ed.: S. Huber), Wiley, **2021**, pp. 1–41.

[129] *Halogen Bonding in Solution*, (Ed.: S. Huber), Wiley, **2021**.

[130] H. A. Bent, *Chem. Rev.* **1968**, *68*, 587–648.

[131] S. Scheiner, *Acc. Chem. Res.* **2013**, *46*, 280–288.

[132] K. T. Mahmudov, A. V. Gurbanov, V. A. Aliyeva, G. Resnati, A. J. Pombeiro, *Coord. Chem. Rev.* **2020**, *418*, 213381.

[133] P. C. Ho, J. Z. Wang, F. Meloni, I. Vargas-Baca, *Coord. Chem. Rev.* **2020**, *422*, 213464.

[134] K. T. Mahmudov, M. N. Kopylovich, M. F. C. Guedes Da Silva, A. J. L. Pombeiro, *Dalton Trans.* **2017**, *46*, 10121–10138.

[135] K. T. Mahmudov, A. V. Gurbanov, V. A. Aliyeva, M. F. C. Guedes Da Silva, G. Resnati, A. J. Pombeiro, *Coord. Chem. Rev.* **2022**, *464*, 214556.

[136] L. Vogel, P. Wonner, S. M. Huber, *Angew Chem Int Ed* **2019**, *58*, 1880–1891.

[137] A. Bauzá, T. J. Mooibroek, A. Frontera, *The Chemical Record* **2016**, *16*, 473–487.

[138] A. Frontera, *C* **2020**, *6*, 60.

[139] P. Scilabra, V. Kumar, M. Ursini, G. Resnati, *J Mol Model* **2018**, *24*, 37.

[140] R. M. Gomila, A. Frontera, *Dalton Trans.* **2025**, *54*, 3095–3105.

[141] A. Bauzá, A. Frontera, *Coord. Chem. Rev.* **2020**, *404*, 213112.

[142] S. J. Grabowski, *Coord. Chem. Rev.* **2020**, *407*, 213171.

[143] F. Yashmin, L. J. Mazumder, P. K. Sharma, A. K. Guha, *Phys. Chem. Chem. Phys.* **2024**, *26*, 8115–8124.

[144] K. T. Mahmudov, F. E. Huseynov, V. A. Aliyeva, M. F. C. Guedes Da Silva, A. J. L. Pombeiro, *Chemistry A European J* **2021**, *27*, 14370–14389.

[145] J. J. Colin, *Ann. Chim.* **1814**, 252–272.

[146] A. Lachman, *J. Am. Chem. Soc.* **1903**, *25*, 50–55.

[147] R. S. Mulliken, *J. Am. Chem. Soc.* **1950**, *72*, 600–608.

[148] O. Hassel, *Science* **1970**, *170*, 497–502.

[149] R. L. Flurry, *J. Phys. Chem.* **1965**, *69*, 1927–1933.

[150] R. L. Flurry, *J. Phys. Chem.* **1969**, *73*, 2111–2117.

[151] T. Brinck, J. S. Murray, P. Politzer, *Int. J. Quantum Chem.* **1992**, *44*, 57–64.

[152] P. Politzer, P. Lane, M. C. Concha, Y. Ma, J. S. Murray, *J Mol Model* **2007**, *13*, 305–11.

[153] T. Clark, M. Hennemann, J. S. Murray, P. Politzer, *J Mol Model* **2007**, *13*, 291–6.

[154] S. Triguero, R. Llusar, V. Polo, M. Fourmigué, *Crystal Growth & Design* **2008**, *8*, 2241–2247.

[155] A. D. Becke, K. E. Edgecombe, *J. Chem. Phys.* **1990**, *92*, 5397–5403.

[156] Y.-X. Lu, J.-W. Zou, Y.-H. Wang, Y.-J. Jiang, Q.-S. Yu, *J. Phys. Chem. A* **2007**, *111*, 10781–10788.

[157] K. E. Riley, J. S. Murray, P. Politzer, M. C. Concha, P. Hobza, *J. Chem. Theory Comput.* **2009**, *5*, 155–163.

[158] H. G. Wallnoefer, T. Fox, K. R. Liedl, C. S. Tautermann, *Phys. Chem. Chem. Phys.* **2010**, *12*, 14941.

[159] L. N. Anderson, F. W. Aquino, A. E. Raeber, X. Chen, B. M. Wong, *J Chem Theory Comput* **2018**, *14*, 180–190.

[160] G. R. Desiraju, P. S. Ho, L. Kloo, A. C. Legon, R. Marquardt, P. Metrangolo, P. Politzer, G. Resnati, K. Rissanen, *Pure Appl. Chem.* **2013**, *85*, 1711–1713.

[161] M. Brezgunova, K.-S. Shin, P. Auban-Senzier, O. Jeannin, M. Fourmigué, *Chem Commun (Camb)* **2010**, *46*, 3926–8.

[162] P. Metrangolo, C. Präsang, G. Resnati, R. Liantonio, A. C. Whitwood, D. W. Bruce, *Chem Commun (Camb)* **2006**, 3290–2.

[163] *Halogen Bonding II: Impact on Materials Chemistry and Life Sciences*, (Eds.: P. Metrangolo, G. Resnati), Springer International Publishing, Cham, **2015**.

[164] J. A. Schlueter, H. Park, G. J. Halder, W. R. Armand, C. Dunmars, K. W. Chapman, J. L. Manson, J. Singleton, R. McDonald, A. Plonczak, J. Kang, C. Lee, M.-H. Whangbo, T. Lancaster, A. J. Steele, I. Franke, J. D. Wright, S. J. Blundell, F. L. Pratt, J. deGeorge, M. M. Turnbull, C. P. Landee, *Inorg. Chem.* **2012**, *51*, 2121–2129.

[165] X. Pang, X. R. Zhao, H. Wang, H.-L. Sun, W. J. Jin, *Crystal Growth & Design* **2013**, *13*, 3739–3745.

[166] R. T. Butcher, J. J. Novoa, J. Ribas-Ariño, A. W. Sandvik, M. M. Turnbull, C. P. Landee, B. M. Wells, F. F. Awwadi, *Chem. Commun.* **2009**, 1359.

[167] M. Atzori, F. Artizzu, E. Sessini, L. Marchiò, D. Loche, A. Serpe, P. Deplano, G. Concas, F. Pop, N. Avarvari, M. Laura Mercuri, *Dalton Trans.* **2014**, *43*, 7006–7019.

[168] Sushila, R. Siddiqui, S. Patra, K. Shivam, A. Sil, B. Guchhait, H. Tian, R. Kataria, S. Goswami, P. Venugopalan, R. Patra, *Inorg. Chem.* **2022**, *61*, 11484–11496.

[169] Q. Wu, M. Huang, T. Li, L. Jiao, Y. Tu, X. Xu, X. Ma, H. Tian, Y. Qiao, *J. Mol. Struc.* **2021**, *1225*, 129054.

[170] K. P. Carter, C. H. F. Zulato, C. L. Cahill, *CrystEngComm* **2014**, *16*, 10189–10202.

[171] K. P. Carter, K. E. Thomas, S. J. A. Pope, R. J. Holmberg, R. J. Butcher, M. Murugesu, C. L. Cahill, *Inorg. Chem.* **2016**, *55*, 6902–6915.

[172] K. P. Carter, S. J. A. Pope, M. Kalaj, R. J. Holmberg, M. Murugesu, C. L. Cahill, *Zeitschrift anorg allge chemie* **2017**, *643*, 1948–1955.

[173] J. A. Smith, M. A. Singh-Wilmot, K. P. Carter, C. L. Cahill, J. A. Ridenour, *Crystal Growth & Design* **2019**, *19*, 305–319.

[174] W. Heisenberg, *Z. Physik* **1928**, *49*, 619–636.

[175] J. H. Van Vleck, *The Theory of Electric and Magnetic Susceptibilities*, Oxford University Press, **1932**.

[176] B. C. Guha, *Proc. R. Soc. Lond. A* **1951**, *206*, 353–373.

[177] B. Bleaney, K. Bowers, *Proc. R. Soc. Lond. A* **1952**, *214*, 451–465.

[178] K. W. H. Stevens, *Proc. R. Soc. Lond. A* **1952**, *214*, 237–246.

[179] J. H. Van Vleck, *J. Chem. Phys.* **1937**, *5*, 320–337.

[180] E. Ishiguro, K. Kambe, T. Usui, *Physica* **1951**, *17*, 310–318.

[181] C. J. O'Connor in *Progress in Inorganic Chemistry*, *Vol. 29*, (Ed.: S. J. Lippard), Wiley, **1982**, pp. 203–283.

[182] N. F. Chilton, R. P. Anderson, L. D. Turner, A. Soncini, K. S. Murray, *J. Comput. Chem.* **2013**, *34*, 1164–75.

[183] A. Palii, B. Tsukerblat, J. M. Clemente-Juan, E. Coronado, *International Reviews in Physical Chemistry* **2010**, *29*, 135–230.

[184] B. Bleaney, K. W. H. Stevens, *Rep. Prog. Phys.* **1953**, *16*, 108–159.

[185] E. Moreno-Pineda, N. F. Chilton, R. Marx, M. Dörfel, D. O. Sells, P. Neugebauer, S.-D. Jiang, D. Collison, J. van Slageren, E. J. L. McInnes, R. E. P. Winpenny, *Nat Commun* **2014**, *5*, 5243.

[186] W. Wernsdorfer, N. Aliaga-Alcalde, D. N. Hendrickson, G. Christou, *Nature* **2002**, *416*, 406–409.

[187] Y.-N. Guo, G.-F. Xu, W. Wernsdorfer, L. Ungur, Y. Guo, J. Tang, H.-J. Zhang, L. F. Chibotaru, A. K. Powell, *J. Am. Chem. Soc.* **2011**, *133*, 11948–51.

[188] M. A. Dunstan, R. A. Mole, C. Boskovic, *Eur J Inorg Chem* **2019**, *2019*, 1090–1105.

[189] F. J. Kettles, V. A. Milway, F. Tuna, R. Valiente, L. H. Thomas, W. Wernsdorfer, S. T. Ochsenbein, M. Murrie, *Inorg. Chem.* **2014**, *53*, 8970–8978.

[190] M. Loewenhaupt, P. Tils, K. Buschow, R. Eccleston, *Journal of Magnetism and Magnetic Materials* **1996**, *152*, 10–16.

[191] X. Yi, K. Bernot, O. Cador, J. Luzon, G. Calvez, C. Daiguebonne, O. Guillou, *Dalton Trans.* **2013**, *42*, 6728–31.

[192] R. F. Pfleger, M. Briganti, N. Bonde, J. Ollivier, J. Braun, T. Bergfeldt, S. Piligkos, T. Ruppert, C. E. Anson, M. Perfetti, J. Bendix, A. K. Powell, *Chemistry A European J* **2025**, *31*, e202403002.

[193] T. G. Tziotzi, D. Gracia, S. J. Dalgarno, J. Schnack, M. Evangelisti, E. K. Brechin, C. J. Milios, *J. Am. Chem. Soc.* **2023**, *145*, 7743–7747.

[194] J. Braun, D. Seufert, C. E. Anson, J. Tang, A. K. Powell, *IJMS* **2023**, *25*, 264.

[195] J. W. Sharples, Y.-Z. Zheng, F. Tuna, E. J. L. McInnes, D. Collison, *Chem. Commun.* **2011**, *47*, 7650.

[196] J. W. Sharples, D. Collison, E. J. L. McInnes, J. Schnack, E. Palacios, M. Evangelisti, *Nat Commun* **2014**, *5*, 5321.

[197] A. Tishin, Y. Spichkin, *The Magnetocaloric Effect and Its Applications*, 0th ed., CRC Press, **2016**.

[198] J. Tang, I. Hewitt, N. T. Madhu, G. Chastanet, W. Wernsdorfer, C. E. Anson, C. Benelli, R. Sessoli, A. K. Powell, *Angew Chem Int Ed* **2006**, *45*, 1729–1733.

[199] K. Hymas, A. Soncini, *Magnetochemistry* **2022**, *8*, 58.

[200] G. T. Nguyen, L. Ungur in *Computational Modelling of Molecular Nanomagnets*, *Vol. 34*, (Ed.: G. Rajaraman), Springer International Publishing, Cham, **2023**, pp. 111–153.

[201] M. R. Hermes, B. Jangid, V. Agarawal, L. Gagliardi, *J. Chem. Theory Comput.* **2025**, *21*, 6446–6463.

[202] R. Costa, D. Reta, I. D. P. R. Moreira, F. Illas, *J. Phys. Chem. A* **2018**, *122*, 3423–3432.

[203] J. J. Phillips, J. E. Peralta, *J. Chem. Theory Comput.* **2012**, *8*, 3147–3158.

[204] I. D. P. R. Moreira, R. Costa, M. Filatov, F. Illas, *J. Chem. Theory Comput.* **2007**, *3*, 764–774.

[205] R. Valero, R. Costa, I. De P. R. Moreira, D. G. Truhlar, F. Illas, *J. Chem. Phys.* **2008**, *128*, 114103.

[206] G. David, F. Wennmohs, F. Neese, N. Ferré, *Inorg. Chem.* **2018**, *57*, 12769–12776.

[207] P. Rivero, I. D. P. R. Moreira, F. Illas, G. E. Scuseria, *J. Chem. Phys.* **2008**, *129*, 184110.

[208] O. Guillou, P. Bergerat, O. Kahn, E. Bakalbassis, K. Boubekeur, P. Batail, M. Guillot, *Inorg. Chem.* **1992**, *31*, 110–114.

[209] J. Paulovi, F. Cimpoesu, M. Ferbinteanu, K. Hirao, *J. Am. Chem. Soc.* **2004**, *126*, 3321–3331.

[210] F. Yan, Z. Chen, *J. Phys. Chem. A* **2000**, *104*, 6295–6300.

[211] C. Benelli, A. J. Blake, P. E. Y. Milne, J. M. Rawson, R. E. P. Winpenny, *Chemistry A European J* **1995**, *1*, 614–618.

[212] C. Benelli, A. Caneschi, D. Gatteschi, O. Guillou, L. Pardi, *Inorg. Chem.* **1990**, *29*, 1750–1755.

[213] G. Rajaraman, F. Totti, A. Bencini, A. Caneschi, R. Sessoli, D. Gatteschi, *Dalton Trans.* **2009**, 3153–61.

[214] J. Cirera, E. Ruiz, *Comptes Rendus Chim.* **2008**, *11*, 1227–1234.

[215] R. Essajai, N. Ennassiri, M. Balli, M. Zidane, E. Salmani, O. Mounkachi, M. Rouchdi, A. Abbassi, H. Ez-Zahraouy, A. Mzerd, N. Hassanain, *Phys. Scr.* **2020**, *96*, 015808.

[216] T. Rajeshkumar, S. K. Singh, G. Rajaraman, *Polyhedron* **2013**, *52*, 1299–1305.

[217] T. Rajeshkumar, R. Jose, P. R. Remya, G. Rajaraman, *Inorg. Chem.* **2019**, *58*, 11927–11940.

[218] S. K. Singh, G. Rajaraman, *Dalton Trans.* **2013**, *42*, 3623.

[219] S. K. Singh, K. S. Pedersen, M. Sigrist, C. A. Thuesen, M. Schau-Magnussen, H. Mutka, S. Piligkos, H. Weihe, G. Rajaraman, J. Bendix, *Chem. Commun.* **2013**, *49*, 5583.

[220] S. K. Singh, N. K. Tibrewal, G. Rajaraman, *Dalton Trans.* **2011**, *40*, 10897.

[221] T. Gupta, T. Rajeshkumar, G. Rajaraman, *Phys. Chem. Chem. Phys.* **2014**, *16*, 14568–14577.

[222] L. E. Roy, T. Hughbanks, *J. Am. Chem. Soc.* **2006**, *128*, 568–575.

[223] P. W. Anderson in *Solid State Physics*, *Vol. 14*, Elsevier, **1963**, pp. 99–214.

[224] J. B. Goodenough, *Phys. Rev.* **1955**, *100*, 564–573.

[225] P. W. Anderson, *Phys. Rev.* **1950**, *79*, 350–356.

[226] J. Kanamori, *Journal of Physics and Chemistry of Solids* **1959**, *10*, 87–98.

[227] C. Zener, *Phys. Rev.* **1951**, *82*, 403–405.

[228] P. W. Anderson, H. Hasegawa, *Phys. Rev.* **1955**, *100*, 675–681.

[229] M. Pinsky, D. Avnir, *Inorg. Chem.* **1998**, *37*, 5575–5582.

[230] M. Llunell, D. Casanova, J. Cirera, P. Alemany, S. Alvarez, *Univ. Barc. Barc. Spain* **2013**, *2103*.

[231] H. W. Kuhn, *Naval Research Logistics* **1955**, *2*, 83–97.

[232] H. W. Kuhn, *Naval Research Logistics* **1956**, *3*, 253–258.

[233] J. Lawrence, J. Bernal, C. Witzgall, *J. RES. NATL. INST. STAN.* **2019**, *124*, 124028.

[234] F.-X. Shen, H.-Q. Li, H. Miao, D. Shao, X.-Q. Wei, L. Shi, Y.-Q. Zhang, X.-Y. Wang, *Inorg. Chem.* **2018**, *57*, 15526–15536.

[235] Q.-W. Xie, S.-Q. Wu, W.-B. Shi, C.-M. Liu, A.-L. Cui, H.-Z. Kou, *Dalton Trans.* **2014**, *43*, 11309.

[236] F. Gebhard, Synthese Und Berechnung Dinuklearer 3d-4f Systeme, Vertiefer-Arbeit, Karlsruher Institut für Technologie (KIT), Karlsruhe, **2024**.

[237] I. Oyarzabal, A. Zabala-Lekuona, A. J. Mota, M. A. Palacios, A. Rodríguez-Diéguez, G. Lorusso, M. Evangelisti, C. Rodríguez-Esteban, E. K. Brechin, J. M. Seco, E. Colacio, *Dalton Trans.* **2022**, *51*, 12954–12967.

[238] R. M. Hartshorn, K.-H. Hellwich, A. Yerin, T. Damhus, A. T. Hutton, *Pure Appl. Chem.* **2015**, *87*, 1039–1049.

[239] R. Janicki, A. Mondry, P. Starynowicz, *Coord. Chem. Rev.* **2017**, *340*, 98–133.

[240] J. C. Slater, *Phys. Rev.* **1951**, *81*, 385–390.

[241] S. H. Vosko, L. Wilk, M. Nusair, *Can. J. Phys.* **1980**, *58*, 1200–1211.

[242] Becke, *Phys. Rev. A* **1988**, *38*, 3098–3100.

[243] J. P. Perdew, *Phys. Rev. B* **1986**, *33*, 8822–8824.

[244] C. Lee, W. Yang, R. G. Parr, *Phys. Rev. B* **1988**, *37*, 785–789.

[245] J. P. Perdew, Y. Wang, *Phys. Rev. B* **1992**, *45*, 13244–13249.

[246] J. P. Perdew, K. Burke, M. Ernzerhof, *Phys. Rev. Lett.* **1996**, *77*, 3865–3868.

[247] V. N. Staroverov, G. E. Scuseria, J. Tao, J. P. Perdew, *J. Chem. Phys.* **2003**, *119*, 12129–12137.

[248] J. Tao, J. P. Perdew, V. N. Staroverov, G. E. Scuseria, *Phys. Rev. Lett.* **2003**, *91*, 146401.

[249] J. W. Furness, A. D. Kaplan, J. Ning, J. P. Perdew, J. Sun, *J. Phys. Chem. Lett.* **2020**, *11*, 8208–8215.

[250] A. D. Becke, *J. Chem. Phys.* **1993**, *98*, 1372–1377.

[251] A. D. Becke, *J. Chem. Phys.* **1993**, *98*, 5648–5652.

[252] J. Heyd, G. E. Scuseria, M. Ernzerhof, *J. Chem. Phys.* **2003**, *118*, 8207–8215.

[253] A. V. Krukau, O. A. Vydrov, A. F. Izmaylov, G. E. Scuseria, *J. Chem. Phys.* **2006**, *125*, 224106.

[254] J. P. Perdew, M. Ernzerhof, K. Burke, *J. Chem. Phys.* **1996**, *105*, 9982–9985.

[255] C. Adamo, V. Barone, *J. Chem. Phys.* **1999**, *110*, 6158–6170.

[256] A. D. Becke, *J. Chem. Phys.* **1997**, *107*, 8554–8560.

[257] J.-D. Chai, M. Head-Gordon, *J. Chem. Phys.* **2008**, *128*, 084106.

[258] T. Yanai, D. P. Tew, N. C. Handy, *Chem. Phys. Lett.* **2004**, *393*, 51–57.

[259] N. F. Chilton, D. Collison, E. J. L. McInnes, R. E. P. Winpenny, A. Soncini, *Nat Commun* **2013**, *4*, 2551.

[260] D. B. Chesnut, K. D. Moore, *J Comput Chem* **1989**, *10*, 648–659.

[261] K. Kotrle, I. Nemec, J. Moncol, E. imár, R. Herchel, *Dalton Trans.* **2021**, *50*, 13883–13893.

[262] E. Colacio, J. Ruiz, A. J. Mota, M. A. Palacios, E. Cremades, E. Ruiz, F. J. White, E. K. Brechin, *Inorg. Chem.* **2012**, *51*, 5857–5868.

[263] E. Colacio, J. Ruiz, A. J. Mota, M. A. Palacios, E. Ruiz, E. Cremades, M. M. Hänninen, R. Sillanpää, E. K. Brechin, *Comptes Rendus Chim.* **2012**, *15*, 878–888.

[264] Y. Nakajima, P. Weis, F. Weigend, M. Lukanowski, F. Misaizu, M. M. Kappes, *Phys. Chem. Chem. Phys.* **2025**, *27*, 1017–1030.

[265] M. Dolg, H. Stoll, A. Savin, H. Preuss, *Theoret. Chim. Acta* **1989**, *75*, 173–194.

[266] M. Dolg, H. Stoll, H. Preuss, *Theoret. Chim. Acta* **1993**, *85*, 441–450.

[267] J. Raeder, M. Reiners, R. Baumgarten, K. Münster, D. Baabe, M. Freytag, P. G. Jones, M. D. Walter, *Dalton Trans.* **2018**, *47*, 14468–14482.

[268] K. L. M. Harriman, J. J. Le Roy, L. Ungur, R. J. Holmberg, I. Korobkov, M. Murugesu, *Chem. Sci.* **2017**, *8*, 231–240.

[269] F. Tuna, C. A. Smith, M. Bodensteiner, L. Ungur, L. F. Chibotaru, E. J. L. McInnes, R. E. P. Winpenny, D. Collison, R. A. Layfield, *Angew Chem Int Ed* **2012**, *51*, 6976–80.

[270] Y.-B. Lu, J.-W. Wu, S.-D. Zhu, S.-Q. Wang, S.-Y. Zhang, C.-M. Liu, R. Li, J. Li, J.-H. Ai, Y.-R. Xie, *ACS Omega* **2022**, *7*, 2604–2612.

[271] A. Rasamsetty, S. Mehta, K. U. Ansari, P. Kumar, A. Mondal, M. Shanmugam, *Dalton Trans.* **2022**, *51*, 63–68.

[272] T. Han, Y.-S. Ding, Z.-H. Li, K.-X. Yu, Y.-Q. Zhai, N. F. Chilton, Y.-Z. Zheng, *Chem. Commun.* **2019**, *55*, 7930–7933.

[273] J. Jung, F. Benner, R. Herbst-Irmer, S. Demir, D. Stalke, *Chemistry A European J* **2021**, *27*, 12310–12319.

[274] R. A. Layfield, A. Bashall, M. McPartlin, J. M. Rawson, D. S. Wright, *Dalton Trans.* **2006**, 1660–1666.

[275] S. Mukherjee, J. Lu, G. Velmurugan, S. Singh, G. Rajaraman, J. Tang, S. K. Ghosh, *Inorg. Chem.* **2016**, *55*, 11283–11298.

[276] C.-M. Liu, X. Hao, D.-Q. Zhang, *Applied Organom Chemis* **2020**, *34*, e5893.

[277] P. Kalita, J. Goura, J. Manuel Herrera Martínez, E. Colacio, V. Chandrasekhar, *Eur J Inorg Chem* **2019**, *2019*, 212–220.

[278] Z.-Y. Liu, X.-K. Huang, Z.-L. Chen, D.-C. Liu, H.-H. Zou, F.-P. Liang, *Applied Organom Chemis* **2021**, *35*, e6325.

[279] D. John, W. Urland, *Eur J Inorg Chem* **2006**, *2006*, 3503–3509.

[280] H. Wang, C. Liu, T. Liu, S. Zeng, W. Cao, Q. Ma, C. Duan, J. Dou, J. Jiang, *Dalton Trans.* **2013**, *42*, 15355–60.

[281] M. Machata, R. Herchel, I. Nemec, Z. Trávníek, *Dalton Trans.* **2017**, *46*, 16294–16305.

[282] M. Zhou, L.-H. Wu, X.-Y. Wu, S.-L. Yao, T.-F. Zheng, X. Xie, S.-J. Liu, *J. Mol. Struc.* **2021**, *1227*, 129689.

[283] H. Zhang, S.-Y. Lin, S. Xue, C. Wang, J. Tang, *Dalton Trans.* **2014**, *43*, 6262–6268.

[284] Z.-S. Meng, F.-S. Guo, J.-L. Liu, J.-D. Leng, M.-L. Tong, *Dalton Trans.* **2012**, *41*, 2320–2329.

[285] X.-Y. Chu, W.-M. Wang, Y.-Y. Nie, J.-Z. Cui, H.-L. Gao, *New J. Chem.* **2018**, *42*, 11417–11429.

[286] I. Mylonas-Margaritis, J. Mayans, S.-M. Sakellakou, C. P. Raptopoulou, V. Psycharis, A. Escuer, S. P. Perlepes, *Magnetochemistry* **2017**, *3*, 5.

[287] S.-S. Bao, L.-F. Ma, Y. Wang, L. Fang, C.-J. Zhu, Y.-Z. Li, L.-M. Zheng, *Chemistry A European J* **2007**, *13*, 2333–2343.

[288] K. Ehama, Y. Ohmichi, S. Sakamoto, T. Fujinami, N. Matsumoto, N. Mochida, T. Ishida, Y. Sunatsuki, M. Tsuchimoto, N. Re, *Inorg. Chem.* **2013**, *52*, 12828–12841.

[289] J. Xiong, H.-Y. Ding, Y.-S. Meng, C. Gao, X.-J. Zhang, Z.-S. Meng, Y.-Q. Zhang, W. Shi, B.-W. Wang, S. Gao, *Chem. Sci.* **2017**, *8*, 1288–1294.

[290] S. Ullmann, P. Hahn, L. Blömer, A. Mehnert, C. Laube, B. Abel, B. Kersting, *Dalton Trans.* **2019**, *48*, 3893–3905.

[291] A.-J. Hutchings, F. Habib, R. J. Holmberg, I. Korobkov, M. Murugesu, *Inorg. Chem.* **2014**, *53*, 2102–2112.

[292] A. Rohatgi, *WebPlotDigitizer*, version 5.2, **2024**.

[293] G. E. P. Box, K. B. Wilson in *Breakthroughs in Statistics*, (Eds.: S. Kotz, N. L. Johnson), Springer New York, New York, NY, **1992**, pp. 270–310.

[294] P. Pollak, F. Weigend, *J Chem Theory Comput* **2017**, *13*, 3696–3705.

[295] Y. J. Franzke, L. Spiske, P. Pollak, F. Weigend, *J Chem Theory Comput* **2020**, *16*, 5658–5674.

[296] G. Hong, M. Dolg, L. Li, *Chem. Phys. Lett.* **2001**, *334*, 396–402.

[297] M. Bursch, J.-M. Mewes, A. Hansen, S. Grimme, *Angew Chem Int Ed* **2022**, *61*, e202205735.

[298] Y. Wang, X. Jin, H. S. Yu, D. G. Truhlar, X. He, *Proc. Natl. Acad. Sci. U.S.A.* **2017**, *114*, 8487–8492.

[299] J. Sun, A. Ruzsinszky, J. P. Perdew, *Phys. Rev. Lett.* **2015**, *115*, 036402.

[300] S. Grimme, *J. Phys. Chem. A* **2005**, *109*, 3067–3077.

[301] H. Bahmann, A. Rodenberg, A. V. Arbuznikov, M. Kaupp, *J. Chem. Phys.* **2007**, *126*, 011103.

[302] C. Holzer, Y. J. Franzke, *J. Chem. Phys.* **2022**, *157*, 034108.

[303] C. Holzer, Y. J. Franzke, *J. Chem. Theory Comput.* **2025**, *21*, 202–217.

[304] S. Fürst, M. Kaupp, A. Wodyski, *J. Chem. Theory Comput.* **2023**, *19*, 8639–8653.

[305] I. D. P. R. Moreira, F. Illas, R. L. Martin, *Phys. Rev. B* **2002**, *65*, 155102.

[306] P.-B. Jin, Q.-C. Luo, G. K. Gransbury, R. E. P. Winpenny, D. P. Mills, Y.-Z. Zheng, *Chem. Sci.* **2025**, *16*, 1907–1924.

[307] J. J. Le Roy, M. Jeletic, S. I. Gorelsky, I. Korobkov, L. Ungur, L. F. Chibotaru, M. Murugesu, *J. Am. Chem. Soc.* **2013**, *135*, 3502–3510.

[308] W. Huang, J. J. Le Roy, S. I. Khan, L. Ungur, M. Murugesu, P. L. Diaconescu, *Inorg. Chem.* **2015**, *54*, 2374–2382.

[309] M. Liu, Y.-C. Chen, A. Mondal, H. Wang, M.-L. Tong, R. A. Layfield, F.-S. Guo, *J. Am. Chem. Soc.* **2025**, jacs.5c00707.

[310] K. R. McClain, A. H. Vincent, A. Rajabi, D. X. Ngo, K. R. Meihaus, F. Furche, B. G. Harvey, J. R. Long, *J. Am. Chem. Soc.* **2024**, *146*, 32708–32716.

[311] A. E. Reed, R. B. Weinstock, F. Weinhold, *J. Chem. Phys.* **1985**, *83*, 735–746.

[312] K. Pearson, *Proc. R. Soc. Lond.* **1895**, *58*, 240–242.

[313] C. Spearman, *The American Journal of Psychology* **1904**, *15*, 72.

[314] E. Moreno-Pineda, Y. Lan, O. Fuhr, W. Wernsdorfer, M. Ruben, *Chem. Sci.* **2017**, *8*, 1178–1185.

[315] K. H. Zangana, E. M. Pineda, R. E. P. Winpenny, *Dalton Trans.* **2014**, *43*, 17101–17107.

[316] A. Kovács, *Chem. Phys. Lett.* **2000**, *319*, 238–246.

[317] Vipanchi, K. R. Vignesh, *Inorg. Chem.* **2025**, acs.inorgchem.5c03532.

[318] G. David, B. Le Guennic, D. Reta, *Chem. Commun.* **2024**, *60*, 11988–11991.

[319] *Materials Data on GdCl3 by Materials Project*, LBNL Materials Project; Lawrence Berkeley National Laboratory (LBNL), Berkeley, CA (United States), United States, **2020**.

[320] C. Au, R. Au, *Acta Cryst* **1967**, *23*, 1112–1112.

[321] K. Fink, C. Wang, V. Staemmler, *Int. J. Quant. Chem.* **1997**, *65*, 633–641.

[322] M. Cranmer, Interpretable Machine Learning for Science with PySR and SymbolicRegression.Jl, version 3, **2023**, `https://arxiv.org/abs/2305.01582` (visited on 10/05/2025), pre-published.

[323] C. Wang, K. Fink, V. Staemmler, *Chemical Physics* **1995**, *201*, 87–94.

[324] A. Szabo, N. S. Ostlund, *Modern Quantum Chemistry: Introduction to Advanced Electronic Structure Theory*, Dover Publications, Inc, Mineola, New York, **1996**.

[325] S. Roy, P. Shukla, N. Ahmed, M.-H. Du, I. Tarannum, X.-J. Kong, T. Gupta, S. K. Singh, S. Das, *Dalton Trans.* **2022**, *51*, 18187–18202.

[326] L. H. Ahrens, *Geochim. Cosmochim. Acta* **1952**, *2*, 155–169.

[327] P. Su, H. Li, *J. Chem. Phys.* **2009**, *131*, 014102.

[328] L. Noodleman, E. R. Davidson, *Chemical Physics* **1986**, *109*, 131–143.

[329] J. Corredoira-Vázquez, C. González-Barreira, M. Fondo, A. M. García-Deibe, J. Sanmartín-Matalobos, S. Gómez-Coca, E. Ruiz, E. Colacio, *Inorg. Chem.* **2022**, *61*, 9946–9959.

[330] G. Brunet, F. Habib, I. Korobkov, M. Murugesu, *Inorg. Chem.* **2015**, *54*, 6195–6202.

[331] Z. Xie, K. Chui, Q. Yang, T. C. W. Mak, J. Sun, *Organometallics* **1998**, *17*, 3937–3944.

[332] Y. Huo, Y.-C. Chen, S.-G. Wu, J.-L. Liu, J.-H. Jia, W.-B. Chen, B.-L. Wang, Y.-Q. Zhang, M.-L. Tong, *Inorg Chem* **2019**, *58*, 1301–1308.

[333] W. J. Evans, D. G. Giarikos, M. A. Johnston, M. A. Greci, J. W. Ziller, *J. Chem. Soc. Dalton Trans.* **2002**, 520–526.

[334] W. Lamberts, H. Lueken, U. Elsenhans, *Inorganica Chimica Acta* **1986**, *121*, 81–87.

[335] M. Li, H. Wu, Z. Xia, V. Montigaud, O. Cador, B. Le Guennic, H. Ke, W. Wang, G. Xie, S. Chen, *Chem Commun (Camb)* **2019**, *55*, 14661–14664.

[336] L. Dong, Y.-B. Lu, S.-D. Zhu, J.-W. Wu, X.-T. Zhang, Y. Liao, C.-M. Liu, S.-J. Liu, Y.-R. Xie, S.-Y. Zhang, *CrystEngComm* **2021**, *23*, 645–652.

[337] D. Lüert, A.-K. Kreyenschmidt, C. M. Legendre, R. Herbst-Irmer, D. Stalke, *Inorg. Chem.* **2022**, *61*, 5234–5244.

[338] K. S. Pedersen, G. Lorusso, J. J. Morales, T. Weyhermüller, S. Piligkos, S. K. Singh, D. Larsen, M. Schau-Magnussen, G. Rajaraman, M. Evangelisti, J. Bendix, *Angew Chem Int Ed* **2014**, *53*, 2394–2397.

[339] G. B. Deacon, D. J. Evans, P. C. Junk, E. Lork, R. Mews, B. emva, *Dalton Trans.* **2005**, 2237.

[340] D. A. Buschmann, H. M. Dietrich, J. Durrant, C. Maichle-Mössmer, J. Tang, R. A. Layfield, R. Anwander, *Inorg. Chem.* **2025**, *64*, 2795–2808.

[341] R. F. W. Bader, *Atoms in Molecules: A Quantum Theory*, Clarendon, Oxford, **1990**.

[342] R. F. W. Bader, *J. Phys. Chem. A* **1998**, *102*, 7314–7323.

[343] R. F. W. Bader, H. Essén, *J. Chem. Phys.* **1984**, *80*, 1943–1960.

[344] E. Espinosa, E. Molins, C. Lecomte, *Chem. Phys. Lett.* **1998**, *285*, 170–173.

[345] B. Bankiewicz, P. Matczak, M. Palusiak, *J. Phys. Chem. A* **2012**, *116*, 452–459.

[346] M. L. Kuznetsov, *Int J of Quantum Chemistry* **2019**, *119*, e25869.

[347] S. Shahbazian, *Chemistry A European J* **2018**, *24*, 5401–5405.

[348] C. R. Wick, T. Clark, *J Mol Model* **2018**, *24*, 142.

[349] J. Poater, D. M. Andrada, M. Solà, C. Foroutan-Nejad, *Phys. Chem. Chem. Phys.* **2022**, *24*, 2344–2348.

[350] S. Kozuch, J. M. L. Martin, *J Chem Theory Comput* **2013**, *9*, 1918–31.

[351] A. Siiskonen, A. Priimagi, *J Mol Model* **2017**, *23*, 50.

[352] S. Boys, F. Bernardi, *Molecular Physics* **1970**, *19*, 553–566.

[353] J. R. Alvarez-Idaboy, A. Galano, *Theor Chem Acc* **2010**, *126*, 75–85.

[354] J. Witte, J. B. Neaton, M. Head-Gordon, *J. Chem. Phys.* **2016**, *144*, 194306.

[355] T. Ziegler, A. Rauk, *Inorg. Chem.* **1979**, *18*, 1755–1759.

[356] T. Ziegler, A. Rauk, *Inorg. Chem.* **1979**, *18*, 1558–1565.

[357] K. Kitaura, K. Morokuma, *Int J of Quantum Chemistry* **1976**, *10*, 325–340.

[358] A. E. Reed, F. Weinhold, L. A. Curtiss, D. J. Pochatko, *J. Chem. Phys.* **1986**, *84*, 5687–5705.

[359] B. Jeziorski, R. Moszynski, K. Szalewicz, *Chem. Rev.* **1994**, *94*, 1887–1930.

[360] M. A. Blanco, A. Martín Pendás, E. Francisco, *J. Chem. Theory Comput.* **2005**, *1*, 1096–1109.

[361] A. Martín Pendás, M. A. Blanco, E. Francisco, *J. Chem. Phys.* **2006**, *125*, 184112.

[362] J. Thirman, E. Engelage, S. M. Huber, M. Head-Gordon, *Phys. Chem. Chem. Phys.* **2018**, *20*, 905–915.

[363] J. Wolf, F. Huber, N. Erochok, F. Heinen, V. Guérin, C. Y. Legault, S. F. Kirsch, S. M. Huber, *Angew Chem Int Ed* **2020**, *59*, 16496–16500.

[364] V. V. Sivchik, A. I. Solomatina, Y.-T. Chen, A. J. Karttunen, S. P. Tunik, P.-T. Chou, I. O. Koshevoy, *Angew Chem Int Ed* **2015**, *54*, 14057–14060.

[365] V. P. Oliveira, B. L. Marcial, F. B. C. Machado, E. Kraka, *Materials* **2019**, *13*, 55.

[366] I. Benito, R. M. Gomila, A. Frontera, *CrystEngComm* **2022**, *24*, 4440–4446.

[367] S. S. Xantheas, *J. Chem. Phys.* **1994**, *100*, 7523–7534.

[368] S. S. Xantheas, *Chemical Physics* **2000**, *258*, 225–231.

[369] J. Dominikowska, *Phys Chem Chem Phys* **2020**, *22*, 21938–21946.

[370] J. Dominikowska, A. J. Rybarczyk-Pirek, C. Fonseca Guerra, *Crystal Growth & Design* **2021**, *21*, 597–607.

[371] J. Dominikowska, F. M. Bickelhaupt, M. Palusiak, C. Fonseca Guerra, *Chemphyschem* **2016**, *17*, 474–80.

[372] R. D. Parra, *Computational and Theoretical Chemistry* **2015**, *1066*, 47–54.

[373] R. D. Parra, *Chem. Phys. Lett.* **2022**, *803*, 139825.

[374] S. Scheiner, *J. Phys. Chem. A* **2022**, *126*, 6443–6455.

[375] J. George, V. L. Deringer, R. Dronskowski, *J. Phys. Chem. A* **2014**, *118*, 3193–3200.

[376] P. Vermeeren, L. P. Wolters, G. Paragi, C. Fonseca Guerra, *ChemPlusChem* **2021**, *86*, 812–819.

[377] H. R. Masoodi, S. Bagheri, M. Ranjbar, *Molecular Physics* **2016**, *114*, 3464–3474.

[378] L. P. Wolters, N. W. G. Smits, C. F. Guerra, *Phys. Chem. Chem. Phys.* **2015**, *17*, 1585–1592.

[379] J. Braun, Karlsruher Institut für Technologie (KIT), **2023**.

[380] J. Braun, C. Pachl, O. Fuhr, G. E. Kostakis, J. Tang, C. E. Anson, K. Fink, A. K. Powell, *Crystal Growth & Design* **2025**, *25*, 6593–6603.

[381] M. H. Kolá, P. Deepa, H. Ajani, A. Pecina, P. Hobza in *Halogen Bonding II*, *Vol. 359*, (Eds.: P. Metrangolo, G. Resnati), Springer International Publishing, Cham, **2014**, pp. 1–25.

[382] H. Tian, M. Wang, L. Zhao, Y.-N. Guo, Y. Guo, J. Tang, Z. Liu, *Chemistry* **2012**, *18*, 442–5.

[383] I. Machado, M. Fernández, L. Becco, B. Garat, R. Brissos, N. Zabarska, P. Gamez, F. Marques, I. Correia, J. Costa Pessoa, D. Gambino, *Inorganica Chimica Acta* **2014**, *420*, 39–46.

[384] C. Radunsky, J. Kösters, J. Müller, *Inorganica Chimica Acta* **2015**, *428*, 14–20.

[385] M. Mohan, N. S. Gupta, L. Chandra, N. K. Jha, R. S. Prasad, *Inorganica Chimica Acta* **1988**, *141*, 185–192.

[386] J. Tang, J. S. Costa, G. Aromí, I. Mutikainen, U. Turpeinen, P. Gamez, J. Reedijk, *Eur J Inorg Chem* **2007**, *2007*, 4119–4122.

[387] J. Tang, J. Sánchez Costa, S. Smulders, G. Molnár, A. Bousseksou, S. J. Teat, Y. Li, G. A. Van Albada, P. Gamez, J. Reedijk, *Inorg. Chem.* **2009**, *48*, 2128–2135.

[388] Z.-S. Meng, J.-L. Liu, J.-D. Leng, F.-S. Guo, M.-L. Tong, *Polyhedron* **2011**, *30*, 3095–3099.

[389] L. Basche, Investigation of Ligand Field Modifications on Lanthanide(III) Complexes: Structure, Magnetism and Optical Properties, Karlsruher Institut für Technologie (KIT), **2023**.

[390] J. Goura, J. P. S. Walsh, F. Tuna, V. Chandrasekhar, *Inorg. Chem.* **2014**, *53*, 3385–3391.

[391] J. Goura, J. P. S. Walsh, F. Tuna, V. Chandrasekhar, *Dalton Trans.* **2015**, *44*, 1142–1149.

[392] A. Bondi, *J. Phys. Chem.* **1964**, *68*, 441–451.

[393] F.-S. Guo, B. M. Day, Y.-C. Chen, M.-L. Tong, A. Mansikkamäki, R. A. Layfield, *Angew Chem Int Ed* **2017**, *56*, 11445–11449.

[394] J. Emerson-King, J. Baldwin, S. C. Corner, W. J. A. Blackmore, N. F. Chilton, D. P. Mills, *J. Am. Chem. Soc.* **2025**, *147*, 35555–35566.

[395] F. Benner, R. Jena, A. L. Odom, S. Demir, *J. Am. Chem. Soc.* **2025**, *147*, 8156–8167.

[396] J. Emerson-King, G. K. Gransbury, B. E. Atkinson, W. J. A. Blackmore, G. F. S. Whitehead, N. F. Chilton, D. P. Mills, *Nature* **2025**, *643*, 125–129.

[397] K. L. M. Harriman, J. L. Brosmer, L. Ungur, P. L. Diaconescu, M. Murugesu, *J. Am. Chem. Soc.* **2017**, *139*, 1420–1423.

[398] K. L. M. Harriman, J. Murillo, E. A. Suturina, S. Fortier, M. Murugesu, *Inorg. Chem. Front.* **2020**, *7*, 4805–4812.

[399] K. Yang, R. Sun, J. Zhao, C. Deng, B. Wang, S. Gao, W. Huang, *Inorg. Chem.* **2023**, *62*, 9892–9903.

[400] Y.-S. Ding, N. F. Chilton, R. E. P. Winpenny, Y.-Z. Zheng, *Angew Chem Int Ed* **2016**, *55*, 16071–16074.

[401] C. A. Mattei, N. Mavragani, A. A. Kitos, M. Briganti, D. A. Gálico, M. Murugesu, M. Perfetti, *Inorg. Chem.* **2025**, acs.inorgchem.5c03279.

[402] M. Briganti, G. F. Garcia, J. Jung, R. Sessoli, B. Le Guennic, F. Totti, *Chem. Sci.* **2019**, *10*, 7233–7245.

[403] M. Briganti, E. Lucaccini, L. Chelazzi, S. Ciattini, L. Sorace, R. Sessoli, F. Totti, M. Perfetti, *J. Am. Chem. Soc.* **2021**, *143*, 8108–8115.

[404] A. S. Manvell, R. Pfleger, N. A. Bonde, M. Briganti, C. A. Mattei, T. B. Nannestad, H. Weihe, A. K. Powell, J. Ollivier, J. Bendix, M. Perfetti, *Chem. Sci.* **2024**, *15*, 113–123.

[405] R. Herchel, P. Zoufalý, I. Nemec, *RSC Adv.* **2019**, *9*, 569–575.

[406] B. E. Matheson, T. N. Dais, M. E. Donaldson, G. J. Rowlands, P. G. Plieger, *Inorg. Chem. Front.* **2023**, *10*, 6427–6439.

[407] P. A. Kumar, *Indian J. Chem.* **1998**, 460–465.

[408] A. S. Armenis, G. P. Bakali, C. L. Brantley, C. P. Raptopoulou, V. Psycharis, L. Cunha-Silva, G. Christou, T. C. Stamatatos, *Dalton Trans.* **2022**, *51*, 18077–18089.

[409] V. Lozovan, G. Borodi, I. Perhaia, A. Turza, A. M. Brânzanic, A. Pîrnu, L. E. Murean, *J. Mol. Struc.* **2025**, *1322*, 140397.

[410] J. Arneth, C. Pachl, G. Greif, B. Beier, P. W. Roesky, K. Fink, R. Klingeler, Towards Understanding Prolate 4f Monomers: Numerical Predictions and Experimental Validation of Electronic Properties and Slow Relaxation in a Muffin-shaped Er(III) Complex, version 1, **2025**, https://arxiv.org/abs/2507.15547 (visited on 11/26/2025), pre-published.

[411] U. Meier, V. Staemmler, *Theor. Chim. Acta* **1989**, *76*, 95–111.

[412] B. Yin, C.-C. Li, *Phys. Chem. Chem. Phys.* **2020**, *22*, 9923–9933.

[413] B. Yin, L. Luo, *Phys. Chem. Chem. Phys.* **2021**, *23*, 3093–3105.

[414] Q.-Q. Yang, Y.-F. Wang, Y.-X. Wang, M.-J. Tang, B. Yin, *Phys. Chem. Chem. Phys.* **2023**, *25*, 18387–18399.

[415] N. V. Prokof'ev, P. C. E. Stamp, *J Low Temp Phys* **1996**, *104*, 143–209.

[416] N. V. Prokof'ev, P. C. E. Stamp, *Rep. Prog. Phys.* **2000**, *63*, 669–726.

[417] F. Luis, M. J. Martínez-Pérez, O. Montero, E. Coronado, S. Cardona-Serra, C. Martí-Gastaldo, J. M. Clemente-Juan, J. Sesé, D. Drung, T. Schurig, *Phys. Rev. B* **2010**, *82*, 060403.

[418] A. Bischoff, Vertieferarbeit, Karlsruher Institut für Technologie (KIT), Karlsruhe, **2025**.

[419] M. Stradiotto, R. J. Lundgren, *Ligand Design in Metal Chemistry: Reactivity and Catalysis*, Wiley, Chichester, West Sussex, UK, **2016**.

[420] J. D. Curry, M. A. Robinson, D. H. Busch, *Inorg. Chem.* **1967**, *6*, 1570–1574.

[421] G. Chessa, G. Marangoni, B. Pitteri, V. Bertolasi, V. Ferretti, G. Gilli, *J. Chem. Soc. Dalton Trans.* **1988**, 1479–1485.

[422] B. Chiswell, D. Litster, *Inorganica Chimica Acta* **1978**, *29*, 25–36.

[423] R. F. Pfleger, S. Schlittenhardt, M. P. Merkel, M. Ruben, K. Fink, C. E. Anson, J. Bendix, A. K. Powell, *Chemistry* **2021**, *27*, 15085–15094.

[424] Z.-X. Jiang, J.-L. Liu, Y.-C. Chen, J. Liu, J.-H. Jia, M.-L. Tong, *Chem. Commun.* **2016**, *52*, 6261–6264.

[425] M. Sakamoto, N. Matsumoto, H. Okawa, *Bull. Chem. Soc. Jpn.* **1991**, *64*, 691–693.

[426] R. F. Pfleger, Design of Lanthanide Coordination Compounds with Unusual Ligands and High Symmetry for Molecular Magnetism, Karlsruher Institut für Technologie (KIT), **2022**.

[427] M. A. M. Tummeley, M. H. Hoock, K. Gröpl, R. Pfleger, T. Hochdörffer, T. Hunsicker, J. A. Wolny, J. Zhao, B. Lavina, M. Y. Hu, T. Toellner, E. E. Alp, H. Kämmerer, C. E. Anson, A. K. Powell, V. Schünemann, *Interactions* **2024**, *245*, 18.

[428] G. Paolucci, G. Marangoni, *Inorganica Chimica Acta* **1977**, *24*, L5–L6.

[429] G. Paolucci, G. Marangoni, G. Bandoli, D. A. Clemente, *J. Chem. Soc. Dalton Trans.* **1980**, 459–466.

[430] E. C. Constable, J. M. Holmes, P. R. Raithby, *Polyhedron* **1991**, *10*, 127–132.

[431] E. C. Constable, J. M. Holmes, *Inorganica Chimica Acta* **1987**, *126*, 187–193.

[432] M. Mantina, A. C. Chamberlin, R. Valero, C. J. Cramer, D. G. Truhlar, *J Phys Chem A* **2009**, *113*, 5806–12.

[433] G. R. Desiraju, R. Parthasarathy, *J. Am. Chem. Soc.* **1989**, *111*, 8725–8726.

[434] Y. Schneider, Karlsruher Institut für Technologie (KIT), **2025**.

[435] P. Fuentealba, H. Preuss, H. Stoll, L. Von Szentpály, *Chem. Phys. Lett.* **1982**, *89*, 418–422.

[436] *Riedel Moderne Anorganische Chemie*, (Eds.: C. Janiak, H.-J. Meyer, D. Gudat, P. Kurz, E. Riedel), De Gruyter, **2018**.

[437] J. Bartolomé, E. Bartolomé, F. Luis, E. Burzurí, A. Camón, G. Filoti, A. M. Ako, J. Braun, V. Mereacre, C. E. Anson, A. K. Powell, *Inorg. Chem.* **2024**, *63*, 24262–24273.

[438] R. D. Cannon, U. A. Jayasooriya, R. Wu, S. K. arapKoske, J. A. Stride, O. F. Nielsen, R. P. White, G. J. Kearley, D. Summerfield, *J. Am. Chem. Soc.* **1994**, *116*, 11869–11874.

[439] W. Cañón-Mancisidor, P. Hermosilla-Ibáñez, E. Spodine, V. Paredes-García, C. J. Gómez-García, G. M. Espallargas, D. Venegas-Yazigi, *Crystal Growth & Design* **2021**, *21*, 6213–6222.

[440] A. N. Georgopoulou, I. Margiolaki, V. Psycharis, A. K. Boudalis, *Inorg. Chem.* **2017**, *56*, 762–772.

[441] B. Kintzel, M. Böhme, D. Plaul, H. Görls, N. Yeche, F. Seewald, H.-H. Klauss, A. A. Zvyagin, E. Kampert, T. Herrmannsdörfer, G. Pascua, C. Baines, H. Luetkens, W. Plass, *Inorg. Chem.* **2023**, *62*, 3420–3430.

[442] J. Schnack, *Dalton Trans.* **2010**, *39*, 4677.

[443] F. E. Sowrey, C. Tilford, S. Wocadlo, C. E. Anson, A. K. Powell, S. M. Bennington, W. Montfrooij, U. A. Jayasooriya, R. D. Cannon, *J. Chem. Soc. Dalton Trans.* **2001**, 862–866.

[444] J. Luzon, K. Bernot, I. J. Hewitt, C. E. Anson, A. K. Powell, R. Sessoli, *Phys. Rev. Lett.* **2008**, *100*, 247205.

[445] P.-H. Guo, J.-L. Liu, Z.-M. Zhang, L. Ungur, L. F. Chibotaru, J.-D. Leng, F.-S. Guo, M.-L. Tong, *Inorg. Chem.* **2012**, *51*, 1233–1235.

[446] Y.-X. Wang, W. Shi, H. Li, Y. Song, L. Fang, Y. Lan, A. K. Powell, W. Wernsdorfer, L. Ungur, L. F. Chibotaru, M. Shen, P. Cheng, *Chem. Sci.* **2012**, *3*, 3366.

[447] S. Xue, X.-H. Chen, L. Zhao, Y.-N. Guo, J. Tang, *Inorg. Chem.* **2012**, *51*, 13264–13270.

[448] G. Fernandez Garcia, D. Guettas, V. Montigaud, P. Larini, R. Sessoli, F. Totti, O. Cador, G. Pilet, B. Le Guennic, *Angew Chem Int Ed* **2018**, *130*, 17335–17339.

[449] Q. Yang, L. Ungur, L. F. Chibotaru, J. Tang, *Chem. Commun.* **2022**, *58*, 1784–1787.

[450] L. Ungur, S. K. Langley, T. N. Hooper, B. Moubaraki, E. K. Brechin, K. S. Murray, L. F. Chibotaru, *J. Am. Chem. Soc.* **2012**, *134*, 18554–18557.

[451] S.-Y. Lin, W. Wernsdorfer, L. Ungur, A. K. Powell, Y.-N. Guo, J. Tang, L. Zhao, L. F. Chibotaru, H.-J. Zhang, *Angew Chem Int Ed* **2012**, *51*, 12767–12771.

[452] Q. Zhang, M. L. Baker, S. Li, M. P. Sarachik, J. J. Baldoví, A. Gaita-Ariño, E. Coronado, D. I. Alexandropoulos, T. C. Stamatatos, *Nanoscale* **2019**, *11*, 15131–15138.

[453] K. R. Vignesh, A. Soncini, S. K. Langley, W. Wernsdorfer, K. S. Murray, G. Rajaraman, *Nat Commun* **2017**, *8*, 1023.

[454] J. Wu, X.-L. Li, M. Guo, L. Zhao, Y.-Q. Zhang, J. Tang, *Chem. Commun.* **2018**, *54*, 1065–1068.

[455] H. Kaemmerer, A. Baniodeh, Y. Peng, E. Moreno-Pineda, M. Schulze, C. E. Anson, W. Wernsdorfer, J. Schnack, A. K. Powell, *J. Am. Chem. Soc.* **2020**, *142*, 14838–14842.

[456] A. Gharu, K. R. Vignesh, *Dalton Trans.* **2024**, 10.1039.D4DT01800A.

[457] J. Goura, E. Colacio, J. M. Herrera, E. A. Suturina, I. Kuprov, Y. Lan, W. Wernsdorfer, V. Chandrasekhar, *Chemistry A European J* **2017**, *23*, 16621–16636.

[458] H.-L. Zhang, Y.-Q. Zhai, L. Qin, L. Ungur, H. Nojiri, Y.-Z. Zheng, *Matter* **2020**, *2*, 1481–1493.

[459] A. S. Zimmermann, D. Meier, M. Fiebig, *Nat Commun* **2014**, *5*, 4796.

[460] K. R. Vignesh, G. Rajaraman, *ACS Omega* **2021**, *6*, 32349–32364.

[461] G. Lu, Y. Liu, W. Deng, G.-Z. Huang, Y.-C. Chen, J.-L. Liu, Z.-P. Ni, M. Giansiracusa, N. F. Chilton, M.-L. Tong, *Inorg. Chem. Front.* **2020**, *7*, 2941–2948.

[462] F. Weigend, R. Ahlrichs, *Phys Chem Chem Phys* **2005**, *7*, 3297–305.

[463] K. Eichkorn, F. Weigend, O. Treutler, R. Ahlrichs, *Theor. Chim. Acta* **1997**, *97*, 119–124.

[464] F. Weigend, *Phys. Chem. Chem. Phys.* **2002**, *4*, 4285–4291.

[465] D. Peng, N. Middendorf, F. Weigend, M. Reiher, *J. Chem. Phys.* **2013**, *138*, 184105.

[466] C. van Wüllen, *J. Chem. Phys.* **2004**, *120*, 7307–13.

[467] C. van Wüllen, C. Michauk, *J. Chem. Phys.* **2005**, *123*, 204113.

[468] T. pandas development team, *Pandas-Dev/Pandas: Pandas*, version v2.3.3, Zenodo, **2025**.

9. List of Publications

1. J. Braun, C. Pachl, O. Fuhr, G. E. Kostakis, J. Tang, C. E. Anson, K. Fink, A. K. Powell, "An Unexpected Tetragonal Network of Seven-Connected Er6 Clusters Stabilized by Multiple Halogen Bonds through Cooperative Effects" *Crystal Growth & Design* **2025**, 25, 65936603.

2. J. Arneth, C. Pachl, G. Greif, B. Beier, P. W. Roesky, K. Fink, R. Klingeler, "Towards Understanding Prolate 4f Monomers: Numerical Predictions and Experimental Validation of Electronic Properties and Slow Relaxation in a Muffin-shaped Er^{III} Complex" *Inorganic Chemistry* **2026**, 65, 7, 3929-3939.

3. S. K. Kuppusamy, C. Pachl, Z. Jing, S. Paul, B. Heinrich, O. Fuhr, S. Klayatskaya, W. Wernsdorfer, A. Powell, K. Fink, M. Ruben, "Ligand-field symmetry and magneto-optical correlations in a luminescent Dy(III) single-molecule magnet", *Dalton Transactions*, **submitted**.

4. C. Pachl, J. Braun, C. Anson, K. Fink, "A Gd-Dimer Benchmark Study: Is DFT an accurate Method for the Prediction of Gadolinium Exchange Coupling Constants?", **to be submitted**.

10. Acknowledgments

This feels like a good time to say thank you to some outstanding people. I want to express my sincerest gratitude to my "Doktormütter" Prof. Karin Fink and Prof. Annie K. Powell, giving me the chance to work on these interesting topics. Thank you for all of the helpful comments and insights, thank you for the chance to travel and present my research on these international conferences and thank you particularly for supporting me to follow my ideas.

I would like to thank three people which I consider something like mentors in the field of molecular magnetism. Dr. Jonas Braun for all his insights and ideas throughout the years, Dr. Chengyu Jin for teaching me when I learned about these calculations and Dr. Christopher Anson for all of the helpful thoughts on crystallography and symmetry.

I would like to extend my gratitude to the amazing people measuring the compounds I made, Dr. Olaf Fuhr and Prof. Dieter Fenske for the SC-XRD measurements as well as Dr. Barbora Brachňaková and Prof. Yan Peng for the magnetic measurements.

I would like to thank the fantastic Johannes Werner, Constantin Weeber, Nikita Matsokin and Florian Bruder for their helpful thoughts and comments on various chapters.

Clearly, I cannot forget about the two students I had the pleasure to supervise, Franziska Gebhard and Andreas Bischoff.

Something I particularly love about my research was how cooperative it is. I would like to thank all of the talented synthetic chemists and physicists I have worked with on the projects throughout my PhD, not all of which found a space in this thesis. These are Dr. Jonas Braun , Daniel Seufert , Dr. Yannik Schneider, Dr. Sukhen Bala and Prashant Anand (AK Powell), Dr. Gerlinde Greif and Dr. Xiaofei Sun (AK Roesky), Rwitabrita Panda (AK Hanf), Dr. Jan Arneth (AK Klingeler), Dr. Sagar Paul (AK Wernsdorfer), Dr. Sören Schlittenhardt and Dr. Senthil Kumar Kuppusamy (AK Ruben).

I also want to thank the entire research groups Powell and Fink for providing such a wonderful work environment where we can value, help and support each other not forgetting that we are all here for a good time (and science). I want to thank especially Daniel Seufert and Constantin Weeber with whom I shared offices at Campus South and North.

Clearly, I would like to thank the Landesgraduiertenförderung and the CRC 1573 "4f for future" for providing me with funding over the past years.

I am very grateful for all of the amazing friends that kept me sane over the last years. This includes those that found me at the beginning of our studies, those I had before, those that play Geoguessr, those that don't and of course the wonderful people I got to know in the recent years.

Finally it is time to thank my family, my amazing brother Alexander, my ever supporting parents Jutta and Norbert, as well as my aunt Karen and grandparents Maria, Franz and Ilse.

This leaves my gifted, loving and enduring Lena. Without you these past years would have been a lot harder. I am just glad that you are with me and excited where we are going next.

A. Appendix

A.1. Appendix for Chapter 3.2

Table A.1.: Unit cell metrics for the three sets of isostrutural Co/Zn-Y/Dy compounds.

	(CoDy)	**(ZnDy)**	**(CoY)**
XRD - Ideal Testbed			
SG	$P2_1/c$	$P2_1/c$	$P2_1/c$
a	19.1521(5)	19.1061(4)	19.2119(6)
b	12.1723(3)	12.1714(3)	12.1547(2)
c	19.5469(5)	19.5184(4)	19.5337(6)
α	90	90	90
β	107.177(2)	107.1520(10)	107.333(2)
γ	90	90	90
XRD - Shen *et al.*[234]			
SG	$P2_1/c$	$P2_1/c$	$C2/c$
a	11.0883(11)	10.864(3)	12.1435(6)
b	16.8917(16)	16.713(5)	20.1725(10)
c	19.9826(15)	18.983(6)	14.3553(7)
α	90	90	90
β	111.442(4)	101.335(4)	97.265(2)
γ	90	90	90
XRD - Xie *et al.*[235]			
SG	$P\bar{1}$	$P\bar{1}$	$P\bar{1}$
a	13.2896(14)	11.3016(16)	11.2773(13)
b	15.4553(18)	11.4641(16)	11.4817(11)
c	17.974(2)	23.981(3)	23.930(3)
α	88.507(5)	102.188(6)	102.194(6)
β	73.305(3)	92.647(6)	92.759(5)
γ	69.809(3)	107.389(5)	107.234(5)

Table A.2.: Continuous SHAPE measures (CSM) for three sets of isostrutural Co/Zn-Y/Dy compounds. 5-7 vertex-polyhedra refer to Co/Zn environments; 8-10 vertex polyhedra refer to the Y/Dy environments.

	(CoDy)	**(ZnDy)**	**(CoY)**
SHAPE - Ideal Testbed			
JCSAPR-9	2.918	2.909	2.844
CSAPR-9	1.788	1.809	1.720
TCTPR-9	2.856	2.747	2.760
MMF-9	1.892	1.859	1.806
vOC-5	3.555	3.619	3.517
TBPY-5	2.273	2.295	2.315
SPY-5	2.650	2.360	2.645
SHAPE - Shen *et al.*[234]			
JBCSAPR-10	3.417	3.244	3.451
JSPC-10	3.929	3.870	4.263
SDD-10	3.784	3.873	4.210
TD-10	2.880	2.993	3.165
HD-10	5.295	5.391	4.709
PBPY-7	0.274	0.299	0.274
CTPR-7	5.457	4.945	4.700
JPBPY-7	4.243	4.053	4.271
SHAPE - Xie *et al.*[235]			
TDD-8	4.513	2.670	2.577
JBTPR-8	2.701	3.218	3.071
BTPR-8	2.863	3.311	3.193
JSD-8	4.856	3.348	3.218
OC-6	1.130	1.943	1.927

Table A.3.: List of reference shapes.

Label	Shape
VOC-5	Vacant octahedron (Johnson square pyramid (J1))
TBPY-5	Trigonal bipyramid
SPY-5	Square pyramid
OC-6	Octahedron
PBPY-7	Pentagonal bipyramid
CTPR-7	Capped trigonal prism
JPBPY-7	Johnson pentagonal bipyramid (J13)
TDD-8	Triangular dodecahedron
JBTPR-8	Johnson - Biaugmented trigonal prism (J50)
BTPR-8	Biaugmented trigonal prism
JSD-8	Snub disphenoid (J84)
JCSAPR-9	Capped square antiprism
	(Gyroelongated square pyramid (J10))
CSAPR-9	Capped square antiprism
TCTPR-9	Tricapped trigonal prism
MMF-9	Muffin
JBCSAPR-10	Bicapped square antiprism
	(Gyroelongated square bipyramid (J17))
JSPC-10	Sphenocorona (J87)
SDD-10	Staggered dodecahedron (2:6:2)
TD-10	Tetradecahedron (2:6:2)
HD-10	Hexadecahedron (2:6:2 or 1:4:4:1)

Table A.4.: RMSD values between coordination polyhedral for three sets of isostructural Co/Zn-Y/Dy compounds. The left columns compare the Y/Dy environments, the right columns compare the Co/Zn environments.

	(CoDy)	**(ZnDy)**	**(CoY)**	**(CoDy)**	**(ZnDy)**	**(CoY)**
Ideal Testbed						
CoDy	0	x	x	0	x	x
ZnDy	0.0613	0	x	0.0841	0	x
CoY	0.0222	0.0299	0	0.0073	0.0508	0
Shen *et al.*[234]						
CoDy	0	x	x	0	x	x
ZnDy	0.0218	0	x	0.0793	0	x
CoY	0.7887	0.7812	0	1.6204	1.6204	0
Xie *et al.*[235]						
CoDy	0	x	x	0	x	x
ZnDy	0.6530	0	x	0.7605	0	x
CoY	0.6463	0.0213	0	0.7574	0.0243	0

Table A.5.: Calculated coupling constants in cm^{-1} for compound **(MnGd)** as part of Franziska Gebhard's Vertiefer Thesis.[236,237] All calculations use the x2c-TZVPPall basis set and use one-component X2C.

functional	***J***
s-vwn	-1.83641
b-p	-1.51136
b-lyp	-1.69323
pbe	-1.52327
tpss	-1.06713
r2scan	-0.46546
tpssh	-0.45400
b3-lyp	-0.35711
hse06	-0.28941
pbe0	-0.28068
m06	-0.30684
bh-lyp	-0.18952
m06-2x	-0.03264
wb97-x	-0.28212
cam-b3lyp	-0.29375

Table A.6.: Mean Absolute Errors (in cm^{-1}) of the excited states in the ground state multiplet calculated for the ideal testbed structure with respect to the model where the H-positions are optimized.

molecule	unopt	pbe
(ZnGd)	0.0087	0.0657
(CoGd)	0.0077	0.0627
(ZnTb)	3.0545	23.9523
(CoTb)	2.3634	16.3752
(ZnDy)	2.5911	24.4791
(CoDy)	2.9140	21.6666
(ZnHo)	0.4043	11.1906
(CoHo)	0.5149	10.1398
(CoEr)	0.4554	9.3897

Table A.7.: Mean Absolute Errors (in cm^{-1}) of the excited states in the ground $^6H_{15/2}$ multiplet calculated for the different ideal testbed structures with respect to the model where the H-positions are optimized. Here, the values of the Dy-calculations are compared when the lanthanide is replaced to Dy directly (opt) or subsequently optimized with DFT (pbe).

	opt		**pbe**	
	Zn	Co	Zn	Co
Y	x	1.8852	x	21.4994
Gd	12.7601	19.3810	23.6497	21.1334
Tb	4.4896	2.8790	25.2746	20.4879
Dy	0	0	24.4791	21.6666
Ho	11.7014	5.4914	25.1066	21.0986
Er	x	3.7216	x	20.6601

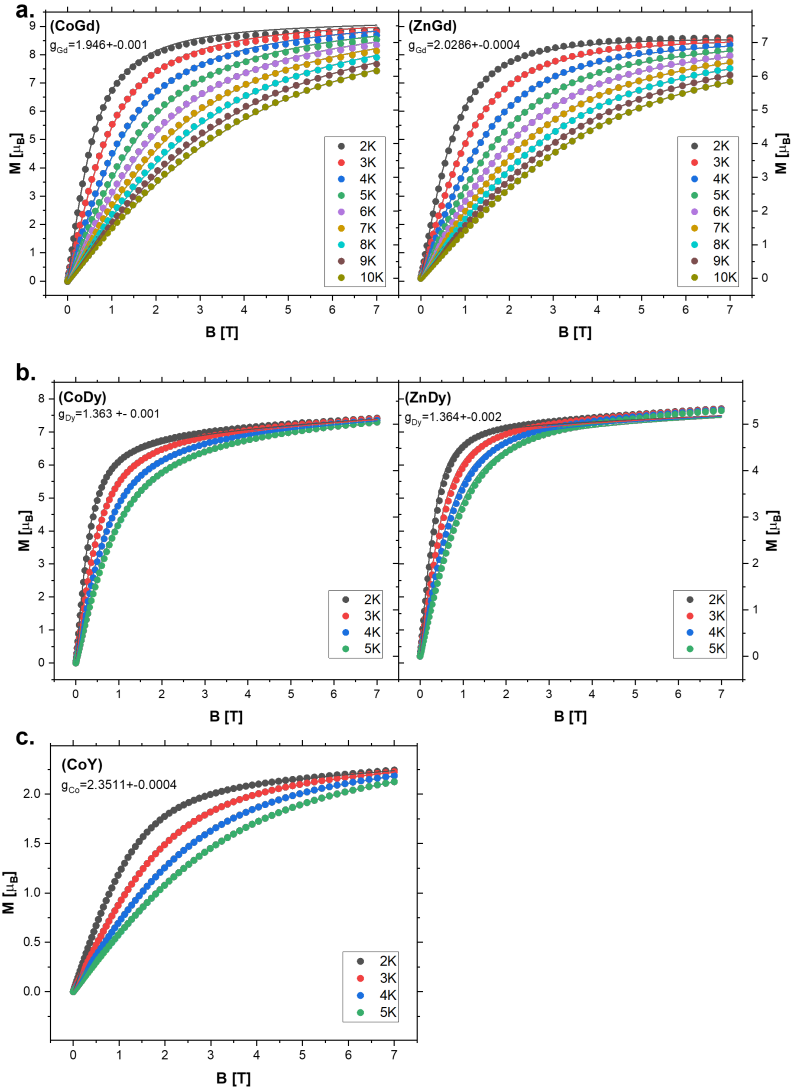

Figure A.1.: Isothermal magnetization for a. **(CoDy)** and **(ZnDy)**, b. **(CoGd)** and **(ZnGd)** and c. **(CoY)**. These are calculated the same way as described shown in Figure 3.11, but with individual g-factors as shown in the figure.

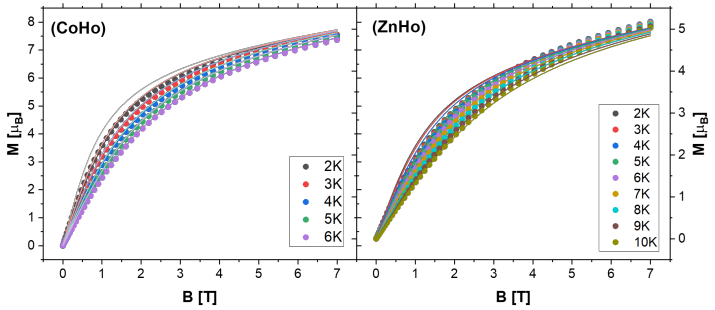

Figure A.2.: Isothermal magnetization for **(CoHo)** and **(ZnHo)**. With respect to **(CoHo)**, the pale lines are simulated using the BS-DFT *J* value and no fit of g, while the colorful lines are fitted with g = 1.255 $\pm$ 0.000 and *J* = -0.010 $\pm$ 0.001. The magnetization for **(ZnHo)** is fitted with g = 1.248 $\pm$ 0.002.

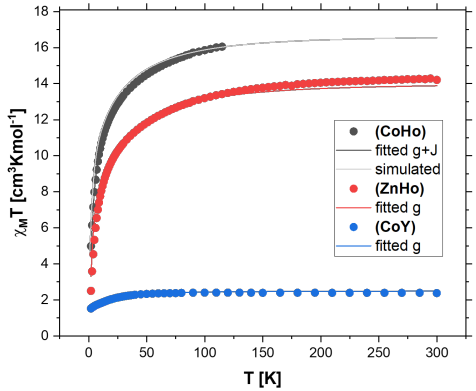

Figure A.3.: Molar susceptibility for compounds **(CoHo)**, **(ZnHo)** and **(CoY)**. With respect to **(CoHo)**, the pale lines are simulated using the BS-DFT *J* value and no fit of g, while the colorful lines are fitted with g=1.255 $\pm$ 0.000 and *J*=-0.010 $\pm$ 0.001. The susceptibility for **(ZnHo)** is fitted with g = 1.248 $\pm$ 0.002.

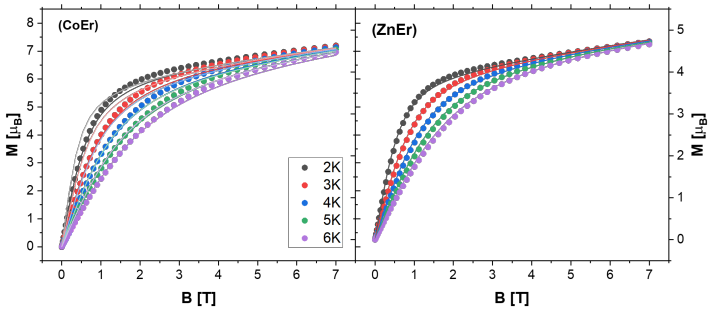

Figure A.4.: Isothermal magnetization for **(CoEr)** and **(ZnEr)**. With respect to **(CoEr)**, the pale lines are simulated using the BS-DFT *J* value and no fit of g, while the colorful lines are fitted with g = 1.205 $\pm$ 0.001 and *J* = 0.018 $\pm$ 0.001. The magnetization for **(ZnEr)** is fitted with g = 1.182 $\pm$ 0.001.

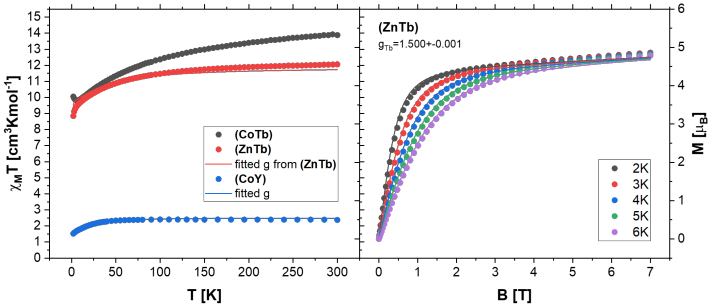

Figure A.5.: Magnetic susceptibility of **(CoTb)**, **(ZnTb)** and **(CoY)** as well as the fits for **(ZnTb)** and **(CoY)**. **(ZnTb)** was fitted with g = 1.501 $\pm$ 0.001. It is immediately clear that the data for **(CoTb)** does not make sense: Firstly, it does not saturate at high temperatures. Secondly, it shows an upturn at low temperatures indicating ferromagnetic coupling. But if it couples ferromagnetically, $\chi_M T$ must always be greater or equal to the sum of **(CoY)** and **(ZnTb)**. Considering that the experimental values for **(CoTb)** and **(ZnTb)** touch at around 20 K this cannot be fulfilled. consequently, the data for **(CoTb)** is not further evaluated.

A.2. Appendix for Chapter 3.3

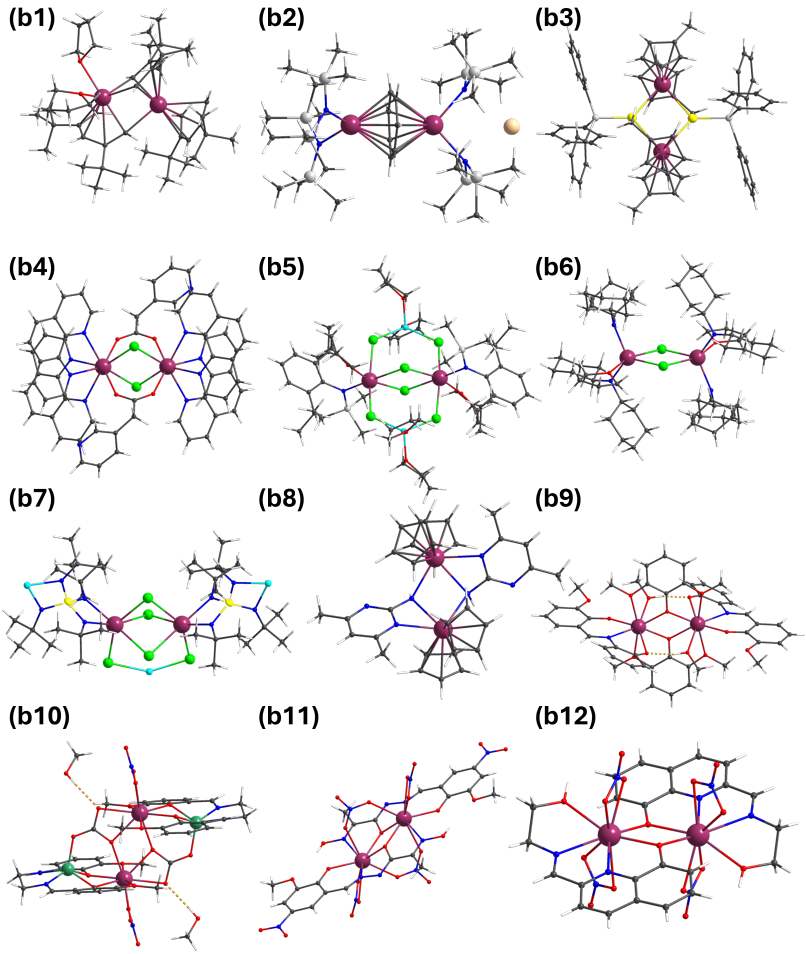

Figure A.6.: Pictures of compounds **(b1)**-**(b12)**.

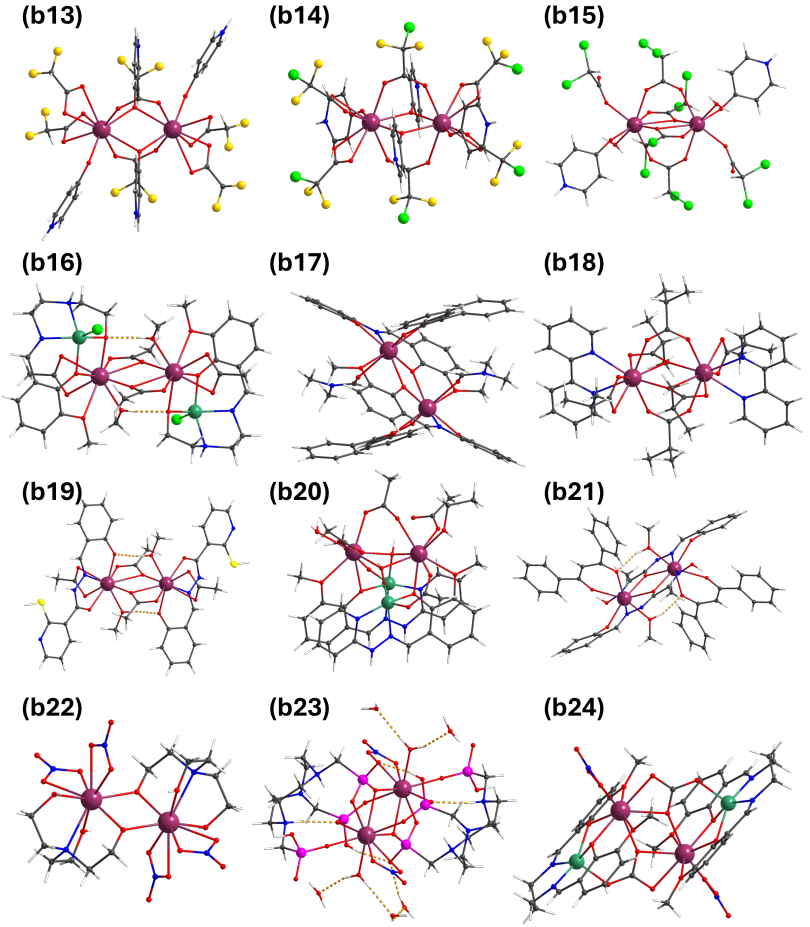

Figure A.7.: Pictures of compounds **(b13)**-**(b24)**.

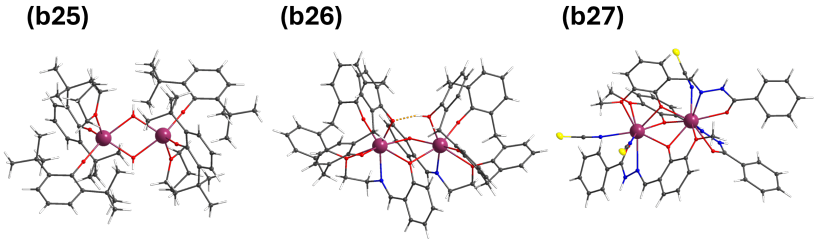

Figure A.8.: Pictures of compounds **(b25)**-**(b27)**.

Table A.8.: NBO charges of the HS state for compounds **(b1)**–**(b27)** using the bh-lyp functional.

nr.	NBO charge		Gd1 NBO occupation			Gd1 NBO occupation		
	Gd1	Gd2	6s	5d	4f	6s	5d	4f
(b1)	1.92852	1.88749	0.14	0.83	7.03	0.16	0.87	7.03
(b2)	2.04156	1.95041	0.10	0.74	7.05	0.1	0.79	7.05
(b3)	1.89266	1.89262	0.15	0.80	7.03	0.15	0.80	7.03
(b4)	1.86537	1.86537	0.21	0.84	7.03	0.21	0.84	7.03
(b5)	1.83332	1.83332	0.19	0.80	7.04	0.19	0.80	7.04
(b6)	1.97764	1.97764	0.12	0.73	7.04	0.12	0.73	7.04
(b7)	1.77332	1.77335	0.20	0.87	7.04	0.2	0.87	7.04
(b8)	1.70863	1.72333	0.15	1.08	7.03	0.14	1.06	7.03
(b9)	2.14326	2.14326	0.14	0.65	7.03	0.14	0.65	7.03
(b10)	2.00513	2.00514	0.16	0.74	7.03	0.16	0.74	7.03
(b11)	1.8105	1.81048	0.20	0.92	7.03	0.20	0.92	7.03
(b12)	1.88535	1.88530	0.18	0.85	7.03	0.18	0.85	7.03
(b13)	2.00898	2.00899	0.19	0.72	7.03	0.19	0.72	7.03
(b14)	2.01642	2.01640	0.18	0.72	7.03	0.18	0.72	7.03
(b15)	2.02873	2.02874	0.16	0.75	7.03	0.16	0.75	7.03
(b16)	2.07567	2.07567	0.16	0.66	7.03	0.16	0.66	7.03
(b17)	2.13596	2.13594	0.16	0.64	7.03	0.16	0.64	7.03
(b18)	2.02461	2.02459	0.18	0.71	7.03	0.18	0.71	7.03
(b19)	1.90724	1.90725	0.18	0.84	7.03	0.18	0.84	7.03
(b20)	2.05156	2.10411	0.16	0.72	7.03	0.15	0.66	7.03
(b21)	2.02378	2.02378	0.17	0.75	7.03	0.17	0.75	7.03

Continued on next page

nr.	NBO charge		Gd1 NBO occupation			Gd1 NBO occupation		
	Gd1	Gd2	6s	5d	4f	6s	5d	4f
(b22)	1.97761	1.95962	0.17	0.76	7.03	0.17	0.78	7.03
(b23)	2.07141	2.07002	0.16	0.69	7.03	0.16	0.69	7.03
(b24)	1.96961	1.96958	0.16	0.78	7.03	0.16	0.78	7.03
(b25)	2.37735	2.37735	0.07	0.40	7.04	0.07	0.40	7.04
(b26)	2.37454	2.37375	0.10	0.45	7.02	0.10	0.46	7.02
(b27)	2.01986	2.04226	0.18	0.77	7.01	0.18	0.74	7.01

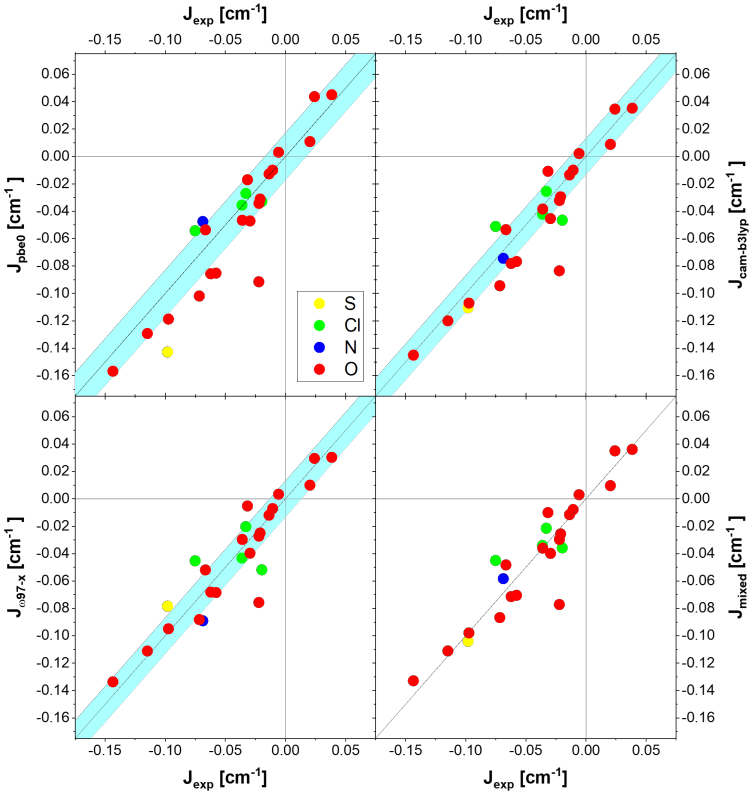

Figure A.9.: Overview of the functionals pbe0, cam-b3lyp, ωb97-x and an average of the three with bh-lyp compared to the experimental values. The light blue areas indicate the MAE.

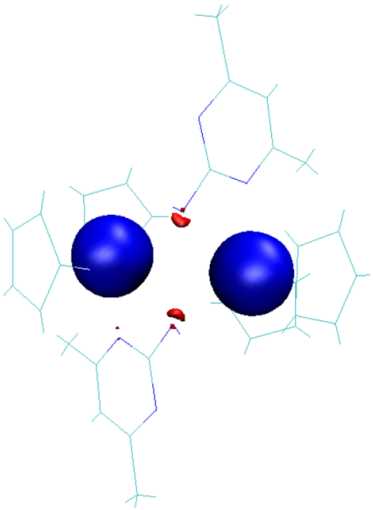

Figure A.10.: Spin density of **(b8)** using the m06 functional. A clear difference between alpha (blue) and beta (red) spin density is indicative a spin polarization.

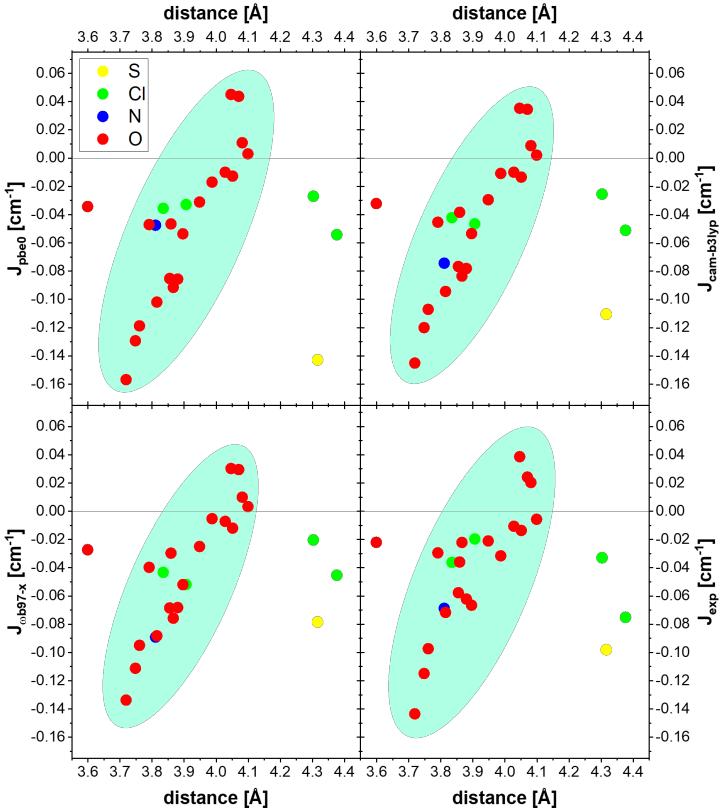

Figure A.11.: Calculated (for the functionals pbe0, cam-b3lyp, and ωb97-x) and fitted coupling constants against the Gd(III)-Gd(III) distance. The green area highlights a possible correlation.

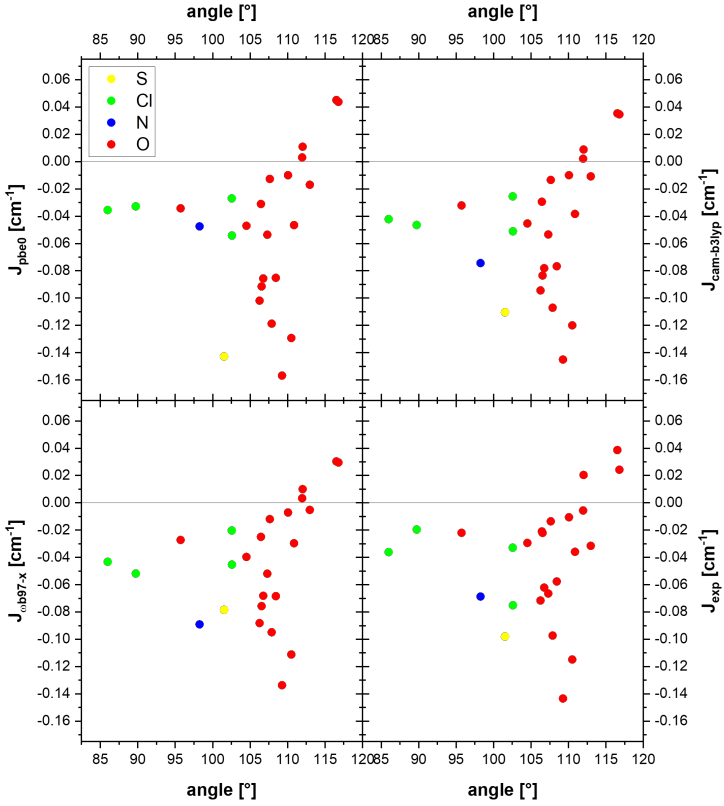

Figure A.12.: Calculated (for the functionals pbe0, cam-b3lyp, and ωb97-x) and fitted coupling constants against the Gd(III)-L-Gd(III) angle.

Table A.9.: Calculated coupling constants for all interactions in compounds **(b28)** and **(b29)**.

Interaction	**bh-lyp**	**pbe0**	**cam-b3lyp**	**ωb97-x**
	Gd1	[cm^{-1}]	[cm^{-1}]	[cm^{-1}]
		(b28)		
Gd1-Gd2	-0.034991	-0.055269	-0.051447	-0.047307
Gd1-Gd3	0.001500	0.002332	0.001809	0.001571
Gd1-Gd4	-0.001174	-0.003031	-0.002710	-0.003001
Gd2-Gd3	-0.000963	-0.002989	-0.002724	-0.002960
Gd2-Gd4	0.000418	0.000660	0.000419	0.000313
Gd3-Gd4	-0.034937	-0.055242	-0.051459	-0.047318
		(b29)		
Gd1-Gd2	0.000775	0.001476	0.000280	-0.000428
Gd1-Gd3	0.001082	0.001244	-0.000154	-0.000635
Gd1-Gd4	0.000937	0.000815	0.000015	-0.000528
Gd2-Gd3	-0.041791	-0.071508	-0.066742	-0.058849
Gd2-Gd4	-0.039504	-0.066890	-0.063211	-0.057235
Gd3-Gd4	-0.020962	-0.036760	-0.034891	-0.029612

Table A.10.: Calculated coupling constants the truncated models of compound **(b29)**.

Interaction	**bh-lyp**	**pbe0**	**cam-b3lyp**	**ωb97-x**
	Gd1	[cm^{-1}]	[cm^{-1}]	[cm^{-1}]
		(truncation 1)		
Gd2-Gd3	-0.043908	-0.075283	-0.070115	-0.062221
Gd2-Gd4	-0.040926	-0.070256	-0.066764	-0.060052
Gd3-Gd4	-0.023144	-0.040678	-0.038215	-0.032362
		(truncation 2)		
Gd2-Gd3	-0.043841	-0.075467	-0.069984	-0.061205
Gd2-Gd4	-0.041689	-0.071227	-0.066770	-0.059396
Gd3-Gd4	-0.022573	-0.040888	-0.038018	-0.032061
		(truncation 3)		
Gd2-Gd3	-0.037955	-0.063630	-0.059914	-0.052753
Gd2-Gd4	-0.036028	-0.060419	-0.057118	-0.051643
Gd3-Gd4	-0.018095	-0.031364	-0.030138	-0.025479
		(truncation 4)		
Gd2-Gd3	-0.038055	-0.063458	-0.059769	-0.052594
Gd2-Gd4	-0.035808	-0.059955	-0.056884	-0.051460
Gd3-Gd4	-0.018132	-0.031736	-0.030420	-0.026083

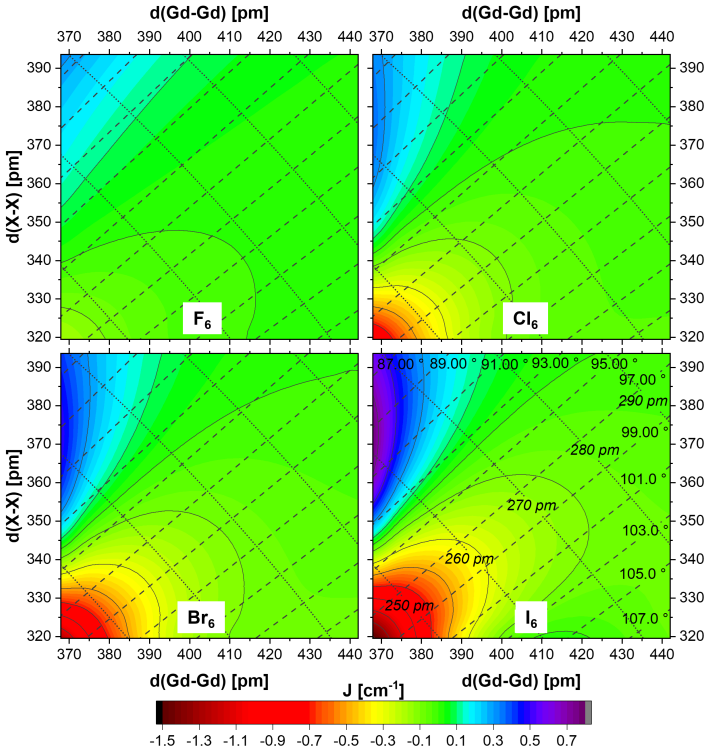

Figure A.13.: A heat map of the calculated coupling constants on the 15x15 grid for Gd_2X_6 (X=F, Cl, Br, I) using the bh-lyp functional. In addition to the Gd-Gd distance (x-axis) and bridging X-X distances (y-axis) two dependent parameters are shown: The Gd-X distance is shown as dotted lines, the Gd-X-Gd angle is shown as dashed lines.

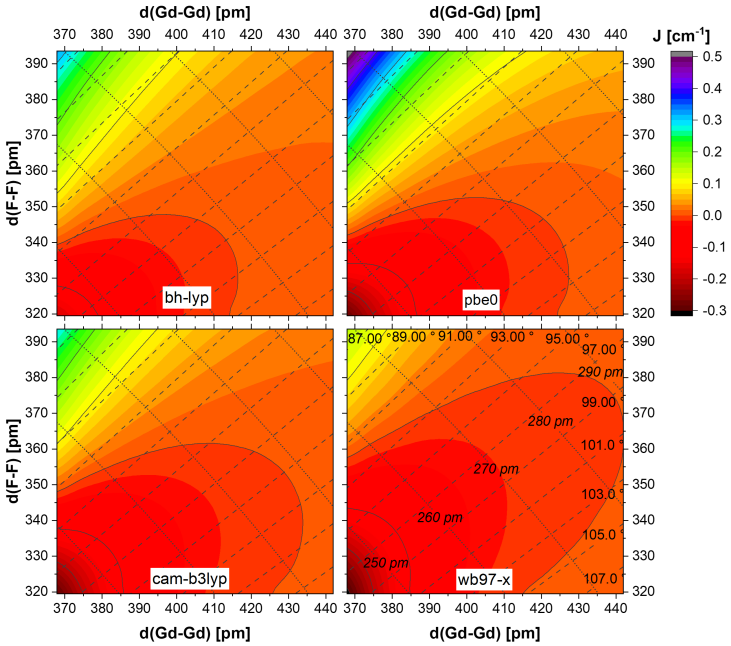

Figure A.14.: A heat map of the calculated coupling constants on the 15x15 grid for Gd_2F_6 using the four different functionals. In addition to the Gd-Gd distance (x-axis) and bridging X-X distances (y-axis) two dependent parameters are shown: The Gd-X distance is shown as dotted lines, the Gd-X-Gd angle is shown as dashed lines.

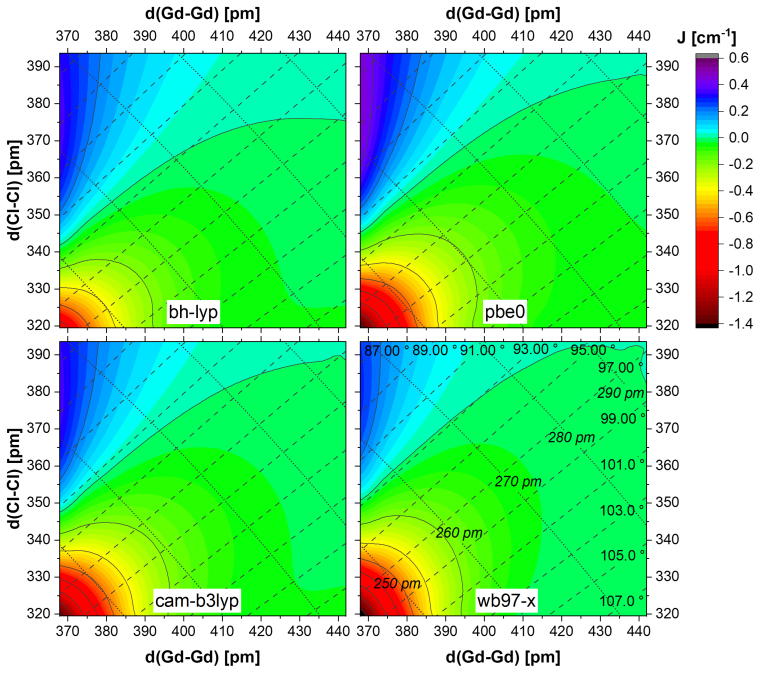

Figure A.15.: A heat map of the calculated coupling constants on the 15x15 grid for Gd_2Cl_6 using the four different functionals. In addition to the Gd-Gd distance (x-axis) and bridging X-X distances (y-axis) two dependent parameters are shown: The Gd-X distance is shown as dotted lines, the Gd-X-Gd angle is shown as dashed lines.

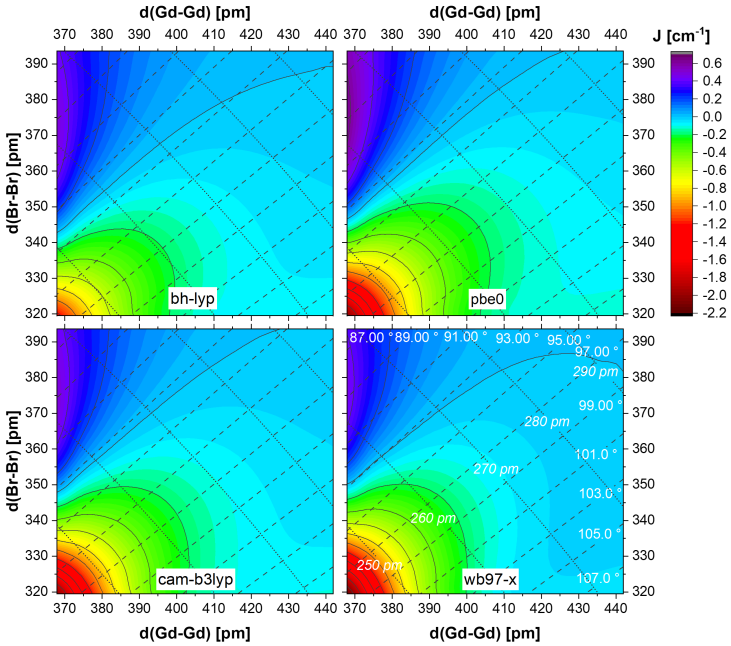

Figure A.16.: A heat map of the calculated coupling constants on the 15x15 grid for Gd_2Br_6 using the four different functionals. In addition to the Gd-Gd distance (x-axis) and bridging X-X distances (y-axis) two dependent parameters are shown: The Gd-X distance is shown as dotted lines, the Gd-X-Gd angle is shown as dashed lines.

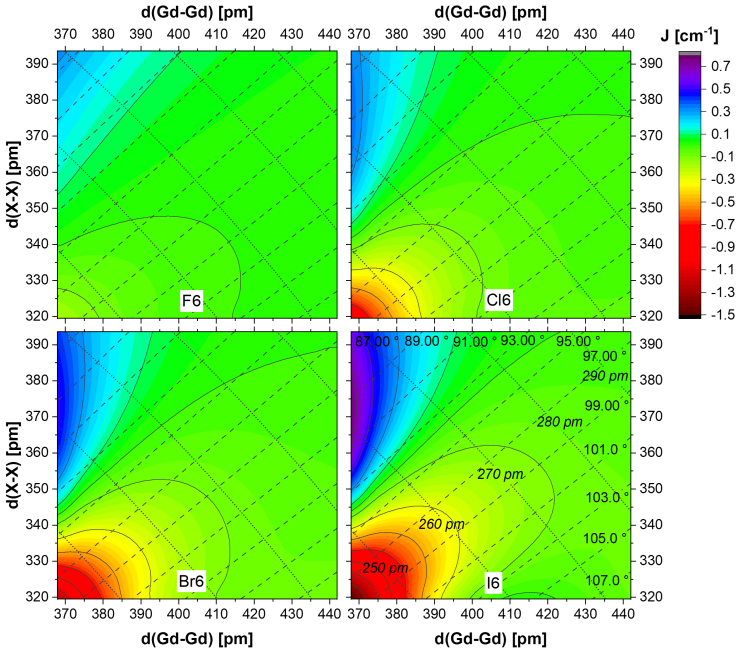

Figure A.17.: A heat map of the calculated coupling constants on the 15x15 grid for Gd_2I_6 using the four different functionals. In addition to the Gd-Gd distance (x-axis) and bridging X-X distances (y-axis) two dependent parameters are shown: The Gd-X distance is shown as dotted lines, the Gd-X-Gd angle is shown as dashed lines.

Table A.11.: Equations optimized using the four geometric features: Gd-Gd-distance (GdGd), X-X distance (XX), Gd-X-Gd angle (angle), and Gd-X distance (GdX). The equations are optimized with PySr as outlined in Section 7.2. The equations marked with a * are those shown in Figure A.18.

Complex	Loss	equation
		Gd_2F_6
1	0.004914	0.033078
3	0.003558	angle * -0.049514964
4	0.00131	0.029192584 / exp(angle)
5	0.001206	exp(exp(angle) * -8.748476)
6	0.00094	(0.036931507 / exp(angle)) + -0.026456194
7	0.000819	0.48807332 / exp(exp(angle) * 5.0722513)
8	0.000113	((XX * 0.030604664) + 0.018641124) / exp(GdGd)
10*	8.44E-05	(((XX + 0.51925844) * 0.030604977) / exp(GdGd)) - -0.007988524
12	6.80E-05	(((XX - -0.6906375) * exp(1.2688942 - GdGd)) + GdGd) * 0.008604313
13	6.72E-05	(exp(-3.487008 - GdGd) * (XX - inv(-3.4821322 - GdGd))) + 0.013426781
14	6.12E-05	(((XX - -0.5798722) * (XX + exp(1.8408784 - GdGd))) + angle) * 0.0049021486
15	5.95E-05	(((XX - -0.5588628) * (GdX + exp(2.4577618 - GdGd))) + exp(angle)) * 0.0026870235
		Gd_2Cl_6
1	0.025372	-0.02016
3	0.015971	XX * 0.09905848
5	0.01357	XX / (GdX + 8.384999)
6	0.005234	0.06690589 * (XX / exp(GdGd))
8	0.003602	XX / (exp(GdGd + 2.8408375) + XX)
9	0.003494	(XX / exp(GdGd + exp(GdX))) * 0.10590434
10	0.001609	-0.027696809 * ((angle + 0.52770364) / exp(GdX + GdGd))
11	0.001006	(-0.25519514 * (angle + 0.70066446)) / exp(GdX + exp(angle))
12	0.000703	(angle + 0.6759111) * (-0.04677632 / exp((GdX + GdX) - XX))
13	0.00038	((angle + 0.62549984) * -0.19024096) / exp((GdX * 1.2543544) + exp(angle))
15*	0.000186	((angle + 0.6171059) / (exp(exp(angle * 0.71096945) + GdX) - 0.13395151)) * -0.1954038

Continued on next page

complex	Loss	equation
		Gd_2Br_6
1	0.051761	-0.05079
3	0.033687	XX * 0.14371537
4	0.032652	-0.062152416 / exp(GdX)
5	0.024939	XX / (GdX + 5.3818107)
6	0.011507	(XX / exp(GdX)) * 0.07220161
8	0.008944	(XX * 0.13317773) / exp(XX + angle)
9	0.006811	(XX / exp(GdGd + exp(GdX))) * 0.15466988
10	0.003488	((angle + 0.57133603) * -0.038712643) / exp(GdGd + GdX)
11	0.002204	(angle + 0.74694055) * (-0.36337972 / exp(GdX + exp(angle)))
12	0.001068	log((angle * -0.33877203) + 0.7679608) / exp(GdX + exp(angle))
13	0.001032	((angle * -0.2902453) + -0.19959764) / exp(GdX - (exp(angle) * -0.72248095))
14	0.000715	log((angle * -0.30552712) + 0.80194306) / exp(exp(angle) + (GdX / 0.8862922))
15*	0.000447	((angle * -0.2358854) + -0.1522002) / (exp(GdX - (exp(angle) * -0.6840789)) + -0.071560524)
		Gd_2I_6
1	0.095159	-0.06741
3	0.068491	XX / 5.659476
4	0.063892	-0.07986422 / exp(GdX)
5	0.049689	XX / (GdX + 4.2408156)
6	0.025013	exp(-2.0593207 - GdGd) * XX
7	0.023827	XX / exp(exp(GdGd + 0.9768942))
8	0.018153	exp(-1.8340856 - GdGd) * (-0.93317753 - angle)
9	0.015371	XX * exp(-1.5797935 - (exp(GdX) + GdGd))
10	0.01258	exp(-2.9786458 - (GdX + GdGd)) * (-0.5669866 - angle)
11	0.001422	exp(-0.69417053 - (exp(angle) + GdX)) * (-0.7443413 angle)
13	0.000858	(-0.70540375 - angle) * exp(-0.8329607 - ((GdX * 1.1196458) + exp(angle)))
15*	0.000455	(-0.6982602 - angle) * (exp(-0.90933025 - (exp(angle) + (GdX * 1.1541191))) + 0.019144751)

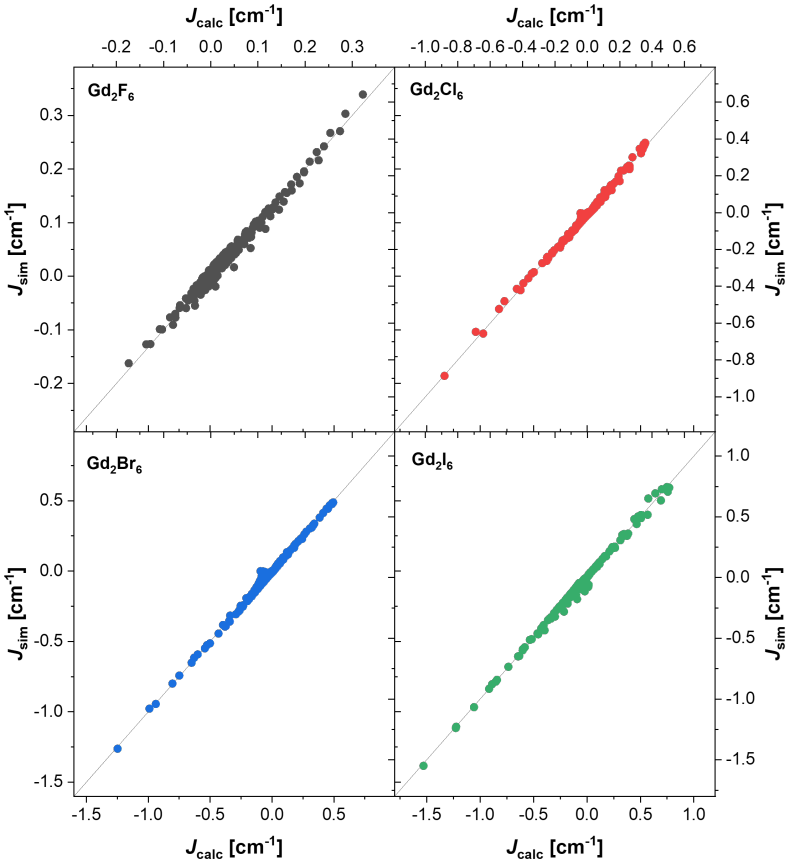

Figure A.18.: Correlation between the calculated coupling constants using the bh-lyp functional J_{calc} and the ones simulated using symbolic regression. Plotted here are the best equations as summarized in Table A.11

Table A.12.: Equations optimized using the two dependent features csotrace (sum of overlap between α and β corresponding spin orbitals) and DS2 (difference in spin-polarization of HS- and BS-state) The equations are optimized with PySr as outlined in Section 7.2.

Complex	Loss	equation
		Gd_2F_6
1	0.004914	0.033078
3	0.001842	DS2 * 0.06455256
5	0.000747	0.03310013 - (DS2 * -0.06455105)
9	0.000366	(csotrace * -0.020349221) - ((DS2 * -0.07030326) + -0.033098087)
11	0.00021	((-3.3465722 - csotrace) * ((DS2 * -0.01761139) - -0.017831799)) - -0.08777646
13	0.000169	(((csotrace * (csotrace - DS2)) * -0.01176176) - (DS2 * -0.05802995)) + 0.041535113
15	0.000148	((csotrace * (csotrace - (DS2 * 1.6565571))) * -0.010515079) - ((DS2 * -0.054599486) + -0.038689263)
		Gd_2Cl_6
1	0.025372	-0.02016
3	0.018387	DS2 * 0.085990556
5	0.00555	(csotrace - DS2) * -0.121624246
7	0.005144	((csotrace + 0.16562597) - DS2) * -0.121656924
9	0.001955	(csotrace - DS2) * ((-2.2396994 - csotrace) * 0.03682191)
11	0.001198	((DS2 * 1.3394213) - csotrace) * ((csotrace * 0.041775044) + 0.06598397)
13	0.000843	(DS2 * 0.09466117) + (csotrace * (((csotrace - -1.0423484) - DS2) * -0.046879597))
15	0.000662	((DS2 * 0.091647334) + 0.015220935) - (csotrace * (((csotrace - -0.80243677) - DS2) * 0.051754303))
		Gd_2Br_6
1	0.05176	-0.05071
3	0.032768	DS2 * 0.14685646
5	0.011766	(DS2 - csotrace) * 0.15863664
7	0.005603	(csotrace - DS2) / (csotrace + -7.496779)
9	0.002763	((4.243118 - DS2) / (csotrace + -6.3811736)) - -0.63476413
11	0.002261	(csotrace * ((csotrace * -0.0562383) + -0.05745561)) - (DS2 / -6.315554)

Continued on next page

complex	Loss	equation
13	0.001223	((csotrace * ((-0.8696033 - (csotrace - DS2)) * -0.45604083)) - DS2) / -7.724682
15	0.001026	(csotrace * (((DS2 * 0.04363108) + -0.048399247) + (csotrace * -0.061144833))) - (DS2 / -7.328618)
		Gd_2I_6
1	0.095159	-0.06741
3	0.030492	DS2 * 0.26307327
5	0.011914	DS2 / (4.7005014 - csotrace)
7	0.007729	(DS2 - 0.28755328) / (4.865017 - csotrace)
9	0.003839	(csotrace * (csotrace * -0.07554408)) - (DS2 * -0.22467984)
11	0.002581	((csotrace - DS2) * (csotrace * -0.060223255)) - (DS2 * -0.19046606)
13	0.002447	((((csotrace + (DS2 * -0.7143097)) * csotrace) * 0.32846355) - DS2) * -0.19771948
15	0.002375	((csotrace * (csotrace + ((DS2 - 0.25071) * -0.7254717))) * -0.06195311) - (DS2 * -0.19851327)

Table A.13.: Fits for the coupling constants using Equation 3.6 for the four Gd_2X_6 model complexes. These are the parameters used to simulate the values in Figure 3.34.

Gd_2X_6	a	Err_a	b	Err_b	c	Err_c
F	-0.01176176	0.00135035	0.05802995	0.00090300	0.04153511	0.00092361
Cl	-0.06692352	0.00128453	0.07630504	0.00248152	0.0255926	0.00262574
Br	-0.07581687	0.00150792	0.11439832	0.00337575	0.01336771	0.00355042
I	-0.06060433	0.00135035	0.19001297	0.00377549	0.00253674	0.00374593

Table A.14.: Correlation parameters between the fits from Table A.13 and the calculated values from BS-DFT. Calculated are R2-value, Mean Square Error (MSE), Root Mean Square Error (RMSE) and Pearson correlation coefficient (r_P).

Gd_2X_6	R2	MSE	RMSE	r_P
F	0.9657	0.0002	0.0130	0.9827
Cl	0.9464	0.0014	0.0369	0.9728
Br	0.9529	0.0024	0.0494	0.9762
I	0.9729	0.0026	0.0508	0.9864

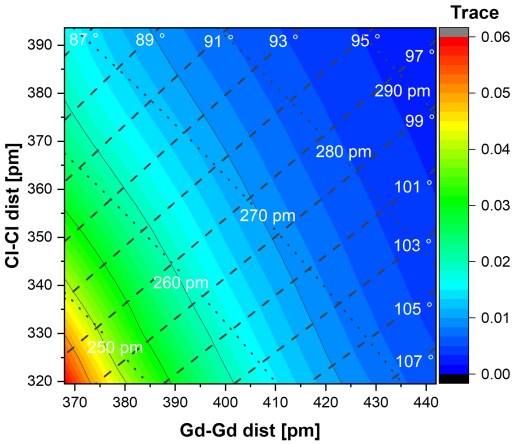

Figure A.19.: Trace of the cso-spatial overlap matrix plotted on the grid for the Gd_2Cl_6-molecule and the bh-lyp functional.

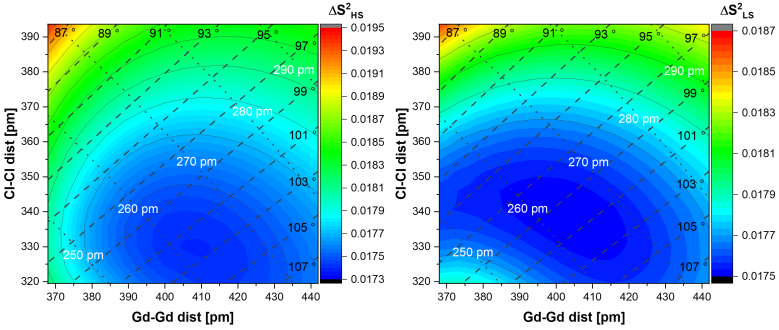

Figure A.20.: Spin polarization of the HS- and LS states in the Gd_2Cl_6 molecule using the bh-lyp functional.

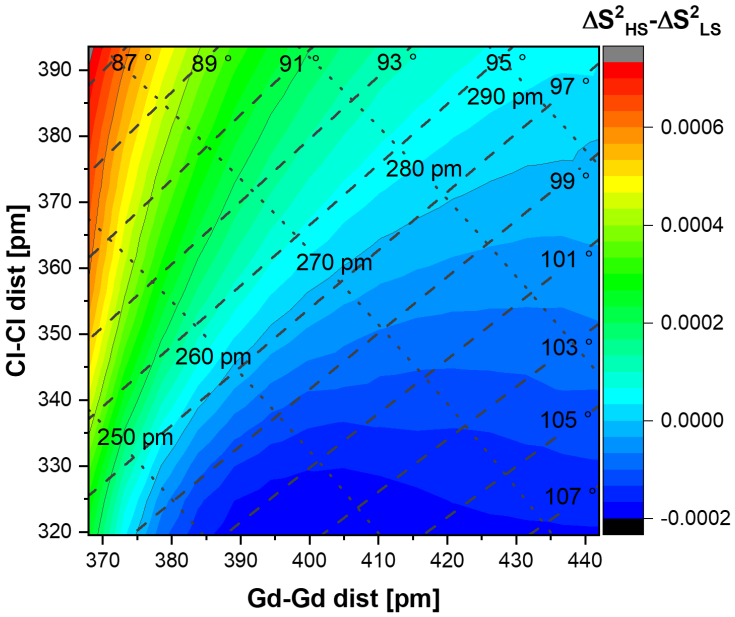

Figure A.21.: Difference in spin polarization between the HS- and LS states in the Gd_2Cl_6 molecule using the bh-lyp functional.

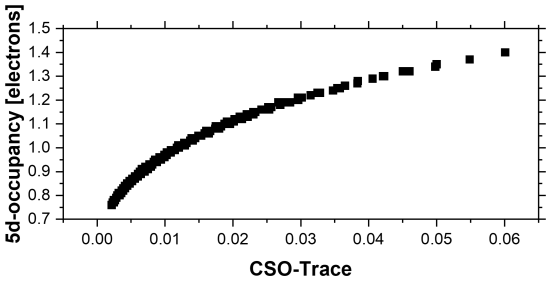

Figure A.22.: 5d-NBO occupation plotted against the trace of the spatial overlap matrix of corresponding spin orbitals in the BS-state for Gd_2Cl_6 calculated with bh-lyp.

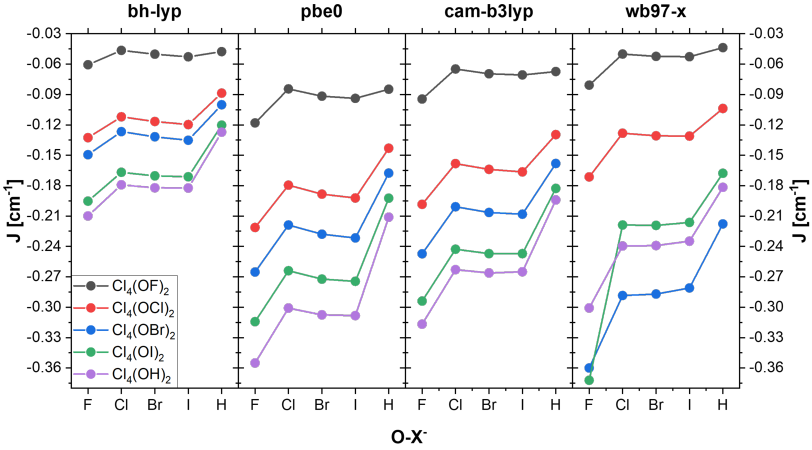

Figure A.23.: Using the basic models optimized for the different hypohalite ions (lines) the halogen atom is varied (x-axis). The calculated coupling is shown for the different functionals used.

A.3. Appendix for Section 4.2

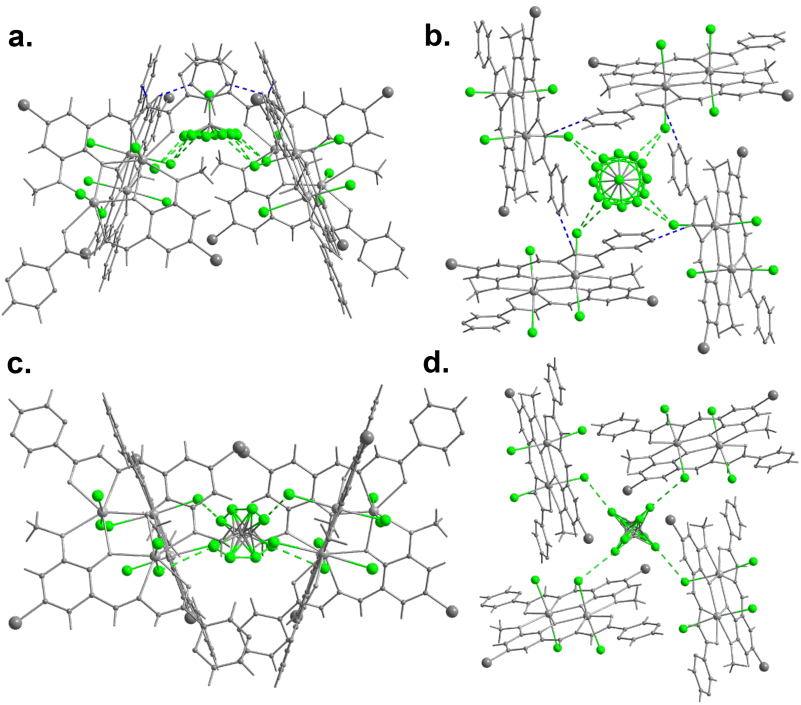

Figure A.24.: Top and side view of the crystal cavities with a/b. C_4- and c/d. S_4-symmetry. Only Cl-atoms are highlighted.

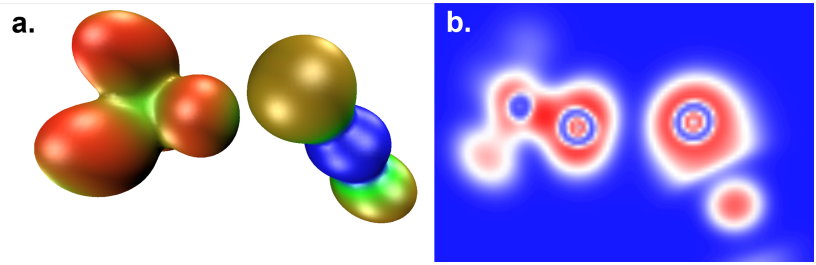

Figure A.25.: a. MEP for the geometry of C_4(1). For simplicity, the Dy-complex was replaced with a $[YCl_2]^+$-moitiy. The MEP is plotted on an isodensity of 0.02 from 0.09 (red) to 0.50 (blue). b. ELF of the same interaction, plotted from 0 (blue) to 1 (red) The σ-hole can be clearly observed in both pictures. The density was optimized on a m06-2x-d4/rij/def2-QZVP level of theory.

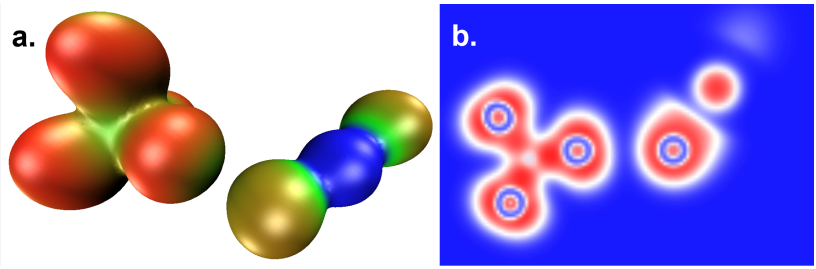

Figure A.26.: a. MEP for the geometry of C_4(2). For simplicity, the Dy-complex was replaced with a $[YCl_2]^+$-moitiy. The MEP is plotted on an isodensity of 0.02 from 0.09 (red) to 0.50 (blue). b. ELF of the same interaction, plotted from 0 (blue) to 1 (red) The σ-hole can be clearly observed in both pictures. The density was optimized on a m06-2x-d4/rij/def2-QZVP level of theory.

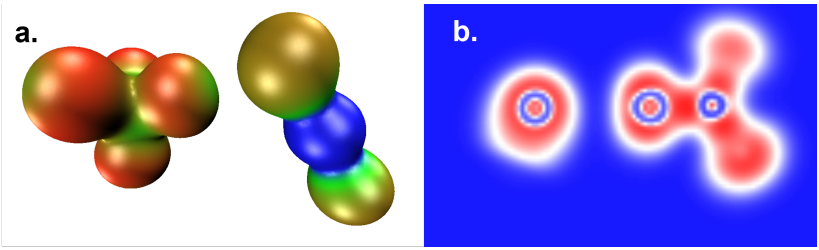

Figure A.27.: a. MEP for the geometry of $S_4(2)$. For simplicity, the Dy-complex was replaced with a $[YCl_2]^+$-moitiy. The MEP is plotted on an isodensity of 0.02 from 0.09 (red) to 0.50 (blue). b. ELF of the same interaction, plotted from 0 (blue) to 1 (red) The σ-hole can be clearly observed in both pictures. The density was optimized on a m06-2x-d4/rij/def2-QZVP level of theory.

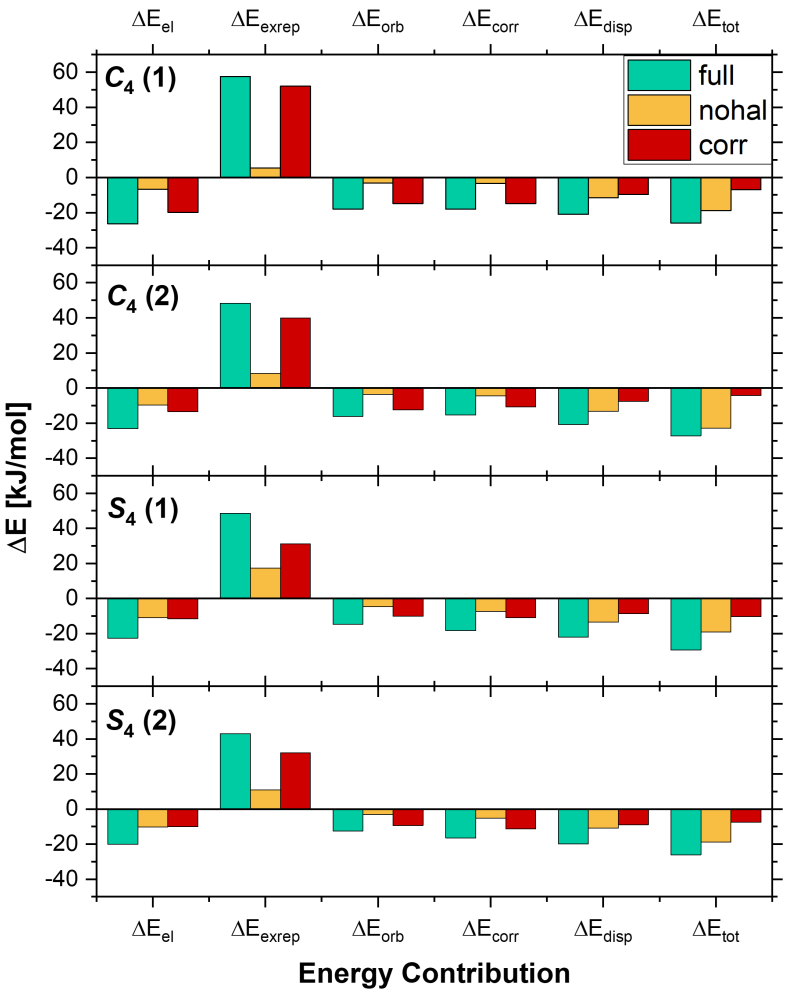

Figure A.28.: Energy Decomposition Analysis (EDA) for the four interactions investigated for compound **(X1)**. Shown are the full interaction, the interaction with Cl replaced to H (nohal) and the difference (corr).

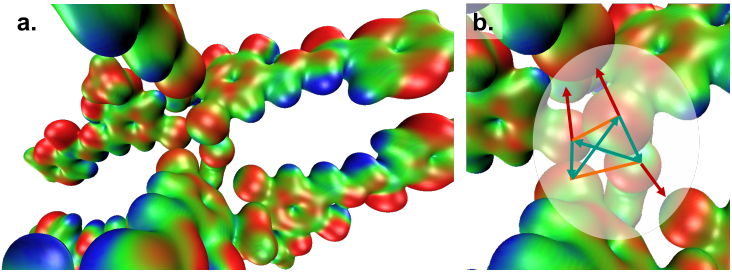

Figure A.29.: a. Molecular Electrostatic Potential (MEP) for the central halogen bonding motif in compound **(X2)**. The isodensity is 0.02, the color ranges from 0.04 (red) to 0.20 (blue). The calculation was carried out on a model cluster including the full, protonated ligands on a m06-2x-d4/rij/def2-TZVP level of theory using S_4-symmetry. The blue areas at the Br-atoms indicate the σ hole. b. A zoomed in version of a., overlayed with a schematic of which halogen bonds can be observed. Adapted with permission from Ref. [380].

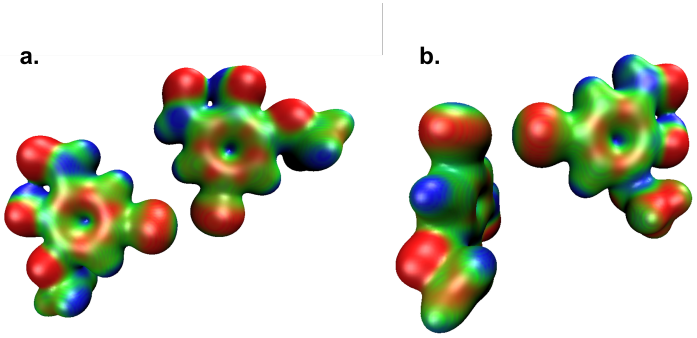

Figure A.30.: a. Molecular Electrostatic Potential (MEP) for the halogen bond between Br2 and Br6 motif in compound **(X2)**. b. Molecular Electrostatic Potential (MEP) for the halogen bond between Br3 and Br5 motif in compound **(X2)**. The isodensity is 0.02, the color ranges from 0.04 (red) to 0.15 (blue). The calculation was carried out on a model cluster using the 5-bromo-*o*-vanillin ligand on a m06-2x-d4/rij/def2-TZVP level of theory Adapted with permission from Ref. [380].

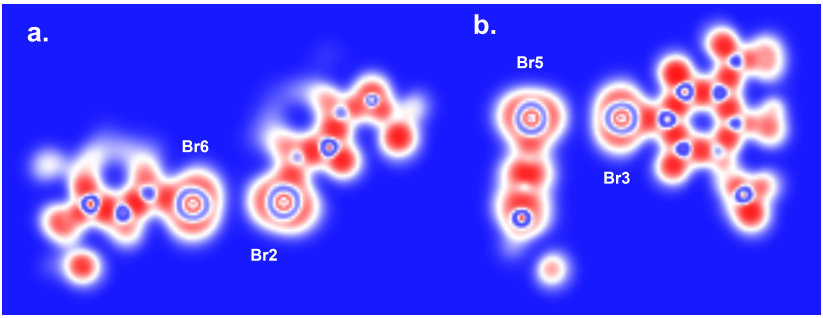

Figure A.31.: a. Electron Localization Function (ELF) for the halogen bond between Br2 and Br6 motif in compound **(X2)**. b. Molecular Electrostatic Potential (MEP) for the halogen bond between Br3 and Br5 motif in compound **(X2)**. The calculation was carried out on a model cluster using the 5-bromo-*o*-vanillin ligand on a m06-2x-d4/rij/def2-TZVP level of theory Adapted with permission from Ref. [380].

Table A.15.: Summary of different total interaction energies as well as calculated synergy energies. "Full" references the models with Br, "diff" those corrected with the replacement of H to Br. Importantly, while the total energies differ significantly, when looking at the relative synergy effect it is the same with and without the H-correction.

	$E_{int,X}$	$E_{syn,X}$	$\%_X$	$E_{int,corr}$	$E_{syn,corr}$	$\%_{corr}$
m06-2x	-84.4	-30.5	36.2	-70.8	-26.5	37.4
pbe0	-97.0	-25.8	26.6	-83.2	-21.1	25.4
cam-b3lyp	-89.7	-22.9	25.5	-79.0	-20.0	25.5
Average	-90.3	-26.4	29.5	-77.7	-22.6	29.4

A.4. Appendix for Section 4.3

Table A.16.: Crystallographic data for compounds **(C1)** and **(C2)**.

Compound	**(C1)**	**(C2)**
Empirical formula	$C_{30}H_{28}Cl_2Dy_2N_{12}O_{16}$	$C_{30}H_{28}Br_2Dy_2N_{12}O_{16}$
Formula weight (g/mol)	1208.54	1297.46
Temperature (K)	180	180
Crystal system	triclinic	triclinic
Space group	$P\bar{1}$	$P\bar{1}$
a [Å]	9.8599(4)	9.7831(4)
b [Å]	10.1327(4)	10.1821(4)
c [Å]	11.2465(4)	11.2969(4)
$\alpha[^\circ]$	66.943(3)	111.790(3)
$\beta[^\circ]$	109.2070(10)	104.529(3)
$\gamma[^\circ]$	89.688(3)	92.852(3)
Volume [$Å^3$ **]**	991.00(7)	998.63(7)
Z	1	1
ρ_{calc} **(g/cm^3)**	2.025	2.157
μ **(mm^{-1})**	3.963	5.800
F(000)	586.0	622.0
Crystal size (mm^3)	0.2 Œ 0.15 Œ 0.1	0.15 Œ 0.12 Œ 0.1
Radiation	Mo Kα (λ = 0.71073)	Mo Kα (λ = 0.71073)
2 Θ range for data collection ($^\circ$)	4.106 to 69.324	4.058 to 64.986
Index ranges	-15 $\leq$ h$\leq$ 15, -7 $\leq$ k $\leq$ 16, -17 $\leq$ l $\leq$ 17	-14 $\leq$ h $\leq$ 14, -10 $\leq$ k $\leq$ 15, -17 $\leq$ l $\leq$ 15
Reflections collected	21811	17023
Independent reflections	7942 [R_{int} = 0.0383, R_{sigma} = 0.0367]	7173 [R_{int} = 0.0274, R_{sigma} = 0.0339]
Data/restraints/parameters	7942/0/282	7173/0/282
Goodness-of-fit on F^2	0.989	1.044
Final R indexes [I>=2σ(I)]	R_1 = 0.0288, wR_2 = 0.0697	R_1 = 0.0351, wR_2 = 0.0896
Final R indexes [all data]	R_1 = 0.0359, wR_2 = 0.0712	R_1 = 0.0449, wR_2 = 0.0930
Largest diff. peak/hole / e Å^{-3}	1.62/-1.79	2.14/-1.44

Table A.17.: Crystallographic data for compound **(C3)**.

Compound	**(C3)**
Empirical formula	$C_{57}H_{64}Br_4Gd_2N_{14}O_{19}$
Formula weight (g/mol)	1883.36
Temperature (K)	180
Crystal system	triclinic
Space group	$P\bar{1}$
a [Å]	13.9068(3)
b [Å]	14.1822(3)
c [Å]	19.4857(4)
$\alpha[^\circ]$	87.146(2)
$\beta[^\circ]$	84.685(2)
$\gamma[^\circ]$	65.275(2)
Volume [Å^3]	3475.56(14)
Z	2
ρ_{calc} **(g/cm^3)**	1.800
μ **(mm^{-1})**	4.269
F(000)	1848.0
Crystal size (mm^3)	0.18 Œ 0.14 Œ 0.1
Radiation	Mo Kα (λ = 0.71073)
2 Θ range for data collection (°)	3.714 to 61.998
Index ranges	-20 $\leq$ h $\leq$ 20, -20 $\leq$ k $\leq$ 20, -28 $\leq$ l $\leq$ 16
Reflections collected	55063
Independent reflections	21846 [R_{int} = 0.0332, R_{sigma}= 0.0744]
Data/restraints/parameters	21846/8/868
Goodness-of-fit on F^2	0.945
Final R indexes [I>=2σ(I)]	R_1 = 0.0393, wR_2 = 0.0893
Final R indexes [all data]	R_1 = 0.0785, wR_2 = 0.0975
Largest diff. peak/hole / e Å^{-3}	1.45/-1.05

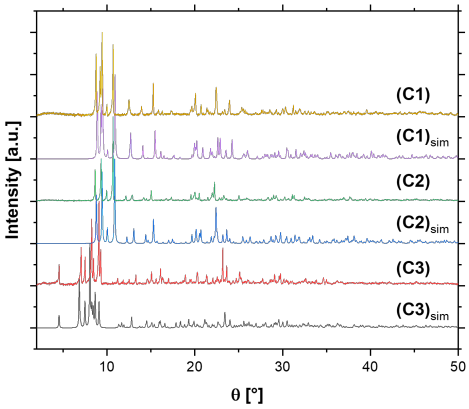

Figure A.32.: Simulated and measured PXRD patterns for compounds **(C1)**, **(C2)** and **(C3)**.

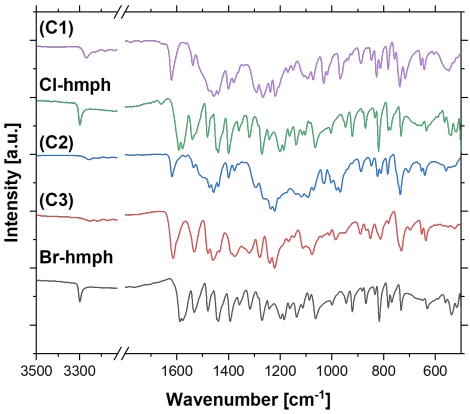

Figure A.33.: Measured ATR-IR spectra for compounds **(C1)**, **(C2)**, **(C3)** as well as the two ligands Cl-hmph and Br-hmph.

Table A.18.: BS-DFT coupling constants for compounds **(C1)**–**(C3)** using the respective Gd(III) model structures with two spins S = 7/2 and calculated with four DFT-functionals. Values are given in cm^{-1}.

Functional	C1	C2	C3
bhlyp	-0.09842047	-0.102142974	-0.054016751
pbe0	-0.163779337	-0.169334562	-0.090342425
cam-b3lyp	-0.155749724	-0.161221415	-0.081777636
ωb97-x	-0.147154886	-0.152777908	-0.072403386

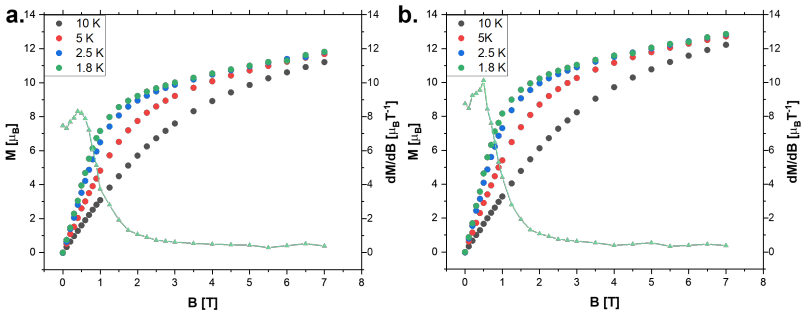

Figure A.34.: Isothermal magnetization at four different at 1.8 K, 2.5 K, 5 K and 10 K as well as the derivative at 1.8 K for compounds a. **(C1)**, b. **(C2)**. Maxima in the derivative can be observed between 0.4 T and 0.5 T indicating a antiferromagnetic interaction.

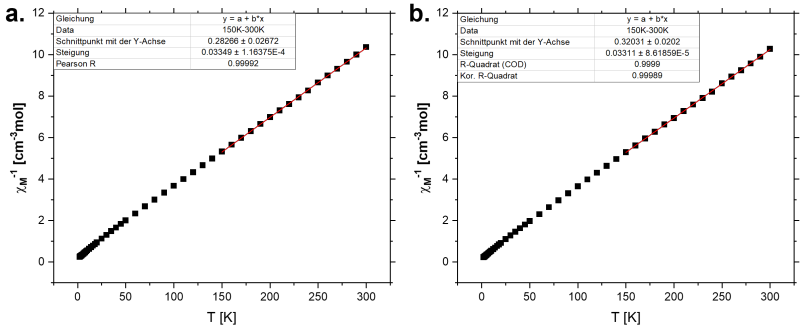

Figure A.35.: Curie-Weiss plot and linear fit above 150 K for compounds a. **(C1)**, b. **(C2)**. The linear fits intersect with the x-axis at around -0.1 K indicating antiferromagnetic interaction.

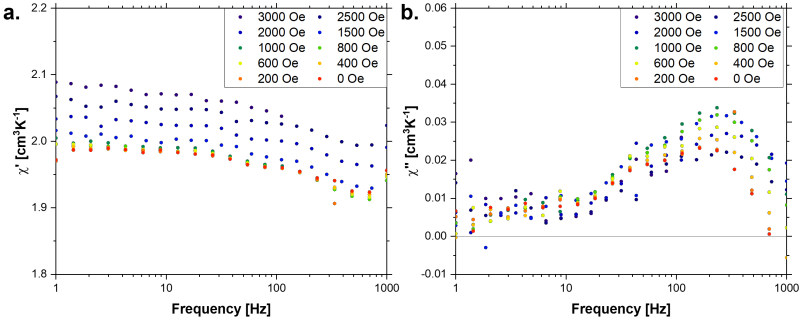

Figure A.36.: a. In-phase susceptibility at 2 K and different fields for **(C1)**. a. Out-of-phase susceptibility at 2 K and different fields for **(C1)**.

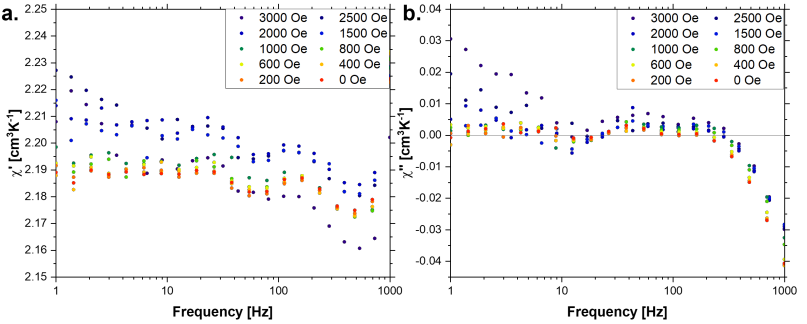

Figure A.37.: a. In-phase susceptibility at 2 K and different fields for **(C2)**. a. Out-of-phase susceptibility at 2 K and different fields for **(C2)**.

Figure A.38 shows the preliminary data evaluation for DC-SQUID measurements performed in compound **(C3)**. The expected high temperature susceptibility value for two Gd(III) ions is 15.75, significantly lower than the observed 16.5. However, the downturn of this curve at higher temperatures cannot be explained. This cannot be solely attributed to the diamagnetic correction considering that a multiple of the noted eicosane would have to be used which is unreasonable. Furthermore, the high field value of the magnetization should approach 14, whereas 25.2 is observed. As in the χT-data no saturation can be observed.

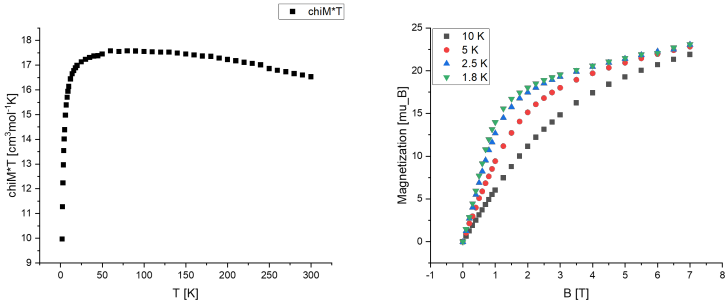

Figure A.38.: Preliminary results of DC-SQUID measurements for compound **(C3)**. χT (left) and magnetization (right).

A.5. Appendix for Section 5.2

Table A.19.: Crystallographic data for compounds **(C4)** and **(C5)**.

Compound	**(C4)**	**(C5)**
Empirical formula	$C_{21.75}CH_{36.5}Cl_3DyN_9O_9$	$C_{50}H_{52}Dy_2N_{20}Na_2O_{14}$
Formula weight (g/mol)	836.95	1528.09
Temperature (K)	180	180
Crystal system	monoclinic	monoclinic
Space group	$P2_1/c$	$C2/c$
a [Å]	13.0383(3)	31.1894(9)
b [Å]	17.8958(3)	8.7247(2)
c [Å]	14.9963(3)	30.6457(8)
$\alpha[^\circ]$	90	90
$\beta[^\circ]$	113.585(2)	133.119(2)
$\gamma[^\circ]$	90	90
Volume [$Å^3$ **]**	3206.81(12)	6087.1(3)
Z	4	4
ρ_{calc} **(g/cm^3)**	1.734	1.667
μ **(mm^{-1})**	13.935	2.529
F(000)	1676.0	3032.0
Crystal size (mm^3)	0.1 Œ 0.09 Œ 0.08	0.24 Œ 0.2 Œ 0.16
Radiation	Ga Kα (λ = 1.34143)	Mo Kα (λ = 0.71073)
2 Θ range for data collection ($^\circ$)	6.436 to 124.998	3.578 to 65.256
Index ranges	-12 $\leq$ h $\leq$ 17, -18 $\leq$ k $\leq$ 23, -19 $\leq$ l $\leq$ 19	-39 $\leq$ h $\leq$ 44, -13 $\leq$ k $\leq$ 12, -44 $\leq$ l $\leq$ 27
Reflections collected	24646	24559
Independent reflections	7618 [R_{int} = 0.0204, R_{sigma} = 0.0205]	10108 [R_{int} = 0.0274, R_{sigma} = 0.0443]
Data/restraints/parameters	7618/14/474	10108/0/403
Goodness-of-fit on F^2	1.034	0.976
Final R indexes [I>=2σ(I)]	R_1 = 0.0267, wR_2 = 0.0666	R_1 = 0.0307, wR_2 = 0.0726
Final R indexes [all data]	R_1 = 0.0309, wR_2 = 0.0685	R_1 = 0.0456, wR_2 = 0.0752
Largest diff. peak/hole / e Å^{-3}	0.92/-0.95	0.80/-0.72

Table A.20.: Crystallographic data for compound **(C6)**.

Compound	**(C6)**
Empirical formula	$C_{52}H_{58}Dy_4N_{18}O_{20}$
Formula weight (g/mol)	1905.138
Temperature (K)	180
Crystal system	monoclinic
Space group	$P2_1/c$
a [Å]	11.2402(4)
b [Å]	19.7762(5)
c [Å]	15.1599(5)
$\alpha[^\circ]$	90
$\beta[^\circ]$	109.055(3)
$\gamma[^\circ]$	90
Volume [Å^3]	3185.22(18)
Z	2
ρ_{calc} **(g/cm^3)**	1.986
μ **(mm^{-1})**	24.476
F(000)	1806.1
Crystal size (mm^3)	0.06 Œ 0.04 Œ 0.03
Radiation	Ga Kα (λ = 1.34143)
2 Θ range for data collection (°)	6.62 to 124.98
Index ranges	-14 $\leq$ h $\leq$ 14, -26 $\leq$ k $\leq$ 14, -20 $\leq$ l $\leq$ 17
Reflections collected	30394
Independent reflections	7611 [R_{int} = 0.0433, R_{sigma} = 0.0574]
Data/restraints/parameters	7611/0/431
Goodness-of-fit on F^2	0.855
Final R indexes [I>=2σ(I)]	R_1 = 0.0280, wR_2 = 0.0525
Final R indexes [all data]	R_1 = 0.0517, wR_2 = 0.0570
Largest diff. peak/hole / e Å^{-3}	0.94/-1.23

Table A.21.: RMSD of the excited KD energies between structures with different H-optimization of **(C4)** for models m0–m4 in cm^{-1}.

	m0	**m1**	**m2**	**m3**	**m4**
unopt-opt1	1.271	0.605	2.923	3.179	1.998
unopt-opt2	20.427	9.761	2.825	11.045	9.376
unopt-opt3	17.588	7.256	5.016	8.275	9.290
opt1-opt2	19.350	9.496	3.592	8.035	7.630
opt1-opt3	16.499	6.998	7.485	5.871	7.481
opt2-opt3	3.319	2.817	4.671	4.324	1.519

Table A.22.: RMSD of the excited KD energies between structures with different H-optimization of **(C4)** for models m5–m9 in cm^{-1}.

	m5	**m6**	**m7**	**m8**	**m9**
unopt-opt1	1.072	2.304	2.615	2.599	2.475
unopt-opt2	14.125	50.811	66.083	57.587	54.938
unopt-opt3	10.490	45.771	60.405	51.940	52.085
opt1-opt2	14.628	48.668	63.628	55.136	52.629
opt1-opt3	10.998	43.633	57.953	49.489	49.783
opt2-opt3	4.337	5.102	5.702	5.680	2.947

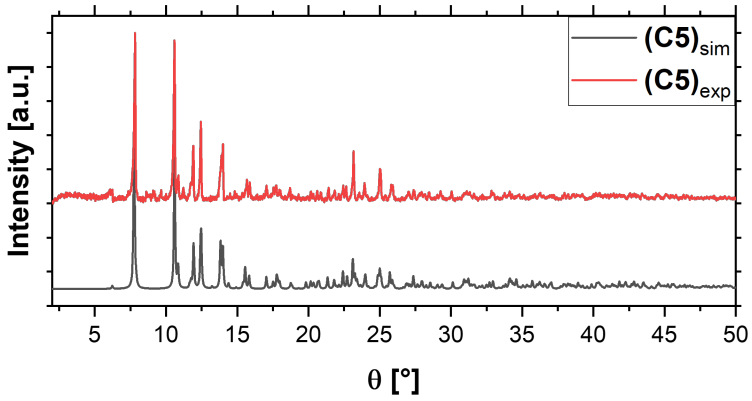

Figure A.39.: Simulated and measured PXRD for compound **(C5)**.

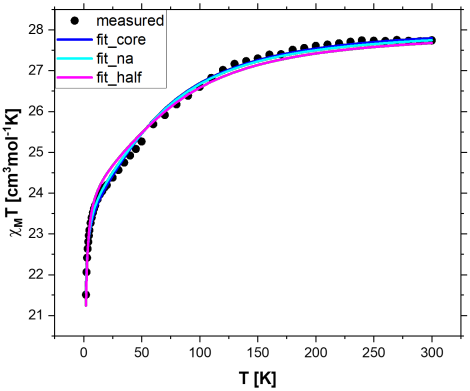

Figure A.40.: Simulated and measured χ_MT values where the ESOs for the respective single center models where used and a coupling constant between the two centers fitted.

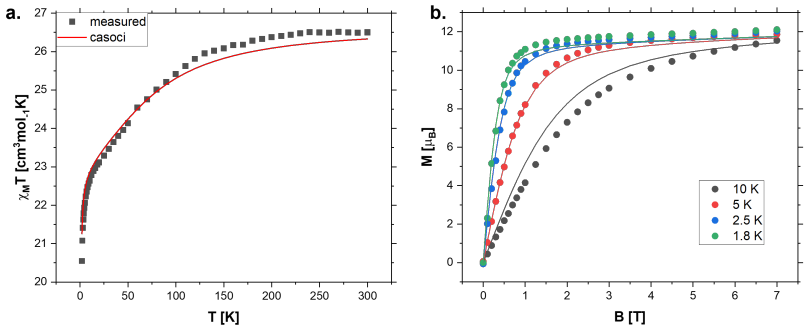

Figure A.41.: Simulated susceptibility and isothermal magnetization curves by using only the ESOs from CASOCI for the full model, the ground state dipolar coupling for a pseudospin $\tilde{S}$ = 15/2 and fitting a g-factor to the experimental data. This is compared to the theoretical value of 4/3 this resulted in g = 1.29 and 1.52, respectively. The large deviation can in part be attributed to the loss of MeCN crystal solvent.

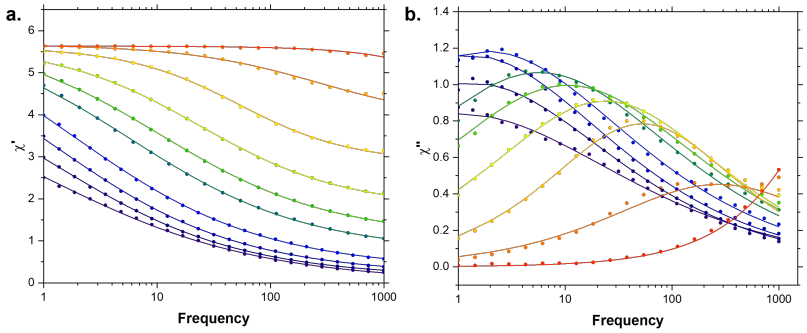

Figure A.42.: a. In-phase b. Out-of-phase susceptibility measured for compound **(C5)** at 2 K at different fields as well as a generalized Debye fit.

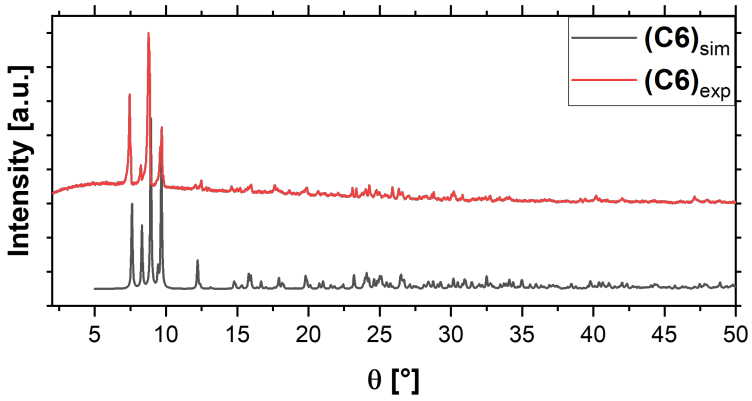

Figure A.43.: Simulated and measured PXRD for compound **(C6)**.

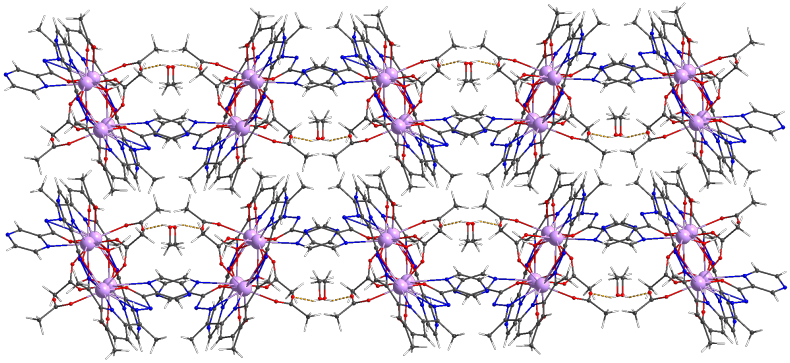

Figure A.44.: Packing diagram for compound **(C6)** viewed along the crystallographic c-axis.

A.6. Appendix for Section 5.3

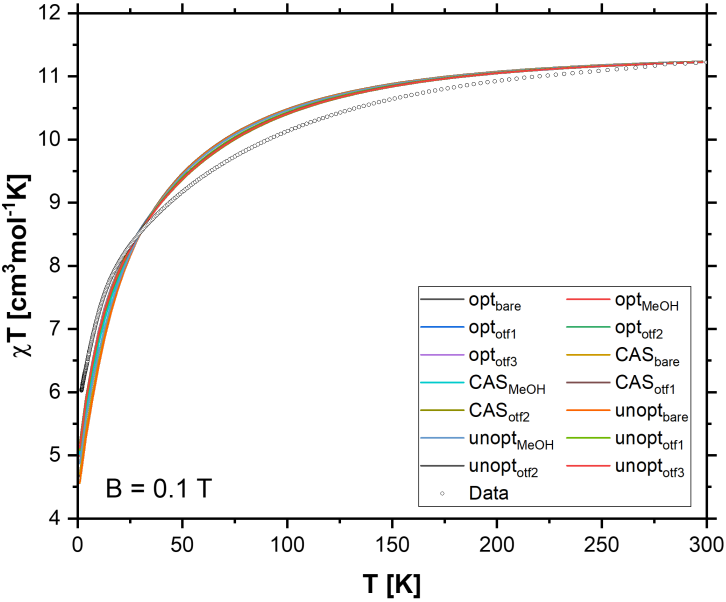

Figure A.45.: Molar susceptibility calculated for all model structures and calculations for compound **(G1)**. Reprinted with permission from Ref. [**arneth.2026**].

Table A.23.: R^2, Mean Absolute Error (MAE), and Root Mean Squared Error/Deviation (RMSD) for models of **(G1)** with respect to the experimental data. MAE and RMSD are given in cm^{-1}.

	bare	**MeOH**	**otf1**	**otf2**	**otf3**
unopt					
R^2	0.993	0.948	0.949	0.953	0.959
MAE	0.514	1.622	1.718	1.670	1.552
RMSD	0.779	1.947	2.047	1.906	1.784
opt					
R^2	0.979	0.917	0.966	0.968	0.977
MAE	0.920	2.062	1.436	1.289	1.085
RMSD	1.227	2.533	1.899	1.557	1.391
cas					
R^2	0.985	0.932	0.983	0.986	-
MAE	0.764	1.837	1.008	1.288	-
RMSD	1.124	2.237	1.124	1.537	-

Table A.24.: Relaxation times calculated for **(G1)**. 1. The model by Yin *et al.* based on time dependent perturbation theory.[412,413] 2. The model by Prokof'ev and Stamp based on instanton theory.[415–417] All relaxation times are given in 10^{-8} s. 3. The magnetic transition moment in the lowest KD.

	opt			CAS			unopt		
model	Yin	PS	TM	Yin	PS	TM	Yin	PS	TM
bare	2.2	0.4	0.2998	2.5	0.5	0.2770	1.3	0.3	0.4171
MeOH	1.5	0.3	0.3813	1.5	0.3	0.3971	5.5	1.1	0.1646
otf1	0.5	0.0	0.7228	0.5	0.1	0.6695	0.7	0.1	0.5801
otf2	0.9	0.2	0.5154	1.2	0.2	0.4493	0.9	0.2	0.5132
otf3	0.9	0.2	0.5091	-	-	-	0.9	0.2	0.5187

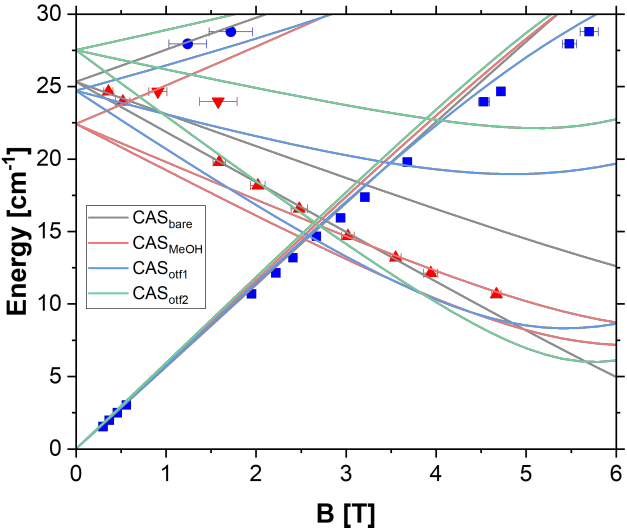

Figure A.46.: Measured and simulated Zeeman-splitting for compound **(G1)** using the cas-models. Reprinted with permission from Ref. [**arneth.2026**].

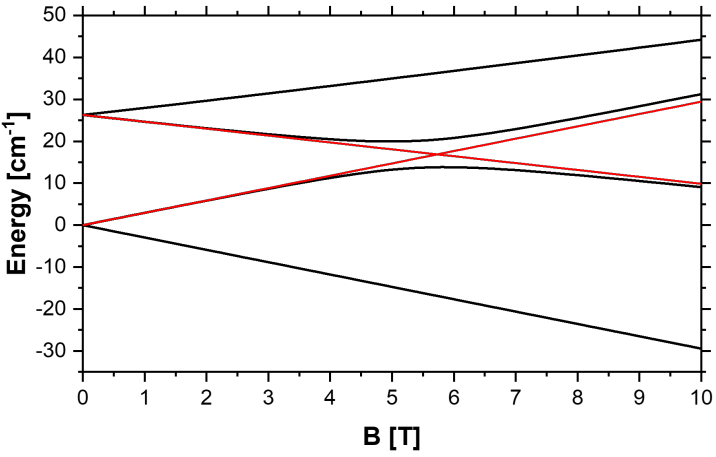

Figure A.47.: Zeeman diagram for the lowest two KDs of the model opt-otf3 for **(G1)**. The red line indicates a linear continuation of the slopes close to zero field. Reprinted with permission from Ref. [**arneth.2026**].

A.7. Appendix for Section 5.4

Table A.25.: Crystallographic data for compounds **(C7)** and **(C8)**.

Compound	**(C7)**	**(C8)**
Empirical formula	$C_{20}H_{18.5}Cl_2DyN_{10.5}O_9$	$Dy_2N_{14}Cl_4C_{40}H_{40}O_{18}$
Formula weight (g/mol)	783.35	1471.66
Temperature (K)	180	180
Crystal system	monoclinic	monoclinic
Space group	*C*2/*c*	$P2_1/c$
a [Å]	26.5554(7)	19.9982(4)
b [Å]	14.1961(3)	11.3000(2)
c [Å]	15.1979(4)	28.0941(6)
$\alpha[^\circ]$	90	90
$\beta[^\circ]$	105.529(2)	110.543(2)
$\gamma[^\circ]$	90	90
Volume [Å^3]	5520.2(2)	5945.0(2)
Z	8	4
ρ_{calc} **(g/cm^3)**	1.885	1.644
μ **(mm^{-1})**	15.595	14.498
F(000)	3072.0	2888.0
Crystal size (mm^3)	0.06 Œ 0.05 Œ 0.04	0.2 Œ 0.083 Œ 0.02
Radiation	Ga Kα (λ = 1.34143)	Ga Kα (λ = 1.34143)
2 Θ range for data collection ($^\circ$)	6.01 to 124.996	7.408 to 127.976
Index ranges	-34 $\leq$ h $\leq$ 35, -13 $\leq$ k $\leq$ 18, -20 $\leq$ l $\leq$ 16	-26 $\leq$ h $\leq$ 24, -14 $\leq$ k $\leq$ 12, -26 $\leq$ l $\leq$ 37
Reflections collected	48302	43936
Independent reflections	6675 [R_{int} = 0.0424, R_{sigma} = 0.0352]	14398 [R_{int} = 0.0352, R_{sigma} = 0.0344]
Data/restraints/parameters	6675/7/417	14398/1/849
Goodness-of-fit on F^2	0.949	1.001
Final R indexes [I>=2σ(I)]	R_1 = 0.0247, wR_2 = 0.0523	R_1 = 0.0378, wR_2 = 0.0965
Final R indexes [all data]	R_1 = 0.0383, wR_2 = 0.0545	R_1 = 0.0478, wR_2 = 0.1012
Largest diff. peak/hole / e Å^{-3}	0.78/-0.61	1.21/-1.40

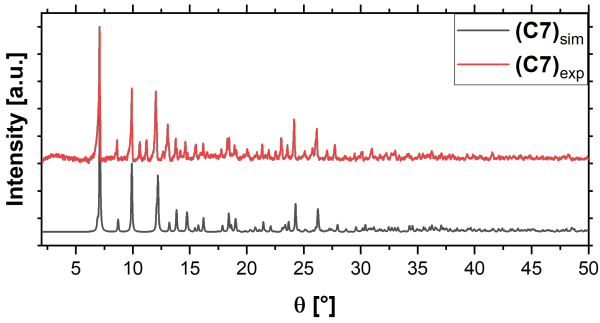

Figure A.48.: Simulated and measured PXRD for **(C7)**.

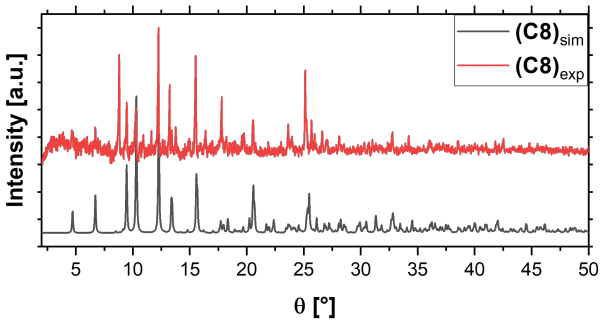

Figure A.49.: Simulated and measured PXRD for **(C8)**.

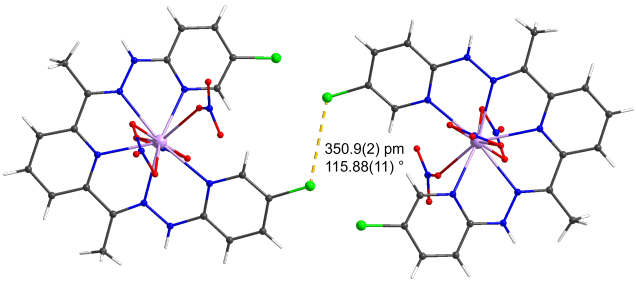

Figure A.50.: Shortest intermolecular Cl-Cl contact in **(C7)**.

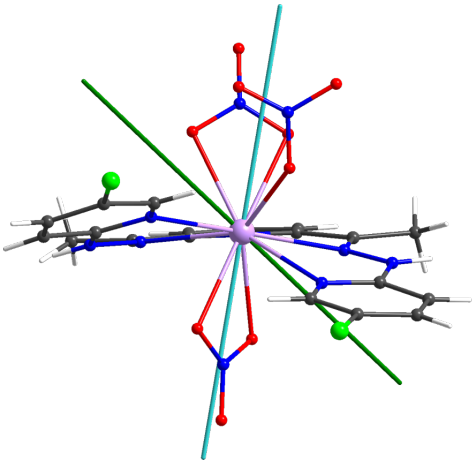

Figure A.51.: Ground state magnetic main axis of **(C7)** calculated with CASOCI (green) for the model with optimized H positions and calculated with a purely electrostatic model MAGELLAN (blue).

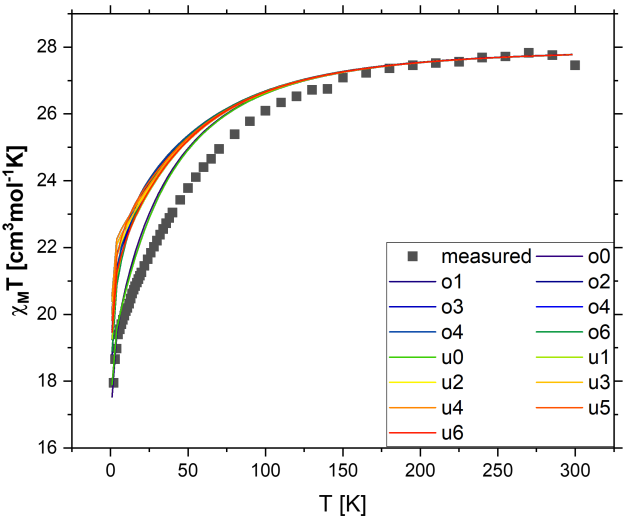

Figure A.52.: Measured versus simulated χ_MT versus T plots for **(C8)** for the 7 different simulated models.

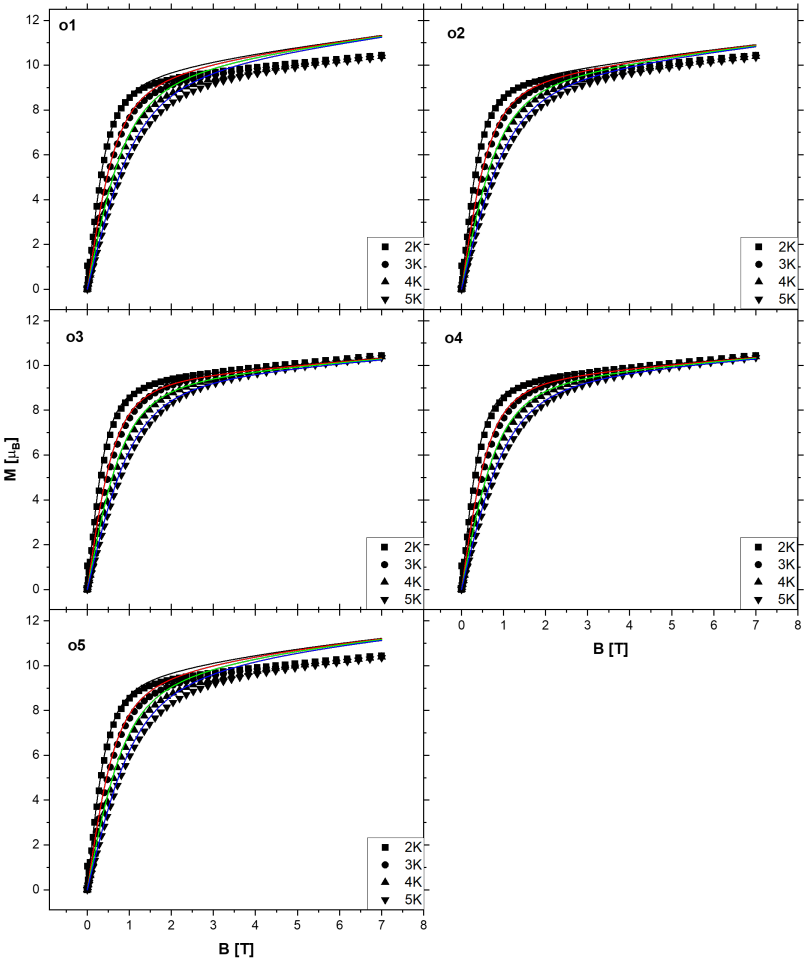

Figure A.53.: Measured versus simulated M versus B plots for compound **(C8)** for five different simulated models. o refers to the fact that these include optimize H-positions, the numbers indicate the amount of included counter ions. o1 refers to a combination of structures m11, m22 and m32, o2 to m12, m23 and m33, and so on.

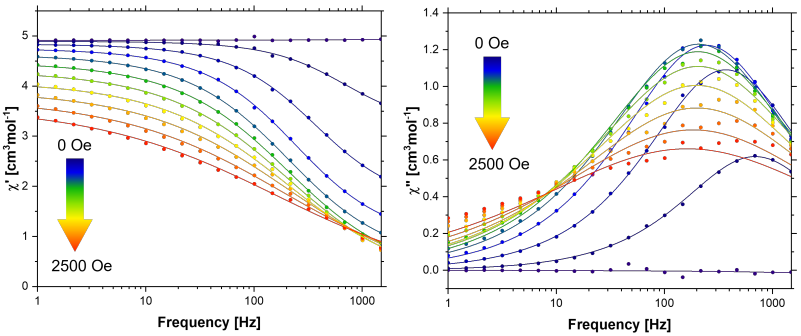

Figure A.54.: In-phase (left) and out-of-phase (right) AC-SQUID field tests from 0 Oe to 2500 Oe for **(C7)** fitted with a general Debye model.

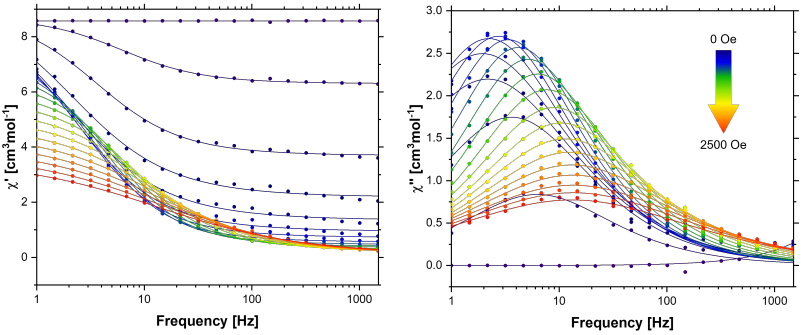

Figure A.55.: In-phase (left) and out-of-phase (right) AC-SQUID field tests from 0 Oe to 2500 Oe for **(C8)** fitted with a general Debye model.

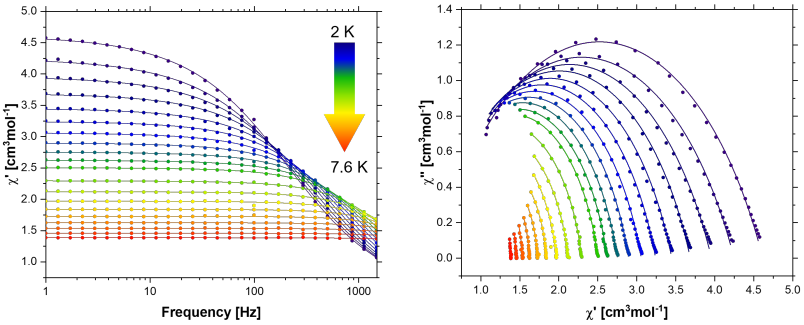

Figure A.56.: In-phase susceptibility (left) and Cole-Cole plot (right) at 1000 Oe for **(C7)** fitted with a general Debye model.

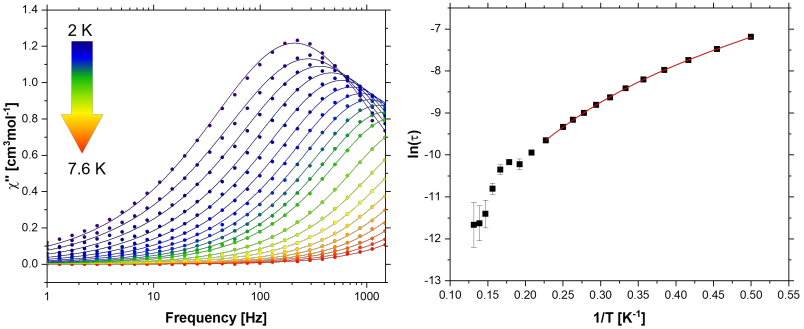

Figure A.57.: Out-of-phase susceptibility fitted with a general Debye model at 1000 Oe (left). and Arrhenius plot at 1000 Oe for **(C7)** fitted with Equation 5.7 (right).

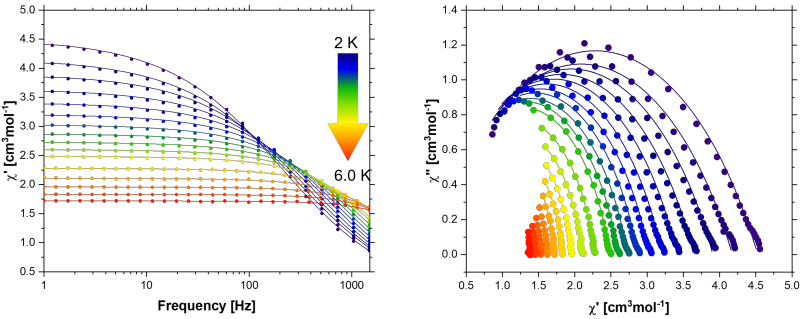

Figure A.58.: In-phase susceptibility (left) and Cole-Cole plot (right) at 1250 Oe for **(C7)** fitted with a general Debye model.

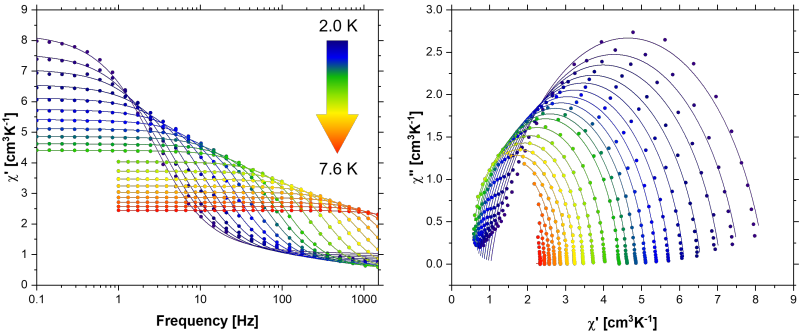

Figure A.59.: In-phase susceptibility (left) and Cole-Cole plot (right) at 1250 Oe for **(C8)** fitted with a general Debye model.

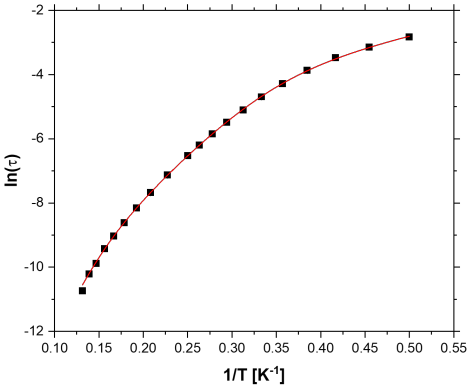

Figure A.60.: Arrhenius plot at 1250 Oe for **(C8)** fitted with Equation 5.7 modified to use two Raman processes.

A.8. Appendix for Section 5.5

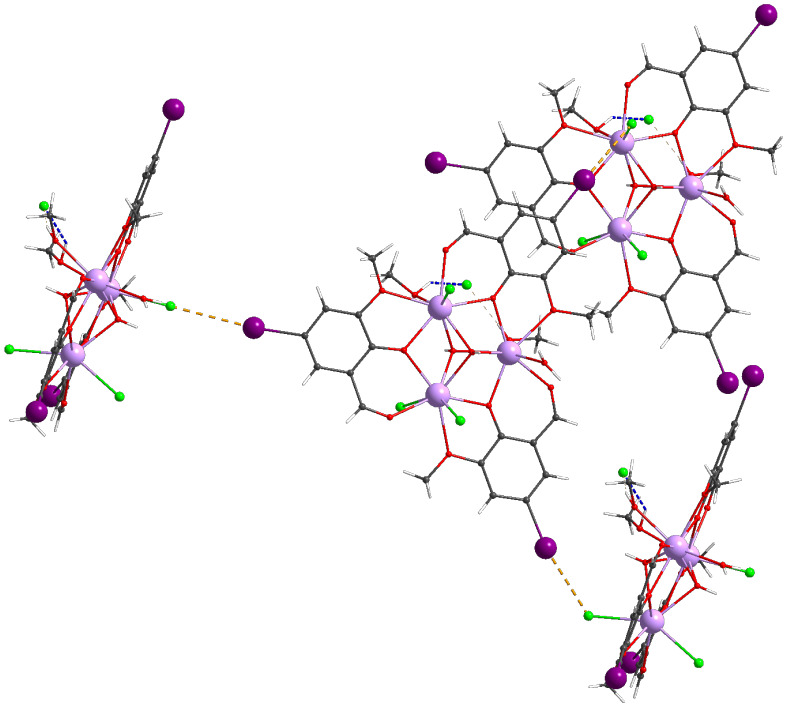

Figure A.61.: Halogen interaction between adjacent molecules in compound **(X5)**. The ligand-halogen atom acts as the XB_D for a terminal ligand atom of the neighboring molecule.

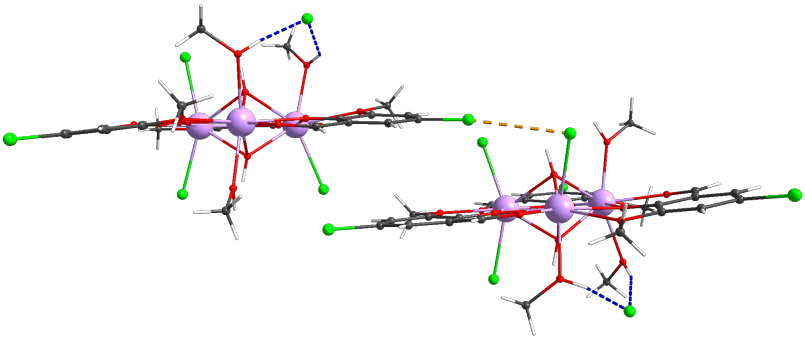

Figure A.62.: Halogen interaction between adjacent molecules in compound **(X3)**. The ligand-halogen atom acts as the XB_D for a terminal ligand atom of the neighboring molecule.

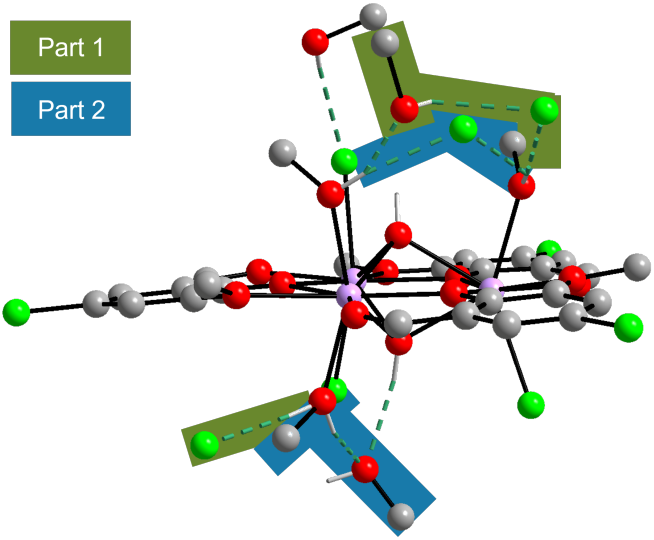

Figure A.63.: Structure of compound **(X3)** with highlighted disorders indicating which part these belong to. Most H-atoms are omitted for clarity.

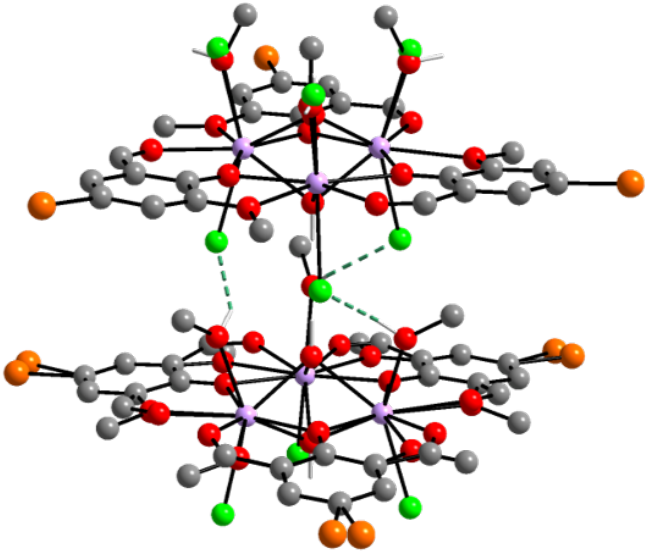

Figure A.64.: Structure of compound **(X4)** with disorders. The upper molecule is monoanionic where always one MeOH and two Cl^- ligands are coordinating on the top. The bottom molecule is monocationic and disordered in terms of the direction of the *o*-vanillin groups around the central triangle. Most H-atoms are omitted for clarity.

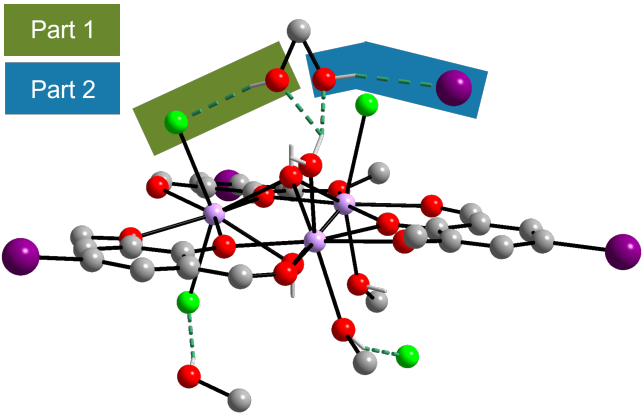

Figure A.65.: Structure of compound **(X5)** with highlighted disorders indicating which part these belong to. Most H-atoms are omitted for clarity. The additional I atom belongs to the ligand of a neighboring molecule.

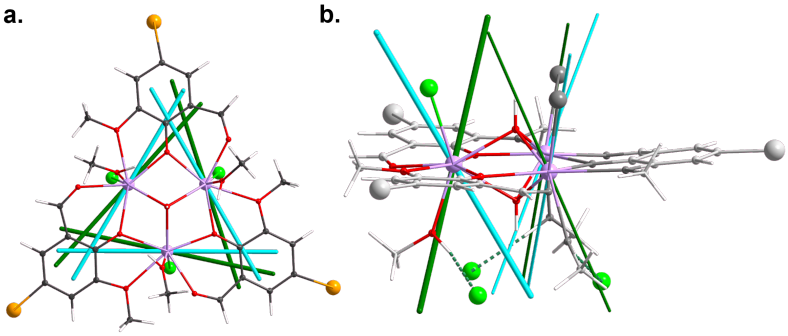

Figure A.66.: a. Axis of easy magnetization for the bare cluster in compound **(X4)** calculated with MAGELLAN[259] (blue) and CASOCI (green). b. Axis of easy magnetization for the full cluster (including Cl^--ions from neighboring molecule) in compound **(X4)** calculated with MAGELLAN[259] (blue) and CASOCI (green). Adapted with permission from Ref.[434].

B. Supplementary Information

All tables labeled with the letter B are provided in a separate document. This supplementary information can be found on KIT Open under the following link:
https://doi.org/10.35097/5s73k506yak49edj